Proceedings: Workshop on Forward Physics and QCD at the LHC, the Future Electron Ion Collider, and Cosmic Ray Physics

November 18–21, 2019
Guanajuato, Mexico

Edited by
Cristian Baldenegro, David Delepine,
Martin Hentschinski, Christophe Royon

Proceedings:
Workshop on Forward Physics and QCD at the LHC, the Future Electron Ion Collider, and Cosmic Ray Physics

November 18–21, 2019
Guanajuato, Mexico

Edited by
Cristian Baldenegro, David Delepine,
Martin Hentschinski, Christophe Royon

Published by the University of Kansas Libraries
Lawrence, KS 66045

Contents

Images

Preface: Workshop of QCD and Forward Physics at the EIC, the LHC, and Cosmic Ray Physics 2019

The 2019 edition of the Workshop on QCD and Forward Physics at the EIC, the LHC, and Cosmic Ray Physics (https://indico.cern.ch/event/823693/) took place from November 18 to November 21 in the City of Guanajuato, a picturesque colonial-style town in the center of Mexico in the state of Guanajuato. This workshop has been the 4th in the series of Workshop on QCD and Forward Physics at the EIC, the LHC, and Cosmic Ray Physics, with previous editions held in Nagoya, Japan (2015 and 2017) and Stony Brook, USA (2018).

The workshop has been attended by 46 participants from 8 countries, including a large fraction of students from Mexican universities and research institutes. During the entire workshop, 36 talks have been presented and seven discussion sessions have been held. The central topics of the workshop where heavy ion physics, production of vector mesons and intrinsic charm in the nucleon, diffractive events, future experiments and instrumentation, cosmic ray physics, forward physics, and the physics of gluon saturation. On these topics both theoretical studies and recent experimental results have been presented. Experimental results were in particular presented by the RHIC collaborations STAR and RHICf, by the LHC collaborations ATLAS, CMS,LHCb, ALICE, TOTEM, LHCf, and MoEDAL as well as the DUNE collaboration. Furthermore prospects of physics at the future Electron Ion Collider have been discussed.

Group photo of workshop participants

The workshop has been jointly organized by the University of Kansas, the Universidad de Guanajuato and the Universidad de las Americas Puebla. Financial support through Consejo Nacional de Ciencia y Tecnología (Conacyt México) is gratefully acknowledged.

The editors of these proceedings wish to thank all participants for their highly valuable contributions. In particular we would like to thank Melina Goméz Bock, Michal Broz, James Pinfold, Janusz Chwastowski, Michael Murray, Yuji Goto, Michael Murray, Yuji Goto, and Cesar Luiz Da Silva for their availability as discussion leaders as well as Irais Bautista Guzmán, Abhay Deshpande, Arturo Fernández Téllez, Melina Gómez Bock, Gerardo Herrera Corral, Antonio Ortiz Velásquez, Takashi Sako, Mario Rodríguez Cahuantzi, María Elena Tejeda Yeomans, and Paulina Valenzuela Coronado for forming part of the international advisory committee of the workshop. We also want to thank Suzanne Scales, Pam LeRow, and Marianne Reed of the University of Kansas for their valuable support in publishing these proceedings. In particular we would like to remember the contribution by Janusz Chwastowski who despite of suffering a robbery on the morning of the first day of the workshop did not let himself be deterred from presenting his presentation on the "Measurement of single diffraction using forward proton tagging at ATLAS". Last, but not least, we would like to thank the University of Guanajuato, Departamento de Física, for hosting and organizing the workshop and for its generous financial contribution and indispensable help in the local organization of this workshop.

Evolution of the pp total cross-section, through a grey disk, from the LHC energies to the limit of asymptotic energy

J. Ricardo Alvarado, Cristal Robles, Irais Bautista

E-Mail: j.ricardo.alvarado@cern.ch

Facultad de Ciencias Físico Matemáticas, Benemérita Universidad Autónoma de Puebla

Presented at the Workshop of QCD and Forward Physics at the EIC, the LHC, and Cosmic Ray Physics in Guanajuato, Mexico, November 18-21 2019

Abstract

By using the interplay between the growth of the transverse size of the proton in the high energy limit and the gluonic matter density, with unitarity saturation, we use the Grey Disc parametrization to explore the evolution of the cross section at very high energies.

1 Introduction

Recent measurements of the pp cross sections of the Auger and LHC experiments[1, 2] had increased the interest in the discussions that the proton can develop asymptotically on a Black Bisk[3–5].

The Geometric Scaling in the Froissart's limit gives

$$\mathrm{Im}F(s,t) = \mathrm{Im}F(s,0)\varphi(\tau), \tag{1.1}$$

where $\mathrm{Im}F(s,t)$ is the imaginary part of the amplitude and φ is the entire function of the scaling variable $\tau = -t\sigma^{\mathrm{tot}}$.

One can separately describe the contributions of the imaginary part of the amplitude, one of the apparent growth of the hadron 'cross-sectional' area with energy, $R(s)$, and the other that modulates the gluonic saturation scale, $f(s)$ that also depends on energy. By following the optical theorem, one neglects the real part of the amplitude, thus the average of the imaginary part of the elastic amplitude is related to gluonic saturation scale, $f(s)$:

$$\langle \mathrm{Im}G(\beta)\rangle \simeq f(s), \tag{1.2}$$

where $G(s,b)$ is the Fourier transformation of $F(s,t)$. As $s \to \infty$, $f(s) \to 1$ and $\sigma^{\mathrm{el}}/\sigma^{\mathrm{tot}} \to 1/2$, which means Black Disk behavior[6].

2 Parametrization

Using the continuous partial wave approximation, one writes the transition amplitude in terms of an integral in the impact parameter space, from which the relations of the total and elastic cross-section are obtained as follows

$$\sigma^{\text{tot}} = 2\pi \int db^2 \text{Im}G(s,b) = 2\pi R^2(s) f(s), \tag{2.3a}$$

$$\sigma^{\text{el}} = \pi \int db^2 [\text{Im}G(s,b)]^2 = \pi R^2(s) f^2(s), \tag{2.3b}$$

to the right of the previous equations are the relationships provided by the gray disk model, neglecting the contribution of the real part, and considering the high energy asymptotic regime, where $R(s)$ is proportional to a maximum angular momentum $L(s)$ as required by the Froissart bound. We have consider $R(s)$ with a logarithmic dependence on energy with the same parametrization used in [7]

$$R(s) = R_0 + \beta \ln\left(\frac{s}{s_0}\right), \tag{2.4}$$

where $\sqrt{s_0}$ is an energy threshold parameter, R_0 is a constant related to the valence quark content of beam and target particles, and the second term is a universal behavior.

For $f(s)$ we have $f(s) = 2(\gamma_1 + \gamma_2 \ln s + \gamma_3 \ln^2 s)$, as used in [8], one can reduce the parameters with out losing generality with the parametrization

$$f(s) = (\alpha + \gamma \ln(s/s_1))^2 \tag{2.5}$$

where s_1 is a threshold parameter for the Froissart bound and the t-slope $\sim \ln^2(s/s_1)$.

$$\frac{\sigma_{\text{tot}}^2}{2\sigma_{\text{el}}} = 2\pi R^2(s) \equiv \sigma_{BD} \tag{2.6}$$

gives the Black Disk formation at the very high energy $\sigma_{\text{tot}} \to \sigma_{BD}$, it predicts no analytic dependence on $f(s)$ and thus one can fix the parametrization for the radius with data in Fig. 1. By assuming the same $R(s)$ growth on np collisions we found the corresponding values to describe $f(s)$ in np collisions.

To fit the Gray Disk model parametrization 2.4 and 2.5 over the experimental data taken from the direct and indirect measurements of the cross section in pp and np collisions, from the energies of the Bevatron, Lawrence Berkeley National Laboratory (LBNL)[9], the Proton Synchroton, National Institute Machine Radiating on Downs (Nimrod), Rutherford Appleton Laboratory (RAL)[10], the German Electron Synchrotron DESY[11], the Proton Synchrotron (PS), CERN[12–17], the Alternating Gradient Synchrotron(AGS), Brookhaven National Laboratory (BNL)[18], the Particle Accelerator of the Russian Institute of High Energy Physics IHEP[19, 20], the Mirabelle Bubble Chamber, the Serpukhov Throttle[21], the Bubble Chamber [22, 23] and the Single Arm Spectrometer [24–28] of the National Accelerator Laboratory of Fermilab, and the National Acceletar Laboratory of Argonne[29, 30], the Intersecting Storage Rings (ISR) [31–38] to the energies of LHC measures measured in the TOTal Elastic and diffractive cross section Measurement (TOTEM) [39, 40] from CERN. Arriving at astronomical cosmic ray observatories such as Astrophysical Radiation with Ground-based Observatory at YangBaJing (ARGO-YBJ)[41], Akeno[42], the High Resolution detector Fly's Eye (HiRes)[43] and the observatory Pierre Auger[44]. Such data was collected by the Particle Data Group[45]. The energy of the center of mass is used, changing the data from the fixed-target experiments using the Mandelstam relations, from 10GeV to 20TeV, the fit is shown in figure 1 and the parameters obtained for this system in the table 1.

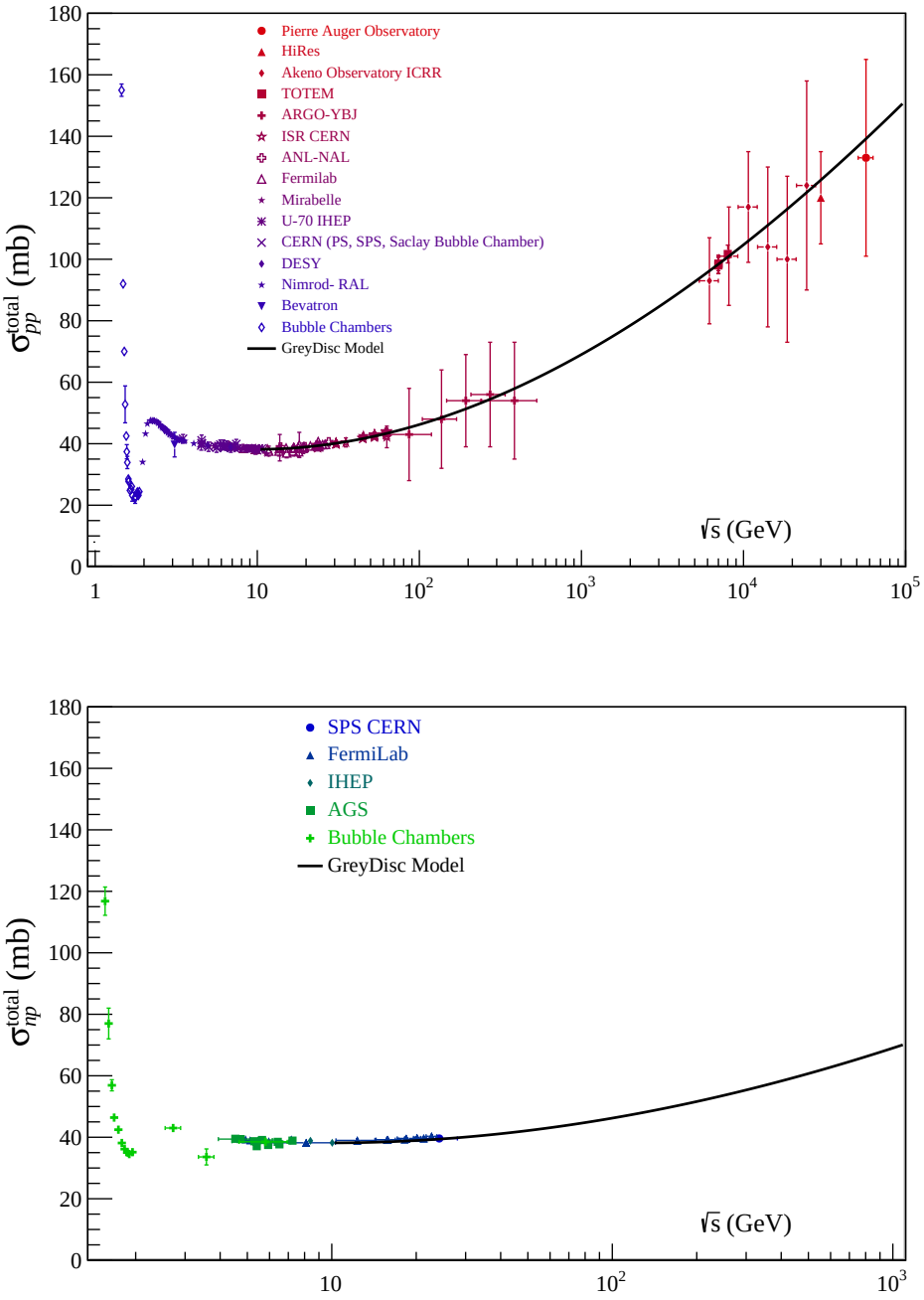

Figure 1: The graph shows the fit of the equations 2.3, with parametrization 2.4, 2.5 over pp (upper graph) and np (down graph with $f(s)$ modification) total cross section from a center of mass energy of $\sqrt{s} = 10$GeV to 20TeV, on the experimental data collected by the PDG [45]. The values of the parameters are reported in the table 1.

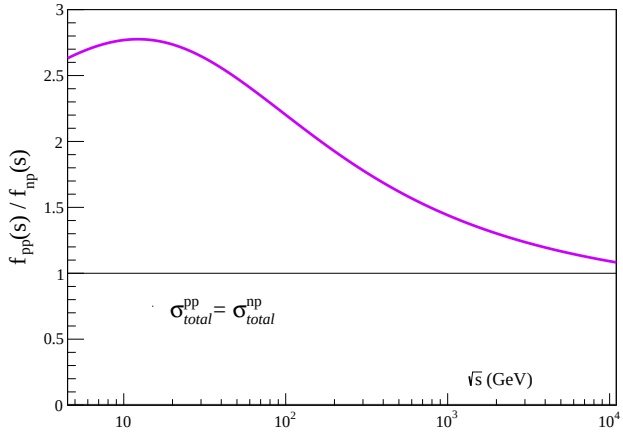

Figure 2: The comparison of the gluonic density of the two systems is shown, observing a local maximum around $\sqrt{s} = 10$GeV, it is observed that both systems approach the Same behavior at energies above 10TeV

3 Results

The parametrization allow us to estimate the profile function for elastic cross section using unitarity relation which leads to the probability of the inelastic interaction for a given b as $1 - |1 - \Gamma(b)|^2$. This means that at high energies the memory of the colliding particles is not longer maintain and the growth of the gluon production generates the blackening interaction, this is in agreement with Unitarization and Universality[46, 47] which leads that the ratio of total cross section for any colliding particle should become one as seen in Figure 1.

	pp	np
$2\pi R_0^2$(mb)	87.2707 ± 4.3952	
β^2(mb)	0.000243 ± 0.000668	
$\sqrt{s_0}$(GeV)	3.7164 ± 0.1340	
$\sqrt{s_1}$(GeV)	8.0947 ± 0.0227	8.7474 ± 0.0077
α	-17.2363 ± 2.5092	-18.5524 ± 0.6670
γ	0.00224 ± 0.00036	0.00267 ± 0.00012

Table 1: Parameters obtained from the cross section fits for pp and np collisions with energies of the center of mass from 10GeV to 20TeV for collisions pp.

It is observed that the parameterization of the Gray Disc proposed for proton-proton collisions and neutron-proton collisions in both cases has a good description for the growth of the cross section as a function of the energy $\sqrt{s}$. This description proposes that, based on the description of the geometric scaling, the cross section slowly evolves to the formation of a Black Disk as the energy in the center of collision mass increases and this growth is dominated by the function $\sim \ln^2(s)$ that dominates the imaginary part of the amplitude in the limit of saturation and that presents a modification in the saturation limit that changes due to the part distribution function, as shown in figure 2. The comparison in both systems show consistency with the evolution to a Black Disc.

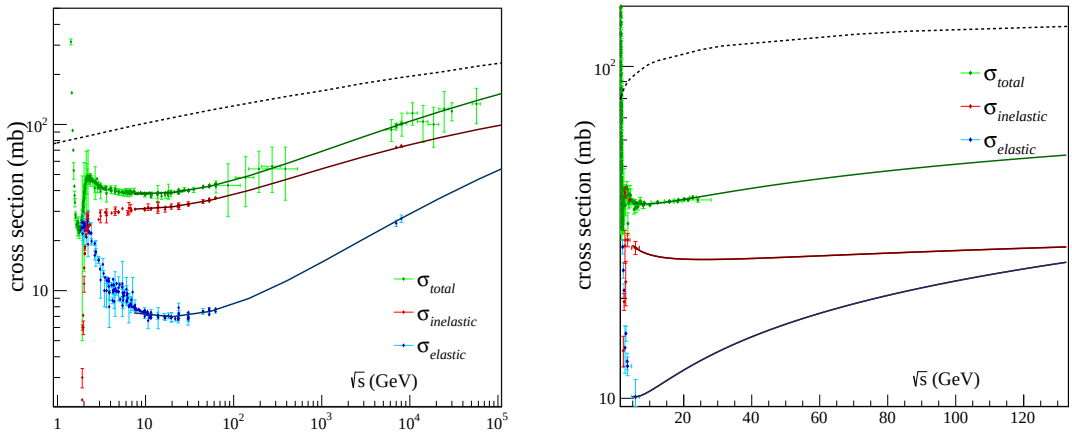

Figure 3: Data behavior of the elastic, inelastic, and total cross section is shown and described by fits of the model for pp collisions on the left and np on the right, showing the black disk boundary with the dotted black line.

4 Conclusions

It is observed that the Gray Disc model has a good description of the pp and np total cross section. In addition, it has the advantage that it separates the gluonic saturation function and allows the description of systems with the same apparent growth mediated by the $R(s)$ function.

There is no immediate evidence that the Froissart's limit is violated, so the Unitarity property of the dispersion amplitude is retained and there are no violation of fundamental principles

The formation of an asymptotic state of gluon saturation is of great interest to explain various results of LHC experiments and astronomical data and allows us to understand the description of the growth of the total cross section of hadronic interaction at high energies whose understanding is fundamental in the description of the composition of cosmic rays.

Acknowledgements

I thank the organizers of the event for giving me the support to be able to participate and especially Dr. M. Hentschinsky for the invitation.

References

[1] **TOTEM** Collaboration, G. Latino, *Summary of Physics Results from the TOTEM Experiment*, *EPJ Web Conf.* **49** (2013) 02005, [arXiv:1302.2098].

[2] **Pierre Auger** Collaboration, P. Abreu et al., *The Pierre Auger Observatory II: Studies of Cosmic Ray Composition and Hadronic Interaction models*, in *32nd International Cosmic Ray Conference*, vol. 3, p. 208, 7, 2011. arXiv:1107.4804.

[3] M. M. Block and F. Halzen, *Commentary on 'Total Hadronic Cross Section Data and the Froissart-Martin Bound', by Fagundes, Menon and Silva*, *Braz. J. Phys.* **42** (2012) 465, [arXiv:1210.3008].

[4] M. M. Block and F. Halzen, *New experimental evidence that the proton develops asymptotically into a black disk*, *Phys. Rev. D* **86** (2012) 051504, [arXiv:1208.4086].

[5] J. Dias De Deus, *Geometric Scaling, Multiplicity Distributions and Cross-Sections*, *Nucl. Phys. B* **59** (1973) 231–236.

[6] A. Buras and J. Dias de Deus, *Scaling law for the elastic differential cross-section in p p scattering from geometric scaling*, *Nucl. Phys. B* **71** (1974) 481–492.

[7] R. Conceicao, J. de Deus, and M. Pimenta, *Proton-proton cross-sections: the interplay between density and radius*, *Nucl. Phys. A* **888** (2012) 58–66, [arXiv:1107.0912].

[8] I. Bautista and J. Dias de Deus, *The black disk and the dip in the differential elastic cross section at asymptotic energy*, *Phys. Lett. B* **718** (2013) 1571–1573, [arXiv:1212.1764].

[9] M. Blue, J. Lord, J. Parks, and C. Tsao, *Proton-Proton Collisions at 4.2 Bev*, *Phys. Rev.* **125** (1962) 1386–1393.

[10] D. Bugg, D. Salter, G. Stafford, R. George, K. Riley, and R. Tapper, *Nucleon-Nucleon Total Cross Sections from 1.1 to 8 GeV/c*, *Phys. Rev.* **146** (1966) 980–992.

[11] **Bonn-Hamburg-Munich** Collaboration, V. Blobel et al., *Multiplicities, topological cross-sections, and single particle inclusive distributions from p p interactions at 12-GeV/c and 24-GeV/c*, *Nucl. Phys. B* **69** (1974) 454–492.

[12] P. Breitenlohner et al., *Small-angle elastic scattering of 24.5 GeV/c protons on hydrogen nuclei*, *Phys. Lett.* **7** (1963), no. 1 73–75.

[13] G. Alexander, O. Benary, G. Czapek, B. Haber, N. Kidron, B. Reuter, A. Shapira, E. Simopoulou, and G. Yekutieli, *Proton-Proton Interactions at 5.5 GeV/c*, *Phys. Rev.* **154** (1967) 1284–1304.

[14] S. Almeida et al., *P-P Interactions at 10 GEV/C*, *Phys. Rev.* **174** (1968) 1638–1661.

[15] A. Ashmore, G. Cocconi, A. Diddens, and A. Wetherell, *Total Cross Sections of Protons with Momentum Between 10 and 28 Gev/c*, *Phys. Rev. Lett.* **5** (1960) 576–578.

[16] J. Badier et al., *The sigma- p and sigma- d total cross-sections at 19 gev*, *Phys. Lett. B* **41** (1972) 387–392.

[17] G. Bellettini, G. Cocconi, A. Diddens, E. Lillethun, J. Pahl, J. Scanlon, J. Walters, A. Wetherell, and P. Zanella, *Absolute measurements of proton-proton small-angle elastic scattering and total cross section at 10, 19 and 26 GeV/ c*, *Phys. Lett.* **14** (1965), no. 2 164–168.

[18] L. W. Jones, M. Longo, T. Mccorriston, E. Parker, S. Powell, and M. Kreisler, *Neutron total cross-sections on protons and nuclei in the 10 to 30 gev/c momentum range*, *Phys. Lett. B* **36** (1971) 509–512.

[19] V. Apokin et al., *Elastic pi+ p, K+ p and p p Scattering in the Region of Coulomb-Nuclear Interference at Momenta 42.5-GeV/c and 52.2-GeV/c*, *Yad. Fiz.* **25** (1977) 94–102.

[20] S. Denisov, S. Donskov, Y. Gorin, A. Petrukhin, Y. Prokoshkin, D. Soyanova, J. Allaby, and G. Giacomelli, *Total cross-sections of pi+, K+ and p on protons and deuterons in the momentum range 15-GeV/c to 60-GeV/c*, *Phys. Lett. B* **36** (1971) 415–421.

[21] V. Ammosov et al., *Average charged particle multiplicity and topological cross-sections in 50-GeV/c and 69-GeV/c p p interactions*, *Phys. Lett. B* **42** (1972) 519–521.

[22] D. Brick et al., *Topological, Total and Elastic Cross-sections for K^+p, π^+p and pp Interactions at 147-GeV/c*, *Phys. Rev. D* **25** (1982) 2794.

[23] T. Kafka et al., *Correlations Between Neutral and Charged Pions Produced in 300-GeV/cpp Collisions*, *Phys. Rev. D* **19** (1979) 76.

[24] A. Brenner et al., *Experimental Study of Single Particle Inclusive Hadron Scattering and Associated Multiplicities*, *Phys. Rev. D* **26** (1982) 1497.

[25] V. Bartenev et al., *Small Angle Elastic Proton Proton Scattering from 25-GeV to 200-GeV.*, *Phys. Rev. Lett.* **29** (1972) 1755–1758.

[26] F. Dao, D. Gordon, J. Lach, E. Malamud, T. Meyer, R. Poster, and W. Slater, *p p Interactions at 303-GeV/c: Multiplicity and Total Cross-Section.*, *Phys. Rev. Lett.* **29** (1972) 1627–1630.

[27] A. Carroll et al., *Total Cross-Sections of $\pi^{\pm}$, $K^{\pm}$, p and $\bar{p}$ on Protons and Deuterons Between 200 GeV/c and 370 GeV/c*, *Phys. Lett. B* **80** (1979) 423–427.

[28] A. Firestone et al., *pp Interactions at 300-GeV/c: Measurement of the Charged Multiplicity, Total and Elastic Cross-Sections*, *Phys. Rev. D* **10** (1974) 2080.

[29] S. Barish et al., *Updated Charged-Particle Multiplicity Distribution from 205-GeV/c Proton Proton Interactions*, *Phys. Rev. D* **9** (1974) 2689.

[30] C. Bromberg et al., *Cross-Sections and Charged Particle Multiplicities at 102-GeV/c and 405-GeV/c.*, *Phys. Rev. Lett.* **31** (1973) 1563–1566.

[31] U. Amaldi et al., *The Real Part of the Forward Proton Proton Scattering Amplitude Measured at the CERN Intersecting Storage Rings*, *Phys. Lett. B* **66** (1977) 390–394.

[32] U. Amaldi et al., *Precision Measurement of Proton Proton Total Cross-section at the CERN Intersecting Storage Rings*, *Nucl. Phys. B* **145** (1978) 367–401.

[33] **CERN-Naples-Pisa-Stony Brook** Collaboration, M. Ambrosio et al., *Measurements of Elastic Scattering in $\alpha^{-}\alpha$ and α - Proton Collisions at the CERN Intersecting Storage Rings*, *Phys. Lett. B* **113** (1982) 347–352.

[34] N. A. Amos et al., *Measurement of Small Angle $\bar{p}p$ and Proton Proton Elastic Scattering at the CERN Intersecting Storage Rings*, *Nucl. Phys. B* **262** (1985) 689–714.

[35] G. Carboni et al., *Precise Measurements of Proton - Anti-proton and Proton Proton Total Cross-sections at the CERN Intersecting Storage Rings*, *Nucl. Phys. B* **254** (1985) 697–736.

[36] K. Eggert et al., *A Measurement of the Proton Proton Cross-Section at the CERN ISR*, *Nucl. Phys. B* **98** (1975) 93–99.

[37] D. Favart et al., *Measurement of $\bar{p}p$ Elastic Scattering at $\sqrt{s} = 52.8$-GeV at the CERN Intersecting Storage Rings*, *Phys. Rev. Lett.* **47** (1981) 1191.

[38] L. Baksay et al., *Measurement of the Proton Proton Total Cross-Section and Small Angle Elastic Scattering at ISR Energies*, *Nucl. Phys. B* **141** (1978) 1–28. [Erratum: Nucl.Phys.B 148, 538–539 (1979)].

[39] G. Antchev et al., *First measurement of the total proton-proton cross section at the LHC energy of $\sqrt{s}$ =7 TeV*, *EPL* **96** (2011), no. 2 21002, [arXiv:1110.1395].

[40] **TOTEM** Collaboration, G. Antchev et al., *Measurement of proton-proton elastic scattering and total cross-section at S**(1/2) = 7-TeV*, *EPL* **101** (2013), no. 2 21002.

[41] **ARGO-YBJ** Collaboration, G. Aielli et al., *Proton-air cross section measurement with the ARGO-YBJ cosmic ray experiment*, *Phys. Rev. D* **80** (2009) 092004, [arXiv:0904.4198].

[42] M. Honda, M. Nagano, S. Tonwar, K. Kasahara, T. Hara, N. Hayashida, Y. Matsubara, M. Teshima, and S. Yoshida, *Inelastic cross-section for p-air collisions from air shower experiment and total cross-section for p p collisions at SSC energy*, *Phys. Rev. Lett.* **70** (1993) 525–528.

[43] R. Baltrusaitis, G. Cassiday, J. Elbert, P. Gerhardy, S. Ko, E. Loh, Y. Mizumoto, P. Sokolsky, and D. Steck, *Total Proton Proton Cross-Section at s**(1/2) = 30-TeV*, *Phys. Rev. Lett.* **52** (1984) 1380–1383.

[44] **Pierre Auger** Collaboration, P. Abreu et al., *Measurement of the proton-air cross-section at $\sqrt{s} = 57$ TeV with the Pierre Auger Observatory*, *Phys. Rev. Lett.* **109** (2012) 062002, [arXiv:1208.1520].

[45] **Particle Data Group** Collaboration, M. Tanabashi et al., *Review of Particle Physics*, *Phys. Rev. D* **98** (2018), no. 3 030001.

[46] L. Frankfurt and M. Strikman, *Dynamics of p p collisions at small impact parameters, universality of cross sections of hadron hadron collisions and critical phenomena at superhigh energies*, *Czech. J. Phys.* **56** (2006) A63–A75.

[47] I. Ivanov, N. Nikolaev, and A. Savin, *Diffractive vector meson production at HERA: From soft to hard QCD*, *Phys. Part. Nucl.* **37** (2006) 1–85, [hep-ph/0501034].

Review of results using heavy ion collisions at CMS

Georgios Konstantinos Krintiras
(on behalf of the CMS Collaboration)

E-Mail: gkrintir@cern.ch

The University of Kansas

Presented at the Workshop of QCD and Forward Physics at the EIC, the LHC, and Cosmic Ray Physics in Guanajuato, Mexico, November 18–21 2019

Abstract

Ultrarelativistic heavy ion collisions at the laboratory provide a unique chance to study quantum chromodynamics (QCD) under extreme temperature ($\approx$150 MeV) and density ($\approx$1 GeV/ fm^3) conditions. Over the past decade, experimental results from LHC have shown further evidence for the formation of the quark-gluon plasma (QGP), a phase that is thought to permeate the early Universe and is formed in the high-density neutron-star cores. Various QCD predictions that model the behavior of the low-x gluon nuclear density, a poorly explored region, are also tested. Since the photon flux per ion scales as the square of the emitting electric charge Z^2, cross sections of so far elusive photon-induced processes are extremely enhanced as compared to nucleon-nucleon collisions. Here, we review recent progress on CMS measurements of particle production with large transverse momentum or mass, photon-initiated processes, jet-induced medium response, and heavy quark production. These high-precision data, along with novel approaches, offer stringent constraints on initial state, QGP formation and transport parameters, and even parametrizations beyond the standard model.

1 Introduction

The Compact Muon Solenoid (CMS) is a "general purpose" detector, however, equally well suited for the study of heavy ion collisions at LHC [1]. Since the first lead-lead (PbPb) collisions recorded at CMS in 2010, and after almost ten years of operation, a wealth of measurements are available for understanding hadron and nuclear "static" (e.g., mass generation and spectra) and "dynamic" (e.g., cross sections) properties. Initially, heavy ion collisions were proposed to study basic features of quantum chromodynamics (QCD) matter via its excitation to phases where quarks and gluons are no more confined into hadrons. Although high-density regimes of QCD are routinely formed in the laboratory using nucleus-nucleus collisions [2], and might exist in the present Universe [3], we witness signatures for their existence in "small-systems", e.g., proton-proton (pp) [4] as well as proton-nucleus [5] collisions. Although in the former case the physical origin of "long-range correlations", i.e., two-particle angular correlations with large pseudorapidity gap, is interpreted

as a consequence of hydrodynamic expansion of the produced medium with initial-state fluctuations, the underlying mechanisms are not yet understood in pp and proton-nucleus collisions [6]. Collisions of point-like objects, e.g., electron-positron [7], can serve as reference to the observed long-range correlations in the small systems.

The extracted properties of the quark-gluon plasma (QGP), created in the extreme environment of high temperature ($\approx$150 MeV) and energy density ($\approx$1 GeV/ fm^3), signify an almost ideal liquid with short lifetime ($\approx$10 fm) and large opacity against the partons traversing it [8]. The QGP response strongly depends on the geometrical overlap ("centrality") of heavy ion collisions. "Central" collisions, at small impact parameter b, yield large and round interaction regions, whereas peripheral collisions, characterized by larger values of b, result in smaller interaction regions with more pronounced spatial anisotropy. The centrality dependence of various observables provides, then, insight into their dependence on global geometry. Instances with no overlap, i.e., b being larger than twice the radius of the nuclei, are well suited to study photon (γ)-mediated interactions: "ultraperipheral" collisions (UPC) are the energy frontier for the photoproduction of heavy quark and antiquark bound states ("quarkonia"), and "dijets", i.e., pairs consisting of the most ("leading") and the second most ("subleading") energetic jets, reaching at LHC γp ($\gamma\gamma$) center of mass energies $\sqrt{s}$ significantly higher than at HERA (LEP) [9]. Here, we briefly present the latest results from the CMS Collaboration on "quark matter and beyond", i.e., including novel measurements and beyond the standard model (BSM) searches that are competitive with, or at least complementary to, pp studies.

2 Heavy ion collisions at LHC

Four LHC experiments recorded data with heavy ion collisions during "Run 2" (2015–2018), rendering the so-called "fair luminosity sharing" among them challenging. Physics runs have also been carried out with proton-lead (pPb) collisions, a mode of operation [10] that was not initially foreseen [11]. The standard LHC operation includes heavy ion or "reference" pp collisions at the same nucleon-nucleon $\sqrt{s}$ energy ($\sqrt{s_{\mathrm{NN}}}$) during roughly one month per year. The performance until the end of Run 2 has been excellent, reaching instantaneous luminosities of about six (eight) times higher than the design (physics-case) value of $10^{27}(10^{29})$ cm^{-2} s^{-1} in PbPb (pPb), equivalent to a nucleon-nucleon luminosity of $\mathcal{L}_{\mathrm{NN}} \sim 10^{32}$ cm^{-2} s^{-1}. The $\mathcal{L}_{\mathrm{NN}}$-integrated luminosity delivered to CMS [12] is shown in Fig. 1 for PbPb and pPb collisions.

The excellent performance was made possible through a series of improvements in the LHC and the injector chain. For the next PbPb run in 2021, it is planned to further increase the total LHC beam intensity through a decrease of bunch spacing to 50 ns , resulting to a total of 1 232 bunches in the ring. However, any increase of ion luminosity is intrinsically limited by the risk of superconductivity loss in the magnets. As mitigation, it is therefore planned to install additional collimators during the second long shutdown (2018–2021) to allow for higher luminosity and intensity [13–15]. Using the predicted beam and machine configuration [16], the future luminosity performance during one-month runs is estimated about 3 and 700 nb^{-1} for PbPb and pPb, respectively.

3 Hard probes and photon-induced processes

The proton structure at high momentum-transfer Q^2, as encoded in the collinearly factorized parton distribution functions (PDFs), enters the weighted product with high-energy ("hard") parton-parton scattering cross sections. While the latter are process specific and are computed in perturbative QCD (pQCD) at different levels of accuracy, PDFs are deemed universal functions of

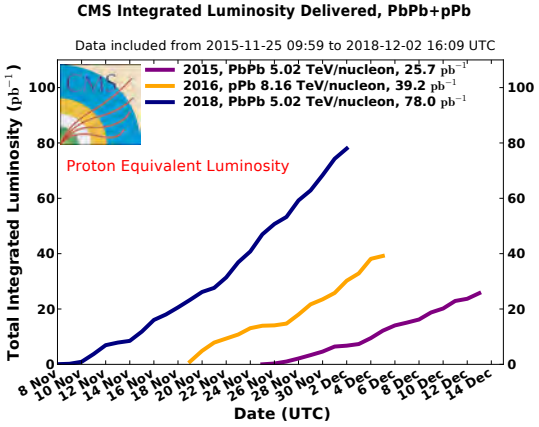

Figure 1: The $\mathcal{L}_{\mathrm{NN}}$-integrated luminosity delivered to CMS for PbPb and pPb collisions in Run 2 [12].

Q^2 and Bjorken-x obtained by the well-established means of global analyses ("fits") using hard-process data. Likewise, their counterparts for nucleons bound in nuclei, i.e., the nuclear PDFs (nPDFs), are essential in studying the production of hard probes in QGP. As such, the uncertainty in nPDFs mainly stems from the available data, and hence the lack of constraints in certain phase space regions.

A recent example is the measurement of dijet pseudorapidity (η_{dijet}) spectra in pp and pPb collisions at 5.02 TeV [17], where the uncertainty in the nuclear modification factor R_{pPb} between the pPb and pp spectra appears significantly smaller than predictions with various nPDFs (Fig. 2 from Ref. [18]). Processes involving electroweak gauge (e.g., W or Z) bosons and top quarks are also powerful probes of the light quark and gluon nPDFs, respectively. The production of W bosons [19] and top quarks [20] is studied in pPb collisions at $\sqrt{s_{\mathrm{NN}}} = 8.16\,\mathrm{TeV}$. In the former case, the results already favor PDF calculations that include nuclear modifications, and provide constraints on the nPDF global fits. In the latter case, although the top quark is a novel and theoretically precise probe of nPDFs due to its high mass [21], the measured cross section of its pair ($\mathrm{t\bar{t}}$) production, $\sigma_{\mathrm{t\bar{t}}}$, is still consistent with the expectations from scaled pp data. The exploration of parton densities in nuclei in a broad (x, Q^2) kinematic range [22] is a priority for the high-luminosity PbPb and pPb physics programs (see Section 2).

Ultrarelativistic heavy ions are accompanied by strong electromagnetic fields; the latter can be treated as a flux of quasi-real photons that scale with the square of the emitting electric charge Z^2 thus their radiation from Pb ions is strongly enhanced compared to the p case. Quasi-real photons can fluctuate into a quark-antiquark pair, which can then turn into a vector meson (VM) upon interacting with the other nucleon in UPC. In particular, "exclusive" VM photoproduction, $\gamma\mathrm{p} \rightarrow \mathrm{VMp}$, bridge previously unexplored regions of parton fractional momenta from the HERA measurements, e.g., $x \approx 10^{-4}$–10^{-2} in the case of Ref. [25] where $\mathrm{VM} \equiv \Upsilon(\mathrm{nS})$ (with $n = 1, 2, 3$), meaning UPC can be used in the same way as electron-proton collisions. The incoming nucleons remain intact after the interaction and only the VM is produced, with the process referred to as "exclusive". Also, in these events, contrary to symmetric colliding systems, one can determine the γ direction and hence the $\gamma\mathrm{p}$ centre-of-mass energy, $W_{\gamma\mathrm{p}}$, unambiguously. The data, within their currently large statistical uncertainty, are consistent with various pQCD approaches that model the behavior of the low-x gluon density (Fig. 3, left) and provide new insights on the gluon distribution in the proton in this poorly explored region. Some models suggest that the energy dependence of

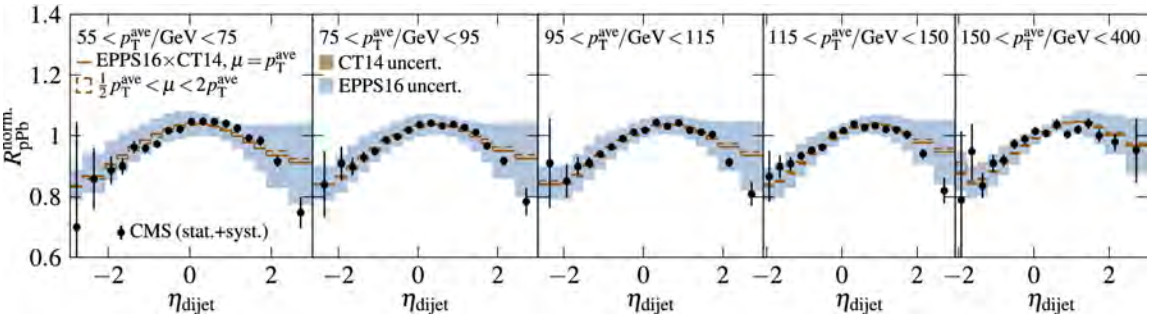

Figure 2: The nuclear modification factor between pPb and pp dijet pseudorapidity differential cross sections. Black markers show the data from CMS [17] with vertical bars showing the statistical and systematical uncertainties added in quadrature. Solid lines represent the pQCD calculation with average p_T scale choice using the central nPDF set of CT14 [23] and EPPS16 [24]. Figure extracted from Ref. [18].

the integrated cross section may provide evidence of gluon saturation, as investigated in Ref. [26] where the exclusive $\rho(770)^0$ photoproduction is measured, for the first time, in UPC pPb collisions at $\sqrt{s_{NN}} = 5.02$ TeV (Fig. 3, right).

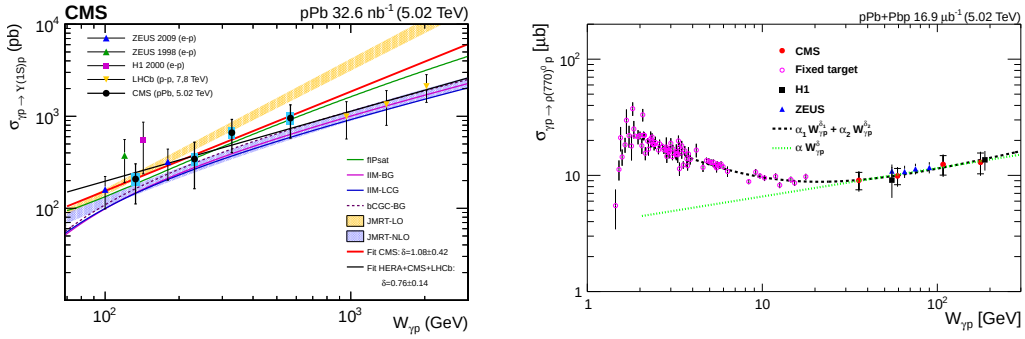

Figure 3: Cross section for the exclusive $\Upsilon(1S)$ [25] (left) and $\rho(770)^0$ [26] (right) photoproduction as a function of $W_{\gamma p}$ compared to previous data as well as to various theoretical predictions or theory-inspired fits. The bars show the statistical uncertainty, while the boxes or outer bars represent the systematic uncertainty or the statistical and systematic uncertainties added in quadrature.

Even accounting for roughly 100 times lower instantaneous luminosity than pp collisions, several BSM searches appear more competitive in nuclear than pp collisions [27]. For instance, in case that BSM is manifested with low couplings to the SM and at relatively low masses, experimental conditions related to heavy ion collisions—with almost vanishing pileup, optimal primary vertex reconstruction, low-p_T thresholds applied to online filters, and "clean" exclusive final states in UPC—present relative merits compared to pp studies. A characteristic example is Ref. [28] where the measured exclusive $\gamma\gamma$ invariant mass distribution is used to search for narrow resonances such as pseudoscalar axion-like (a) particles (ALPs) produced in the process $\gamma\gamma \to a \to \gamma\gamma$. Exclusion limits at 95% confidence level (CL) are set on the $\gamma\gamma \to a \to \gamma\gamma$ cross section for ALPs with masses $m_a = 5$–90 GeV. The cross section limits are then used to set exclusion limits in the two-dimensional plane of the ALP coupling to photons $g_{aPGg} \equiv 1/\Lambda$ (with Λ being the BSM energy scale) and m_a. For ALPs coupling to the electromagnetic (and electroweak) current, the derived

exclusion limits are currently the best over the $m_{\mathrm{a}} = 5$–50 (5–10) GeV mass range, as shown in Fig. 4.

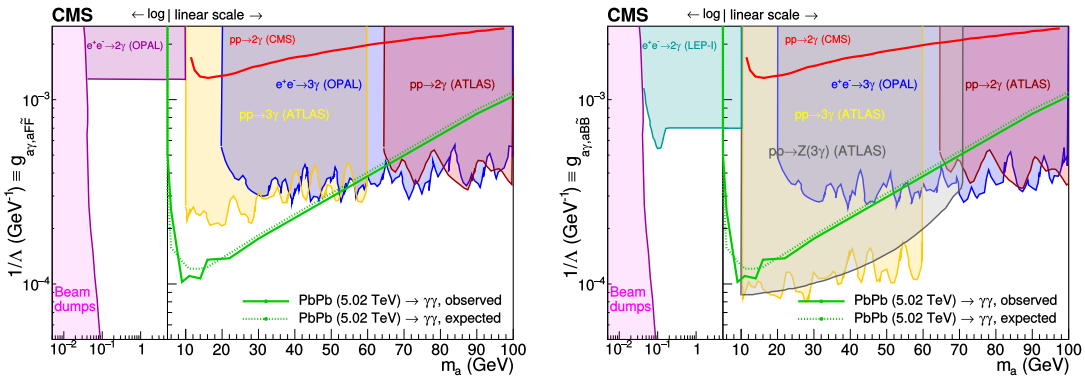

Figure 4: Exclusion limits at 95% CL in the $g_{\mathrm{a}\gamma}$–m_{a} plane, assuming ALP coupling to γ only (left) and including the hypercharge coupling, hence involving the Z boson (right), from previous measurements and compared to the present limits using PbPb collisions [28].

4 Jet modifications

High-momentum partons are produced by hard scatterings that occur over a timescale $\tau \sim p_{\mathrm{T}}^{-1} < 10$ fm thus are expected to undergo "energy loss" as they traverse the QGP. The mechanisms by which the partons distribute their energy to the medium (radiative or collisional energy loss) as well as the color dependence (e.g., energy loss due to the different color charges, coherent or incoherent gluon radiation, etc), are still not fully understood. The particles resulting from the parton fragmentation and hadronization are clustered into jets (of cone size $R = \sqrt{(\Delta y)^2 + (\Delta\phi)^2}$) that are used as parton proxies to examine the QGP properties. Parton energy loss manifests itself in various experimental observables, including the suppression R_{AA} of high-p_{T} hadrons [8] and jets, including its system size dependence [29], as well as modifications of the jet properties (e.g., dijet momentum balance [30], charged particle number densities, jet fragmentation functions, and jet shape [31–34]) and parton shower [35]. These phenomena are collectively referred to as "jet quenching" that can be related to the transport and thermodynamic QGP properties.

Recently, and for the first time, strong suppression of high-p_{T} large-R jets is observed in the 0–10% most central collisions [36]. Whereas the various predictions from quenched jet event generators, theoretical models, and analytical calculations grasp reasonably the R_{AA} p_{T} evolution for jets reconstructed with $R \lesssim 0.4$, they produce a less uniform description of the QGP-induced behavior of jets at larger R (Fig. 5). Another observation, which does not support previous interpretations based on color-charge-dependent jet quenching, is achieved with a template-fitting method using the "jet charge" observable [37]. Jet charge, defined as the momentum-weighted sum of the electric charges of particles inside a jet, is sensitive to the electric charge of the particle initiating a parton shower and can be used to discriminate between gluon- and quark-initiated jets. No evidence is seen for a significant decrease (increase) in gluon- (quark-) like prevalence in a sample of high-p_{T} jets in PbPb collisions. In contrast to the PbPb and xenon-xenon systems, in pPb collisions no suppression is observed in the low-p_{T} region, whereas a weak momentum dependence is seen for $p_{\mathrm{T}} > 10$ GeV, leading to a moderate excess above unity [38].

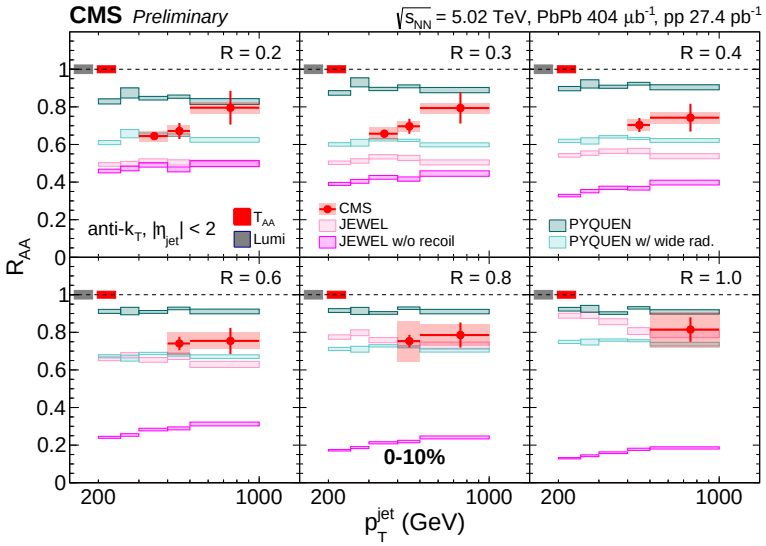

Figure 5: The QGP-induced modification on jets as a function of jet p_{T} for various R and 0–10% centrality class [36]. The statistical uncertainty is represented as a vertical line, while the systematic uncertainty is shown as a shaded box. The uncertainty due to luminosity and nuclear overlap function for pp and PbPb collisions, respectively, are shown as colored boxes on the dashed line at 1. Data are compared to predictions from Jewel [39] (orange and purple) and PYQUEN [40] (teal and green) generators.

5 Heavy quark dynamics

The majority of secondary particle production in heavy ion collisions ends up as collective, thermalized bulk QCD matter which is well described using almost ideal relativistic fluid dynamics. The QGP behavior is largely governed by an equation of state that exhibits a phase transition from confined matter with hadronic degrees of freedom below the transition and deconfined partonic matter above [41]. The long-range two- or higher-order particle (with large η gap) and near-side azimuthal correlations constitute an effective tool to probe these QGP properties. These "radial" or "anisotropic flow" correlations [42–44] are typically parametrized by coefficients in a Fourier expansion, v_n ($n \geq 1$), and can provide information about the initial collision geometry (e.g., the "elliptic" flow harmonic, v_2) and its fluctuations (e.g., the "triangular" flow harmonic, v_3).

Recent measurements [45] of prompt D^0 ($\overline{\mathrm{D}}^0$) meson v_2 and v_3 in PbPb collisions at $\sqrt{s_{\mathrm{NN}}}$ = 5.02 TeV, as a function of p_{T}, rapidity and centrality, extend the p_{T} coverage up to ∼60 GeV and provide more differential information. Motivated by the search for a strong electric field possibly created in PbPb collisions, the first measurement of the v_2 difference (Δv_2) between D^0 and $\overline{\mathrm{D}}^0$ as a function of rapidity is studied. The rapidity-averaged v_2 difference is measured $\langle \Delta v_2 \rangle = 0.001 \pm 0.001\,(\mathrm{stat}) \pm 0.003\,(\mathrm{syst})$. No effect of electric field on charm hadron collective flow is thus observed, within the experimental uncertainty, and future model comparisons can provide constraints on the QGP electric conductivity [46].

In the case of quarkonia states with different binding energies, their azimuthal dependence, which is largely independent of nPDFs, can reflect the extent of the "screening", i.e., at what level their binding energy is weakened by the surrounding partons, hence revealing the QGP thermal environment. The v_2 values for $\Upsilon(1\mathrm{S})$ and, for the first time, $\Upsilon(2\mathrm{S})$ mesons are measured (Fig. 6, left) and found to be consistent with zero over the kinematic range studied [47], contrasting with

the measured J/ψ results in PbPb collisions [48], and suggesting different QGP effects for charmonia and bottomonia. Because of different contribution of regeneration between $\Upsilon(1S)$ and $\Upsilon(2S)$ meson production, this measurement additionally provides new inputs to the production mechanisms of bottomonia, complementing the sequential suppression pattern already seen for $\Upsilon(nS)$ (with $n = 1, 2, 3$) mesons [49].

Heavy flavor quark collectivity is also seen in small-system collisions [50], measuring $v_2 > 0$ for prompt D^0 in pp collisions—comparable to light-flavor hadron species—and extracting a mass dependence of heavy flavor hadron v_2 in pPb collisions, including, for the first time, open beauty hadrons via nonprompt D^0 mesons (Fig. 6, right) .

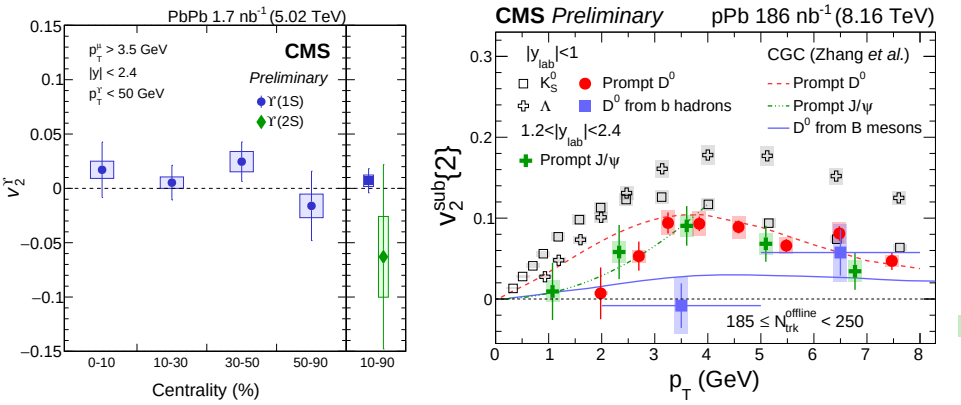

Figure 6: (Left) The p_T-integrated v_2 values for $\Upsilon(1S)$ and $\Upsilon(2S)$ mesons measured in PbPb collisions $\sqrt{s_{NN}} = 5.02$ TeV in the 0–90% centrality range [47]. The error bars (bands) denote the statistical (systematic) uncertainty. (Right) Results of v_2 for prompt and nonprompt D^0 mesons [50], as well as K^0_S, Λ, and J/ψ, as a function of p_T in pPb collisions at $\sqrt{s_{NN}} = 8.16$ TeV [51, 52]. The error bars (shaded areas) correspond to the statistical (systematic) uncertainty. Lines show the theoretical calculations under the color glass condensate framework of Ref. [53].

6 New probes

The multi-TeV energies available at the LHC heavy ion collisions have opened up the possibility to measure, for the first time, various exotic mesons and high-mass elementary particles. The $X(3872)$, also known as $\chi_{c1}(3872)$, is such an exotic meson, first observed by the BELLE Collaboration [54] and subsequently studied at electron-position and hadron colliders (most recently in Ref. [55]), whose nature is still not fully understood. In the QGP, the production of the $\chi_{c1}(3872)$ state can be enhanced or depleted depending on the spatial configuration of the exotic state. The recent measurement of the inclusive prompt $\chi_{c1}(3872)$ production [56], here reconstructed via the decay chain $\chi_{c1}(3872) \to J/\psi\,\pi^+\pi^- \to \mu^+\mu^-\pi^+\pi^-$ (Fig. 7, left), could also provide a new test on the statistical hadronization mechanism [41], a remarkably successful phenomenological description of the yields of "stable" (with respect to strong interactions) hadrons in central relativistic heavy ion collisions.

The characteristic feature of experimental signatures is their sensitivity to initial- or final-state effects integrated over the QGP lifetime, the latter increasing as a function of $\sqrt{s_{NN}}$ and the atomic mass A of the ions being collided. At variance with measurements considered so far in the literature, top quark, a colored particle that decays mostly within the QGP, provides a novel way to study differentially the space-time evolution of the QGP, hence offering the opportunity to resolve

the QGP and "unveiling its yoctosecond structure" [57]. We demonstrate [58], for the first time, that top quark decay products are identified, irrespective of whether interacting with the medium (bottom quarks) or not (leptonically decaying W bosons). Dilepton final states are selected, and the $t\bar{t}$ cross section is measured from a likelihood fit to a multivariate discriminator using lepton kinematic variables. The measurement is additionally performed considering the jets originating from the hadronization of bottom quarks, which improve the sensitivity to the signal process. The measurements, $\sigma_{t\bar{t}} = 2.02 \pm 0.69$ and $2.56 \pm 0.82\,\mu$b, consistent with each other and the expectations from scaled proton-proton data as well as perturbative QCD (Fig. 7, right), constitute the first step towards using the top quark as a novel tool to probe the QGP.

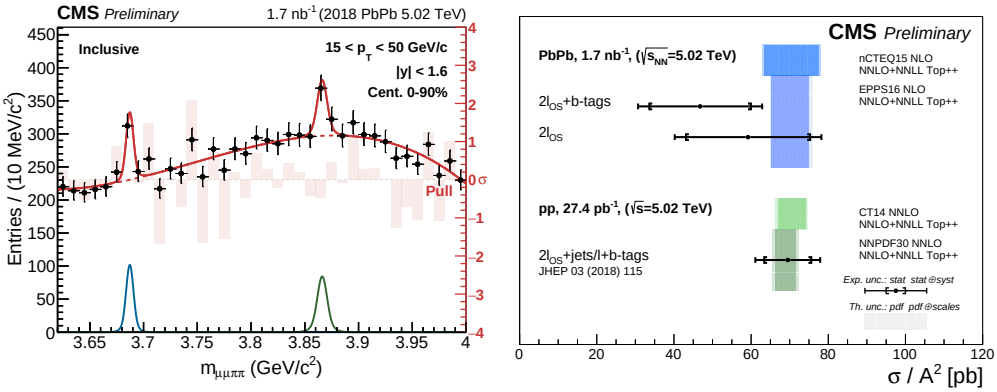

Figure 7: (Left) Invariant mass distribution $m_{\mu^+\mu^-\pi^+\pi^-}$ in PbPb collisions at $\sqrt{s_{\mathrm{NN}}} = 5.02\,\mathrm{TeV}$ [56], denoting the production of $\psi(2S)$ (blue) and $\chi_{c1}(3872)$ (green) particles. The red line presents the unbinned maximum-likelihood fit result, with the "pull" distribution represented by the red boxes. (Right) Inclusive $t\bar{t}$ cross sections measured with two methods in dilepton final states in PbPb collisions at $\sqrt{s_{\mathrm{NN}}} = 5.02\,\mathrm{TeV}$ (scaled by A^{-2}) [58], and pp results at $\sqrt{s} = 5.02\,\mathrm{TeV}$ [59]. The measurements are compared with theory predictions at higher-order accuracy in QCD [60]. The inner (outer) experimental uncertainty bars include statistical (statistical and systematic, added in quadrature) uncertainties. The inner (outer) theory uncertainty bands correspond to nuclear [24, 61] or free-nucleon [23, 62] PDF (PDF and scale, added in quadrature) uncertainties.

7 Summary

The quark-gluon plasma (QGP) is a state of transient nuclear matter in which composite quantum chromodynamics (QCD) states loose their identity and dissolve into a nearly ideal, strongly interacting fluid of quarks and gluons. The existence of QGP was proposed already in the mid-seventies after it was realized that asymptotic freedom in QCD predicts force weakening at short distances. Therefore, one of the most challenging questions in nuclear physics is to identify the QGP structure and its phases.

Despite the successful description provided by the QCD Lagrangian, our knowledge away from the perturbative limit is still limited. The aim of ultrarelativistic heavy ion collisions is to bridge this gap and to contribute to the understanding of thermodynamics and collective QCD phenomena. Hard probes and photon-initiated interactions serve in this context to provide information and constraints for cold and hot nuclear matter effects which cannot be obtained by studying bulk QCD matter alone. Imaging the QGP formation and evolution via initial- and final-state interactions of produced and outgoing partons lies at the heart of nuclear PDF and tomography

studies, respectively. Altogether these measurements contribute to comprehensive modeling of all aspects of the dynamics of heavy ion collisions.

Some of the features of the QGP are the strong collective anisotropic flow and high opacity to jets. Collective flow is observed, among others, as the mass-dependent transverse momentum (p_{T}) spectra of light or heavy particles, while parton energy loss comes out as the suppression in the production of high-p_{T} particles. Recent measurements in high-multiplicity proton-proton and proton-nucleus collisions revealed flow-like patterns, and along with the nuclear modification factors, already covering p_{T} ranges up to the TeV scale, can provide stringent constraints on cold and hot nuclear matter effects.

With the advent of the LHC, the energy reach for ultraperipheral collisions extended significantly, including studies on nuclear structure and modifications, and even searches for beyond the standard model signatures. Additional measurements like the evidence of exotic meson and top quark production demonstrate the versatility of the CMS experiment, and provide novel probes of the locally deconfined state with a lifetime of a few fm. The future opportunities for high-density QCD studies with ion and proton beams at the LHC are unprecedented given the enlarged per month integrated luminosity.

Acknowledgements

The work is supported in whole by the Nuclear Physics (NP) program of the U.S. Department of Energy (DOE) with number DOE DE-SC0019389.

References

[1] CMS Collaboration, "The CMS experiment at the CERN LHC", *JINST* **3** (2008) S08004, doi:10.1088/1748-0221/3/08/S08004.

[2] HotQCD Collaboration, "Chiral crossover in QCD at zero and nonzero chemical potentials", *Phys. Lett. B* **795** (2019) 15, doi:10.1016/j.physletb.2019.05.013, arXiv:1812.08235.

[3] L. R. Weih, M. Hanauske, and L. Rezzolla, "Postmerger gravitational wave signatures of phase transitions in binary mergers", *Phys. Rev. Lett.* **124** (2020) 171103, doi:10.1103/PhysRevLett.124.171103, arXiv:1912.09340.

[4] CMS Collaboration, "Observation of long-range near-side angular correlations in proton-proton collisions at the LHC", *JHEP* **09** (2010) 091, doi:10.1007/JHEP09(2010)091, arXiv:1009.4122.

[5] CMS Collaboration, "Observation of long-range near-side angular correlations in proton-lead collisions at the LHC", *Phys. Lett. B* **718** (2013) 795, doi:10.1016/j.physletb.2012.11.025, arXiv:1210.5482.

[6] C. Shen, "Studying QGP with flow: A theory overview", in *28th International Conference on Ultrarelativistic Nucleus-Nucleus Collisions*. 1, 2020. arXiv:2001.11858.

[7] A. Badea et al., "Measurements of two-particle correlations in $\mathrm{e^+e^-}$ collisions at 91 GeVwith ALEPH archived data", *Phys. Rev. Lett.* **123** (2019) 212002, doi:10.1103/PhysRevLett.123.212002, arXiv:1906.00489.

[8] CMS Collaboration, "Studies of beauty suppression via nonprompt D^0 mesons in PbPb collisions at $Q^2 = 4\,\mathrm{GeV}^2$", *Phys. Rev. Lett.* **123** (2019) 022001, doi:10.1103/PhysRevLett.123.022001, arXiv:1810.11102.

[9] S. Klein and P. Steinberg, "Photonuclear and two-photon interactions at high-energy nuclear colliders", arXiv:2005.01872.

[10] C. Salgado et al., "Proton-nucleus collisions at the LHC: Scientific opportunities and requirements", *J. Phys. G* **39** (2012) 015010, doi:10.1088/0954-3899/39/1/015010, arXiv:1105.3919.

[11] J. Jowett and C. Carli, "The LHC as a proton nucleus collider", *Conf. Proc. C* **060626** (2006) 550.

[12] CMS Collaboration, "CMS luminosity measurement using 2016 proton-nucleus collisions at nucleon-nucleon center-of-mass energy of 8.16 TeV", CMS Physics Analysis Summary CMS-PAS-LUM-17-002, 2018.

[13] R. Bruce, A. Marsili, and S. Redaelli, "Cleaning performance with 11T *d*ipoles and local dispersion suppressor collimation at the LHC", in *Proceedings, 5th International Particle Accelerator Conference (IPAC 2014): Dresden, Germany, June 15-20, 2014*, p. MOPRO042. 2014. doi:10.18429/JACoW-IPAC2014-MOPRO042.

[14] A. Lechner et al., "Power deposition in LHC magnets with and without dispersion suppressor collimators downstream of the betatron cleaning insertion", in *Proceedings, 5th International Particle Accelerator Conference (IPAC 2014): Dresden, Germany, June 15-20, 2014*, p. MOPRO021. doi:10.18429/JACoW-IPAC2014-MOPRO021.

[15] G. Apollinari et al., "High-Luminosity Large Hadron Collider (HL-LHC)", *CERN* (2017) doi:10.23731/CYRM-2017-004.

[16] Z. Citron et al., "Future physics opportunities for high-density QCD at the LHC with heavy ion and proton beams", (2018). arXiv:1812.06772.

[17] CMS Collaboration, "Constraining gluon distributions in nuclei using dijets in proton-proton and proton-lead collisions at $\sqrt{s_{\mathrm{NN}}} = 5.02$ TeV", *Phys. Rev. Lett.* **121** (2018) 062002, doi:10.1103/PhysRevLett.121.062002, arXiv:1805.04736.

[18] K. J. Eskola, P. Paakkinen, and H. Paukkunen, "Impact of CMS dijets in 5.02 TeV pPb and pp collisions on EPPS16 nuclear PDFs", *PoS* **345** (2019) 124, doi:10.22323/1.345.0124, arXiv:1812.05438.

[19] CMS Collaboration, "Observation of nuclear modifications in $\mathrm{W}^{\pm}$ boson production in pPb collisions at $\sqrt{s_{\mathrm{NN}}} = 8.16$ TeV", *Phys. Lett. B* **800** (2020) 135048, doi:10.1016/j.physletb.2019.135048, arXiv:1905.01486.

[20] CMS Collaboration, "Observation of top quark production in proton-nucleus collisions", *Phys. Rev. Lett.* **119** (2017) 242001, doi:10.1103/PhysRevLett.119.242001, arXiv:1709.07411.

[21] CMS Collaboration, "Running of the top quark mass from proton-proton collisions at $\sqrt{s} = 13$ TeV", *Phys. Lett. B* **803** (2020) 135263, doi:10.1016/j.physletb.2020.135263, arXiv:1909.09193.

[22] CMS Collaboration, "Constraining nuclear parton distributions with heavy ion collisions at the HL-LHC with the CMS experiment", CMS Physics Analysis Summary CMS-PAS-FTR-18-027, 2018.

[23] S. Dulat et al., "New parton distribution functions from a global analysis of quantum chromodynamics", *Phys. Rev. D* **93** (2016) 033006, doi:10.1103/PhysRevD.93.033006, arXiv:1506.07443.

[24] K. J. Eskola, P. Paakkinen, H. Paukkunen, and C. A. Salgado, "EPPS16: Nuclear parton distributions with LHC data", *Eur. Phys. J. C* **77** (2017) 163, doi:10.1140/epjc/s10052-017-4725-9, arXiv:1612.05741.

[25] CMS Collaboration, "Measurement of exclusive Υ photoproduction from protons in pPb collisions at $\sqrt{s_{\mathrm{NN}}} = 5.02$ TeV", *Eur. Phys. J. C* **79** (2019) 277, doi:10.1140/epjc/s10052-019-6774-8, arXiv:1809.11080.

[26] CMS Collaboration, "Measurement of exclusive $\rho(770)^0$ photoproduction in ultraperipheral pPb collisions at $\sqrt{s_{\mathrm{NN}}} = 5.02$ TeV", *Eur. Phys. J. C* **79** (2019) 702, doi:10.1140/epjc/s10052-019-7202-9, arXiv:1902.01339.

[27] R. Bruce et al., "New physics searches with heavy ion collisions at the LHC", (12, 2018). arXiv:1812.07688. Accepted by *Phys. Rev. D*.

[28] CMS Collaboration, "Evidence for light-by-light scattering and searches for axion-like particles in ultraperipheral PbPb collisions at $\sqrt{s_{\mathrm{NN}}} = 5.02$ TeV", *Phys. Lett. B* **797** (2019) 134826, doi:10.1016/j.physletb.2019.134826, arXiv:1810.04602.

[29] CMS Collaboration, "Charged-particle nuclear modification factors in XeXe collisions at $\sqrt{s_{\mathrm{NN}}} = 5.44$ TeV", *JHEP* **10** (2018) 138, doi:10.1007/JHEP10(2018)138, arXiv:1809.00201.

[30] CMS Collaboration, "Jet momentum dependence of jet quenching in PbPb collisions at $\sqrt{s_{\mathrm{NN}}} = 2.76$ TeV", *Phys. Lett. B* **712** (2012) 176, doi:10.1016/j.physletb.2012.04.058, arXiv:1202.5022.

[31] CMS Collaboration, "Observation of medium-induced modifications of jet fragmentation in PbPb collisions at $\sqrt{s_{\mathrm{NN}}} = 5.02$ TeVusing isolated photon-tagged jets", *Phys. Rev. Lett.* **121** (2018), no. 24, 242301, doi:10.1103/PhysRevLett.121.242301, arXiv:1801.04895.

[32] CMS Collaboration, "Jet properties in PbPb and pp collisions at $\sqrt{s_{\mathrm{NN}}} = 5.02$ TeV", *JHEP* **05** (2018) 006, doi:10.1007/JHEP05(2018)006, arXiv:1803.00042.

[33] CMS Collaboration, "Jet shapes of isolated photon-tagged jets in PbPb and pp collisions at $\sqrt{s_{\mathrm{NN}}} = 5.02$ TeV", *Phys. Rev. Lett.* **122** (2019), no. 15, 152001, doi:10.1103/PhysRevLett.122.152001, arXiv:1809.08602.

[34] CMS Collaboration, "Studies of charm quark diffusion inside jets using PbPb and pp collisions at $\sqrt{s_{\mathrm{NN}}} = 5.02$ TeV", arXiv:1911.01461. Submitted to *Phys. Rev. Lett.*

[35] CMS Collaboration, "Measurement of b jet shapes in pp collisions at $\sqrt{s_{\mathrm{NN}}} = 5.02$ TeV", CMS Physics Analysis Summary CMS-PAS-HIN-18-020, 2019.

[36] CMS Collaboration, "Measurement of jet nuclear modification factor in PbPb collisions at $\sqrt{s_{\mathrm{NN}}} = 5.02$ TeV with CMS", CMS Physics Analysis Summary CMS-PAS-HIN-18-014, 2019.

[37] CMS Collaboration, "Measurement of quark- and gluon-like jet fractions using jet charge in PbPb and pp collisions at 5.02 TeV", (2020). arXiv:2004.00602. Submitted to *JHEP*.

[38] CMS Collaboration, "Charged particle nuclear modification factors in PbPb and pPb collisions at $\sqrt{s_{\mathrm{NN}}} = 5.02$ TeV", *JHEP* **04** (2017) 039, doi:10.1007/JHEP04(2017)039, arXiv:1611.01664.

[39] K. C. Zapp, "JEWEL 2.0.0: Directions for use", *Eur. Phys. J. C* **74** (2014) 2762, doi:10.1140/epjc/s10052-014-2762-1, arXiv:1311.0048.

[40] I. Lokhtin and A. Snigirev, "A model of jet quenching in ultrarelativistic heavy ion collisions and high-p_{T} hadron spectra at RHIC", *Eur. Phys. J. C* **45** (2006) 211, doi:10.1140/epjc/s2005-02426-3, arXiv:hep-ph/0506189.

[41] A. Andronic, P. Braun-Munzinger, K. Redlich, and J. Stachel, "Decoding the phase structure of QCD via particle production at high energy", *Nature* **561** (2018) 321, doi:10.1038/s41586-018-0491-6, arXiv:1710.09425.

[42] J.-Y. Ollitrault, "Determination of the reaction plane in ultrarelativistic nuclear collisions", *Phys. Rev. D* **48** (1993) 1132, doi:10.1103/PhysRevD.48.1132, arXiv:hep-ph/9303247.

[43] S. Voloshin and Y. Zhang, "Flow study in relativistic nuclear collisions by Fourier expansion of azimuthal particle distributions", *Z. Phys. C* **70** (1996) 665, doi:10.1007/s002880050141, arXiv:hep-ph/9407282.

[44] A. M. Poskanzer and S. Voloshin, "Methods for analyzing anisotropic flow in relativistic nuclear collisions", *Phys. Rev. C* **58** (1998) 1671, doi:10.1103/PhysRevC.58.1671, arXiv:nucl-ex/9805001.

[45] CMS Collaboration, "Search for strong electromagnetic fields in PbPb collisions at 5.02 TeV via azimuthal anisotropy of D^0 and $\overline{\mathrm{D}}^0$ mesons", CMS Physics Analysis Summary CMS-PAS-HIN-19-008, 2019.

[46] U. Gürsoy et al., "Charge-dependent flow induced by magnetic and electric fields in heavy ion collisions", *Phys. Rev. C* **98** (2018) 055201, doi:10.1103/PhysRevC.98.055201, arXiv:1806.05288.

[47] CMS Collaboration, "Measurement of the elliptic flow of $\Upsilon(1S)$ and $\Upsilon(2S)$ mesons in PbPb collisions at $\sqrt{s_{NN}} = 5.02$ TeV", CMS Physics Analysis Summary CMS-PAS-HIN-19-002, 2019.

[48] CMS Collaboration, "Suppression and azimuthal anisotropy of prompt and nonprompt J/ψ production in PbPb collisions at $\sqrt{s_{NN}} = 2.76$ TeV", *Eur. Phys. J. C* **77** (2017) 252, doi:10.1140/epjc/s10052-017-4781-1, arXiv:1610.00613.

[49] CMS Collaboration, "Measurement of nuclear modification factors of $\Upsilon(2S)$, $\Upsilon(2S)$, and $\Upsilon(3S)$ mesons in PbPb collisions at $\sqrt{s_{NN}} = 5.02$ TeV", *Phys. Lett. B* **790** (2019) 270, doi:10.1016/j.physletb.2019.01.006, arXiv:1805.09215.

[50] CMS Collaboration, "Studies of charm and beauty long-range correlations in pp and pPb collisions", CMS Physics Analysis Summary CMS-PAS-HIN-19-009, 2019.

[51] CMS Collaboration, "Elliptic flow of charm and strange hadrons in high-multiplicity pPb collisions at $\sqrt{s_{NN}} = 8.16$ TeV", *Phys. Rev. Lett.* **121** (2018) 082301, doi:10.1103/PhysRevLett.121.082301, arXiv:1804.09767.

[52] CMS Collaboration, "Observation of prompt J/ψ meson elliptic flow in high-multiplicity pPb collisions at $\sqrt{s_{NN}} = 8.16$ TeV", *Phys. Lett. B* **791** (2019) 172, doi:10.1016/j.physletb.2019.02.018, arXiv:1810.01473.

[53] C. Zhang et al., "Elliptic flow of heavy quarkonia in pA collisions", *Phys. Rev. Lett.* **122** (2019) 172302, doi:10.1103/PhysRevLett.122.172302, arXiv:1901.10320.

[54] Belle Collaboration, "Observation of a narrow charmonium-like state in exclusive $B^{\pm} \to K^{\pm}\pi^{+}\pi^{-}J/\psi$ decays", *Phys. Rev. Lett.* **91** (2003) 262001, doi:10.1103/PhysRevLett.91.262001, arXiv:hep-ex/0309032.

[55] CMS Collaboration, "Observation of the $B_s^0 \to X(3872)\phi$ decay", (2020). arXiv:2005.04764. Submitted to *Phys. Rev. Lett.*

[56] CMS Collaboration, "Evidence for $\chi_{c1}(3872)$ in PbPb collisions and studies of its prompt production at $\sqrt{s_{NN}} = 5.02$ TeV", CMS Physics Analysis Summary CMS-PAS-HIN-19-005, 2019.

[57] L. Apolinário, G. Milhano, C. A. Salgado, and G. Salam, "Unveiling the yoctosecond structure of the QGP with top quarks", *Nucl. Phys. A* **982** (2019) 795, doi:10.1016/j.nuclphysa.2018.11.014.

[58] CMS Collaboration, "Evidence for top quark production in nucleus-nucleus collisions", CMS Physics Analysis Summary CMS-PAS-HIN-19-001, 2019.

[59] CMS Collaboration, "Measurement of the inclusive $t\bar{t}$ cross section in pp collisions at $\sqrt{s} = 5.02$ TeV using final states with at least one charged lepton", *JHEP* **03** (2018) 115, doi:10.1007/JHEP03(2018)115, arXiv:1711.03143.

[60] M. Czakon, P. Fiedler, and A. Mitov, "Total top quark pair production cross section at hadron colliders through $\mathcal{O}(\alpha_S^4)$", *Phys. Rev. Lett.* **110** (2013) 252004, doi:10.1103/PhysRevLett.110.252004, arXiv:1303.6254.

[61] A. Kusina et al., "Vector boson production in pPb and PbPb collisions at the LHC and its impact on nCTEQ15 PDFs", *Eur. Phys. J. C* **77** (2017) 488, doi:10.1140/epjc/s10052-017-5036-x, arXiv:1610.02925.

[62] NNPDF Collaboration, "Parton distributions for the LHC Run 2", *JHEP* **04** (2015) 040, doi:10.1007/JHEP04(2015)040, arXiv:1410.8849.

Probing dense QCD: from Heavy Ion Collisions to the EIC

Yacine Mehtar-Tani

E-Mail: mehtartani@bnl.gov

Physics Department and RIKEN BNL Research Center, Brookhaven National Laboratory, Upton, NY 11973, USA.

Presented at the Workshop of QCD and Forward Physics at the EIC, the LHC, and Cosmic Ray Physics in Guanajuato, Mexico, November 18-21 2019

Abstract

In this talk, I give a brief overview of heavy ion physics. I discuss QCD dynamics at high energy and high parton density in a wide momentum range spanning collective dynamics in the soft sector to jet quenching at high momentum. I will also touch upon the physics of gluon saturation that will be probed at the future EIC.

1 Introduction

There is today a plethora of experimental evidence confirming Quantum-Chromodynamics (QCD) as the fundamental theory of strong interactions in the high momentum transfer regime. Perturbative QCD provides a natural explanation of the partonic nature of proton structure observed in Deep-Inelastic Scattering (DIS) that is a consequence of asymptotic freedom. In electron-positron (e^+e^-) experiment the so-called R ratio of the total hadronic cross-section to the muon cross-section provides a direct measure of color and flavor degrees of freedom [1]. In addition, 3 jet events provide the most direct evidence of the existence of the gluon [2].

The standard understanding of hadronic structure is rooted in the partonic picture which is manifest in the Bjorken limit, at high momentum transfer Q^2 but moderate Bjorken x_{Bj}, where both the longitudinal and transverse partonic wave length are small compered to the size of the proton. In this dilute partonic regime, quarks and gluons are weakly interacting. However, at very small values of x, gluon density rises rapidly until gluon recombination are non longer negligible leading to saturation effects [3, 4]. This phenomenon is associated with a semi-hard scale, the saturation scale, $Q_s^2(x) \sim A^{1/3}x^{-0.3}$ that increases when x decreases. It is also larger for large nuclei with atomic number A (for review see [5]). Gluon saturation was first investigated in HERA in e-p collisions, then, at RHIC and the LHC in d-Au and p-Pb collisions respectively. Although no conclusive evidence for gluon saturation was found yet it provides a natural, first principle based, initial condition for the onset of the quark-gluon plasma in heavy ion collisions (HIC).

The heavy ion programs at RHIC and LHC aims at exploring new facets of QCD at high energy and high parton density where strong final state interactions take place. The collision of two ultra-relativistic heavy ions is expected to lead to the formation of a new state of deconfined matter if sufficiently high energy density is achieved. At a critical temperature of order $T_c \sim 145 - 163$ GeV [6] a cross over phase transition takes place from hadronic matter to a new state of hot matter characterized by freely roaming quarks and gluons, the so-called quark-gluon plasma (QGP). Following up on the SPS heavy ion experimental program, the advent of the RHIC collider in early 2000's opened up new perspectives for probing this novel regime of QCD and its transport properties. The strong suppression of high pt hadrons and quarkonia (such as J/Ψ melting) in addition to the success of ideal hydrodynamics in describing bulk observables such as Elliptic Flow constitute overwhelming evidence of the creation of such deconfinement phase transition [7].

The study of high pT particles with jet quenching observables at RHIC and the LHC provides a tool to investigate the out-of-equilibrium dynamics of QCD. Jets that are born from energetic partons in colliders tend to fragment into a collimated bunch of particles. However, in contrast to jet production in smaller systems, in heavy ion collisions jets do not evolve in vacuum but instead propagate and fragment inside the QGP (see Refs. [8, 9] for reviews). The detailed interactions of this coherent multi-partonic system with the quark gluon plasma is the subject of active research. Among of the questions being investigated is how energy flows from the energetic jet components to the plasma where dissipation takes place and hence, how thermal equilibrium is reach in QCD and how the jet substructure is modified by interactions with the plasma.

In spite of the complexity of the many-body dynamics inherent to HIC they provide nevertheless a rich laboratory to study dense QCD and associated emergent phenomena from the TeV to the GeV scale.

2 Soft QCD observables in HIC

Perhaps the major discovery of the RHIC program is that the QGP behaves as a perfect liquid [10–13]. The extensive study of flow harmonics has established the fact the QGP is a strongly interacting fluid with very low sheer viscosity closed to the AdS/CFT lower bound $\eta/s = 1/4\pi$ [14].

Collective flow is a response of the system to initial geometry. In the presence of collectivity in the aftermath of the collision initial spacial anisotropy that is generated by non-central collisions is transformed into momentum anisotropy. This information is encoded in the anisotropic Fourier harmonics the v_n's [15], that are extracted from low momentum particle distributions, up to 3 GeV,

$$\frac{\mathrm{d}N}{\mathrm{d}^3p} = \frac{\mathrm{d}N}{2\pi p \mathrm{d}p \mathrm{d}y}\left\{1 + 2\sum_{n=1}^{\infty} v_n \cos\left[n\left(\varphi - \Phi_{\mathrm{RP}}\right)\right]\right\}, \tag{2.1}$$

where Φ_{RP} is the reaction plane angle and φ the measured particle azimuthal angle. The first few flow harmonics, v_2, v_3, that are the Elliptic and Triangular flow harmonics, respectively were measured at RHIC and LHC to high precision and successfully described by viscous hydrodynamics [16]. This allows an extraction of the sheer to entropy ratio of the order of 0.1 - 0.2. The state of the art theory to data comparison uses Bayesian fitting techniques (see [17] and references therein) and multiple-stage modeling such as IP-Glasma [18].

Surprisingly enough, the success of hydrodynamics extents to smaller collision systems such as proton-Pb collisions albeit for high enough multiplicities [19]. This begs the question as to whether a droplet of QGP is formed in those rare events, where initial eccentricity is generated by fluctuation rather than geometry as in nucleus-nucleus collisions, and what role initially born

correlations play in the final momentum anisotropy such as predicted by the theory of the color glass condensate [20]. These questions are being currently intensively debated. To answer this question the approach to hydrodynamization from a system of partons in a coherent quantum state before the collision to a quasi-thermal medium need to be fully addressed. A recent study using kinetic theory at weak coupling have shown that hydrodynamic behavior can set in when the system is still far from thermal equilibrium as early as 1 fm/c for $\eta/s = 0.16$ that is compatible with phenomenological studies [21]. In the bottom-up thermalization scenario that discusses thermalization in non-Abelian plasmas in heavy ion collisions [22], the system right after the collision is characterized by high occupation of gluons described by strong classical gauge field within the Glasma picture [23]. It evolves first towards a non-thermal fixed point driven by Bjorken expansion at high occupation numbers [24]. In the final stage occupation numbers drop below unity and the hard partons undergo a radiative breakup akin to the jet quenching phenomenon. Hence, by studying jet quenching observables one learns about the approach to equilibrium in QCD plasmas.

Going up in momentum we encounter one of the most emblematic observables to probe the QGP in HIC first suggested by Matsui and Satz [25], that is, quarkonia suppression. Depending on their binding energy quark-antiquark bound states would melt into the plasma at different temperature thus the hierarchy of quarkonium dissociation probes the temperature of the medium, providing a so-called "QGP thermometer" [26]. This was most remarkably achieved by the CMS collaboration in their mesure of $\Upsilon(1)$, $\Upsilon(2)$ and $\Upsilon(3)$ suppression in PbPb collisions [27].

3 Jet quenching and color decoherence

In the early 1980's, J. D. Bjorken has suggested that high energy jets may suffer differential energy loss in a QGP and therefore, the suppression of jets could signal the creation of a QGP [28]. The classical observable that was extensively studied is the jet nuclear modification factor

$$R_{AA} = \frac{1}{N_{\rm coll}} \frac{\mathrm{d}N_{AA}/\mathrm{d}^2 p_T}{\mathrm{d}N_{pp}/\mathrm{d}^2 p_T} \,, \tag{3.1}$$

that compares the jet spectrum in A+A collisions to that of proton-proton collisions scaled by the number of binary nucleon-nucleon collisions. A value of $R_{AA} \ll 1$ signals the fact that jets lose energy due to final state interactions with the the QGP.

High energy quarks and gluons lose energy in the medium via elastic processes for which energy loss grows linearly with the length of the medium L, however, although gluon radiation comes at the cost of an additional power of the weak coupling constant, in large media inelastic processes become dominant as they scale as L^2 [29–33].

Medium-induced gluon radiation is driven by coherent multiple scattering that act a single scattering center during the quantum mechanical formation time $t_f \equiv \omega/k_\perp^2$. During this time the radiated gluon accumulate a transverse momentum of order $k_\perp^2 \sim \hat{q} t_f$, where $\hat{q}$ is a diffusion coefficient in transverse momentum space [30],

$$\hat{q} = \frac{\mathrm{d}\langle k_\perp^2 \rangle}{\mathrm{d}t} \simeq \alpha_s m_D^2 T \log Q^2/m_D^2 \,, \tag{3.2}$$

where $m_D \sim gT$ is the Debye mass, T the plasma temperature and Q the relevant UV scale of the problem. Combining the above expressions expressions we find that $t_f = \sqrt{\omega/\hat{q}}$ decreases with decreasing gluon frequency. The resulting radiative spectrum reads $\omega \mathrm{d}I/\mathrm{d}\omega = \bar{\alpha}\sqrt{\omega_c/\omega}$ where $\omega_c = \hat{q}L^2/2$. Hence, the medium-induced radiative spectrum is suppressed at large frequency due to destructive interferences. This is the QCD analog of the Landau-Pemeranchuk-Migdal [31, 34, 35]. Although the average energy loss is dominated by rare emissions, $\mathcal{O}(\bar{\alpha})$, with frequency ω_c,

i.e., $\Delta E \sim \bar{\alpha}\omega_c$, it was shown that owing to the steeply falling jet spectrum, $\mathrm{d}\sigma/\mathrm{d}p_T \sim p_T^{-n}$ with $n \gg 1$, the final jet spectrum is sensitive to the typical energy loss $\omega_s =\equiv \bar{\alpha}^2\omega_c$ that is smaller than the average energy loss and is carried by abundant medium-induced gluons [36]. In this case, because soft gluons have short formation times multiple gluon emission can be treated as independent. It follows that the probability for an energetic quark to lose ϵ amount of energy is given by a Poisson-like distribution, where $\epsilon = \omega_1 + \omega_2 + ... + \omega_n$. The final spectrum can be calculated with the help of the factorized formula [36, 37]

$$\frac{\mathrm{d}\sigma_{\mathrm{med}}}{\mathrm{d}^2 p_T} = \int \mathrm{d}\epsilon P(\epsilon) \frac{\mathrm{d}\sigma_{\mathrm{vac}}}{\mathrm{d}^2 p_T'}(p_T' = p_T + \epsilon). \tag{3.3}$$

The above qualitative physical picture becomes more complicated as far as fully reconstructed jets are concerned. Although to a first approximation a jet can be thought of as a single parton, due to collinearly enhanced splittings that result from the decay of highly virtual partons, a high p_T jet is composed of a large number of collinear partons that are correlated in color. Furthermore, a jet is defined by its opening angle R. Hence, in addition to understanding how a multi-partonic system loses energy, which requires a generalization to higher orders of the single parton energy loss picture, one also need to understand how energy is transported out of the jet cone.

Primary gluon radiation undergo further medium induced branching triggering a gluon cascade of a new kind. Due to to the LPM suppression that suppresses small angle splitting this cascade tends to form at large angles. Moreover, it is characterized on average by democratic branchings. This results in local energy transport (in frequency space) from high to low frequencies akin to wave turbulence [38] and to large angles [39]. This is the most efficient mechanism for energy transport from the TeV scale down to the temperature of the plasma $T < 1$ GeV as energy flows without accumulation until dissipative forces take place. The associated Kolmogorov-Zakharov power spectrum is $\omega^{-1/2}$. It provides a natural explanation for the missing jet pt in dijet event that is recovered at wide angles w.r.t. the dijet axes [40].

As alluded to above, due to the inherent quantum nature of jet evolution and medium-induced radiation, quantum interferences play a crucial role in jet-medium interactions. In vacuum, due to color coherence large angle soft gluon radiation does not resolve the internal structure of the jet and thus, is sensitive to the total color charge. For example, gluon radiation off a collimated quark anti-quark pair produced in the decay of a boosted W or Top bosons will be suppressed since the dipole system is in a color singlet state. This feature is at the core of angular ordering in QCD parton cascades implemented in various Monte Carlo event generators.

In the presence of a dense color medium color coherence is bound to be altered in the soft sector due to the induced rapid color precession that jet constituents undergo inside the plasma. This results in the decoherence of the decay products in color space and thus, opening up a phase-space for larger angle soft radiation that was forbidden in vacuum [41–43]. This mechanism may explain the soft enhancement of medium-modified fragmentation functions [44, 45]. The number of effective color charges that lose energy in the plasma depends on the plasma transverse resolution power which related to transverse momentum broadening $\Lambda_{\mathrm{med}} \sim (\hat{q}L)^{-1/2}$. In the limiting case where $\Lambda_{\mathrm{med}}^2 \gg RL$, where RL is the typical transverse size of the jet in the plasma, the plasma "sees" one single color charge.

Hence, jet energy loss depends on the fluctuations of the jet substructure so long as the angular separation between two subjets is larger than the characteristic angular scale $\theta_c = (\hat{q}L^3)^{-1/2}$. A detailed analysis of the phase-space of high-order corrections to jet quenching leads to Sudakov-like suppression (in the strong quenching limit) [46]

$$R_{\mathrm{AA}} = \mathcal{Q}_q(p_T) \times \mathcal{C}_q(p_T, R)\,, \tag{3.4}$$

where $\mathcal{Q}_q(p_T)$ the single quark quenching factor (neglecting gluon jets) and

$$\mathcal{C}_q(p_T, R) \simeq \exp\left[-2\bar{\alpha}\ln\frac{R}{\theta_c}\left(\ln\frac{p_T}{\omega_c} + \frac{2}{3}\ln\frac{R}{\theta_c}\right)\right], \tag{3.5}$$

is the collimator function that the effect of fluctuations of the jet substructure to leading logarithmic accuracy.

Color coherence was recently implemented in a Monte Carlo event generator to leading logarithmic accuracy [47].

4 QCD at the EIC

The future Electron-Ion-Collider will allow to address several critical physics questions pertaining to proton and nuclear structure. What is the origin of the proton mass, given that the valence quarks account for a negligible fraction? How is the proton spin generated? How much the the spin is carried by gluons and quarks spins and how much by their orbital momenta? [48] The goal of the EIC is to probe the 3D structure. This multi-dimensional tomography of proton structure can shed light on the distribution of gluons and quarks in transverse momentum $k_\perp$ by investigating transverse momentum dependent distributions (TMD's) and impact parameter $b_\perp$ space via Generalized Parton Distributions (GPD's), in addition to the standard longitudinal momentum fraction x in parton distribution functions (PDF's). All of these distributions are related to a phase-space Wigner function distribution that reduces to one of the aforementioned distribution by integrating one or more of its variables [49].

TMD's can be accessed with processes such as semi-inclusive DIS (SIDIS) where a hadron is measured in the final state with a certain $k_\perp$ while a standard observable to probe GPD's is deeply virtual Compton scattering (DVCS).

At small x, high gluon density effects are expected to take place. In this regime, accessible in the Regge limit, i.e., $s \gg Q^2$, gluons dominates the dynamics and non-linear recombination effects are no longer negligible leading eventually to the phenomenon of gluon saturation. The relevant degrees of freedom are no longer isolated partons but instead strong classical gauge fields [50]. Quantum evolution equation of structure functions at small x were derived in the late 1990's, leading to the establishment of the color glass condensate effective theory (CGC) [51, 52, 54]. Next-to-leading order corrections to small x evolution was recently achieved [55] and high order corrections to various observables are being currently developed (see for instance [56]). The latter will play a crucial role in probing saturation physics with high precision at the EIC where the values of Bjorken x that may be accessible are of order $10^{-3} - 10^{-4}$ for a $\sqrt{s} = 140$ GeV.

Finally, a recent feasibility study [57] have demonstrated that fully reconstructed jets can be measured at and EIC where $\sqrt{s} = 100 - 140$ GeV. Jet observables will provide additional handles to test QCD while reducing the non-perturbative effects of hadronization. In electron-nucleus collisions, by studying jet broadening and energy loss one may hope to access transport properties of cold nuclear matter.

Acknowledgements

This work was supported by the U.S. Department of Energy, Office of Science, Office of Nuclear Physics, under contract No. DE- SC0012704, and by Laboratory Directed Research and Development (LDRD) funds from Brookhaven Science Associates. We also acknowledge support from the RHIC Physics Fellow Program of the RIKEN BNL Research Center.

References

[1] W. M. Yao *et al.* [Particle Data Group], J. Phys. G **33** (2006), 1-1232 doi:10.1088/0954-3899/33/1/001

[2] R. Brandelik *et al.* [TASSO], Phys. Lett. B **86** (1979), 243-249 doi:10.1016/0370-2693(79)90830-X

[3] L. Gribov, E. Levin and M. Ryskin, Phys. Rept. **100**, 1-150 (1983) doi:10.1016/0370-1573(83)90022-4.

[4] A. H. Mueller and J. w. Qiu, Nucl. Phys. B **268**, 427-452 (1986) doi:10.1016/0550-3213(86)90164-1.

[5] R. Venugopalan, [arXiv:hep-ph/0412396 [hep-ph]].

[6] A. Bazavov *et al.* [HotQCD], Phys. Rev. D **90** (2014), 094503 [arXiv:1407.6387 [hep-lat]].

[7] W. Busza, K. Rajagopal and W. van der Schee, Ann. Rev. Nucl. Part. Sci. **68** (2018), 339-376 [arXiv:1802.04801 [hep-ph]].

[8] J. P. Blaizot and Y. Mehtar-Tani, Int. J. Mod. Phys. E **24** (2015) no.11, 1530012 [arXiv:1503.05958 [hep-ph]].

[9] Y. Mehtar-Tani, J. G. Milhano and K. Tywoniuk, "Jet physics in heavy-ion collisions," Int. J. Mod. Phys. A **28**, 1340013 (2013) [arXiv:1302.2579 [hep-ph]].

[10] I. Arsene *et al.* [BRAHMS], Nucl. Phys. A **757** (2005), 1-27 [arXiv:nucl-ex/0410020 [nucl-ex]].

[11] B. B. Back *et al.* [PHOBOS], Nucl. Phys. A **757** (2005), 28-101 [arXiv:nucl-ex/0410022 [nucl-ex]].

[12] J. Adams *et al.* [STAR], Nucl. Phys. A **757** (2005), 102-183 [arXiv:nucl-ex/0501009 [nucl-ex]].

[13] K. Adcox *et al.* [PHENIX], Nucl. Phys. A **757** (2005), 184-283 [arXiv:nucl-ex/0410003 [nucl-ex]].

[14] G. Policastro, D. T. Son and A. O. Starinets, Phys. Rev. Lett. **87** (2001), 081601 [arXiv:hep-th/0104066 [hep-th]].

[15] S. Voloshin and Y. Zhang, Z. Phys. C **70** (1996), 665-672 doi:10.1007/s002880050141 [arXiv:hep-ph/9407282 [hep-ph]].

[16] S. Jeon and U. Heinz, Int. J. Mod. Phys. E **24** (2015) no.10, 1530010 doi:10.1142/S0218301315300106 [arXiv:1503.03931 [hep-ph]].

[17] C. Shen, [arXiv:2001.11858 [nucl-th]].

[18] B. Schenke, P. Tribedy and R. Venugopalan, Phys. Rev. Lett. **108** (2012), 252301 [arXiv:1202.6646 [nucl-th]].

[19] C. Aidala *et al.* [PHENIX], Nature Phys. **15** (2019) no.3, 214-220 [arXiv:1805.02973 [nucl-ex]].

[20] M. Mace, V. V. Skokov, P. Tribedy and R. Venugopalan, Phys. Lett. B **788** (2019), 161-165 [arXiv:1807.00825 [hep-ph]].

[21] A. Kurkela, A. Mazeliauskas, J. F. Paquet, S. Schlichting and D. Teaney, Phys. Rev. C **99** (2019) no.3, 034910 [arXiv:1805.00961 [hep-ph]].

[22] R. Baier, A. H. Mueller, D. Schiff and D. T. Son, Phys. Lett. B **502** (2001), 51-58 doi:10.1016/S0370-2693(01)00191-5 [arXiv:hep-ph/0009237 [hep-ph]].

[23] T. Lappi and L. McLerran, Nucl. Phys. A **772** (2006), 200-212 [arXiv:hep-ph/0602189 [hep-ph]].

[24] J. Berges, M. P. Heller, A. Mazeliauskas and R. Venugopalan, [arXiv:2005.12299 [hep-th]].

[25] T. Matsui and H. Satz, Phys. Lett. B **178** (1986), 416-422

[26] A. Andronic *et al* Eur. Phys. J. C **76** (2016) no.3, 107 [arXiv:1506.03981 [nucl-ex]].

[27] [CMS], CMS-PAS-HIN-15-001.

[28] J. D. Bjorken, "Energy Loss of Energetic Partons in Quark - Gluon Plasma: Possible Extinction of High p(t) Jets in Hadron - Hadron Collisions," FERMILAB-PUB-82-059-THY, FERMILAB-PUB-82-059-T.

[29] R. Baier, Y. L. Dokshitzer, A. H. Mueller, S. Peigne and D. Schiff, "Radiative energy loss and p(T) broadening of high-energy partons in nuclei," Nucl. Phys. B **484**, 265 (1997) [hep-ph/9608322].

[30] R. Baier, Y. L. Dokshitzer, A. H. Mueller, S. Peigne and D. Schiff, "Radiative energy loss of high-energy quarks and gluons in a finite volume quark - gluon plasma," Nucl. Phys. B **483**, 291 (1997) [hep-ph/9607355].

[31] B. G. Zakharov, "Fully quantum treatment of the Landau-Pomeranchuk-Migdal effect in QED and QCD," JETP Lett. **63**, 952 (1996) [hep-ph/9607440].

[32] M. Gyulassy, P. Levai and I. Vitev, "Reaction operator approach to nonAbelian energy loss," Nucl. Phys. B **594**, 371 (2001) [nucl-th/0006010].

[33] X. N. Wang and X. f. Guo, "Multiple parton scattering in nuclei: Parton energy loss," Nucl. Phys. A **696**, 788 (2001) doi:10.1016/S0375-9474(01)01130-7 [hep-ph/0102230].

[34] L. D. Landau and I. Pomeranchuk, "Electron cascade process at very high-energies," Dokl. Akad. Nauk Ser. Fiz. **92**, 735 (1953).

[35] A. B. Migdal, "Bremsstrahlung and pair production in condensed media at high-energies," Phys. Rev. **103**, 1811 (1956).

[36] R. Baier, Y. L. Dokshitzer, A. H. Mueller and D. Schiff, JHEP **09** (2001), 033 doi:10.1088/1126-6708/2001/09/033 [arXiv:hep-ph/0106347 [hep-ph]].

[37] C. A. Salgado and U. A. Wiedemann, "Calculating quenching weights," Phys. Rev. D **68**, 014008 (2003) [hep-ph/0302184].

[38] J. P. Blaizot, E. Iancu and Y. Mehtar-Tani, "Medium-induced QCD cascade: democratic branching and wave turbulence," Phys. Rev. Lett. **111**, 052001 (2013) [arXiv:1301.6102 [hep-ph]].

[39] J. P. Blaizot, Y. Mehtar-Tani and M. A. C. Torres, Phys. Rev. Lett. **114** (2015) no.22, 222002 [arXiv:1407.0326 [hep-ph]].

[40] [CMS], CMS-PAS-HIN-14-010.

[41] Y. Mehtar-Tani, C. A. Salgado and K. Tywoniuk, Phys. Rev. Lett. **106** (2011) 122002

[42] Y. Mehtar-Tani, C. A. Salgado and K. Tywoniuk, Phys. Lett. B **707** (2012) 156

[43] J. Casalderrey-Solana and E. Iancu, JHEP **1108** (2011) 015

[44] Y. Mehtar-Tani and K. Tywoniuk, Phys. Lett. B **744** (2015), 284-287 [arXiv:1401.8293 [hep-ph]].

[45] P. Caucal, E. Iancu, A. H. Mueller and G. Soyez, Phys. Rev. Lett. **120** (2018) 232001 [arXiv:1801.09703 [hep-ph]].

[46] Y. Mehtar-Tani and K. Tywoniuk, Phys. Rev. D **98**, no. 5, 051501 (2018) [arXiv:1707.07361 [hep-ph]].

[47] P. Caucal, E. Iancu and G. Soyez, JHEP **10** (2019), 273 doi:10.1007/JHEP10(2019)273 [arXiv:1907.04866 [hep-ph]].

[48] A. Accardi *et al*, Eur. Phys. J. A **52** (2016) no.9, 268 doi:10.1140/epja/i2016-16268-9 [arXiv:1212.1701 [nucl-ex]].

[49] Y. Hatta, [arXiv:2004.05336 [hep-ph]].

[50] L. D. McLerran and R. Venugopalan, Phys. Rev. D **49**, 2233-2241 (1994) [arXiv:hep-ph/9309289 [hep-ph]]

[51] I. Balitsky, Nucl. Phys. B **463** (1996), 99-160 doi:10.1016/0550-3213(95)00638-9 [arXiv:hep-ph/9509348 [hep-ph]].

[52] Y. V. Kovchegov, Phys. Rev. D **60** (1999), 034008 [arXiv:hep-ph/9901281 [hep-ph]].

[53] J. Jalilian-Marian, A. Kovner, A. Leonidov and H. Weigert, Phys. Rev. D **59** (1998), 014014 [arXiv:hep-ph/9706377 [hep-ph]] ; E. Iancu, A. Leonidov and L. D. McLerran, Nucl. Phys. A **692** (2001), 583-645 [arXiv:hep-ph/0011241 [hep-ph]].

[54] J. Jalilian-Marian, A. Kovner, A. Leonidov and H. Weigert, Phys. Rev. D **59** (1998), 014014 doi:10.1103/PhysRevD.59.014014 [arXiv:hep-ph/9706377 [hep-ph]] ; E. Iancu, A. Leonidov and L. D. McLerran, Nucl. Phys. A **692** (2001), 583-645 doi:10.1016/S0375-9474(01)00642-X [arXiv:hep-ph/0011241 [hep-ph]].

[55] I. Balitsky and G. A. Chirilli, Phys. Rev. D **77**, 014019 (2008) doi:10.1103/PhysRevD.77.014019 [arXiv:0710.4330 [hep-ph]].

[56] K. Roy and R. Venugopalan, Phys. Rev. D **101** (2020) no.3, 034028 doi:10.1103/PhysRevD.101.034028 [arXiv:1911.04530 [hep-ph]].

[57] E. C. Aschenauer, S. Fazio, J. H. Lee, H. Mantysaari, B. S. Page, B. Schenke, T. Ullrich, R. Venugopalan and P. Zurita, Rept. Prog. Phys. **82** (2019) no.2, 024301 doi:10.1088/1361-6633/aaf216 [arXiv:1708.01527 [nucl-ex]].

Study of initial conditions in small systems at LHC energies with String Percolation Model.

Pablo Fierro* [1], Irais Bautista [2], J. Ricardo Alvarado [2], Miguel Ortiz [2], Alan Ruiz [2]

E-Mail: pablo.fierro.rojas@cern.ch

Instituto de Física Luis Rivera Terrazas, Benemérita Universidad Autónoma de Puebla [1]
Facultad de Ciencias Físico Matemáticas, Benemérita Universidad Autónoma de Puebla[2]

Presented at the Workshop of QCD and Forward Physics at the EIC, the LHC, and Cosmic Ray Physics in Guanajuato, Mexico, November 18-21 2019

Abstract

sing the Color String Percolation Model, a review is made of the results obtained for p-p and p-Pb collisions at Large Hadron Collider (LHC) energies. These results show the description of a state that presents common characteristics with the Quark Gluon Plasma (QGP) status formed in nuclear collisions. However, studies of this system in the framework of the string percolation model imply the presence of particularities that are not observed in the QGP system in nuclear collisions and that lead to an important conceptual differentiation of these states.

1 The Model

The phase transition in QCD can be described from percolation theory by using critical orden parameters. In the String Percolation Model (SPM) we use the 2-dimensional percolation theory over the overlapping area of a collision, S, considering the chromodynamic interaction as color flux tubes stretched among the colliding partons of the proyectiles or targets. By the Schwinger mechanism more strings are created and more particles are produced, which are then identified by the detectors.

The number of initial strings, $\bar{N}^s$, depends on the energy of the collision, on the number of participants and, of course, on the centrality of the event.

$$\bar{N}^s = 2 + 4\frac{S_0}{S}\left(\frac{\sqrt{s}}{m_p}\right)^{2\lambda}, \tag{1.1}$$

where $m_p = 938.3$MeV is the mass of the proton and the power $\lambda = 0.186$ describes the multiplicity increase with the energy in p-p and A-A collisions. The transverse area of a string is $S_0 = \pi r_0^2$, with $r_0 = 0.25$fm[1]. As the multiplicity increases the string density will increase to and the strings will start to overlap to form macroscopic clusters, thus marking a phase transition defined by the

percolation threshold $\xi_c \approx 1.2$, the critical string density, to classify the events the string density is defined as

$$\xi = \frac{S_0}{S}\bar{N}_s. \tag{1.2}$$

The average multiplicity at central rapidity region, $\mu \equiv dN/d\eta$, for each energy is related to the average number of initial strings through the following geometrical scalling function of the string density[2]

$$\mu = \kappa F(\xi)\bar{N}^s, \tag{1.3a}$$

which has the form

$$F(\xi) = \sqrt{(1 - e^{-\xi})/\xi}. \tag{1.3b}$$

2 Fits over the experimental data

Using the above equations, we parametrize $S(b) = \pi(R_p - b/2)\sqrt{R_p^2 - (b/2)^2}$ through the impact parameter b, we made a global fit over the minimum bias mutiplicity dependence of the center of mass energy experimental data [3-11].

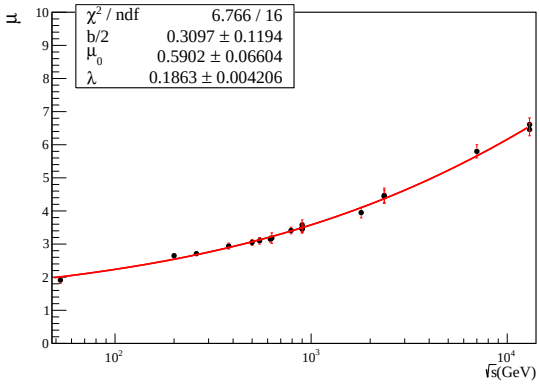

Figure 1: Multiplicity dependence of energy fit.

The transverse momentum distribution for charged pions behaves as the following power law

$$\frac{1}{N}\frac{d^2N_{ch}}{d\eta dp_T}\bigg|_{\eta=0} \sim \frac{p_0^{\alpha-2}}{(p_T + p_0)^{\alpha-1}}, \tag{2.1}$$

In order to obtain p_0 and α, which are energy parameters, it is necessary to make a fit over the minimum bias transverse momentum distributions from data [12-14], as shown in the figure 1, the values of these parameters are shown in table 1.

	$\sqrt{s}$(TeV)	p_0(GeV)	α
p-Pb	5.02	2.780±0.171	9.937±1.716
p-p	13	2.478±1.862	9.980±0.297
	7	2.305±0.079	9.752±0.140
	2.76	2.032±0.074	9.448±0.147
	0.9	1.785±0.071	9.287±0.165
	0.2	1.98±0.1215	9.40 ± 1.80

Table 1: Model energy parameter values

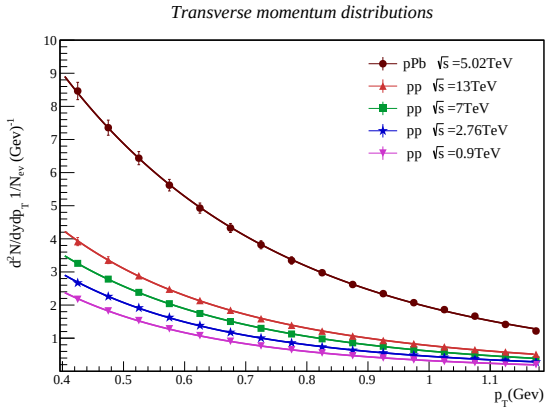

Figure 2: Fit of the equation (4) over the transverse moment distributions of charged pions in p-p collisions at energies of 0.9, 2.76, 7 and 13 TeV and p-Pb collisions at 5.02 TeV, in region 0.4 $< p_T <$1.175, data from the CMS collaboration [12-14].

We use the deviation between high multiplicity (ξ) and minimum bias events (ξ_0) through $p_0 \to p_0\sqrt{F(\xi_0)/F(\xi)}$. We use this relation in eq. (4) to make a new fit over the high multiplicity events obtaining the corresponding Color Reduction Factors for each multiplicity class.

To include the spectra of different hadron species H, we use the relation[15,16]

$$P(H) = \left.\frac{1}{N}\frac{d^2N}{d\eta dp_T}\right|_H \sim \exp\left(\frac{-m_H^2 F(\xi_0)}{\langle p_T\rangle^2 + \langle p_H\rangle^2}\right)\left.\frac{1}{N}\frac{d^2N}{d\eta dp_T}\right|_\pi . \tag{2.2}$$

The Λ_c/D^0 production ratio is obtained by fitting $P(\Lambda_c)/P(D^0)$ to the data [17]. Using $P_{HM} \sim F(\xi_{HM})\exp\left(\frac{-m_H}{\langle p_H\langle + p_T}\right)$ to obtain the different multiplicity class, with the corresponding string density parameter ξ_H, we make a prediction for the production ratio spectra behavior (fig 2).

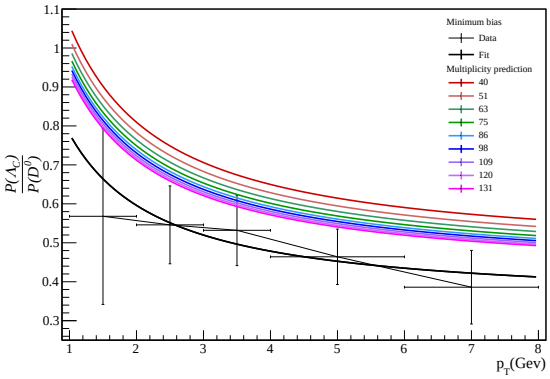

Figure 3: The figure shows the fit to the min bias data[8] and the prediction of the Λ_c/D^0 production for different multiplicity classes at $\sqrt{s}$ =7TeV.

3 Thermodynamical quantities

The stress of the macroscopic clusters in SMP fluctuates around their mean value due to chromo-electric field fluctuations from the nature of the quantum vacuum in QCD. These fluctuations determine a Gaussian distribution in terms of the color reduction factor that is related to a thermal

distribution. The average temperature of the system is proportional to the average moment of the produced particles, in this way a local temperature is defined as:

$$T(\xi) = \sqrt{\langle p_T^2 \rangle_0 / 2F(\xi)}, \tag{3.1}$$

where $\sqrt{\langle p_T^2 \rangle_0}$ =190.25MeV obtained at $T(\xi_c) = T_c = 154$MeV[18].

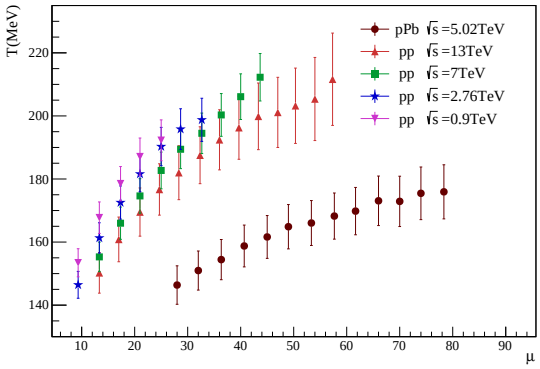

Figure 4: The figure shows the fit to the min bias data[8] and the prediction of the Λ_c/D^0 production for different multiplicity classes at $\sqrt{s}$ =7TeV.

The local order parameter of QCD phase transition is the energy density ε, which has a critical value ε_0, the relation of ε and ξ is directly proportional, where $\varepsilon_c/\xi_c \approx 0.56$ GeV/fm^3, obtained in [2].

The indirect measurement of the Shear Viscosity over entropy density η_s/s was proposed as a measure of the fluidity of the medium; the relativistic kinetic theory for the viscosity establishes the relation $\eta_s/s = T\lambda_{\text{mfp}}/5$, where the mean free path is $\lambda_{\text{mfp}} = 1/(\sigma_{tr} n) = L/(1 - e^{-\xi})$, so

$$\frac{\eta_s}{s} = \frac{TL}{5(1 - e^{-\xi})}. \tag{3.2}$$

4 Bulk properties

Using thermodynamic identities we can write the adiabatic speed of sound as $c_s^2 = s\left(\frac{\partial T}{\partial \varepsilon}\right)_V$. With the fundamental relation $Ts = \varepsilon + P$, we obtain c_s^2 in terms of the model parameters:

$$c_s^2 = \frac{sT}{4\varepsilon}\left(1 - \frac{e^{-\xi}}{F(\xi)^2}\right), \tag{4.1}$$

this quantity behaves quite similar to the Lattice QCD results[19]. As a first approximation of the hydrodynamical expansion the increasing entropy is considered with a cylindrical expansion with one of the longitudinal dimensions, L, fixed. In this way, the dissipative speed of sound is defined as:

$$c_{sL}^2 = \left(\frac{\partial P}{\partial \varepsilon}\right)_L = \frac{P}{\varepsilon} + \frac{T^3 \Delta}{3s} c_s^2, \tag{4.2}$$

where Δ is the expected value of the trace of the energy-moment tensor in QCD, $\langle T_\mu^\mu \rangle = \varepsilon - 3P$ weighted by T^4, that measures the deviation with respect to the conformal behavior and identifies the residual interactions in the medium. Qualitatively it has been verified that the behavior of this observable is inversely proportional to the η_s/s ratio. For the QGP system, we can consider

soft equations of state and Gaussian-like initial profiles of the energy density given by the Bag Model[20], starting from the equation

$$P = c_s^2 \varepsilon - \left(1 + c_s^2\right) B_Q, \tag{4.3}$$

where B_Q is the Bag constant[20], we calculate the liquid-like correction to the energy density:

$$\varepsilon = \frac{1}{3} \frac{T^4 \Delta + \left(1 + c_s^2\right) B_Q}{\frac{1}{3} + c_S^2}. \tag{4.4}$$

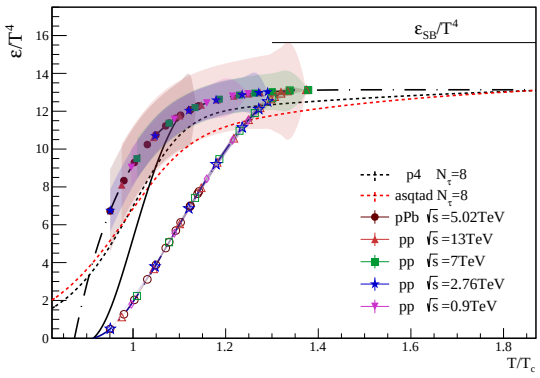

Figure 5: Behavior of ε/T^4 with T/T_c compared to Lattice QCD predictions for 2 + 1 flavors (two light and one heavy) using 8 lattices with p4 action in blue and asqtad action in red [19], the theoretical curve of the model is represented by the dashed black line, the liquid-like corrections from the Bag Model are represented by the non filled marks, and the continuos curve is the Bag Model correction with the dissipative speed of sound.

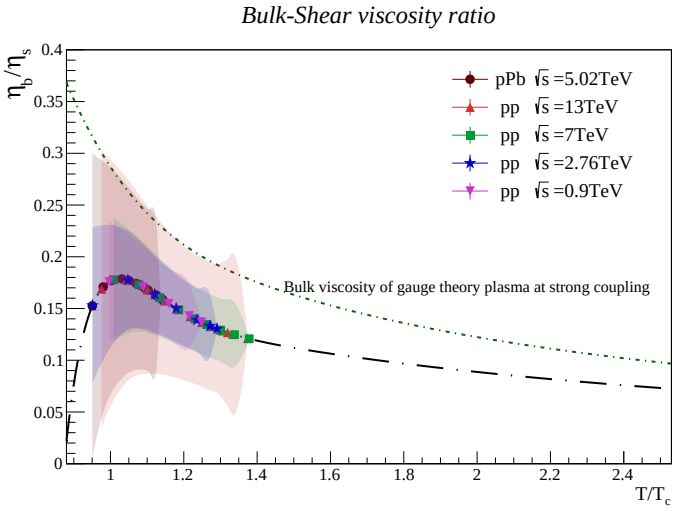

Figure 6: Figure shows the behavior of the shear viscosity over the bulk viscosity, which is well carried out causally using the modification for the speed of sound, the quotient between the two viscosities shows a change in the steep slope that suggests a second-order phase transition for these systems, the quotient is below of the dotted green line, that represents the result based on dual holography, where it is speculated that $\eta_b/\eta_s \geq 2(1/3 - c_2^s)$[22].

For the calculation of bulk viscosity, the projection operator's approach was considered to derive the microscopic formulas for the transport coefficients in Causal Dissipative Relativistic Fluid-dynamics that can be seen as a generalization of the Navier-Stokes equation[21]:

$$\frac{\eta_b}{s} = \left(\frac{1}{3} - c_{sL}^2\right)\tau_\Pi T - \frac{2T^4\tau_\Pi\Delta}{9s}. \tag{4.5}$$

5 Event by event $\langle p_T \rangle$ fluctuations

The event by event (EbE) fluctuations were proposed as a probe of the properties of the hot and dense matter generated in high-energy heavy-ion collisions. QGP phase transition goes along with the appearance of fluctuations of thermodynamic quantities that can be related to the EbE $\langle p_T \rangle$ fluctuations of final-state charged particles.

In the SPM we can understand EbE fluctuations as a superposition of partially independent particle-emitting sources [23]

- At low ξ: we have very little fluctuations
- Over critical ξ: we have no fluctuations
- Below critical ξ: fluctuations are maximal

$$F_{p_T} = \frac{1}{\sqrt{\langle z^2\rangle}}\sqrt{\frac{\langle Z^2\rangle}{\langle\mu\rangle}} - 1 \tag{5.1}$$

Experimentally, fluctuations of the $\langle p_T \rangle$ are measured though correlations between two particles rather than the variance of the $\langle p_T \rangle$ as in F_{p_T}, but the correlator is proportional to F_{p_T} [24]

$$C_m \simeq 2F_{p_T}\frac{var(p_T)}{\langle N\rangle} \tag{5.2}$$

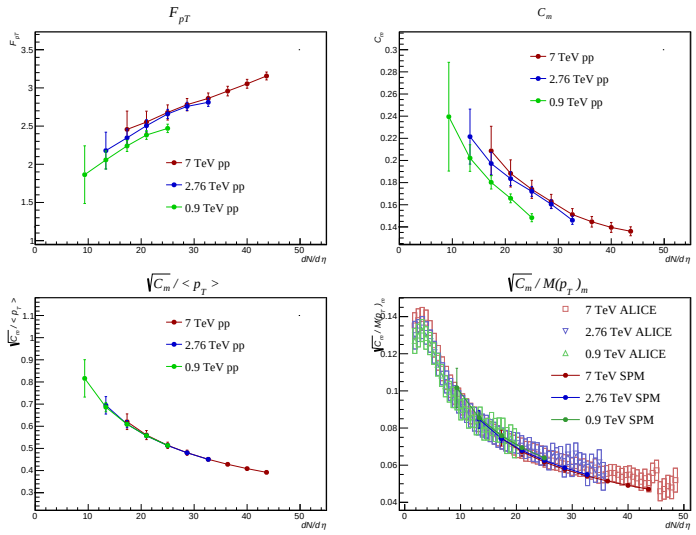

Figure 7: Fluctuation observable F_{p_T}, C_m and $\sqrt{C_m}/\langle p_T \rangle$ and comparing with experimental data from [24].

6 Temperature fluctuations

width, remove 'span=2' fluctuations of any observable of a system have two distinct origins, one quantum that has initial state fluctuations and classical thermodynamical fluctuations which occur after elapse of sufficient time after a collision. initial state fluctuations arise because of internal structures of the colliding nuclei and these appearas EbE fluctuations of energy density or Temperature [23].
Temperature fluctuations may also arise as fluctuations of p_T or it's correlations and are given by:

$$\frac{\Delta T}{\langle T_{eff}\rangle_{overall}} = \frac{\sum_i \langle T_{eff}\rangle - T_i}{\langle T_{eff}\rangle_{overall}} \tag{6.1}$$

If the initial state correlations can survive after the thermalization, teperature fluctuations are a good tool to see them and collect information about the initial state.

6.1 Tsallis model

The Tsallis model takes a more statistical approach, given that, we first define the p_T spectra as the standard distribution taken form the integration in the phase space [25].

$$\frac{1}{N}\frac{d^3N}{dp^3} = \frac{gV}{(2\pi)^3}E\left[\left(1 \pm \frac{q-1}{T}(E-\mu)\right)^{\pm 1/(q-1)} + S\right]^{-1} \tag{6.2}$$

the terms $E = \sqrt{p_T^2 + m_0^2}\cosh(\eta)$ and S indicates us of the statistic which will be taken, so for practical reasons we will take $S = 0$ which corresponds to the Maxwell statistics, in the sense that we want the particles to be distinguishable for this to correspond with the SPM. So we will have [26]:

$$\frac{1}{N}\frac{d^2N}{d\eta dp_T} = \frac{C_T p_T \sqrt{p_T^2 + m_0^2}\cosh(\eta)}{\left[\left(1 \pm \frac{q-1}{T}(\sqrt{p_T^2 + m_0^2}\cosh(\eta) - \mu)\right)^{\pm 1/(q-1)}\right]} \tag{6.3}$$

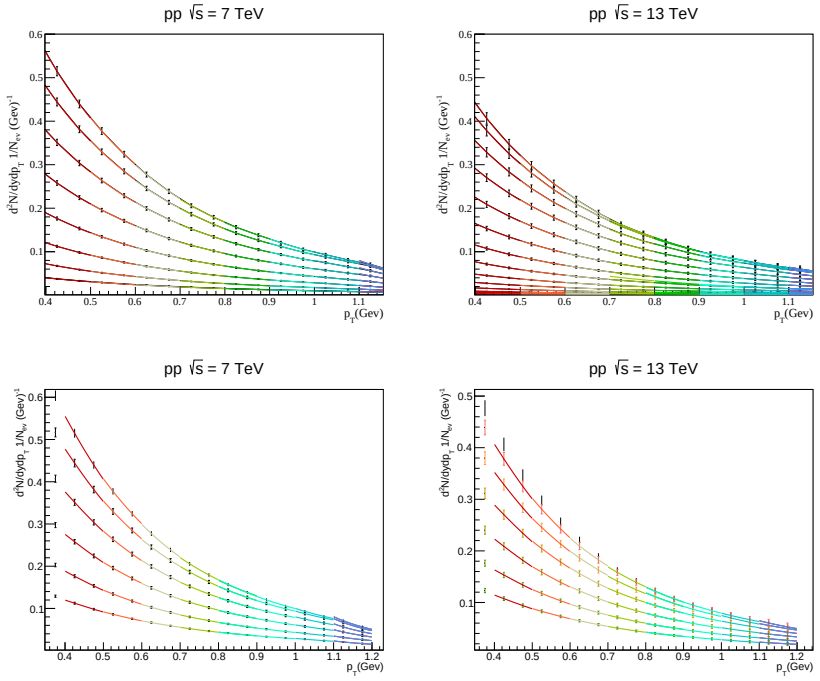

Figure 8: Fits to the p_T spectra [12] using the SPM (up) andT salis model (bottom) at 7 and 13 TeV.

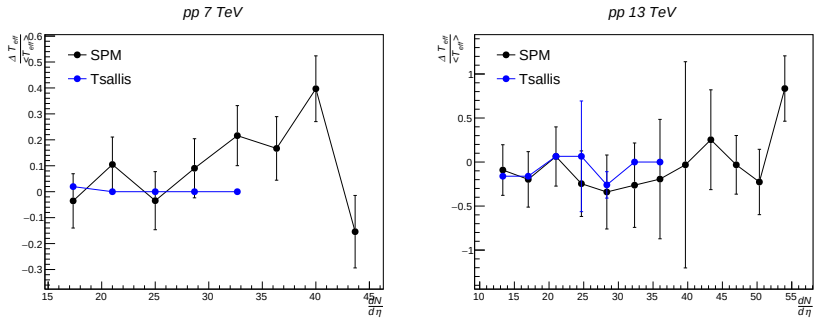

Figure 9: Temperature fluctuations on the SPM and Tsallis model from the fit on data from [12]. Where SPM shows higher fluctuations due to the picture of the internal structure of partons.

7 Conclusions

1. The model allows us to make good descriptions of the phenomena present in small collisions systems.

2. The signals observed show that perhaps these systems probably do not reach thermalization, which implies the bulk properties for these systems.

3. The fact of considering soft equations and dissipative properties allows us to obtain new physics results that are relevant.

8 Acknowledgments

We would thank the organizers for the opportunity to present our work and invite me on this talk, specially to Dr. Martin Hentschinsky.

References

[1] I. Bautista, J. G. Milhano, C. Pajares and J. Dias de Deus, Phys. Lett. B 715 (2012) 230
[2] M. A. Braun, J. Dias de Deus, C. Pajares, B. K. Srivastava et al. Phys. Rept. 599 (2015) 1
[3] C. Albajar et al. [UA1 Collaboration], Nucl. Phys. B 335 (1990) 261
[4] G. J. Alner et al. [UA5 Collaboration], Phys. Rept. 154 (1987) 247
[5] B. I. Abelev et al. [STAR Collaboration], Phys. Rev. C 79 (2009) 034909
[6] F. Abe et al. [CDF Collaboration], Phys. Rev. D 41 (1990) 2330
[7] K. Aamodt et al. [ALICE Collaboration], Eur. Phys. J. C 68 (2010) 89
[8] V. Khachatryan et al. [CMS Collaboration], JHEP 1002 (2010) 041
[9] V. Khachatryan et al. [CMS Collaboration], Phys. Rev. Lett. 105 (2010) 022002
[10] J. Adam et al. [ALICE Collaboration], Phys. Lett. B 753 (2016) 319
[11] V. Khachatryan et al. [CMS Collaboration], Phys. Lett. B 751 (2015) 143
[12] S. Chatrchyan et al. [CMS Collaboration], Eur. Phys. J. C 72 (2012) 2164
[13] A. M. Sirunyan et al. [CMS Collaboration], Phys. Rev. D 96 (2017) no.11, 112003
[14] S. Chatrchyan et al. [CMS Collaboration], Eur. Phys. J. C 74 (2014) no.6, 2847
[15] I. Bautista, L. Cunqueiro, J. D. de Deus and C. Pajares, J. Phys. G 37 (2010) 015103

[16] I. Bautista and C. Pajares, Phys. Rev. C 82 (2010) 034912
[17] Acharya, Shreyasi et al. [ALICE Collaboration], JHEP 1804 (2018) 108
[18] A. Bazavov et al., Phys. Rev. D 85 (2012) 054503
[19] A. Bazavov et al., Phys. Rev. D 80 (2009) 014504
[20] L. M. Satarov, I. N. Mishustin, A. V. Merdeev, H. S. Phys. Rev. C 75 (2007) 024903
[21] X. G. Huang and T. Koide, Nucl. Phys. A 889 (2012) 73
[22] A. Buchel, Phys. Lett. B 663 (2008) 286 [23] E. G. Ferreiro, F. del Moral and C. Pajares,Phys. Rev. C **69** (2004) 034901
[24] S. T. Heckel [ALICE Collaboration],Phys. Rept. **599** (2015) 1.
[25] S. Basu, R. Chatterjee, B. K. Nandi and T. K. Nayak, arXiv:1504.04502 [nucl-ex].
[26] R. F. Si, H. L. Li and F. H. Liu, Adv. High Energy Phys. **2018** (2018) 7895967, doi:10.1155/2018/7895967, [arXiv:1710.09645 [nucl-th]]


Callejón
Cinco Señores
SALMIANA
AGAVE BAR
METATE
GALERIA

A Forward Multiparticle Spectrometer for the LHC: Hadron spectra and Long-lived particle search

Michael G. Albrow

E-Mail: albrow@fnal.gov

Fermi National Accelerator Laboratory, Batavia, IL 60510, USA

Presented at the Workshop of QCD and Forward Physics at the EIC, the LHC, and Cosmic Ray Physics in Guanajuato, Mexico, November 18-21 2019

Abstract

I describe a possible Forward Multiparticle Spectrometer (FMS) that could be installed downstream of the superconducting recombination dipole D1 in Run 4, between z = 96 m - 126 m to measure multi-TeV hadron spectra in low luminosity pp collisions at $\sqrt{s}$ = 14 TeV, as well as p+O and O+O collisions as relevant for cosmic ray showers. Light antinuclei and charmed hadrons at high Feynman x_F can be measured, both of importance for astrophysics. At the full high luminosity HL-LHC a search for new long-lived neutral particles (LLPs) decaying in a 20 m long, 70 cm diameter vacuum pipe to visible decay modes (including $\gamma\gamma, e^+e^-, \mu^+\mu^-, \tau^+\tau^-, c\bar{c}$ and jets) can be made. The FMS is especially well suited for LLPs with 1 GeV $< M(X) <$ 10 GeV and lifetimes $c\tau$ from about 10 m to several km.

I discuss this as a possible addition to CMS but it has no formal approval yet, therefore the talk is not given "on behalf of CMS".

1 Introduction

The sparcity of accelerator data on particle production in the forward direction above $\sqrt{s}$ = 63 GeV at the CERN Intersecting Storage Rings (ISR), its importance for understanding cosmic ray showers, and the possibility of measurements at the LHC was addressed in Ref. [1].

We have been developing a forward multiparticle spectrometer, FMS, that could be added as a new subsystem to CMS for Run 4 (2027+). A schematic overview of the spectrometer is shown in Figure 1. The main detectors are situated at z = 116 m - 126 m and surround the beam pipe between radii R_{in} = 12 cm and R_{out} = 35 cm[1]. The LEFT+RIGHT and UP+DOWN azimuthal regions have distinct physics motivations and operational modes; hadron spectroscopy and a new long-lived particle (LLP) search respectively. The detectors can use the same techniques as the CMS Endcap upgrade planned for Run 4, with silicon tracking and calorimetry with precision timing, followed by a magnetised toroid with GEM layers for muon measurement. Transition radiation

[1] All dimensions are provisional and subject to optimisation.

detectors (TRD) for TeV hadron identification are being developed [2]; these are the only detectors not included in the CMS upgrade plans. They are essential for the hadron mode, but optional for the LLP mode. The area is only about 0.3 m^2, which is less that 1% of the future Endcap.

An earlier talk on the hadron mode is given in Ref.[3]. Forward spectra of $\pi^{\pm}, K^{\pm}, p$ and $\bar{p}$ have not been measured above $\sqrt{s}$ = 63 GeV at the ISR [4, 5] but are important to understand cosmic ray showers. At the LHC with $\sqrt{s}$ = 14 TeV we will be 220 times higher in $\sqrt{s}$. In fixed target terms, as appropriate for cosmic ray showers, E_{BEAM} is about 50,000 times higher. The ISR energy is well below the famous knee in the cosmic ray spectrum; the LHC energy is well above. An excess of muons is observed in very high energy showers compared with expectations; forward spectra at the LHC may shed light on this, as well as being relevant for atmospheric neutrinos, which are a background to cosmic neutrinos as seen in ICECUBE.

Event generators such as PYTHIA have not been tuned for this region since there is little data. Low p_T physics being non-perturbative QCD is theoretically more challenging than high p_T and is worthy of more attention; this is the "low-Q^2 frontier" of QCD. At the LHC only leading protons with Feynman-$x_F \gtrsim 0.9$ and neutral particles (mainly π^0 and neutrons) at $\theta = 0^{\circ}$ have been measured [6], demonstrating the very large spread in cosmic ray shower Monte Carlos.

When planning future high energy hadron colliders, such as the $\sqrt{s}$ = 100 TeV FCC (p+p mode, as well as with ions) predictions for radiation levels in the forward direction should benefit from improved knowledge of these cross sections.

2 Description of D1 (81m) to TAXN (127m) region

The straight section downstream of IR1 (ATLAS) and IR5 (CMS) between the end of the new superconducting D1 dipole at z = 81 m and the entrance to the TAXN absorber at 126.5 m is mostly free of equipment, with a new straight beam pipe presently planned to have R = 7.5 cm at the front increasing to 12.5 cm at the back. (The regions downstream of LHCb and ALICE are where the proton beams are injected and are more complicated.) We propose to change the design of this pipe to have an enlarged radius, nominally R = 40 cm over at least 20 m, from z = 96 m to 116 m. Immediately downstream of D1 there is to be a cold diode structure (in DFBX) parallel to the beam pipe which, if it cannot be repositioned, limits the beginning of the proposed detector system, shown schematically in Fig. 1.

The first new element is an iron (ASII 1010 low-carbon steel) toroid (I thank V. Khashikhin, Fermilab, for the study), a cylinder of length 3 m, R_{in} = 8 cm and R_{out} = 40 cm. It is constructed in two halves for easy assembly/disassembly and allowing separation of top and bottom halves for bakeout of the beam pipe. Two water-cooled copper coils, both in the bottom half, with currents of 5 kA each, give a circular field in the iron varying from 1.9 T at the inner radius to 1.5 T at the outer. All charged particles (mostly muons) exiting the toroid steel are measured in a counter hodoscope mounted on the back of the steel, followed by track chambers, e.g. a pair of GEMs or silicon strip layers, separated by 1 m. The field deflects charged particles emerging from the back of D1 inwards or outwards, reducing the flux of muons at the detectors downstream. This is predicted by FLUKA to be 0.9 (0.65) per bunch crossing even with 140 interactions (HL) without (with) the toroid powered.

The field at the center of the beam pipe is less than 3 Gauss; both incoming and outgoing beams are inside the pipe but not centered. If necessary, the field inside the pipe could be reduced by a thin iron shield around it. In the charged hadron spectroscopy mode, the main role of this toroid is additional background reduction; the particles to be measured pass through the central hole.

Immediately after the toroid+tracker the pipe transitions to a wide pipe, similar to the 25.7 m long pipe at ALICE in LSS2. NEG-coated liners inside an 80 cm pipe leave a clear aperture of diam-

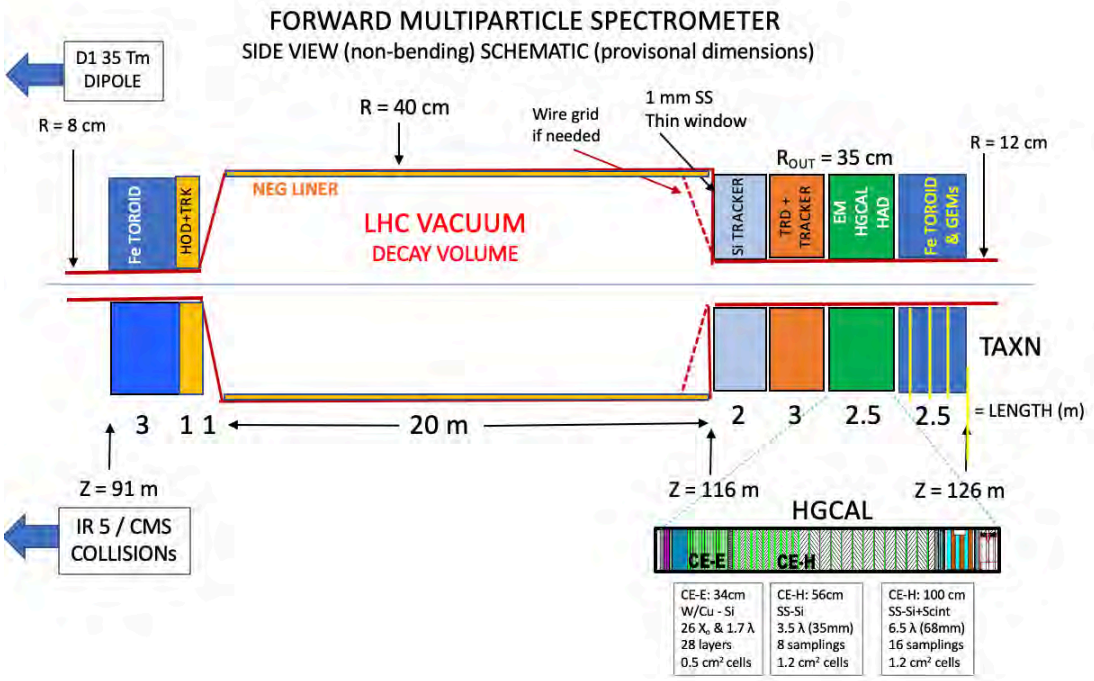

Figure 1: Schematic layout of proposed FMS spectrometer (side view). Dimensions are subject to optimization, in particular the length budget. The start in z could be earlier if the LHC cold diode can be displaced, and the space allocation for the main detectors can be increased at the expense of vacuum volume.

eter 70 cm. (I thank V. Baglin, CERN, for discussions on the beam pipe.) The main difference from the ALICE pipe is that the transition at z = 116 m to the small pipe should be such as to minimize interactions and especially multiple scattering. A 1 mm thick steel window perpendicular to the pipe axis gives a multiple scattering angle $\theta_\circ = 3 \times 10^{-5}$ for 100 GeV/c particles, decreasing like $1/p$. An option is to have a thinner window with strengthening ribs. To avoid the beam "seeing" a sharp change in pipe diameter an internal inclined wire grid or similar can be employed[2].

After exiting the steel window the main elements of the spectrometer could use identical technology to the CMS Endcap upgrade, namely silicon pixel tracking, followed by electromagnetic and hadron calorimetry based on silicon pads with tungsten/copper and steel plates. Precision timing $\sim$ 25 ps is planned, and is important.

The need for precise tracking is very different for the hadron mode and the LLP mode. In the former case (L and R quadrants, hadrons of 1 - 3 TeV) we need to measure the momenta of particles coming directly from the collision region (or from charm decays) using the transport matrix through the magnet lattice, and also to reject beam halo and tracks coming from interactions in the upstream pipe and other material. In the LLP mode the detected particles, from a decay in the vacuum, have not traversed any magnetic field; the essential need is to project the tracks back to a vertex and ensure it is inside the vacuum. Also we need to ensure that the neutral parent points

[2]A detailed design will require an Engineering Change Request from CMS, which has not yet formally considered this project.

back to the collision region through the steel (making allowance for missing neutrinos in any $\tau^+\tau^-$ events!). Particles with momenta as low (*sic*) as 50 GeV/c may be of interest. One may dedicate about 3 m of space for tracking, with $\sigma \sim 20$ μm resolution giving angular resolution $< 10^{-5}$. Transition radiation detectors (needed especially for hadron spectroscopy, but less essential for the LLP search) can incorporate tracking, so one may consider combining them and dedicating up to perhaps 5 m for both silicon strips or pixels and the TRD.

Transition radiation detectors, sensitive to $\gamma = E/m$, have usually been used to help distiguish electrons from pions at low energies. Anatoli Romaniouk and the ATLAS TRD Group have been developing detectors that could distinguish $\pi, K,$ and p in the TeV region [2]. Cherenkov counters are ineffective as β is too close to 1.0. X-rays are emitted from transitions between media of different dielectric constants, or plasma frequencies, with a small probability which rises with γ and then saturates. One can select radiator materials and thicknesses and gap widths to optimise for a selected range. Tests have been done at the SPS using layers of xenon-filled straw tubes between different foils with electrons, muons and pions. The yields, X-ray energy spectra and angular distributions are very well predicted by detailed simulations. Interestingly the typical emission angle decreases like $1/\gamma$, and high granularity silicon or GaAs pixel detectors measuring the emission angles of even a few X-ray photons may improve the separation power.

The imaging calorimeter (HGCAL) layers will be sensitive to muon tracks, and fast timing will be incorporated (perhaps with LGADs) to help with background reduction. The EM part of the calorimeter has very good measurement of high energy shower directions, addressing the challenge of locating the decay point of an $X \to \gamma\gamma$ decay within the vacuum pipe. This has no physics background; probably the main backgrounds are photons from material before the decay region with a mis-measured vertex, or from two unrelated photons that appear to come from a vertex. The tracker + imaging calorimeter combination identifies γ, e, μ and hadrons, and the TRD can provide some distinction between $\pi^+\pi^-$ and K^+K^-. This capability would be especially powerful in searching for $X \to c\bar{c}$ and $X \to \tau^+\tau^-$, even $X \to$ jet + jet. The FMS is particularly well suited to LLPs in the M(X) = 1 GeV to 10 GeV range (fixed target experiments have higher luminosity and are more sensitive to lighter particles, e.g. dark photons with M(A') < 500 MeV).

Behind the calorimeter we propose another iron toroid, identical to the plug at the front end except that it is subdivided longitudinally with a few gaps allowing insertion of muon tracking layers (e.g. GEMs). With 1.5 T the bending angle for a 100 GeV/c muon is 13.5 mrad, compared with the multiple scattering θ_{rms} = 2 mrad. The sensitivity to $X \to \mu^+\mu^-$ needs a full simulation, but the mass resolution is probably a minor issue, since there is no physics background from K^0 decays (B.R < 10^{-8}) or any other SM particles. The back of this toroid is shielded from background coming from behind by the TAXN absorber.

Like the front toroid, the back detectors cover full azimuth but can be separated into top and bottom halves, or quadrants.

Installation of an FMS in both outgoing beams is technically possible and would give twice the data and LLP sensitivity for less than twice the cost.

3 Hadron spectroscopy

When the ISR came into operation in 1971 Feynman proposed that forward hadron spectra should scale with energy $\sqrt{s}$ when plotted as a Lorentz-invariant cross section at fixed p_T vs. $x_F = p_z/p_{beam}$; this is Feynman scaling. It was based on the parton model, pre-QCD, and while it is a good approximation in the ISR energy range for light particles at low-p_T [4, 5], QCD has scaling violations, heavy flavors have thresholds, etc. Feynman scaling should not hold over the large energy range from $\sqrt{s}$ = 63 GeV to 14,000 GeV!

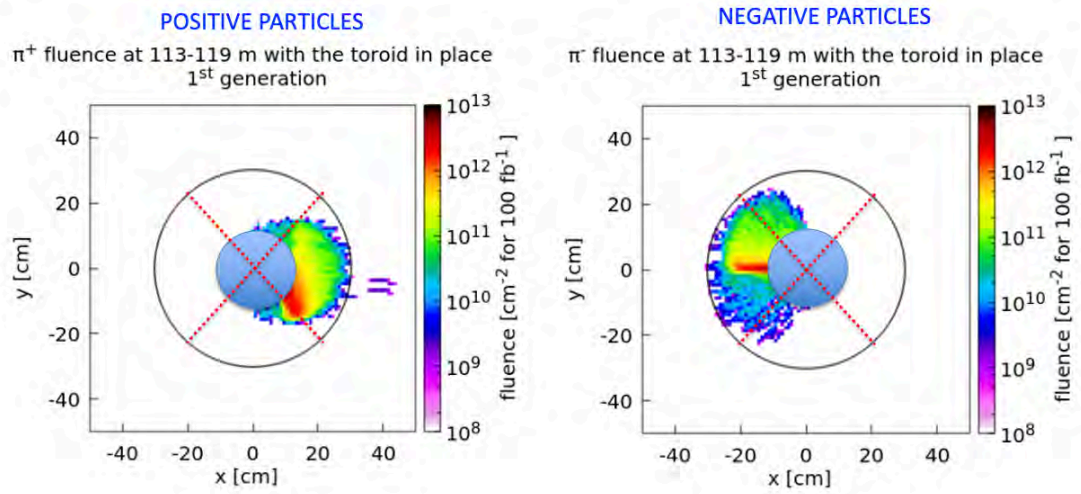

Figure 2: Fluxes of primary charged pions at z = 116 m per 100 fb^{-1} (M. Sabate-Gilarte). The central grey disk is the outgoing beam pipe. To convert to numbers per collision divide by 8×10^{15}. The regions above and below the pipe are clear of primary particles. The outer radius is now planned to be larger than shown, namely 35 cm or 40 cm.

The new 35 Tm beam recombination dipole D1, ending at z = 81 m, is here used as a spectrometer magnet, deflecting charged particles into right (R) and left (L) quadrants. The beam crossing angle (planned to be vertical for CMS, 250 μrad half-crossing angle) and the quadrupoles affect the distributions, as shown in Fig. 2. A large beam pipe, R = 40 cm, from z = 96 m to 116 m at the end of which is a steel vacuum window about 1 mm thick, allows charged particles to enter the spectrometer, where they can be measured in short low luminosity p+p, p+O, and O+O runs. The acceptance for primary charged particles is approximately p_z = 1 - 3 TeV/c. Higher p_z particles remain within the pipe. Fig. 2 shows the spatial distribution of primary charged particles at z = 116 m (M. Sabate-Gilarte and F. Cerutti).

Hadrons from fragmentation of diffractively excited protons, $p \to p^*$ populate this region, and in low pileup data it would be interesting to study in combination with a leading proton in the opposite direction if there are suitable Roman pots.

The FMS can also measure light nuclei and antinuclei ($\bar{d}, \bar{t}, ^3\bar{H}e$) which are relevant for understanding γ-rays from the galactic center and a possible dark matter annihilation signal. It will have acceptance for $J/\psi \to \mu^+\mu^-$ and charmed hadrons, specifically $D^0 \to K^-\pi^+$, $\bar{D^0} \to K^+\pi^-$ and $\Lambda_c^+ \to pK^-\pi^+$ at $x_F >\sim 0.8$; the decay products have low enough momenta to be accepted, shown in Figure 3. Charm production is important for understanding ultra-high energy neutrinos and cosmic rays as well as QCD; intrinsic charm, namely $c\bar{c}$ in the proton wavefunction, can give a large cross section [7]. The challenge of seeing these narrow charm signals on a large combinatorial background drives the need for excellent tracking (traversing only vacuum from the collision point to the window at 116 m) and good $\pi/K/p$ separation. Prompt muons can also be measured, subtracting the spectra from $\pi^\pm$ and $K^\pm$ decays (which will be known) as another measure of c- and b-production. Note that the mean decay length for a 2.5 TeV charged pion(kaon) is 139(18.5) km, and for a 5 TeV D^0 it is 33 cm!

The expected fluxes of charged particles as well as charmed hadrons have been calculated using different cosmic ray Monte Carlos by H. Menjo (priv. comm.) and by M. Sabate-Gilarte (priv. comm. and [8]) using FLUKA with DPMJET including upstream interactions. There is no

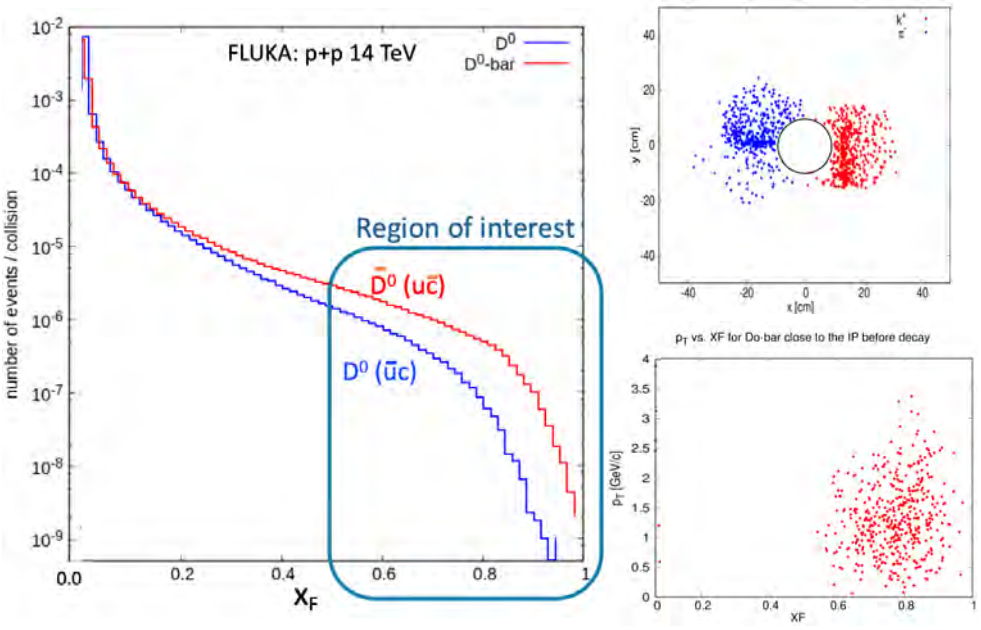

Figure 3: Left: Spectra in x_F of D^0 and $\bar{D^0}$ from FLUKA, p + p at $\sqrt{s} = 14$ TeV. Top right: Spatial distribution of K^+ and π^- from $\bar{D^0}$ decays at z = 116 m. Bottom right: Distribution in the $p_T : x_F$ plane of $\bar{D^0}$ with both K and π in FMS acceptance. (M. Sabate-Gilarte)

space here for details but e.g. the expected flux of $\mu^{\pm}$ within R = 30 cm at z = 116 m is only 0.9 per bunch crossing with 140 interactions, reducing to 0.65 with the front toroid powered, and nearly all of these have p_μ < 50 GeV/c. Most pp collisions produce no direct hadrons in the FMS acceptance (the average is about 0.2) and measurements of the inclusive charged hadron spectra could be made with some pileup, but for multiparticle states like D^0 decays the signal:background may be unacceptable unless there is not much pileup.

If there is a zero-degree calorimeter (ZDC/LHCf) between the beam pipes downstream of the FMS to detect neutrons and π^0, we will be able to study coincident events, e.g. $p \rightarrow n\pi^+\pi^0$ by diffraction dissociation.

4 Long-lived particle (LLP) search

In the absence of a discovery of high mass dark matter particles, searches are turning to the possibility that they are light (e.g. M(X) $<$ 10 GeV) but weakly interacting. There may be "portals" that couple SM particles to dark matter particles, that are weak enough to penetrate a lot of matter but then decay to known Standard Model particles such as $\gamma\gamma, e^+e^-, \mu^+\mu^-, \tau^+\tau^-, c\bar{c}$ and $b\bar{b}$. The FMS can search at full luminosity for penetrating neutrals with all of these decays occurring inside the vacuum pipe. A FLUKA calculation by M. Sabate-Gilarte predicts, exiting the front toroid steel, per bunch crossing with 150 inelastic interactions, 0.6 photons, 0.45 neutrons, 0.15 antineutrons, and 0.12 K^0 above 50 GeV/c. Above 200 GeV/c the fluxes are much less, see Figure 4. The upper (U) and lower (D) quadrants are devoid of primary charged particles since D1 acts as a sweeping magnet, and the detector area is out of the angular range for direct neutral particles. The low occupancy in these quadrants provides an excellent opportunity to search for BSM long-lived neutral particles (LLPs) from the primary collisions that penetrate 35 - 50m of steel (> 190 λ_{int}) [3] in the Q1-Q3 magnets and D1, and decay in the vacuum of the large pipe. The decay products, be they photons, electrons, muons or charged hadrons, can be measured in FMS during high luminosity running. Excellent tracking to show that the vertex is inside the 20 m-long vacuum region, and not initiated by a charged particle (e.g. μ), should eliminate backgrounds; Standard Model LLPs

[3] I thank Francesco Cerutti for the following numbers of interaction lengths, for a straight track from the IP to the end of the D1 cold mass at 81 m: 320 λ_{int} at y = 15 cm, 220 λ_{int} at y = x = 15 cm due to yoke holes at 45°, 300 λ_{int} at y = 20 cm due to the smaller section of the multipole correctors, and 190 λ_{int} at y = 10 cm due to the part of the path in the vacuum.

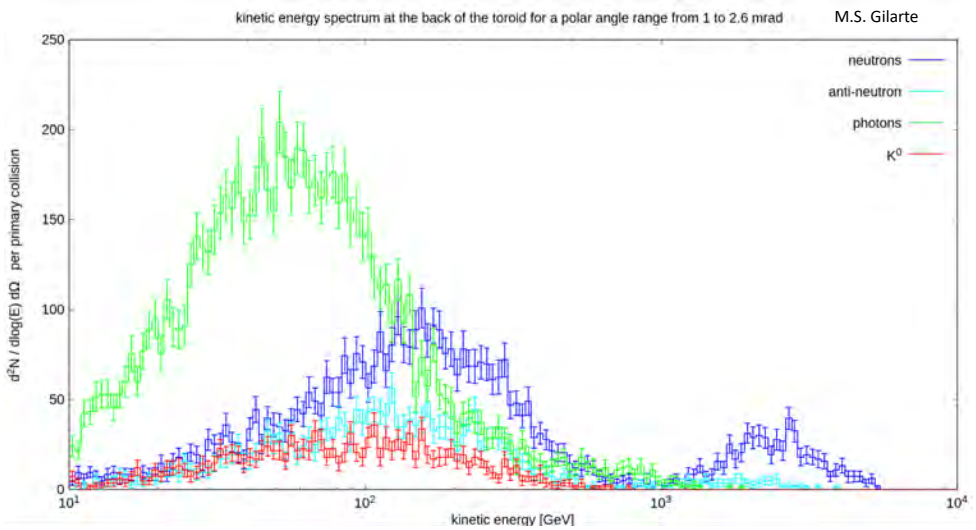

Figure 4: Fluxes of neutral particles emerging from the back of the front toroid (M. Sabate-Gilarte).

such as K^0 and Λ are recognized in the spectrometer which has tracking, calorimetry and muon chambers, and can be reduced using mass and lifetime information.

One may ask about of the sensitivity of the FMS to semi-weakly interacting LLPs that do *not* decay in the vacuum pipe or interact in the steel absorber but interact inside the calorimeter. At first sight it may seem that backgrounds are overwhelming, but the HGCAL will provide sensitivity to single charged particles, detailed shower starting point and directional information, precision timing and energy measurement. The muon chambers immediately behind the calorimeter have information about possible muon content in the shower. Combining time-of-flight and energy measurement gives M(X); look for a peak! For example, if M(X) = 2 GeV/c^2 and p = 50 GeV/c, the flight time to the calorimeter is 200 ps later than that of a neutron; for M(X) = 5(10) GeV/c^2 with p = 100 GeV/c it is more than 0.4(2.0) ns later. While the time resolution on a shower should be $\sim$ 20 ps, the time spread of the collisions themselves, projected in the forward direction, may be a limiting factor. Also for decaying LLPs the time-of-flight from collision to signals in the tracker and HGCAL can be useful information if $\gamma \lesssim 20$. Selecting showers from interacting neutral particles emerging from the back of the 20 λ_{int} absorbers, and (critically) pointing back to the collision region, one might reduce background from scattered high energy neutrons to an acceptable level. This unique capability of FMS merits a detailed study.

4.1 Comparison with FASER

There are several other experiments searching for penetrating then decaying long-lived particles. Here I only compare with that most similar to FMS, FASER, which is approved for a first run in Run 3 with a decay volume length only 1.5 m and radius 10 cm, but is planned to be upgraded to 5 m and 1 m radius for Run 4. It is much further downstream (of IR 1) at z = 480 m - 485 m, after about 100 m of rock absorber. It is centered on the collision axis, and with a radius R = 0.1(1.0) m has pseudorapidity η above 9.2(6.9) neglecting beam crossing angle effects.

The probability of a particle that enters a decay volume decaying in it is:

$$F = e^{-z_{in}/(\gamma c\tau)} - e^{-z_{out}/(\gamma c\tau)} \tag{4.1}$$

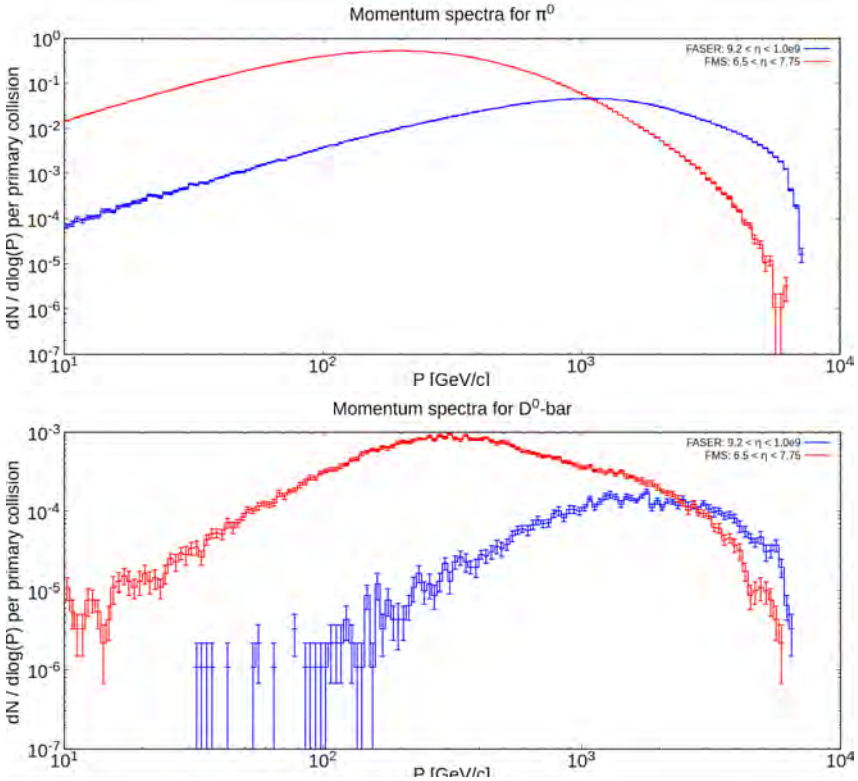

Figure 5: Spectra calculated using FLUKA for π^0 and D^0 for FMS ($6.65 < |\eta| < 7.7$)and FASER($\eta > 9.2$ (Run 3).

For FASER(5m) this exceeds 10^{-3} for $\gamma c\tau$ between 130 m and 20 km, and has a maximum when $\gamma c\tau$ = 480 m at which $F = 3.8 \times 10^{-3}$. The FMS is both closer to the IP and is much longer, and F exceeds 1% between $\gamma c\tau$ = 24 m and 1.85 km, with a maximum of 6.9% at $\gamma c\tau$ = 116 m.

Since FMS(LLP) with $6.65 < |\eta| < 7.7$ is at a larger polar angle than FASER, we should also compare the fluxes of particles as a function of momentum. These have been calculated by F. Cerutti and M. Sabate-Gilarte with FLUKA and two examples are shown in Figure 5. Without having predictions for the production of LLPs of various masses, we assume the spectrum of an A' light enough to come from π^0 decays to be similar to that of π^0 themselves, and that of an LLP with M(X) $\sim$ 2 GeV/c^2 to be similar to that of a D^0. So these are only indicative, but show that the FASER flux is higher for π^0 with momenta above about 1 TeV, but heavier particles have larger mean p_T and the charm flux is much higher in the FMS(LLP) angular region. For the FASER Run 4 proposal their charm flux will be higher, although this prediction has very large uncertainty since there is no data. However FMS in the hadron mode will measure very forward charm, largely resolving this issue.

Of course if an A' or similar BSM particle is discovered before Run 4, the FMS should be able to study it in a novel way.

The FASER-ν extension is to measure neutrino interactions in an emulsion stack at the same location. Since the spectra of charged pions, kaons and charmed hadrons at large x_F presently have an order of magnitude uncertainty, the neutrino cross sections cannot be measured without knowing those spectra. FMS (hadron mode) will measure these up to $x_F \sim 0.4$, thus providing a service to the LHC forward neutrino physics program, as well as to experiments studying cosmic neutrinos, such as ICECUBE.

5 Hadron interactions

In the hadron mode, behind the TRD there will be a flux of identified hadrons of known momenta between about 1 and 3 TeV/c. One could insert thin foil targets, e.g. of carbon and polyethylene (C_2H_4) with some pixel tracking a few meters behind for a special short run. By counting tracks from a vertex in the foil one could get a measure of σ_{inel} and the $N_{charged}$ distribution for the different beam particles (including light nuclei and antinuclei) on both protons and carbon. To make longitudinal space for this the calorimeter may need to be displaced.

6 Triggers and data collection

In the hadron spectroscopy mode the ideal running condition would be to have an average of about one inelastic collision per bunch crossing (μ = 1), with a level-one trigger based on one or more tracks or EM-calorimeter signals. The full CMS detector would be read out to study correlations, and the single-track rate would need pre-scaling. To maximize statistics for charm etc., $\geq$ 2-track triggers could include a fast processor selecting candidates. While the single-particle inclusive spectra could be measured at higher pileup, the charm signal:background would become worse; this needs a study.

In the LLP mode at high luminosity, when a candidate in FMS is accompanied by a large number of inelastic collisions, there does not appear to be any value in reading out the full central detector with an FMS trigger. The DAQ could then have an FMS-only data stream, with a trigger selecting events with charged particles, or an anomalous calorimeter signal, behind the big pipe, with no corresponding charged particle entering at the front.

7 Conclusions

A powerful multiparticle spectrometer could be installed in the 30 m straight section between the D1 dipole and the TAXN for physics in Run 4. In the L and R quadrants hadron spectra can be measured in a few days of low luminosity running. In the U and D quadrants a search can be made at full luminosity for new long-lived particles decaying in a large diameter 20 m-long vacuum pipe. The detectors system uses the techniques of the CMS Endcap upgrade (but with about 1% of the area) with novel transition radiation detectors. A longer write-up is in preparation; new participants are welcome!

8 Acknowledgements

I thank the organizers of the Workshop at Guanajuato inviting me and for allowing me to include in this write-up the LLP search mode, developed since that workshop. I am a CMS member, but this paper is not on behalf of CMS but *ad personam* since the project does not yet have any official standing in CMS. I hope that will change. I especially want to thank Hiroaki Menjo, Anatoli Romaniouk (TRD development), and CERN staff on LHC: Francesco Cerutti, Marta Sabate-Gilarte and Vincent Baglin for information and calculations showing the feasibility of the project.

References

[1] M.G. Albrow, *Accelerator Data for Cosmic Ray Physics*,Contribution to ISVHECR 2010, eprint: 1009.4178 [hep-ex].

[2] N. Belyaev *et al., Development of transition radiation detectors for hadron identification at the TeV energy scale*, J.Phys - Conf.Ser **1390** p.1 (2019).

[3] M.G. Albrow, *A very forward hadron spectrometer for the LHC and cosmic ray physics*, PoS EDSU2018 (2018) 048, eprint: 1811.02047 [physics.ins-det].

[4] M.G. Albrow *et al.* (CHLM Collaboration), *Negative particle production in the fragmentation region at the CERN ISR*, Nucl. Phys. **B56** (1973) 333 - 345.

[5] M.G. Albrow *et al.* (CHLM Collaboration), *Positive particle production in the fragmentation region at the CERN ISR*, Nucl. Phys. **B73** (1974) 40 - 56.

[6] E. Berti *et al.* (LHCf Collaboration), *The LHCf experiment: recent physics results*, PoS ICHEP2018 (2019) 207; CERN-EP-2018-239.

[7] S.J.Brodsky *et al.*, *A review of the intrinsic heavy quark content of the nucleon*, Adv. High Energy Phys. 2015 (2015) 231547; eprint: 1504.06287 [hepph].

[8] See talks at the Workshop on the FMS (April 2020): https://indico.cern.ch/event/868473/timetable/

[9] A. Ariga *et al.*, *FASER:ForwArd Search ExpeRiment at the LHC*, (Jan 11 2019) eprint: 1901.04468 [hep-ex].

Novel Radiation Detector Based on a Metal

Julian Felix

E-Mail: felix@fisica.ugto.mx

Laboratorio de Partículas Elementales, Departamento de Física, División de Ciencias e Ingenierías, CL. Universidad de Guanajuato, México

Presented at the Workshop of QCD and Forward Physics at the EIC, the LHC, and Cosmic Ray Physics in Guanajuato, Mexico, November 18-21 2019

Abstract

In spite of the advancements on radiation detectors, there are not, so far reported, radiation detectors based on solid metals. Here is the design, construction, characterization, and operation of a novel radiation detector, based on an Aluminum 7 cm $\times$ 7 cm $\times$ 0.20 cm plaque. When this detector is exposed to natural radiation, cosmic rays, in horizontal position, with an applied electric field between 0 Vdc/cm and $\mid \pm 4000 \mid$ Vdc/cm, there are no detected pulses (triggers); the pulses start to appear above $\mid \pm 4000 \mid$ Vdc/cm, and with $\mid \pm 40 \mid$ mV of oscilloscope trigger level. This radiation detector was tested extensively over many possibilities on the origin of these randomly produced pulses. All the collected information is consistent with that the pulses are produced by cosmic ray hits; therefore, this is a novel technique based on a metal, to detect ionizing radiation, in particular cosmic rays.

1 Introduction

There are many sort of published radiation detectors based on almost all kind of materials and their physical phase states [1–4]. However, in spite of these developments, there are not, so far, reported radiation detectors based on solid metals.

Here is a proposed, and demonstrated, one; this is, a novel radiation detector based on a machined Aluminum 7 cm x 7 cm x 0.2 cm plaque, with the appropriate basic electronics, in prototype stage. See Figure 1.

2 Design and Construction

It has two 8 cm long, 0.6 cm wide, 10 mil thickness, glued Copper tape collectors at the opposite big surfaces. This first layer is electrically insulated with black electric tape, 10 mil (2.54×10^{-2} cm) thickness, 3M scotchrap; the minimum electronic circuit to read out electrical signals is connected to collectors -to one collector a capacitor, C1, in series with an electric resistance, R1, and then to ground, and to the second collector another electric resistance, R2, and ground; the values are

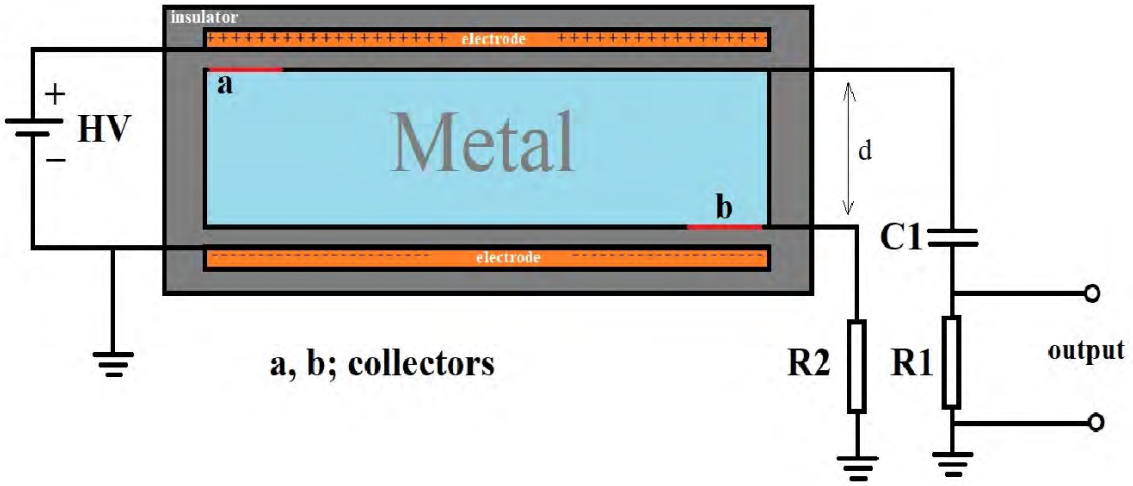

Figure 1: Layout of the radiation detector based on an Aluminum 7 cm $\times$ 7 cm $\times$ 0.2 cm plaque; this is an electron gas radiation detector. Not to scale. For illustration only.

appropriate to match detector and instruments impedances together-; the detector signal is read out at R1 using a Tektronix TDS 3034B four channel color digital phosphor oscilloscope e* Scope, 300 MHz (2.5 GS/s) DPO, or another technically similar oscilloscope. A couple of 7 cm $\times$ 7 cm, 10 mil thickness, Copper sheet electrodes is attached to the 7 cm $\times$ 7 cm parallel surfaces of the electrically isolated metallic plaque; there is where a 0 Vdc | ± 3000 | Vdc, high voltage, is applied using a very stable dc power supply (Fermilab power supply Model 1570 1-3012V, 40 mA, high voltage calibrated DC power source; power designs Inc. Westbury, NY, Palo Alto California). The whole device, in prototype stage, is electrically insolated, compacted, mounted, and operated horizontally on a solderless breadboard. Figure 2.

3 Operation and Characterization

This not so simple, or obvious, device functions as a radiation detector in general, and as a cosmic ray detector in particular. Many tests were performed to study its operation and the way it detects radiation. High Voltage (HV) from 0 Vdc to | ± 1600 | Vdc was applied incrementing its values in steps of | ± 100 | Vdc.

When the applied high voltages were below | ± 800 | Vdc no signals (triggers) appeared at all, with the | ± 40 | mV of trigger level in the oscilloscope, and monitoring for more than one hour; for voltages little higher than | ± 800 | Vdc, some occasional signals (triggers) appeared: With negative values for negative high voltages, and with positive values for positive high voltages. The signals are randomly produced in both amplitude and occurrence, with almost the same decaying and rising time. At these voltages, distinctive signal amplitudes are about | ± 100 | mV, with 10 mVpp of electronic noise, and | ± 40 | mV of oscilloscope trigger. At higher voltages the signal amplitudes are bigger, see Figure 3. The forms of these triggers are perfectly distinguishable from the electrical outlet noise.

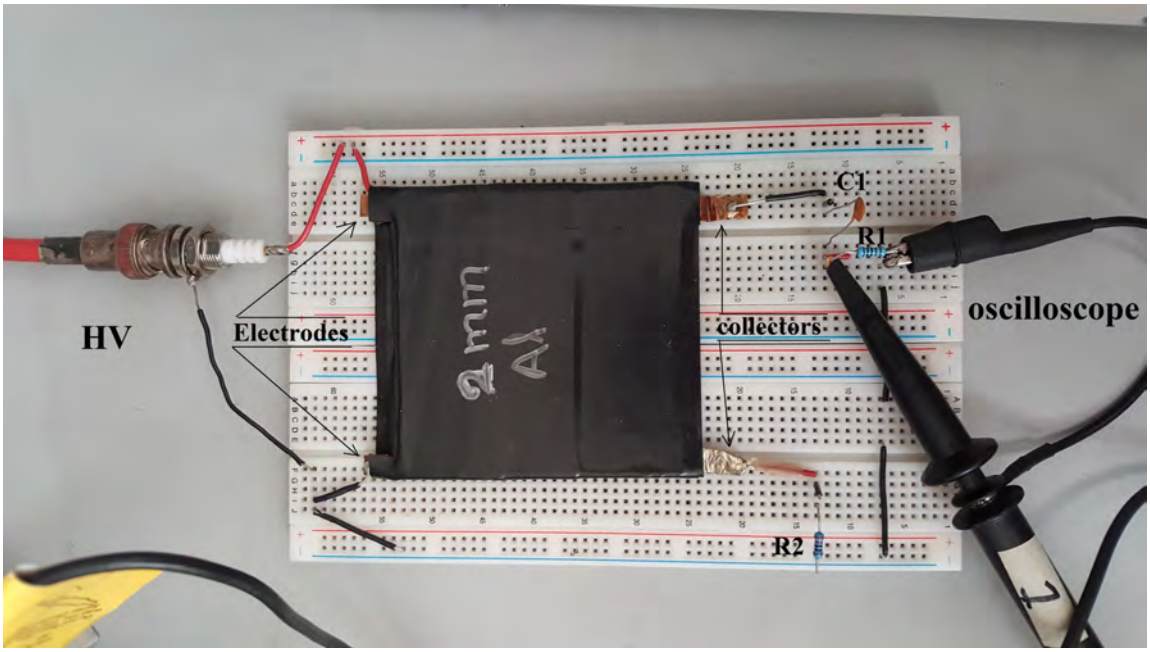

Figure 2: Final configuration and electrical connections to operate the radiation detector based on Aluminum. Working prototype stage.

The process of incrementing applied high voltage in steps of | ± 100 | Vdc was stopped at | ± 1600 | Vdc, for the readout signal amplitudes were very big. No signal amplification electronic circuit is needed, nor really high voltages.

To try and to demonstrate the way this detector works, several tests were performed, and the following results were obtained:

1. Without applied high voltages there are not triggers at all, but noise signal could randomly appear from time to time.

2. The stability of this detector was continuously tested for more than 15 hours, during this period the detector triggered without interruptions, at high voltages above | ± 800 | Vdc and | ± 40 | mV of trigger. No electrical sparks or other malfunctions were observed.

3. When the high voltage is increased, in absolute value, there appears a period of instability, the detector triggers rapidly, with random amplitude and showing up trigger signals. After about one minute the detector regains its stability and starts triggering regularly. This means that the show up triggers are related with momentaneous disturbances (increases) of the external applied electric field. This effect is not observed when the high voltage is decreased, in absolute value, merely the trigger amplitudes decrease.

4. When the detector was entirely protected with 1.0 mil Aluminum foil to shield it from external electromagnetic radiation, the triggers remained without interruption. This means that triggers are generated inside the Aluminum plaque, not as a consequence of electromagnetic induction over the electronic circuits.

5. The Aluminum plaque radiation detector was directly heated using a hot air flux gun, that very common one used for unsolder electronic components, starting from ambience temperature (around 15 °C) up to around 80 °C. The detected triggers haphazardly and dramatically

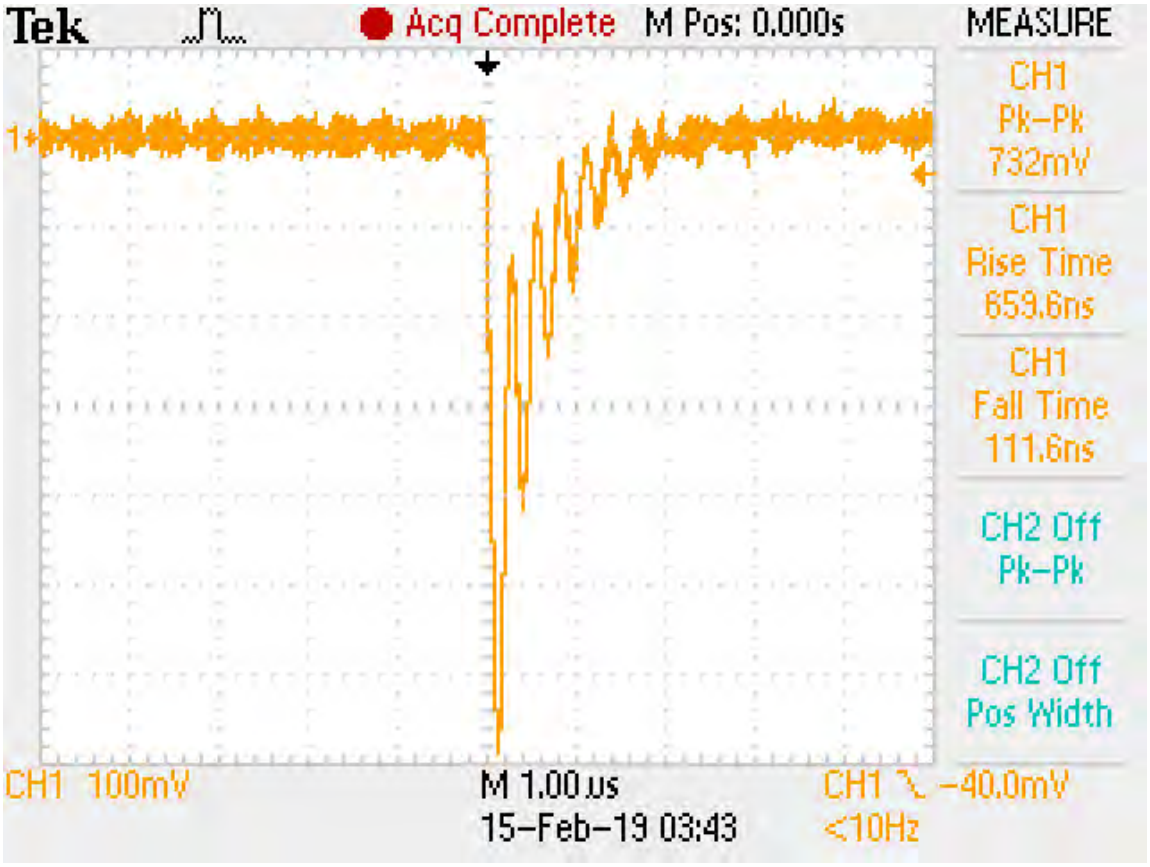

Figure 3: Typical signal (triggers) with positive high voltages. Rising time about 110 ns, falling time about 675 ns.

increased, in both amplitude and showing up. When the detector was freely cooled down, back to ambience temperature, its triggering reduced to its initial triggering activity. When the metallic plaque was cooled down, using iced gel at -2 °C, triggers reduced dramatically in both amplitude and showing up. These facts are interpreted in the sense that the electrical activity (movements of ions) inside the metallic plaque -with the internal electric field- is the cause of the detected signals; and that many of the detected signals are from thermal fluctuations of the metallic plaque, but also from hitting radiation particles which by some nanoseconds disturb the internal electric field. None radiation detector is 100% free of thermal effects; this present radiation detector is not an exception. Some of the detected signals are from the incidence of cosmic ray particles.

6. Very feeble (around 1 microcurie) ^{241}Am radiation source was applied on the top surface of the radiation detector Aluminum plaque. No significant modification of the triggering activity was observed. Normally the oscilloscope is very slow to detect these fast triggers if any was produced by this feeble radiation source.

7. In the prototype Aluminum detector without connecting R1C1 and R2 components, a homemade electroscope was connected to the point **a** or **b** of the detector, Figure 1. Without the applied high voltage there were not electric charges detected, for metallic plaque is electrically neutral. When high voltage is applied, either positive or negative, some electric charges, are

detected; its numerical value depends on the applied high voltage; the higher the applied high voltage, the higher the quantity of electric charge accumulated at either point **a** or**b**. These measurements mean that there is an electrical polarization of the metallic plaque, a spatial separation of electric charges that create an internal electric field that compensates the external electric field, generated by the applied high voltage; these measurements are predicted from the Coulomb Principle in elementary electrostatic.

8. When the components R1C1 and R2 are reconnected, and the homemade electroscope is connected at point **a** or **b** of the Aluminum detector, no electric charges were detected, even if high voltage is applied up to $\mid \pm 2900 \mid$ Vdc. As the detector system is grounded, inside it must be electrically neutral and without some electrical polarization. Therefore, there must be an electric field inside the metal, that exactly corresponds to the external electric field originated by the applied high voltage. This externally originated electric field inside the metallic plaque, after annulling or grounding the polarization electric field, is the operation key of this radiation detector based on a metal.

9. Similar detectors were constructed based on Fe, Cu, Pb. All of them trigger similarly. This means that metallic plaque is fundamental for the operation of this radiation detector.

10. Similar detector was constructed based on an acrylic 5 cm $\times$ 7 cm $\times$ 0.2 cm plaque. The obtained trigger amplitudes were consistent with 0 mV, at high voltages from 0 Vdc to $\mid \pm 2900 \mid$ Vdc. Very small and rare triggers, about $\mid \pm 120 \mid$ mV of amplitude, with the RC discharge shape, at $\mid \sim \pm 3000 \mid$ Vdc, were obtained. These facts are interpreted as that the metallic (Aluminum) plaque is fundamental to generate the big amplitude detected triggers; with a high resistive plaque (acrylic) the triggers have very low amplitude. From this experience, acrylic plaques can be used directly to detect radiation in general, or cosmic rays in particular, but metallic plaques are far better to detect radiation and cosmic rays.

11. Two equal detector devices were operated, horizontally, in stack at the same applied high voltage. Many simultaneous triggers showed up, within times less than 1 ns; others triggers were not inside this period, clearly showing up one after the other sometimes with more than one second of difference in time arrival. This information is consistent with that a radiation particle crosses both detectors and interacts with the metal detectors, leaving some trace of ionized atoms inside the detectors, which originates the trigger in each detector. Two simultaneous triggers are used to define a cosmic ray. This is, cosmic rays are detected by this Aluminum based detector.

From the above experimental facts, detected triggers are not spurious signals from electrical line, power supply, or from anywhere else. Triggers are from electrical disturbances of the electric field inside the metal, either from hitting cosmic ray particles or from thermal fluctuations. Most of the thermal fluctuations can be eliminated, and hitting cosmic ray particles can be selected, using the coincidence signal technique.

This Aluminum based detector has the following plausible way of operation: Incident particles, cosmic rays, ionize the metallic atoms along its trajectory; by the externally applied electric field electrons are accelerated, gain energy and create more ions; an avalanche of electrons is originated, with the R1C1 circuit the electron signal is collected and discharged to be detected as a trigger.

4 Discusions

This Aluminum based detector has some advantages with respect to other kind of radiation detectors: Since liquid Argon ionization energy is 26.4 eV, and Aluminum ionization energy is 5.99 eV [4], a detector based on Aluminum, or another metal, could be a better radiation detector, especially for low intensity or low interacting radiation, for Aluminum is twice denser than liquid Argon and more than two thousand times denser than the gas Argon. In particular, this radiation detector has many advantages with respect to the Resistive Plate Chamber or with respect to the Multiwire Proportional Chamber, or similar detectors: It is easier to construct and maintain, cheaper, no gas problems, safer, no aging problems, simpler, not needed electronic amplifier, not required so high voltages, denser, more suitable to detect low intensity and low interacting radiation like neutrinos or cosmic rays.

This kind of radiation detector could be improved exploiting metal properties like high electric conductivity; for instance, it could be very efficient where speedy, and high dense, instruments are needed, like in neutrino detection, etc., since it could be useful as the base to develop huge neutrino detectors.

5 Conclusions

From all above stated, this is a novel detector based on a metal, with many advantages over other traditionally used radiation detectors. Technological possibilities are immense. Many studies and developments are under way.

Acknowledgements

CONACYT grants. DAIP, UGTO. Apoyo a profesores.

References

[1] F. S. (Editor), *Instrumentation in High Energy Physics. Advanced Series on Directions in High Eenergy Physics*, *World Scientific* **9** (1993), no. 1 583.

[2] F. Sauli, *Gaseous Radiation Detectors, Fundamentals and Application. Cambridge Monographs on Particle physics, Nuclear Physics and Cosmology*, *Cambridge Monographs* **1** (2014) 487.

[3] G. Charpak, *Electronic Imaging of Ionizing Radiation with Limited Avalanches in Gases*, *https://www.nobelprize.org/uploads/2018/06/charpak-lecture.pdf* **1** (1992) 13.

[4] M. Tanabashi et al, *Review of Particle Physics*, *Phys. Rev. D* **98** (2018) 1898.

Physics and detector requirements at zero degree of EIC

Yuji Goto

E-Mail: goto@bnl.gov

RIKEN

Presented at the Workshop of QCD and Forward Physics at the EIC, the LHC, and Cosmic Ray Physics in Guanajuato, Mexico, November 18-21 2019

Abstract

The Electron-Ion Collider (EIC) offers the opportunity to measure three-dimensional structures of nucleons and nuclei, and discover gluon density saturation. An important requirement of the physics program is the tagging of spectator neutrons and the identification of forward photons. We propose to design and build a Zero-Degree Calorimeter (ZDC) to measure photons and neutrons with excellent energy and position resolution.

1 Introduction

EIC is the world's first electron-ion collider. A polarized electron beam is collided with a polarized proton, light ion, or heavy ion beam with high energy and luminosity to perform precise experiments on QCD. The maximum collision energies of the electron-proton and electron-heavy ion collisions are 140 GeV and 90 GeV, respectively. The maximum luminosity of the electron-proton collision is 10^{34} cm^{-2}s^{-1}, which is 1,000 times higher than the HERA electron-proton collider at DESY. The high energy of the accelerator is an advantage because it allows us to study a wide range of kinetic parameters, such as the four-momentum transfer Q^2 and the fraction of the nucleon's momentum carried by the parton x. The expected results of EIC include the discovery of gluon density saturation called color glass condensation (CGC), the precise measurement of three-dimensional structures of nucleons and nuclei, the elucidation of the origin of nucleon spin, and the study of the confinement mechanism of quarks and gluons. Gluons are the key to all of these studies, and EIC will increase its sensitivity to gluons with high resolution by taking advantage of the collider.

We are proposing development of zero-degree apparatus in the EIC experiment. Zero-degree detectors serve critical roles for a number of important physics topics at EIC. We will study requirements and technologies of zero-degree detectors, and develop a position-sensitive Zero-Degree Calorimeter (ZDC).

One of the most important physics topics is identification of nuclear breakup in the exclusive processes on nuclei to distinguish between coherent (nucleus intact) and incoherent (nucleus decays) diffractive scattering. It requires to detector photons, too. Physics topics to be discussed in this Report are $e + A$ collision geometry, spectator tagging in $e + d/^3He$, leading baryons and very forward asymmetries, spectroscopy, and so on. We'd like to maximize physics capability by studying detector design, development and simulation.

2 Physics

2.1 $e + A$ collision geometry

Exclusive vector meson production in diffractive process is one of the key measurements at EIC [1]. For the coherent process where the nucleus remains intact, the momentum-transfer (t) dependent cross-section can be translated to the transverse spatial distribution of gluons in the nucleus, thus considered to be directly sensitive to gluon saturation as a function of Q^2. Exclusive incoherent vector meson production in $e + A \rightarrow e + V + X$ occurs when the nucleus breaks up from its interaction with the vector meson. The probe can be used to characterize spatial density fluctuations in nuclei, and so it will be important to identify these events. This requires accurate determination of the exclusivity of the reaction, which must be determined by identifying break-up of the excited nucleus [2]. It is a strenuous measurement since the incoherent cross-section is expected to be much larger than the coherent cross-section in the moderate and high-t ranges of the coherent process where a precision to extract the spatial distribution is required. Evaporated neutrons from the break-up in the diffraction process can be used to separate the incoherence/coherence most probably ($\sim$90%). The latest study [2] shows that photons from de-excitation of the exited nucleus and also evaporated protons signal incoherence in absence of evaporated neutrons. This leads to a requirement measure neutrons and photons at near zero degree precisely to complete the coverage of coherence tagging in a wide t range.

Collision geometry is an important measure in collisions with nucleus, while the measurement for an event-by-event characterization is rarely discussed in the prior deep-inelastic scattering experiments off a nucleus. It has been proposed that collision geometries can be tagged through forward neutron multiplicities emitted near at zero degree [3]. This type of geometry gauge, if achieved, can be extremely beneficial in constraining nuclear effects for the electron-nucleus collisions at EIC. This neutron number distribution can be measured with a calorimeter at zero degree in the ion-going direction. Constraining collision geometry quantities like "traveling length" of struck parton in nucleus, which is correlated with the impact parameter of the collision, is very meaningful in the studies of nuclear medium effects. Energy deposition in the ZDC can be used as a good measure of traveling length d while the impact parameter b is not as well controlled. Even though the resolution of the traveling length is likely dominated by its intrinsic correlation with the number of emitted neutrons during the evaporation process, it's beneficial to keep the energy resolution for counting neutrons not to be further smeared by the measurement. With the determination of collision geometry in these measurements, our understanding of nuclear structure can be constrained with higher precision.

2.2 Spectator tagging in $e + d/^3He$

Other physics programs at EIC those require tagging forward neutrons are collisions with light ions, like in d and ^3He [4]. Identifying spectators in these processes for identifying that "target" nucleon and constraining kinematics for studies of the Short-Range Correlations (SRC) [5].

The SRC is a nucleon-nucleon interaction at very short distance. It shows how nucleons form a nucleus, and has a deep connection to the EMC effect. Experiments have shown it is universal

that ∼20% of nucleons are in SRC pairs. These SRC pairs have high momentum and spatially very close each other. If the nucleon PDF could be significantly modified for these pairs, but not modified for other nucleons, SRC is the cause of the EMC effect. Almost all of these SRC pairs are found to be similar to a quasi-deuteron at its high momentum tail. In addition to the SRC study in $e + A$ collisions, we will be able to understand the deuteron as a baseline of SRC pair in $e + d$ collisions by measuring $e + d \to e + X + n$ at zero degree.

2.3 Meson structure

EIC enables a quantitative understanding of the structure of hadrons, such as the nucleon, pion and kaon, in terms of quarks and gluons. A precise description of the 1D structure of hadrons; parton distribution functions and form factors will be revealed and the 3D images of hadrons will be constructed as expressed in generalized parton distributions and transverse-momentum dependent distributions. Pion structure will be measured with tagged neutron, and kaon structure will be measured with tagged Λ/Σ. Scattered electrons can be detected in the central detector, and baryon (neutron, Λ) can be detected at very small forward angles and nearly the beam momentum. Neutron measured in the ZDC will have 100% detection efficiency with 60 cm $\times$ 60 cm ZDC size, but need good ZDC angular resolution for the required $|t|$ resolution. In order to detect forward Λ, additional high resolution and granularity EM calorimeter + tracking before ZDC is necessary for neutral channel ($\Lambda \to n + \pi^0$), and additional trackers in opposite direction on the path to ZDC is necessary for charged channel ($\Lambda \to p + \pi^-$) and more challenging. Good hadronic calorimetry is necessary to obtain good x resolution at large x.

2.4 Leading baryons and very forward asymmetries

Leading proton and neutron productions in DIS were measured and their production mechanisms were studied at HERA by comparing with fragmentation process and one pion exchange (OPE) process. The results support that the OPE process dominates the production, but there are still tension in detailed understanding of the mechanism and comparison between ZEUS and H1 data. It is also important to compare the data from $e + p$ collisions and $p + p$ collisions where also some tension exists. In addition to the production cross section measurement, the asymmetry measurement will give us useful additional input for the study of the production mechanism. The very forward inclusive neutron production is known to show a large left-right asymmetry. The spin asymmetry measurement of the leading baryons in $e + p$ collisions will give us useful additional information, too. In order to study them systematically, it is very important to have wide aperture effectively to cover wide x_F ($0.1 < x_F < 1$) and p_T (> 1 GeV/c).

Not only leading baryons, it is also important to measure production of photon and various hadrons in the very forward region. The data will be used to understand energy flow and development of event generator, and applied for understanding air shower evolution of high-energy cosmic ray and neutrino interaction.

2.5 Spectroscopy

The charmonium-like X, Y, Z resonances[6] recently observed are likely exotic candidates in heavy quark sector. They have been provoking much interest experimentally and theoretically recently with an expectation of the states being clear multi-quark candidates. With the proposed energy and luminosity of EIC, the X, Y, Z states can potentially be discovered through meson photoproduction. There are opportunities of studying exotics in hadronic spectroscopy at EIC especially heavy quark (c, b) sector in photoproduction with an extended energy lever arm of EIC, such as charged charmonium-like state $Z_c^+(3900)$, $Z_c^+(4430)$ by the process $\gamma + p \to Z_c^+ n$ [7, 8]. For tagging and kinematically constrain the forward neutrons in these processes, it requires energy and position resolutions sufficient to constrain these processes kinematically.

2.6 Other topics

We're discussing nuclear fragments and isotope tagging as an important topic for the very forward apparatus. The luminosity monitor and polarimetry are also important as application.

3 Detector performance requirement

3.1 Photon detection

Detection capability of not only neutrons but also photons are required to identify the nuclear excitation states as the hint of the coherence of the collision. In order to detect photons from nuclear excitation requires a large (as large as possible) aperture. It is possible that a second IR design will allow a larger ZDC acceptance. The energy of photon can be as low as below 300 MeV. It will require a full absorption calorimeter with a good energy resolution, e.g. made with a crystal scintillator (LYSO, PWO, ...).

3.2 Zero-Degree Calorimeter (ZDC)

The ZDC detectors were installed to each collision points in RHIC primarily as the luminosity monitor by the neutron counting from collision point providing real time feedback to the accelerator operation. On the other hand, the ZDC detector was also used to determine the event plane, centrality determination, and so in heavy ion collisions. Further more, the ZDC itself played central role to discover unexpectedly large transverse single spin asymmetries at almost zero degree in polarized proton + proton[11] and proton + nucleus [12] collisions.

The ZDC detectors [10] implemented for RHIC is designed to detect neutrons at zero degree $\pm$ 18 meters downstream of collision points and have coarse position resolution with a Shower-Max Detector (SMD). ZDC is composed of copper-tungsten alloy absorbers with optical fibers and each module has 1.7 interaction length (λ_I). A photomultiplier collects Cherenkov lights via the optical fibers in each module. Three ZDCs are located in series (5.1 (λ_I) in total) within the small acceptance, covering 10 cm in the transverse plane. SMD consists of x-y scintillator strip hodoscopes and is inserted between the first and second ZDC modules at the position of maximum hadronic shower approximately. The x-coordinate (horizontal) is sampled by 7 scintillator strips of 15 mm width, while the y-coordinate (vertical) is sampled by 8 strips of 20 mm width, tilted by 45 degrees. The ZDC demonstrated performance of about position resolution of approximately 1cm and energy resolution of $\Delta E/E \sim 30$ % at E = 100 GeV. The ZDCs demonstrated radiation hardness and have been operated in physics stores.

Unfortunately, the ZDC implemented for RHIC doesn't satisfy the performance requirement of the ZDC for EIC. Here we develop the new ZDC detector dedicated for EIC.

The number of spectator neutrons is predicted to have somewhat correlation with the collision geometry. The required performance of the detector to identify the coherence of the collision is under development using the BeAGLE simulation [2]. Some of performance parameters are under ongoing study. The optimization of the performance requirements is included in the scope of the detector development based on the requirements known as of now as listed below.

3.2.1 Acceptance

A large acceptance (e.g. 60$\times$60 cm^2) to establish good identification efficiency between coherent and incoherent collisions is necessary for vetoing spectator neutrons from nuclear breakup. This large acceptance is also required to determine the collision geometry[9] . For studying very forward production and asymmetry of hadrons and photons, a large acceptance is also important. The EIC aperture of $\pm$4 mrad gives $p_T < 1$ GeV/c coverage for 275 GeV hadrons and photons,

which covers the transition from elastic/diffraction to incoherent regime; for low-energy hadron beam the acceptance in terms of p_T is more limited e.g. $p_T < 0.4$ GeV/c coverage for 100 GeV beam.

3.2.2 Energy, position, and p_T resolutions

Due to the strong β squeeze < 1 meter for the high luminosity, a beam spread of ∼20 MeV and ∼1 cm of the hadron beam angular divergence is induced. Thus the position resolution of neutron in sub cm won't help. 1 cm position resolution provides 300 μrad angular resolution, which can be translated to transverse momentum resolution $p_{\rm T} \sim 30$ MeV/c of 100 GeV spectator neutron.

The minimum energy resolution $\Delta E/E \sim 50\%/\sqrt{E(GeV)}$ to distinguish number of spectator neutrons from 20 to 30 for collision geometry determination. In order to accommodate a single MIP track to 30 spectator neutrons, wide dynamic energy range in the readout electronics is required.

It is anticipated to be a sampling type calorimeter with a sufficient longitudinal size of ∼10 interaction length[9]. It is also required to have a sufficient transverse size of ∼2 interaction length to avoid transverse leakage of the hadron shower and to have a good enough hadron energy resolution.

3.3 Radiation hardness

From the DIS cross section, 60μb, and 10^{34}cm^{-2}s^{-1} luminosity, the event rate is evaluated to be 600 kHz. The beam-gas rate is evaluated to be 10 MHz by assuming 10^{-7}Pa vacuum pressure, which is 14 times larger than the event rate.

100 GeV dose/event $\sim 1.6 \times 10^{-8}$ Joule/event, and $e+p$ event rate 600 kHz gives 0.01 Joule/s. From LHCf simulation (with about $1\lambda_I$), 1/3 of dose is given in 1 kg material, 30 Gy/nb for $p+p$. For $e+p$ at EIC, this corresponds to 0.003 Gy/s which corresponds to 30 kGy/year with 10^{34}cm^{-2}s^{-1} luminosity. For 14 times larger beam-gas rate, this corresponds to 500 kGy/year. So, we evaluate the radiation dose to be $\sim O$(100k - 1MGy) or $n_{eq} \sim 10^{14-15}$ for 1-year operation of $e+p$ collisions, i.e. 10^{15-16} for lifetime.

Silicon and crystal scintillators (LYSO, PWO, ...) would stand for the expected dose. Some plastic scintillators like PEN may stand for > 0.1 MGy radiation. The plastic scintillator is still an attractive option since it shows good e/h ratio, thus better resolution for hadrons.

4 Summary

Zero-Degree Calorimeters are an essential component of any EIC experiment. The EIC imposes more stringent requirements energy and position resolution than either the RHIC or LHC programs.

For the photon detector study, we will evaluate performance of several crystal scintillators, especially at low energy < 300 MeV. Energy resolution, speed, radiation hardness, etc. will be compared. We will also perform a prototype study of ZDC (EM + Hadron) with position sensitivity. We will study performance of energy and position resolutions with test beam and simulation. It is important to study e/h for hadron energy resolution. Another item is a radiation hardness study for new technology. We will test radiation hardness of several types of plastic scintillators.

References

[1] A. Accardi *et. al* Electron Ion Collider: The Next QCD Frontier - Understanding the glue that binds us all arXiv:1212.1701.

[2] E.C. Aschenauer, M.D. Baker, J.H. Lee, L. Zheng, EIC R&D Project eRD17 Progress Report.

[3] L. Zheng, E.C. Aschenauer, J.H. Lee, Determination of electron-nucleus collision geometry with forward neutrons, Eur. Phys. J. A (2014) 50: 189.

[4] Talks at *Polarized light ion physics with EIC*, Feb. 2018, Ghent University, Belgium.

[5] Talks at *Short-range nuclear correlations at an Electron-Ion Collider*, Sep. 2018, CFNS Brookhaven National Laboratory.

[6] R. Faccini, A. Pilloni, A.D. Polosa, Mod. Phys. Lett. A 27 1230025 (2012).

[7] Q. Lin, X. Liu, H Xu, PRD 88 (2013) 114009.

[8] Talks at *The spectroscopy program at EIC and future accelerators*, Dec. 2018, Trento, Italy.

[9] Electron-Ion Collider Detector Requirements and R&D Handbook (version 1.1).

[10] C. Adler, A. Denisov, E. Garcia, M. J. Murray, H. Strobele, and S. N. White, Nucl. Instrum. Methods Phys. Res., A 470, 488 (2001).

[11] A. Adare, et al., Phys. Rev. **D88**, 032006 (2013).

[12] C. Aidala, et al., Phys. Rev. Lett **120**, 022001 (2018).

Design and Simulation of a Cryostat and a Field Cage for a LArTPC for test in DUNE Collaboration

Everardo Granados, Julián Félix

granadosve2012@licifug.ugto.mx, felix@fisica.ugto.mx

Universidad de Guanajuato

Presented at the Workshop of QCD and Forward Physics at the EIC, the LHC, and Cosmic Ray Physics in Guanajuato, Mexico, November 18-21 2019

Abstract

Currently, the DUNE Collaboration is making several tests in small detectors with the components that will be used in the DUNE detectors to avoid and detect future problems in the massive detectors. The design and simulation of the cryostat and HV system for a LArTPC to make tests of relevance in cool electronics and photodetection for the DUNE Collaboration are shown in the following article.

The design of the cryostat is based in the ASME Code and the simulation of the heat transfer is made in COMSOL Multiphysics. The design of the field cage was made based on the results of the simulation for the shape and the uniformity of the electric field in the active Drift volume. I present the simulated physical results and an estimated quote to construct this cryostat and HV system.

1 Introduction

The neutrino is a neutral particle with a very small mass that just interacts by weak force. It was proposed by Wolfgang Pauli in 1930 to explain the energy conservation violation in beta decay and discovered by Frederic Reines and Clyde Cowan.

Since the neutrino discover, it have been ones of most enigmatic particles. On one side it does not interact much with the matter so that different kind of massive detectors have been created to detect these particles and on the other hand these are the most abundant known particles with mass in the universe. For the detection of the neutrinos, these have to interact with the atoms of the detector. From interaction, charged particles can be observed in the detectors, and using this information, depending of the detector technology, it is possible reconstruct the energy of the neutrinos, flavour, kind of interaction, etc.

Different kind of neutrino detectors have been created, using Cerenkov effect, scintillation, ionization, nuclear reactions, etc. techniques to observe the charged particles products of interactions. Some of these detectors use the combinations of these techniques to reduce the systematic errors.

1.1 LArTPC

The Time Chamber Projection detectors (TPC) were invented by David R. Nygren in 1974 based in the Multiwire Proportional Chambers invented by G. Charpak in 1970. The TPC detector provide of 3-dimensional track and calorimetry information that can be use for particle identification [1]. This is the case of LArTPC, that combines the ionization, scintillation and calorimetry properties of the liquid argon to reconstruct in 3D the trajectory of the particles in the liquid argon.

The TPC works using the ionization and scintillation of a gas or liquid medium. The electrons generated by ionization are carried by electric field to a sensor plane (wires, pixels, etc.); with the information obtained from the sensor plane and knowing when the interaction was generated it is possible to make the reconstruction of the trajectory of the particle in 3 dimensions. The time of the interaction can be obtained by the scintillation, Cerenkov effect in the material or in the case of the a particles beam knowing when are produced the pulses.

The Liquid Argon Time Projection Chamber (LArTPC) is a TPC that uses liquid argon like detection medium. The first concept of this detector was developed by C. Rubbia with the goal to detect neutrinos based in the TPCs developed by Nygren who used mixtures of noble gases as argon with CH4 as target.

There are several reasons for that the liquid argon is considered as ideal target material for a TPC [2]:

- it is dense 1.4g/cm3
- it does not attach electrons in hence it permits long drift-times;
- it has a high electron mobility;
- it is abundant in the atmosphere;
- it is cheap;
- it is easy to obtain and to purify;
- it is inert and can be liquefied whit liquid nitrogen.

1.2 Field Cage

The Field Cage (FC) is a set of electrodes with and specific shape and voltage that provides a uniform electric field in the active drive volume in a TPC. The shape of the FC depend of the geometry, voltages and the distance between the anode and sensor plane on the detector [3].

1.3 Cryostat

A cryostat is a container used to maintain a constant low temperature, lower that 0^{o}C. The cryostat type depend of the insulation technique. These techniques are developed to reduce the heat transfer as possible as. The more usual insulator methods are: vacuum, multilayer insulator, foam insulation, powder and fibrous insulation.

1.4 DUNE Experiment

The Deep Underground Neutrino Experiment (DUNE) is a modern, international experiment for neutrino science and proton decay studies.

DUNE will consist in two neutrino detectors placed in the world's most intense neutrino beam. One of these detectors will be placed near of source in Fermilab, Near detector (ND); and the other will be installed more than a kilometre underground at 1,300 km downstream of the source, Far Detector (FD).

The DUNE Science program contemplates topics as supernova burst physics and astrophysics, nucleon decay, neutrino oscillation physics that includes search for leptonic (neutrino) CP violation, resolve the mass ordering, and other topics.

The near detector will be composed of a set of different detectors a pixel LArTPC, magnetized tracker, 3D scintillator tracker and hadronic and electromagnetic calorimeters. The goals of the near detector are to make precisely measurements of beam neutrino fluxes, constrain the systematic error uncertainties for oscillation neutrino measurements and precise measurements of neutrino interactions.

The far detector will be composed of four massive LArTPC modules. It will be placed 1.5 km underground. Each module will be filled with 17,000 tons of liquid argon. Two kind of LArTPC technology will be used in FD. In two modules the Single Face (SF) technology will be used, and in the other two modules the Dual Face(DF) technology will be used.

In the SF detectors, the electrons are attracted to the sensor plane in horizontal direction. The pros to use this technology is that it has been used for other detectors and these have been tested several times. In the DF detectors, the electrons are carried to the top side of the detector and before to be collected by the sensor plane, these pass for a multiplication stage in gas argon, in this way the signal is amplified and the electronic inside of cryostat is reduced.

2 Design

The design of a cryostat and field cage for a prototype of Pixel LArTPC is presented in this article. The goal of this detector is to make tests for photodetection , cold electronics, etc. of interest for the DUNE Collaboration. The active drift volume is 15 cm x 15 cm x 60 cm in vertical position.

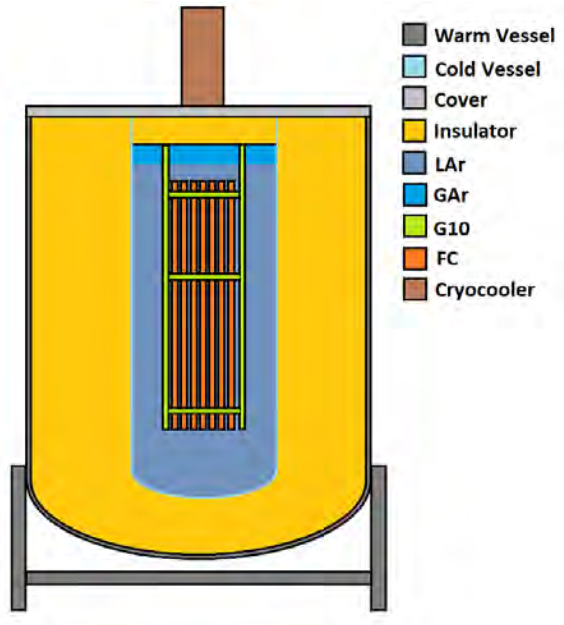

Figure 1: Conceptual scheme of the detector design, in the figure some parts are identified by color.

A LArTPC is composed for these systems:

- Cryostat and slow controls.

- HV System.
- Photodetection system.
- DAQ.
- Electronics for TPC.

In this article are described the design and functionality simulation of some parts of this systems, particularly of the cryostat system and HV system.

Cryostat design

The cryostat is constituted mainly by the following parts: Warm Vessel, it is in contact with the outside, provides mechanical support to the detector; Cold Vessel, it is the container that is in contact with the liquid argon; Insulator, reduce de heat transfer from the outside to the inside of the cryostat; Cryostat cover, in this cover are installed the cold head, slow control devices, connections to cold electronics, HV connectors, etc.

The design of the warm vessel, cold vessel and the cover are based in the ASME code. The Insulator that is contemplated to use is a phenolic foam.

The cold vessel is designed to be constructed from a sheet of SS 304. it is designed to support up to 2.03 ATM of internal pressure, if it is necessary to apply vacuum insulation. The dimensions of the the vessel are 1 m high, internal diameter of 50 cm and 0.61 mm of thickness. In the **Figure** 2-a) the design is shown.

For the warm vessel design was considered that it supports 4 ATM of external pressure in the cylindrical zone and 10 ATM in the spheroidal head. It is designed to use steel plate. The dimensions of the warm vessel are: thickness of 5.7 mm, internal diameter of 1.10 m and 1.31 m hight. In the **Figure** 2-b) an image of the warm vessel design is shown.

Phenolic foam is the insulator material considered to use. This insulator has a thermal conductivity of 0.017 W/m^oC and a low cost compared with other insulators. The thickness of the insulator is 30 cm. Currently, only this option has been considered for the insulator due it has presented good results in the heat transfer simulation. It has enough heat transfer to be able to use a cryocooler that maintains a stable temperature in the cryostat. In the **Figure** 2-c) an image of the insulator is shown.

The cover design consist of a plate of SS304. The design is based on the mandatory appendix 14 of the ASME Code. The cover has 5 through holes, two for the circulation of LAr, one for the pressure control valve, one for the thermostat and the central opening to introduce the TPC, cold electronics and another TPC stuff. The thickness of the plate is 1.8 cm and it has a diameter of 1.11 m. The central hole is 35 cm of diameter. In the **Figure** 2-d) an image of the cover design is shown.

A cryocooler is an advise used to keep the system at cryogenic temperature. Accord to simulation results and looking for a cryocooler that satisfies the power and temperature requirements some cryocoolers were found. These work with 125 W of power and these work in the temperature range was considered to use for this detector.

Other important part for the cryostat is to have a safety valve. The LAr is in continuous evaporation and it increase the internal pressure in the cold vessel and it could create damages to the equipment and operators. Exist some commercial valves considered to be used due these valves meet the pressure requirements and materials of the valves are made are similar to the cryostat materials.

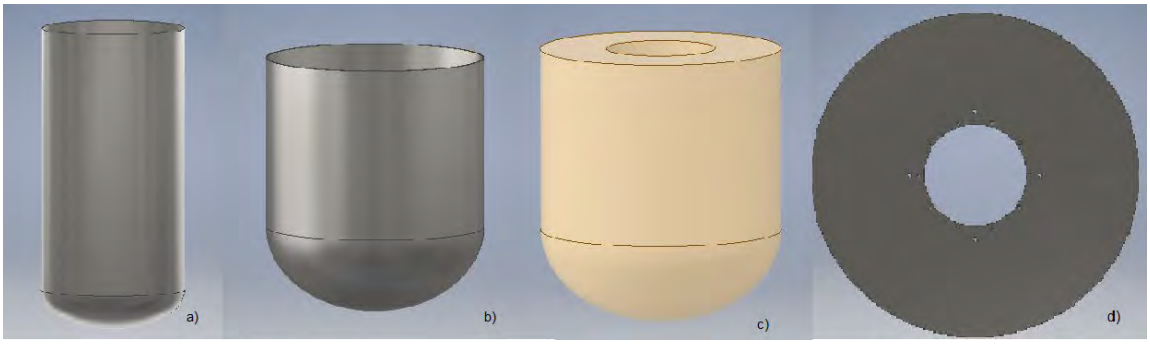

Figure 2: Images of the design of cryostat components, a) image of cold vessel design, b) image of warm vessel design, c) image of insulator design, d) image of cover design.

2.1 HV Design

In the LArTPC detectors it is very important to generate a uniform electric field, because the projection of the trajectory of the particles depends of the electrons being taken to the sensor plane. The HV system has been imposed the followed requirements for its operation:

- Generate a uniform field of 500 V/cm.
- Do not generate electric fields greater than 30 kV/cm.
- Have a stable HV source that does not have large variations. In DUNE 0.9 mV.
- Have a low current in the system.

The HV System consist meanly of the following components:

- Cathode plane.
- Anode Plane.
- Field Cage.
- HV Supply and HV Connectors.

The components will be supported by G10 profiles, because it is a good thermal and electrical insulator.

The cathode plane is designed to be a flat sheet of Stainless Steel 304 with 6 screws welded on the back to hold the plane. The separation between the cathode and the anode is 15 cm, it is necessary to apply -7500 V to generate the 500 V/cm field. The dimensions of the plane are 15 cm wide, 60 cm high, 0.6 mm thickness and SS304 1 /4 in x 1 / 2 in screws. An image of the cathode plane is shown in the **Figure** 3-a).

The Anode Plane (Sensor plane) consists of a perforated G10 plate with the pixels embedded in one of the faces. The pixels are 4 mm x 4 mm copper lamellae. A positive voltage can be applied so that the electrons are attracted to the pixels. The plate contains 3600 pixels (30x120). An image of the anode plane is shown in the **Figure** 3-b).

The Field Cage (FC) is composed of a series of profiles with a potential difference. The shape and the number of profiles is very important to obtain a uniform electric field. For the design of this FC, to define the number and geometry of profiles the simulations were used. For the simulation, the COMSOL software was used using the electrostatic libraries. The design of the

field cage would consist of rectangular profiles of Stainles Steel 304 of 5 mm 3.175 mm(0.125 in) of cross section. Some images of a FC profile and FC designs are shown in the **Figure** 3-c)d)e).

For the HV source, exist some power suppliers that meet the voltage requirements with a low noise, low current and an a highly controllable and stable power.

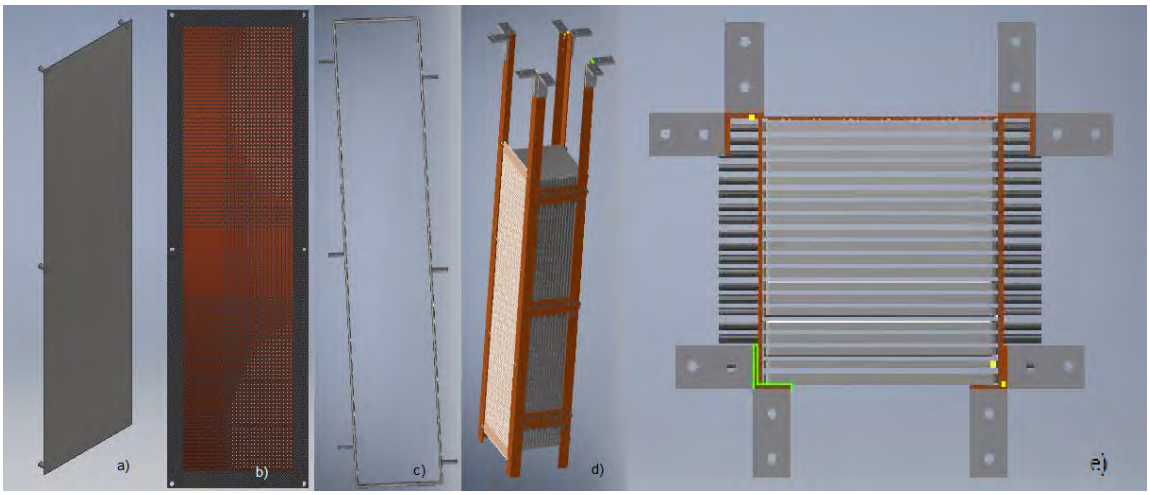

Figure 3: Images of the design of HV System components, a) image of Cathode plane design, b) image of Anode plane design, c) image of FC profile design, d) and e) images of complete FC design.

3 Simulation and Results

The simulations carried out to observe the functionality of the systems designed. For the cryostat, some simulations of heat transfer as function of the external temperature were made. For the HV System, the simulations of the electric field in the FC were made using different geometries and number of profiles. The simulations were made using COMSOL Multyphisics.

For the cryostat simulation, the geometry is based in the design that was showed before. The properties of the materials were imposed from the COMSOL materials library and others for other sources as NIST, FNAL, ASME Code, etc. In the **Figure** 4 the results of the cryostat are shown.

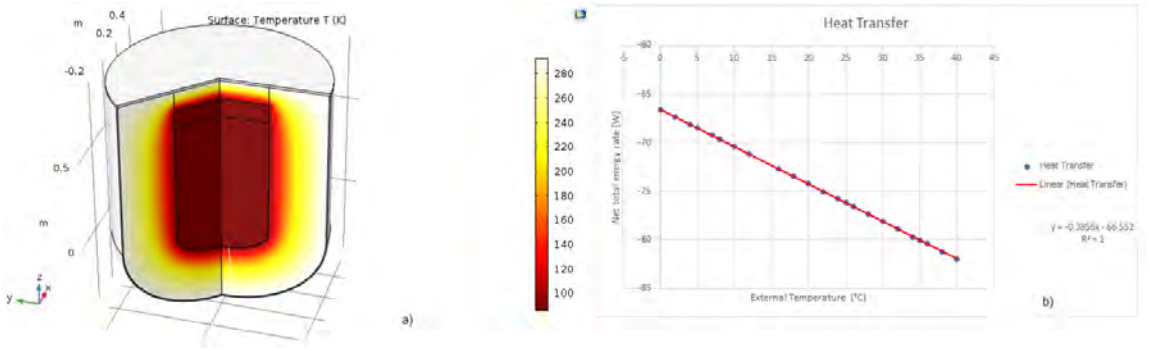

Figure 4: Images of the results of the cryostat simulation are shown. a)3D plot of one simulation. b) Plot of total heat transfer in the cryostat as function of the external temperature.

For the HV system, some simulations of the electric field were obtained. The goal of this simulations is to observe that an uniform electric field in the active drift volume. With the results of this simulations, the geometry of the profiles for the FC was selected. In the **Figure** 5 the geometries for the profiles are shown.

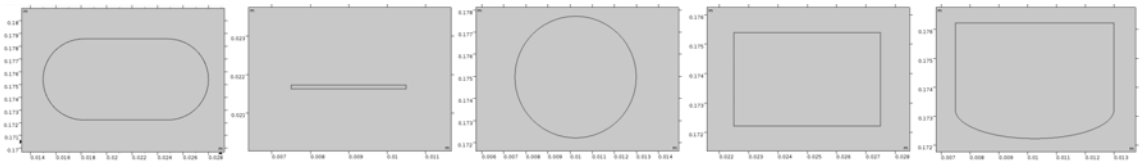

Figure 5: Images of the results of the cryostat simulation are shown. a)3D plot of one simulation. b) Plot of total heat transfer in the cryostat as function of the external temperature.

These geometries were observed in the design of other FC detectors as MicroBooNE or DUNE. The size and the number of the profiles were determined accord to the available space and the results of the simulations. Other important consideration was the ease of building them.

The shape, the magnitude, equipotencial lines and direction of the electric field from the simulation results were compared with the requirements imposed in the HV system design.

The geometries used are:

- Rectangular with two circular sides (10 profiles). In the **Figures** 6-a) some results of the simulation are shown.
- Rectangular thin profiles (20 and 30 profiles). In the **Figures** 6-b) and and **Figure** 6-f) some results of the simulation are shown.
- Circular profiles (20 profiles). In the **Figures** 6-c) some results of the simulation are shown.
- Rectangular profiles (20 profiles). In the figures **Figures** 6-d) some results of the simulation are shown.
- Rectangular-ellipsoidal profiles (20 profiles). In the **Figures** 6-e) some results of the simulation are shown.

4 Conclusions

In the simulation it is observed that the heat transferred is 74.2 W, that is lower that the power of some of the commercial cryocoolers. This is the first option for this detector just using a foam as insulator, it is necessary to contact an expert to have an opinion about it given all specification of the design.

According to the results obtained, all the proposed geometries meet the requirements imposed in the design. It was decided to use the 20 rectangular profiles, because it is more easy to construct, there is a major space between the profiles that with 30 thin profiles, and the shape of the electric field near of the profiles does not change a lot.

The final design for the cryostat and FC are shown in the **Figure** 7.

With the results obtained from the simulations, the conclusions are:

- The cryostat will work satisfactorily, because the heat flow of the cryostat is covered by the cryocooler. It is very important consider that in the future could be a pump for the LAr, and in this case the simulation of the LAr is made with a natural convection.

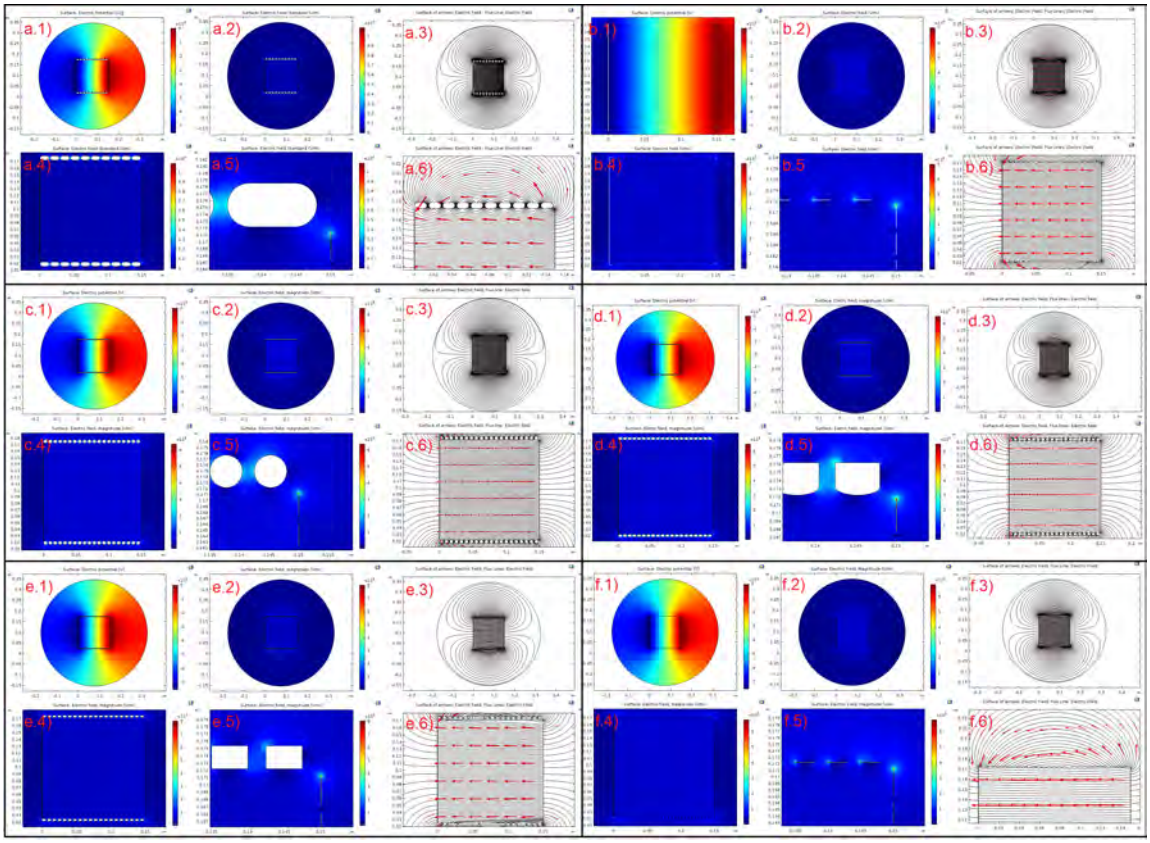

Figure 6: Images of the results of the electric field simulation are shown. The figures are ordered in the groups a), b), c), d), e) and f) that correspond to the different configurations. The subscript number is for the different views of the simulation results. For 1) is to observe the equipotential lines in the active drive volume; 2) In the images the magnitude of the electric field in all the LAr is shown; 3) In these images the lines of the electric field in all the LAr are shown; 4) In the these images the magnitude of the electric field in the active drift volume is shown; 5) In these images the zones with the maximum value for the magnitude of the electric field are shown; 6) In these images the deformation of the electric field close to the profiles are shown.

- The cryostat will work satisfactorily, because the heat flow of the cryostat is covered by the cryocooler. It is very important consider that in the future could be a pump for the LAr, and in this case the simulation of the LAr is made with a natural convection.
- The heat transfer does not change a lot for the change of the temperature of the environment. For that the cooling capacity of the cryocooler is enough to keep the system cold.
- From the field cage simulated was observed that the electric field is very uniform. To choose the geometry depends on some details of the shape of the field near the profiles and the ease of building the system. But any of the designs, according to the simulations, could be candidates for field cage.

Figure 7: Images of the final design of the cryostat and field cage.

Acknowledgements

I would like to thank my family and friends who supported me to continue doing what I like the most and to my advisor for his patience and support during the realization of this project.

References

[1] "Tracking with the pep-4 tpc." https://www.slac.stanford.edu/cgi-bin/getdoc/icbp82-008.pdf. Accessed: 2019-06-24.

[2] C. Rubbia, *The Liquid Argon Time Projection Chamber: A New Concept for Neutrino Detectors*, .

[3] **DUNE** Collaboration, B. Abi et al., *Deep Underground Neutrino Experiment (DUNE), Far Detector Technical Design Report, Volume I Introduction to DUNE*, arXiv:2002.02967.

Performance of CMS Endcap Precision Timing Sensors

Margaret Lazarovits
on behalf of the CMS Collaboration

mlazarovits@ku.edu

University of Kansas

Presented at the Workshop of QCD and Forward Physics at the EIC, the LHC, and Cosmic Ray Physics in Guanajuato, Mexico, November 18-21 2019

Abstract

The Large Hadron Collider, a particle accelerator in Geneva, Switzerland, will enter its High Luminosity (HL) phase, whose upgrade has already started. This phase will include an increase in particle collisions, achieving instantaneous luminosities of 5 to 7 times the nominal luminosity, 1×10^{34} cm^{-2} s^{-1}. This increase gives more opportunities for rare processes to come to light, however it also means that there is more overlapping particle interactions, called pileup, in the detectors. To address this added pileup, the Compact Muon Solenoid (CMS) detector at the LHC will install a new precision timing detector, the MIP Timing Detector (MTD), as part of the upgrades for the HL-LHC. The sensors comprising the endcap section of the MTD are silicon low gain avalanche detectors (LGADs). From extensive tests at the Fermilab test beam facility, it has been shown that prototypes of these sensors perform in accordance to our expectations and requirements for the MTD. Specifically, these sensors have demonstrated a timing resolution within 30-40 picoseconds.

1 Introduction

The Large Hadron Collider (LHC), at 27 km in circumference, is the largest particle accelerator in the world. The LHC currently operates at a center-of-mass energy of 13 TeV for proton-proton colliders, but also collides heavier particles, like lead-lead. Located on the French-Swiss border in Geneva, this collider hosts multiple international experiments, including the Compact Muon Solenoid (CMS) detector. The CMS experiment [1] is a general purpose detector that participates in a variety of physics endeavors, including precision measurements of cross-sections and couplings, as well as searches for beyond Standard Model physics. This detector is designed with onion-like layers of different technologies enveloping each other. These layers include tracking layers, calorimeters, and of course, the eponymous superconducting solenoid.

The LHC has been online since 2008 and has steadily been ramping up its center-of-mass (CoM) energy, the energy at which it collides particles. A higher center-of-mass energy means LHC physicists are able to probe shorter length scales, or observe heavier particles. Many of the

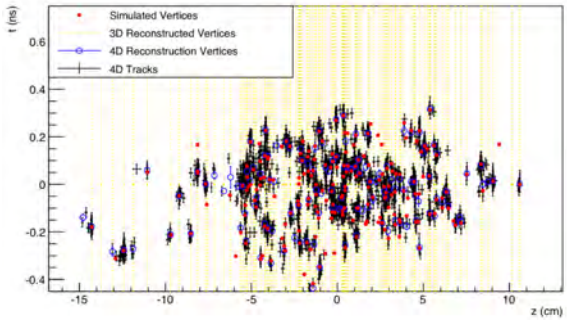

Figure 1: Resolution of pileup with precision timing from the MTD TDR.

particle hypothesized to be beyond the Standard Model have masses on the order of ∼1 TeV, so a higher CoM energy may help us to see these particles. Another way to help see these particles and other rare processes is to simply increase the number of particle collisions.

Increasing the number of particle collisions is called increasing the luminosity, which is a measure of how many particle collisions happen in a given area in a given amount of time. This is exactly what the LHC plans to do in the High Luminosity era (Phase-2) for the LHC, with particle interactions increasing by a factor of 100. An increase in particle interactions, while providing a greater chance to observe rare processes, also produces more noise called pileup, when particle interactions overlap spatially. However, CMS scientists have designed the Minimum Ionizing Particle Timing Detector (MTD) to introduce precision timing in an effort to mitigate the effects of pileup within CMS.

Particle collisions within the CMS detector are likely to happen at the same point in space along the beam line axis. With so many interactions happening at the same point in three dimensions, one can resolve these overlaps by examining the interactions in four dimensions. This implementation of precision timing can be seen in Figure 1 from the MTD Technical Design Report [2]. The yellow vertical lines represent particle interactions in space along the beam-line z (x-axis) while the fourth dimension of time t is expanded along the (y-axis). When these spatial interactions are expanded in time, these yellow lines become blue dots, represented the reconstructed 4D vertices. Even visually, one can see that the blue dots are much more distinguishable from each other than the yellow lines. Even yellow lines overlapping with each other along z (x-axis) become separated vertically in time. The majority of the 4D reconstructed vertices have a time spread of about 200 ps. The goal timing resolution throughout the MTD, in both the barrel and endcap regions, is 30-40 ps, well within this 200 ps range.

Pileup mitigation effects from the MTD has many consequences, including improving b-tagging and lepton isolation, as well as increasing the effective luminosity of rarer signals, like Higgs decays. The MTD will also provide capabilities to do more extensive long-lived particle studies and heavy-ion/low p_T hadron studies.

2 MTD Endcap Structural Overview and Sensor Components

The MTD is comprised of two main sections: the Barrel Timing Layer (BTL) and the Endcap Timing Layer (ETL). The whole detector will be installed between the CMS inner tracker and calorimeters before the beginning of Phase-2 (the HL-LHC era). The ETL structure is a double disk, hermetically sealed as shown in Figure 2a [2], for each endcap. All in all, there will be about 15 m^2 of silicon with ∼10 million readout channels for the whole ETL.

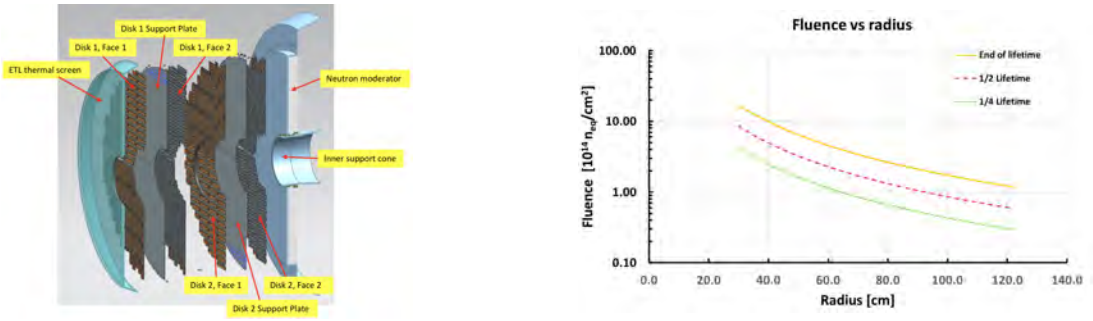

(a) (b)

Figure 2: MTD ETL structure (left) and fluence levels (right) at certain points in the MTD lifetime from the MTD TDR.

The ETL will be comprised of silicon low gain avalanche detectors (LGADs). These LGADs have a p-type gain layer, creating a high electric field, which is cascaded into a current when a minimum ionizing particle passes through. As the name implies, these silicon sensors have a low gain, on the order of 10-30, which is sufficient enough to provide appropriate signal sizes even with thin charge collection (depletion) regions. These thin charge collection (depletion) regions provide fast charge collection

Not only do these sensors have to have a time resolution on the order of 30-40 ps, they also have to be efficient throughout the whole sensor and radiation hard through the entire CMS detector. The closer to the beam line these sensors are, the more radiation the sensors will experience. The sensors will also have had experienced more radiation at the end of life of the MTD. These radiation amounts can be seen in Figure 2b [2]. For the Fermilab test beam, three amounts of fluence were chosen to irradiate the sensors at to simulate detectors at the beginning, middle, and end of the MTD lifetime. These fluences can also correspond to radiation amounts experienced at different areas of the detectors at different points in the lifetime. Our fluence levels are 1.5 $\times 10^{15}$ n_{eq}/cm^2 (high, end of lifetime <40 cm from beamline), 4 $\times 10^{14}$ n_{eq}/cm^2 (medium, end of lifetime $\sim$70 cm from beamline, 1/2 of lifetime $\sim$30 cm from beamline, 1/4 of lifetime <40 cm from beamline), and 0 n_{eq}/cm^2 (beginning of lifetime).

3 Fermilab Test Beam Set-Up

In order to analyze the performance of these LGAD sensors, the Fermilab test beam set-up included a strip tracker (before and after the sensors), pixel trackers, and a scintillator trigger. For these studies, we used a 120 GeV proton beam. The LGADs are housed between the trigger and the end strip trackers in a cold box with the timing reference, a microchannel plate (MCP), which is a precision timing detector. This detector is a precision timing detector, with a known resolution of less than 7 ps [3]. The Fermilab test beam setup can be seen in Figure 3, with a picture of the set-up on the bottom and a cartoon rendering of the elements on top.

With this set-up, we were able to measure various properties of the LGAD sensor, including gain, amplitude, efficiency, and timing resolution. Using the MCP as a precision reference, we recorded the time difference (Δt) between the time of arrival hit on the LGAD and MCP. We plotted these differences and fit them to a Gaussian using an unbinned fit. The standard deviation of this fit (σ_t) is defined as our time resolution. Examples of these measurements can be seen in Figure 3.

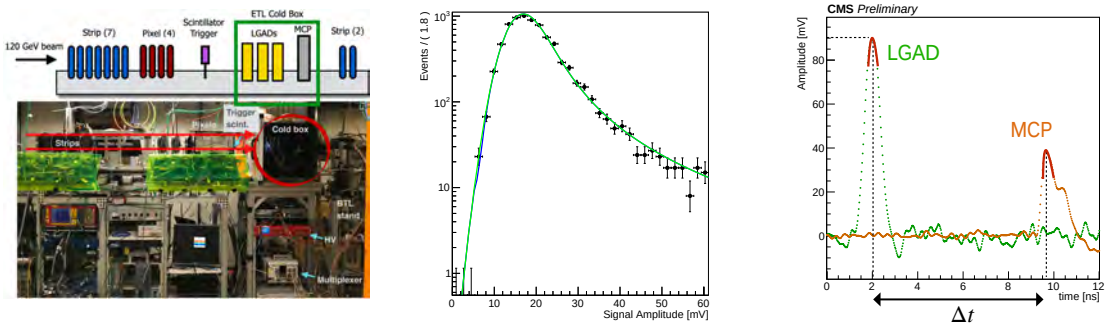

Figure 3: Fermilab test beam setup (left) and example measurements of amplitude (center) and time of arrival (right).

4 Performance of Silicon LGAD Sensors: Results from Test Beam Studies

Previously, studies have shown the timing resolution as a function of signal amplitude or bias voltage, which are also crucial estimating sensor performance [2]. Here we present timing resolution results as a function of position to analyze the uniformity of performance across the sensor. Using this set-up and the method described above, we were able to measure the timing resolution across the sensor in the x- and y-directions to create maps like the one in Figure 4. It is clear that not only do the sensors still perform well within the required range of 30-40 ps, but they achieve this resolution uniformly throughout the sensor. Also mapping the sensor in the $x - y$ plane, we were able to make efficiency maps, also shown in Figure 4 at medium fluence.

These sensors achieved ∼100% efficiency uniformly throughout the sensors at various levels of fluence, confirming their radiation tolerance.

One last aspect of LGAD performance we were able to study is the distance between pads on the sensors. Within these maps, one can see gaps in between the pads on the 4x4 channel sensors. It is important to characterize these gaps, or effective dead areas, because we will be receiving little to no signal in these areas. One of these measurements can be seen in Figure 5, showing efficiency as a function along a profile in y. This particular measurement on a highly irradiated sensor demonstrates that the interpad distance leads to a drop in efficiency on the order of ∼100 micrometers wide.

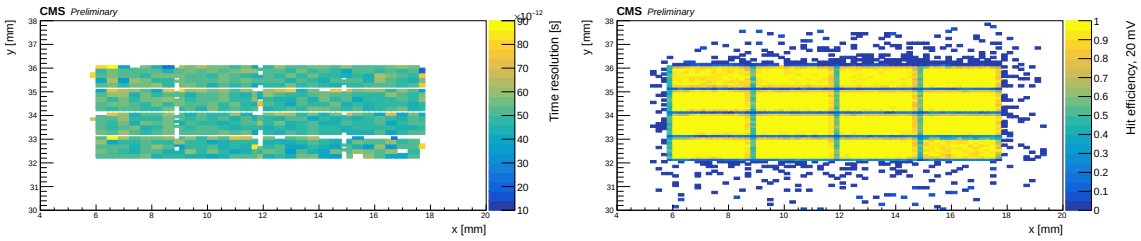

Figure 4: Timing resolution (left) and efficiency (right) maps at medium fluence level.

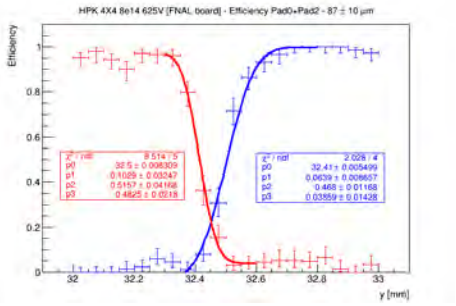

Figure 5: Measurement of distance between sensor pads.

5 Conclusions

With the advent of the HL-LHC era, the CMS detector will begin to employ technologies that adapt to the increase in pileup while still being sensitive to rare signals. The MIP Timing Detector will be a new addition to the CMS detector for this purpose. Comprised of barrel and endcap timing layers, the MTD will add a new layer of precision timing to resolve particle collisions. Here, we report measurements of the performance of the endcap timing layer sensors using a 120 GeV proton test beam. After extensive studies with the Fermilab test beam, we have concluded that these LGAD prototype sensors perform well within our requirements for the MTD. These sensors have demonstrated a uniform timing resolution of 30-40 ps, as well as uniform efficiency, at varied radiation levels. We were also able to measure the interpad distance of the sensors to characterize the effective dead area within the sensor.

Acknowledgements

I would like to thank the Madison and Lila Self Graduate Fund at the University of Kansas for their financial and professional support.

References

[1] **CMS** Collaboration, *The CMS experiment at the CERN LHC. The Compact Muon Solenoid experiment*, *JINST* **3** (2008) S08004. 361 p. Also published by CERN Geneva in 2010.

[2] **CMS** Collaboration, *A MIP Timing Detector for the CMS Phase-2 Upgrade*, Tech. Rep. CERN-LHCC-2019-003. CMS-TDR-020, CERN, Geneva, Mar, 2019.

[3] A. Ronzhin, S. Los, E. Ramberg, A. Apresyan, S. Xie, M. Spiropulu, and H. Kim, *Study of the timing performance of micro-channel plate photomultiplier for use as an active layer in a shower maximum detector*, *Nuclear Instruments and Methods in Physics Research Section A: Accelerators, Spectrometers, Detectors and Associated Equipment* **795** (2015) 288 – 292.

Cosmic-ray physics in ALICE at CERN

Emma González Hernández on behalf of the ALICE Collaboration

E-Mail: emma.gonzalez.hernandez@cern.ch

High Energy Physics Group, Universidad Autónoma de Puebla, Puebla, Mexico

Presented at the Workshop of QCD and Forward Physics at the EIC, the LHC, and Cosmic Ray Physics in Guanajuato, Mexico, November 18-21 2019

Abstract

ALICE is one of the four main experiments at the CERN Large Hadron Collider. The location of the ALICE detector allows us to study the muonic component of cosmic rays, since it is located 52 meters underground with 28 meters of rock above it. The ALICE detector is able to detect atmospheric muons from extensive air showers, making possible the study of topics related to cosmic-ray physics. At this depth, only atmospheric muons with energies greater than 16 GeV can reach the detection zone. The analysis of the multiplicity distribution of atmospheric muons reconstructed by the Time Projection Chamber (TPC) of ALICE is presented. The comparison with post LHC hadronic interaction models solves the long standing issue of the rate of events with an extremely large multiplicity of muons.

1 Introduction

In astroparticle physics, the identification and understanding of the sources of high-energy cosmic-rays is one of the most important open problems. Knowing the elemental composition of cosmic-ray particles arriving at the Earth is of crucial importance to understand the production and propagation of cosmic rays. Unfortunately, due to the low flux of cosmic rays at high energies, cosmic rays can be studied on Earth only with indirect measurements above an energy of 10^{14} eV through the cascades of secondary particles, called extensive air-showers (EAS), that they produce in the atmosphere [1].

With the operation of modern large-scale experiments such as accelerator experiments located underground a cosmic-ray physics program is possible at CERN. Experiments at the LHC are suitable for the study of properties of atmospheric muons.

The study of atmospheric muons using collider experiments started during the era of the Large Electron Positron collider by ALEPH [2], DELPHI [3] and L3 [4] experiments.The main contribution reported by the LEP experiments in the area of cosmic-ray physics was the measurement of the atmospheric muon momentum spectra and the detection of multi-muon events by the central barrel detectors, which at high multiplicities could not be described within the existing hadronic interaction models [5].

By measuring the atmospheric muon multiplicity distribution (MMD), LEP experiments concluded that the bulk of the data can be successfully described using standard hadronic production mechanisms. However, the events with a large number of reconstructed atmospheric muons occur with a frequency that is almost one order of magnitude above the simulation, even when assuming that the primary cosmic rays are purely composed of iron nuclei [2]. The Monte Carlo models at that time failed to describe the abundance of events with high multiplicity of muons [3].

2 Reconstruction of atmospheric muons in ALICE

ALICE is a general-purpose heavy-ion experiment designed to study the physics of strongly interacting matter and the quark–gluon plasma in nucleus–nucleus collisions at the LHC. Nevertheless, the large size and excellent tracking capability of the ALICE TPC (Time Projection Chamber) [6] is exploited to detect the muonic component of the EAS. The rock absorbs all of the electromagnetic and hadronic components of the EAS, while near vertical muons with a surface energy $E \geq 16$ GeV can reach the central barrel ALICE's detectors [7].

There are two main differences between particles coming from LHC collisions and atmospheric muons. A particle created in a collision passes very close to the centre of ALICE generating a track either in the upper half of the TPC or in the lower half. On the contrary, an atmospheric muon crosses the TPC everywhere (usually far from the centre of ALICE) and its track, in most cases, crosses the whole length, from one edge of the TPC to the other end. The TPC was used to reconstruct the trajectory of cosmic-ray muons passing through the active volume of the detector. Cosmic-ray muons are typically reconstructed as two separated tracks in the upper and lower halves of the TPC. We refer to these tracks as up and down tracks. An example of a single atmospheric muon event with both up and down tracks as shown in Fig. 1.

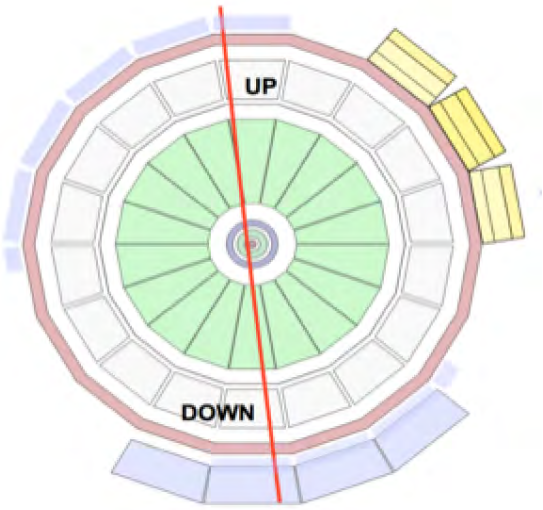

Figure 1: Track reconstruction of one single atmospheric muon with the TPC of ALICE.

Specific triggers were implemented to detect atmospheric muons crossing the central barrel of the ALICE apparatus. To trigger and measure cosmic-ray events, the ACORDE (Alice COsmic Ray DEtector) [8] and TOF (Time of Flight) [9] systems were used.

ACORDE [8] detects cosmic-ray showers by triggering the arrival of muons to the top of the ALICE magnet. It consists of an array of 60 scintillator modules located on the three top octants of the magnet. Atmospheric muons are also used for calibration and alignment of central barrel detectors. The time-of-flight detector is a cylindrical array of multi-gap resistive plate chambers completely surrounding the outer radius of the TPC. The trigger for cosmic-rays is given by a signal in the upper part of the detector in coincidence with a signal in the opposite lower part. A complete description of the apparatus is detailed in [9].

3 ALICE results on cosmic-ray physics

Between 2010 and 2013, ALICE collected 22.6 million events during the cosmic data taking sessions, corresponding to 30.8 days of effective time. Cosmic-ray data were acquired with a combination (logical OR) of the two trigger conditions: ACORDE and TOF.

The main topic related to cosmic-ray physics investigated by ALICE is the study of the muon-multiplicity distribution (MMD) and in particular of events with a large number of muons. The MMD measured by ALICE [10] is shown in Fig. 2. There are 5 events with a number of muons greater than 100.

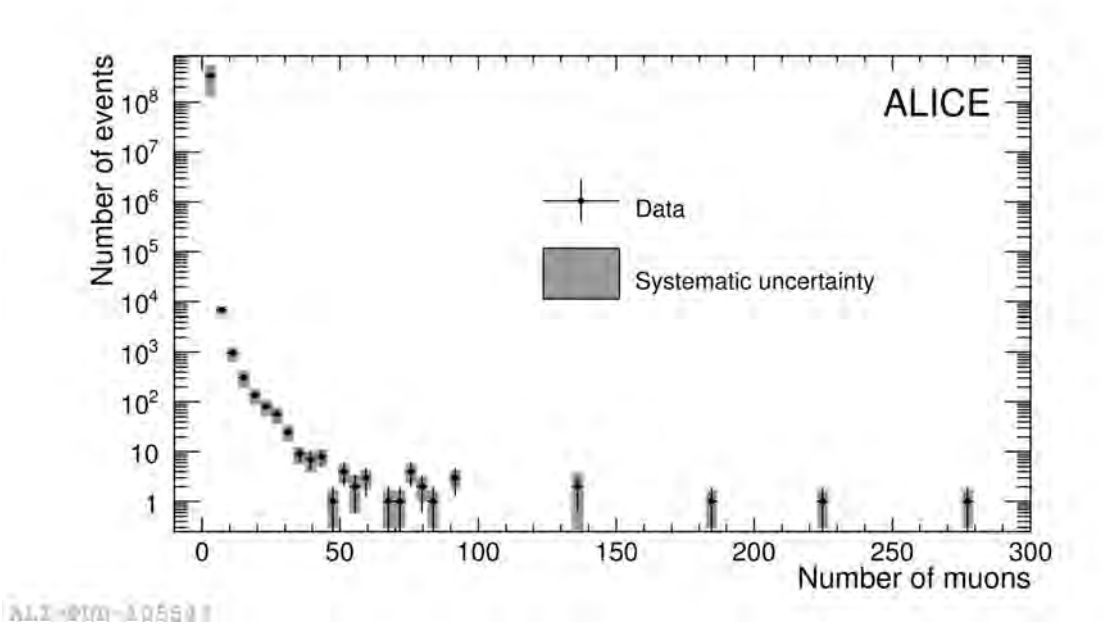

Figure 2: Atmospheric muon multiplicity distribution. Figure taken from [10].

To study the MMD, 30.8 days of data taking were simulated. The first step in the analysis of HMM events was to attempt to reproduce the measured MMD in the low range of multiplicity ($7 \leq N_\mu \leq 60$), using CORSIKA [11] version 6990 with QGSJET-II-03 model [12, 13].

The parameters used in the Monte Carlo simulations were the following:

- two independent samples: pure proton (lighter composition) and Fe (extremely heavy composition),
- energy of the primary cosmic-ray: $10^{14} < E < 10^{18}$ eV,
- the total (all-particle) flux of cosmic-rays with the poly-gonato model taken from [14]

- the core of each shower was scattered with a random flat distribution at surface level, in an area of 205 $\times$ 205 m^2 centered around the ALICE apparatus.

The comparison of the MMD between data and simulations is shown in Fig. 3. The MMD suggests that the average mass of primary cosmic rays increases with increasing energy. At lower multiplicities, corresponding to lower primary energies, ALICE reported that the data approach the proton curve, which represents a light ion composition of the primary cosmic ray flux, while higher multiplicity data lie closer to the iron curve, representing a heavier composition [10].

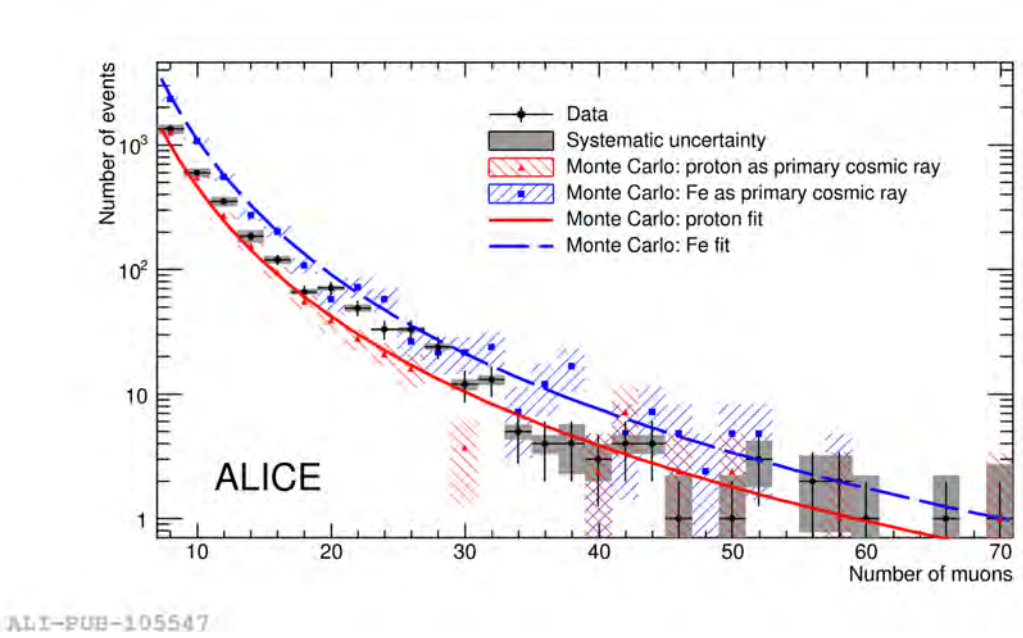

Figure 3: Atmospheric-muon multiplicity distribution of the data compared with the fit obtained with CORSIKA 6990 for proton (red line) and Fe (blue line). Figure taken from [10].

To estimate the rate of HMM events ($N_\mu > 100$) with Monte Carlo models, a simulation of five samples of one year of effective data taking was done using CORSIKA 6990 (QGSJET II-03) and 7350 (QGSJET II-04 tuned with LHC data) and with the energy of the primary cosmic-ray: $10^{16} < E < 10^{18}$ eV.

The final result on the rate of HMM events is summarized in Table 1. In the first line is given the average number of days to have an HMM event for a light composition of cosmic rays (proton), a heavy composition (iron), and data. The rate (number of HMM events per second) is written in the second line while the uncertainty is given in the last line. Independently of the model version, the model calculation of the rate of the HMM events with proton composition has difficulties to reproduce the measurement, while with iron the calculated rate is closer to the data. These results suggest that the HMM events are more likely due to heavy elements, although given the large uncertainties in the measured rate ($\sim 50\%$) a firm conclusion about the chemical elements that produced these events cannot yet be drawn.

HMM events	CORSIKA 6990 QGSJET II-03		CORSIKA 7350 QGSJET II-04		Data
	proton	iron	proton	iron	
Period (days per event)	15.5	8.6	11.6	6.0	6.2
Rate ($\times 10^{-}6$ Hz)	0.8	1.3	1.0	1.9	1.9
Uncertainty (%) (Total)	13	16	8	20	49

Table 1: Rate of HMM events. Table taken from [10].

4 Conclusions

Accelerator apparatuses are suitable for cosmic-ray physics: LEP experiments were the pioneers on this topic. ALICE at the LHC is now also contributing to this field. The MMD measured by ALICE is well reproduced at low and high multiplicities by new hadronic models implemented in CORSIKA 6990 (QGSJET II-03 model). ALICE results for low and intermediate multiplicities suggest a mixed-ion primary cosmic-ray composition with an average mass that increases with energy. This serves as a benchmark of the procedure and of the hadronic interaction models to proceed to the study of HMM events. In 30.8 days, ALICE found 5 HMM events ($N_\mu > 100$). This type of events was also found by ALEPH and DELPHI. The observed rate of HMM events is consistent with that predicted by CORSIKA 7350 (QGSJET II-04 model) using pure Fe composition and primary energy larger than 10^{16} eV.

This is the first time that the rate of HMM events is satisfactorily reproduced using conventional hadron interaction models (an observation that places significant constraints on alternative, more exotic, production mechanisms).

Acknowledgements

This work was supported by CONACyT Project grant number A1-S-13525. The authors thankfully acknowledge computer resources, technical advise and support provided by Laboratorio Nacional de Supercómputo del Sureste de México (LNS), a member of the CONACYT national laboratories, with project 2016/52.

References

[1] D. d'Enterria et al., *Constraints from the first LHC data on hadronic event generators for ultra-high energy cosmic-ray physics*, *Astropart. Phys.* **35** (2011) 98–113, [arXiv:1101.5596].

[2] V. Avati et al., *Cosmic multi-muon events observed in the underground CERN-LEP tunnel with the ALEPH experiment*, *Astropart.Phys.* **19** (2003) 513–523.

[3] **DELPHI** Collaboration, J. Abdallah et al., *Study of multi-muon bundles in cosmic ray showers detected with the DELPHI detector at LEP*, *Astroparticle Physics* **28** (2007) 273–286, [arXiv:0706.2561].

[4] **L3** Collaboration, P. Achard et al., *Measurement of the atmospheric muon spectrum from 20-GeV to 3000-GeV*, *Phys.Lett.* **B598** (2004) 15–32, [hep-ex/0408114].

[5] M. Rodríguez Cahuantzi, *Cosmic-ray physics at CERN*, *J. Phys.: Conf. Ser.* **866** (2017) 012013.

[6] J. Alme et al., *The ALICE TPC, a large 3-dimensional tracking device with fast readout for ultra-high multiplicity events*, *Nucl.Instrum.Meth.A* **622** (2010) 316–367, [arXiv:1001.1950].

[7] **ALICE** Collaboration, B. Alessandro et al., *ALICE: Physics performance report, volume II*, *J.Phys.* **G32** (2006) 1295–2040.

[8] **ACORDE** Collaboration, A. Fernandez et al., *ACORDE a Cosmic Ray Detector for ALICE*, *Nucl.Instrum.Meth. (2007) 102-103* **A572** (2007) 102–103.

[9] **ALICE** Collaboration, K. Aamodt et al., *The ALICE experiment at the CERN LHC*, *JINST* **3** (2008) S08002, [physics/0606051 [physics.ins-det]].

[10] **ALICE** Collaboration, J. Adam et al., *Study of cosmic ray events with high muon multiplicity using the ALICE detector at the CERN Large Hadron Collider*, *JCAP* **01** (2016) 032, [arXiv:1507.07577].

[11] D. Heck et al., *CORSIKA: A Monte Carlo code to simulate extensive air showers*, *FZKA-6019* (1998) 90.

[12] S. Ostapchenko, *Nonlinear screening effects in high energy hadronic interactions*, *Phys. Rev. D* **74** (2006) 151.

[13] K. Boruah, *Comparison of EPOS and QGSJET-II in EAS Simulation using CORSIKA*, arXiv:1202.3661.

[14] J. R. Hoerandel, *On the knee in the energy spectrum of cosmic rays*, *Astropart.Phys.* **19** (2003) 193–220, [astro-ph/0210453].

Photohadronic origin of multi-TeV flarings from high energy peaked blazars

Sarira Sahu, Carlos E. López Fortín*, Shigehiro Nagataki

***E-Mail: carlos.fortin@correo.nucleares.unam.mx**

Instituto de Ciencias Nucleares UNAM

Presented at the Workshop of QCD and Forward Physics at the EIC, the LHC, and Cosmic Ray Physics in Guanajuato, Mexico, November 18-21 2019

Abstract

VHE flaring events have been observed to be a predominant event of the activity of high energy peaked blazars (HBLs). These flaring epochs involve energies in the GeV-TeV range and different timescales, yet their emission mechanisms are still not well understood. The emitted γ-rays en route to Earth undergo energy-dependent attenuation due to the interaction with extragalactic background light. Considering the photohadronic model where Fermi-accelerated protons interact with the seed photons in a double jet scenario, we derived a simple relation for the observed multi-TeV γ-ray flux as a function of two free parameters. We studied 42 flaring epochs from 23 HBLs and found that our model accurately describes the observed VHE spectra for all these cases, supporting the photohadronic origin of multi-TeV γ-rays. Moreover, this model allows to constrain the power spectrum of seed photons during the flaring period even if the simultaneous spectral energy distribution is unknown. We also used this model to set stringent bounds on the redshifts of two HBLs with unknown distances but observed multi-TeV spectra.

1 Introduction

Blazars are a subclass of active galactic nuclei (AGNs) characterized by a non-thermal emission that spans across all the electromagnetic spectrum, with a flux variability that ranges from minutes to days [1]. They stand out in observations due to the fact that their jets are point or closely pointed towards Earth, which is responsible for their very high luminosity and the relativistic beaming of energy [2]. Blazars possess a spectral energy distribution (SED) characterized by two peaks in its flux. The first peak, in the IR to X-ray range, is produced by the synchrotron emission of relativistic electrons accelerated in the jet. The second peak, in the X-ray to γ-ray range, is generally understood to be the result of the scattering of high energy electrons with the self-produced synchrotron photons in the jet (Self-Synchrotron Compton, SSC) [3, 4] or from external nearby sources such as photons from the accretion risk, broad line regions, or the dusty torus (External Compton, EC) [5, 6]. Leptonic models have been widely successful in explaining the multiwavelength emission from blazars [7, 8]. Depending on the location of these two peaks in the energy

range, blazars are classified as: flat-spectrum radio quasars (FSRQs), low energy peaked blazars (LBLs), intermediate energy peaked blazars (IBLs), high energy peaked blazars (HBLs), and extreme high energy peaked blazars (extreme HBLs) [9]. Other classification schemes have also been proposed.

Flaring events in GeV-TeV energies seem to be a predominant component of the activity of blazars [10]. Mrk 421 was the first and nearest HBL to be detected in TeV energies by the Whipple telescopes [11], and other Imaging Atmospheric Cherenkov Telescopes (IACTs) such as VERITAS and MAGIC have been successful in observing several more blazars such as Mrk 501 and 1ES 0229+200 in the very high energy (VHE) range [12, 13]. Flarings have been observed to be unpredictable and to oscillate rapidly between active and quiescent states for different timescales [10]. In many cases, a strong temporal correlation between X-rays and multi-TeV γ-rays has been observed, as predicted by the standard one-zone leptonic models. However, the detection of multi-TeV γ-rays without simultaneous X-ray counterpart during other flarings (orphan flarings) is difficult to explain in the previous scenario [14, 15]. Two-zone leptonic models as well as hadronic and hybrid ones have been developed to explain these observations [8, 16–18]. Multiple multi-wavelength campaigns have been performed to reconstruct the SED of these flarings in order to constrain these theoretical models [10, 19].

In the following work, we analyze the reconstructed VHE γ-ray spectra of 42 flaring events from 23 HBLs and use the photohadronic model to describe the observations.

2 Photohadronic model

In the photohadronic scenario, the observed VHE γ-ray emission is predominantly accounted by the decay of neutral pions produced from a pγ interaction [20, 21]. In this scenario, Fermi-accelerated protons interact with the background seed photons in the jet to produce a Δ resonance ($\sigma_\Delta = 5 \times 10^{-28}\mathrm{cm}^{-2}$), which subsequently decays as,

$$p + \gamma \rightarrow \Delta \rightarrow \begin{cases} p\pi^0 & (\text{fraction } 2/3) \\ n\pi^+ & (\text{fraction } 1/3) \end{cases} \tag{2.1}$$

where $2/3$ and $1/3$ are the branching ratios. The neutral and charged pions subsequently decay into γ-rays and neutrinos, i.e., $\pi^0 \rightarrow \gamma\gamma$ and $\pi^+ \rightarrow e^+\nu_e\nu_\mu\bar{\nu_\mu}$. The kinematical condition for the above process is given by [21],

$$E_\gamma \epsilon_\gamma = \frac{0.032\Gamma\Delta}{(1+z)^2} GeV^2 \tag{2.2}$$

where Γ, Δ, and z are the bulk Lorentz factor, Doppler factor, and redshift, respectively. E_γ and ϵ_γ are the γ-ray and seed photon energy in the observer's frame, respectively.

The photohadronic model relies on the standard leptonic interpretation for the origin of the synchrotron and SSC peaks in blazars, in particular for HBLs [21]. The flaring is assumed to occur within a compact and confined volume of size R'_f inside a blob of radius R'_b (where the prime denotes the jet co-moving frame). In a canonical jet scenario, the production of Δ resonance is low due to low photon density in the jet, and thus super-Eddington power for the proton must be invoked [22]. To avoid this scenario, a double-jet structure for the HBL is proposed: a compact, inner jet of high photon density ($n_{\gamma,f}$) is enclosed by an outer jet of lower photon density (n_γ). The inner and outer jet move with almost the same bulk Lorentz factor as the blob $\Gamma_{in} \approx \Gamma_{out} \approx \Gamma$. The geometry of this structure is shown in Fig. 1 of [21]. In HBLs, it is generally observed that $\mathcal{D} \approx \Gamma$. This composite structure is supported by simulation of similar models [23].

The stability of the jet on large scales during the flaring epoch can be estimated from the ratio σ of the magnetic stress and the kinetic stress. Considering the typical values in HBLs for the magnetic field $B \sim 1$G, proton density $n_p \sim 10^{-1} - 10^{-2}\mathrm{cm}^{-3}$, and bulk Lorentz factor $\Gamma \sim 10$, we get $\sigma \sim 0.4$ which corresponds to a stable inner jet [ref]. The inner photon density is constrained by comparing the jet expansion timescale t'_d with the $p\gamma$ interaction timescale $t'_{p\gamma}$ and by taking into account that the high energy proton luminosity must be smaller than the Eddington luminosity [18].

The produced VHE γ-rays can in principle interact with the background low-energy photons in the jet through electron-positron pair production ($\gamma\gamma \rightarrow e^+e^-$). Nevertheless, it has been observed that the jet medium is transparent to this attenuation where the optical depth ($\tau_{\gamma\gamma}$) is small [24]. However, propagating γ-rays en route to Earth are known to undergo energy-dependent attenuation via the same process through the interaction with extragalactic background light (EBL) [19, 25, 26]. This attenuation significantly modifies the shape of the VHE spectrum and therefore a proper modeling of the EBL SED is fundamental to understand the observed multi-TeV emission. Well-known models are widely used in the description of these VHE phenomena [19, 26].

To reconstruct the observed VHE γ-ray flux F_γ, we observe that it must be proportional to the proton fluxas well as the background seed photon inner density, that is, $F_\gamma \propto F_p n'_{\gamma,f} \propto E_p^2 \frac{dN}{dE_p} n'_{\gamma,f}$. Fermi-accelerated protons have a well known power-law spectrum, $F_p \propto E_p^{-\alpha+2}$, where α is the proton spectral index and $\alpha \geq 2.0$ [27]. Due to adiabatic expansion of the inner jet, its photon density decreases as it crosses into the outer jet. As the inner photon density cannot be directly known a priori, a scaling behavior is assumed between the photon densities of the inner and outer regions, i.e., they have the same slope [21]. As the outer photon density is known to be inversely proportional to the seed photon energy ϵ_γ and proportional to its flux $\Phi(\epsilon_\gamma)$, and using the scaling behavior 2.2, we can express the inner photon density as $n'_{\gamma,f} \propto \Phi(\epsilon_\gamma)\epsilon_\gamma$.

Combining the previous assumptions and taking into account the EBL attenuation, the observed flux is given by,

$$F_\gamma(E_\gamma) = A_\gamma \Phi_{SSC}(\epsilon_\gamma) \left(\frac{E_\gamma}{TeV}\right)^{-\alpha+3} e^{-\tau_{\gamma\gamma}(E_\gamma,z)} \tag{2.3}$$

where A_γ is proportionality constant. The photohadronic model has been previously used to describe the flaring events of several HBLs [20, 21, 28]. In all cases, it has been observed that ϵ_γ always falls in the tail region of the SSC SED, which is not observed due to technical limitations. However, leptonic models have predicted that this tail region is a perfect power-law given by $\Phi_{SSC} \propto \epsilon_\beta$, or using 2.2, $\Phi_{SSC} \propto E_\gamma^{-\beta}$, where β is the seed photon spectral index. Substituting this in 2.3, we arrive at a very straightforward relation for the observed VHE γ-ray flux,

$$F_\gamma(E_\gamma) = F_\gamma^{int} e^{-\tau_{\gamma\gamma}(E_\gamma,z)} = F_0 \left(\frac{E_\gamma}{TeV}\right)^{-\delta+3} e^{-\tau_{\gamma\gamma}(E_\gamma,z)} \tag{2.4}$$

where F_0 is a proportionality factor fixed from the observed VHE spectrum and $\delta = \alpha + \beta$ is the spectral index of the photohadronic model. Here, it is not necessary to know a priori the value of β and thus this model is independent of simultaneous SED modelling. Furthermore, the intrinsic flux follows a single power-law characterized by δ, while the differential intrinsic flux spectral index is $\delta_{int} = -\delta + 1$.

3 Multi-TeV flarings

We extracted the data of 42 flaring epochs of 23 HBLs of different redshifts and applied equation 2.4 to describe their observed VHE spectra. We fitted F_0 and δ using a standard minimization of

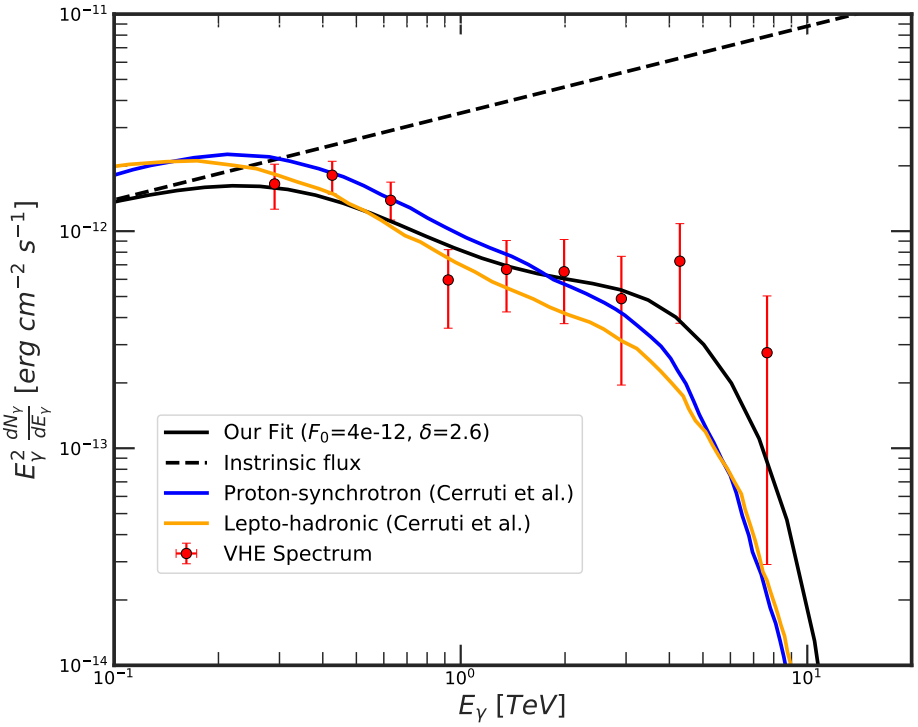

Figure 1: **Multi-TeV SED of 1ES 0229+200**. The VHE spectrum (red points) of 1ES 0229+200 corresponding to the flaring reported between October 2009 and January 2013 [13]. The best fit for the photohadronic model is obtained for $\delta = 2.6$, $F_0 = 3.5 \times 10^{-12}$ erg cm^{-2} s^{-1}. For comparison the proton-synchrotron and lepto-hadronic models of Cerruti et al. [17] are shown.

the cost function and found that the photohadronic model explains very well all these observations with the spectral index δ in the range $2.5 \leq \delta \leq 3.0$. Depending on the value of δ and by comparing with the VHE observations, we were able to roughly classify the flarings into three different states: (i) low state, with $\delta = 3.0$, (ii) high states, with $2.6 < \delta < 3.0$, and (iii) very high state, with $2.5 \leq \delta \leq 2.6$. As we know that $\alpha \geq 2.0$, this constrains the seed photon spectral index β for simultaneous multiwavelength observations in the range $0.0 \leq \beta \leq 1.0$. We briefly adress two of these flaring episodes and compare it with other current theoretical models. The rest of our results are presented in Table 1. For the EBL correction we consider the model of Franchescini et al. [26].

3.1 1ES 0229+200

1ES 0229+200 is a HBL located at $z = 0.1396$ discovered in the Einstein IPC Slew Survey of 1992 [29]. It was observed by VERITAS telescopes during a long-term observation campaign between October 2009 and January 2013, for a total exposure time of 54.3 hours [13]. The observed VHE observations were reported in an energy range 0.29 TeV $\leq E_\gamma \leq 7.6$ TeV. Cerruti et al. [17] explained the observed multiwavelength SED using both a proton-synchrotron and leptohadronic scenario, where the dominant emission in the last one comes from secondary particles product of $p\gamma$ interactions. However, this model uses 19 parameters to fit the entire SED, which limits its predictive power, and the proton-synchrotron scenario requires magnetic fields in the range

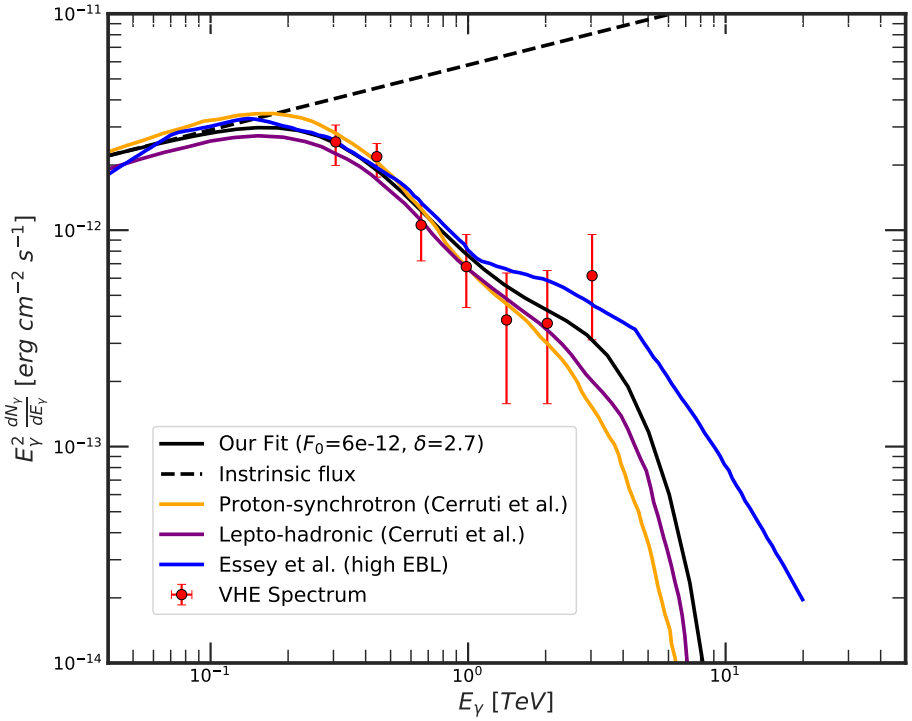

Figure 2: **Multi-TeV SED of 1ES 0347-121**. The VHE spectrum (red points) of 1ES 0347-121 corresponding to the flaring reported between October 2009 and January 2013 [30]. The best fit for the photohadronic model is obtained for $\delta = 2.7$, $F_0 = 6.0 \times 10^{-12}$ erg cm^{-2} s^{-1}. For comparison the proton-synchrotron and lepto-hadronic models of Cerruti et al. [17] are also shown, as well as the hadronic model of Essey et al. [16].

$1-160$ G. Using the photohadronic model, we described the observed VHE spectrum with $\delta = 2.6$ and $F_0 = 3.5 \times 10^{-12}$ erg cm^{-2} s^{-1}, which corresponds to a very high emission state. As the photohadronic model only has two free parameters, it greatly improves its predictive capability and understanding. The intrinsic flux follows $F_\gamma^{int} \propto E_\gamma^{0.4}$. Similarly, the differential spectrum follows $(dN_\gamma/dE_\gamma)_{int} \propto E_\gamma^{-1.6}$ which shows that this spectrum is not hard. Both our model and the one of Cerruti et al. are shown in Figure 1. We see that they are very similar below 2 TeV and slightly differ afterwards.

3.2 1ES 0347-121

1ES 0347-121 is a HBL with a redshift $z = 0.188$. It was observed by HESS telescopes between August and December 2006 for a total exposure time of 25.4 hours [30], and was detected in VHE γ-rays in the energy range 0.25 TeV $\leq E_\gamma \leq 3$ TeV. Essey et al. [16] explained this flaring and two others (1ES 0229+200 and 1ES 1101-232) using a hadronic scenario, where ultra high energy protons escaping from the jet produce secondary VHE γ-rays by interacting with the cosmic microwave background (CMB) and/or EBL. This scenario requires protons in the energy range $10^8 - 10^{10}$ GeV, which are difficult to produce in the jet environment of the HBL, as well as weak extragalactic magnetic fields ($10^{-17} - 10^{-14}$ G). Cerruti et al. [17] also applied a proton-synchrotron

model (with a magnetic field of $1 - 296$ G) as well as 19-parameter leptohadronic model to explain the same VHE spectrum. Using the photohadronic model, we found that the VHE spectrum is best fitted for $\delta = 2.7$ and $F_0 = 6.0 \times 10^{-12}$ erg cm^{-2} s^{-1}, which corresponds to a high state. This corresponds to an intrinsic flux $F_\gamma^{int} \propto E_\gamma^{0.3}$. As the γ-ray carries 10% of the proton energy, the maximum photon energy of 3 TeV corresponds to a 30 TeV proton energy which is easily produced in the HBL jet. We show our model along with the one of Cerruti et al. and Essey et al. in Figure 2. Below 1 TeV we observe that all have similar behaviors.

4 Other flarings

We show in Table 1 the results for the rest of the flaring events of different HBLs for our photohadronic modeling. From a statistical point of view, 48% of these states are low, 38% are high, and 14% are very high, implying that low and high states constitute the major type of flarings in HBLs. A more exhaustive presentation as well as a detailed list of references for each flaring epoch has been published in [28].

5 Discussions

HBLs are important sources of VHE γ-rays and are known to undergo flaring events at different time-scales and fluxes. Their emission mechanisms at these energies are still highly debated, with leptonic, hadronic, and hybrid models being proposed as potential explanations. Most of these models are characterized for having a large parameter space which limits their predictability power, and those with less parameters usually face difficulties such as having large magnetic fields or invoking super-Eddington luminosity. Moreover, the propagating VHE γ-rays suffer energy-depending attenuation on their way to Earth due to the effect of EBL.

In this work we propose a photohadronic scenario by considering that Fermi-accelerated protons interact with the seed background photons of an inner jet with high photon density, producing a Δ resonance which subsequently decays into γ-rays and neutrinos via intermediate π^0 and π^+ particles, respectively. Based on previous works regarding the shape of the SSC SED and considering the EBL model from Francheschini et al., we were able to derive a simple power-law for the observed VHE γ-ray flux which only depends on two free parameters, a proportionality constant F_0 and the spectral index δ. We applied this relation to study 42 flaring events from 23 HBLs and found that it accurately describes their observed VHE spectra, from which we presented here 7 of these flarings. According to our analysis, the spectral index is roughly constrained in the range $2.5 \leq \delta \leq 3.0$, and depending on the value of δ the state can be classified into low, high, and very high state.

It is important to note that the photohadronic scenario has only been observed to be valid for energies $E_\gamma \geq 100$ GeV, as other contributions may come into play at lower energies, e.g., contributions of leptonic origin. Furthermore, in some cases the averaging of long-term VHE observations is difficult to explain likely due to the averaging of many unobserved short flarings with low emission periods that contaminate the data, as well as the mentioned contribution of leptonic processes in the low energy regime.

Finally, it is worth mentioning that since the proton spectral index $\alpha \geq 2.0$, this models allows to constrain the seed photon index β without a priori knowledge of the simultaneous SED, which has so far been a limitation in the accurate description of the observed VHE spectra in some SSC models. Moreover, the photohadronic scenario only relies on the assumption about the shape of the tail of the SSC SED and the scaling behavior, both of which are reasonable in the jet environment during the flaring epoch. Henceforth, the photohadronic model is a very powerful candidate in describing the origin of multi-TeV γ-ray emission from HBLs.

Name	Redshift(z)	Period	$F_{0,11}$	δ	State
Mrk 421	0.031	2004	51.3	2.95	High
		22 Apr 2006	5.2	2.95	High
		24 Apr 2006	10.7	3.0	Low
		25 Apr 2006	6.9	2.95	High
		26 Apr 2006	5.2	3.0	Low
		27 Apr 2006	16	2.95	High
		28 Apr 2006	5.0	3.0	Low
		29 Apr 2006	4.9	3.0	Low
		30 Apr 2006	13.5	2.5	Very High
		16 Feb 2010	12	3.0	Low
		17 Feb 2010	1.5	3.0	Low
		10 Mar 2010	21	2.6	Very High
		10 Mar 2010	16.5	3.0	Low
		28 Dec 2010	6.7	3.00	Low
Mrk 501	0.034	22 - 27 May 2012	6.3	2.9	High
		23 - 24 Jun 2014	28	2.93	High
1ES 2344+514	0.044	4 Oct 2007 - 11 Jan 2008	0.8	3.0	Low
1ES 1959+650	0.048	May 2002	12	3.0	Low
		Nov 2007 - Oct 2013	2.2	3.0	Low
		21-27 May 2006	1.1	3.0	Low
		20 May 2012	80	2.9	High
1ES 1727+502	0.055	1-7 May 2013	0.9	3.0	Low
1ES 1312-423	0.105	Apr 2004 - Jul 2010	0.20	3.0	Low
B32247+381	0.119	30 Sep - 30 Oct 2010	0.17	3.0	Low
RGB J0710+591	0.125	Dec 2008 - Mar 2009	0.5	2.9	High
1ES 1215+303	0.131	Jan - Feb 2011	90	3.0	Low
1ES 0806+524	0.138	Jan - Mar 2011	1.2	2.9	High
1RXS J101015.9-311909	0.14	Aug 2008 - Jan 2011	0.2	2.8	High
1ES 0229+200	0.14	2005 - 2006	0.4	2.5	Very High
H 2356-309	0.165	Jun - Dec 2004	0.3	2.9	High
1ES 1218+304	0.182	Dec 2008 - 2013	1.5	2.9	High
1ES 1101+232	0.186	2004 - 2005	0.60	2.75	High
1ES 1011+496	0.212	6 Feb - 7 Mar 2014	8.2	3.0	Low
1ES 0414+009	0.287	Aug 2008 - Feb 2011	0.70	2.9	High
PG 1553+113	0.50	26 - 27 Apr 2012	48	2.5	Very High
RGB J0152+017	0.80	30 Oct - 14 Nov 2007	0.3	3.0	Low
HESS J1943+213	$0.14 \leq z \leq 0.19$	May - Jun 2014, Apr - Nov 2015	0.69	2.8	High
PKS 1440-389	$0.14 \leq z \leq 0.24$	29 Feb - 27 May 2012	0.90	3.0	Low
RGB J2243+203	$0.75 \leq z \leq 1.1$	21 - 24 Dec 2014	0.28	2.6	Very High

Table 1: The results of photohadronic modeling for the modeling of additional HBL flaring events are shown. The normalization factor (4th column) is expressed in units $F_{0,11} = 1.0 \times 10^{-11}\,\mathrm{erg\,cm^{-2}\,s^{-1}}$.

Acknowledgements

The research of C.E.L.F. is supported by the CONACYT National Graduate Fellowship Program. S.S. is partially supported by DGAPA-UNAM (Mexico) Project No. IN103019. S.N. is partially supported by JSPS Grants-in-Aid for Scientific Research <KAKENHI> (A) 19H00693", Pioneering Program of RIKEN for Evolution of Matter in the Universe (r-EMU)", and Interdisciplinary Theo-

retical and Mathematical Sciences Program of RIKEN". I would like to thank the PAEP program of ICN-UNAM (*Instituto de Ciencias Nucleares*) for financial support in attending this conference as well as S.S. for covering registration and additional travel expenses.

References

[1] G. Romero, M. Boettcher, S. Markoff, and F. Tavecchio, *Relativistic Jets in Active Galactic Nuclei and Microquasars*, *Space Sci. Rev.* **207** (2017), no. 1-4 5–61, [arXiv:1611.09507].

[2] C. Urry and P. Padovani, *Unified schemes for radio-loud active galactic nuclei*, *Publ. Astron. Soc. Pac.* **107** (1995) 803, [astro-ph/9506063].

[3] L. Maraschi, G. Ghisellini, and A. Celotti, *A jet model for the gamma-ray emitting blazar 3C 279*, *Astrophys. J. Lett.* **397** (1992) L5–L9.

[4] H. Gao, W.-H. Lei, and B. Zhang, *Compton Scattering of Self-Absorbed Synchrotron Emission*, *Mon. Not. Roy. Astron. Soc.* **435** (2013) 2520, [arXiv:1204.1386].

[5] M. Sikora, M. C. Begelman, and M. J. Rees, *Comptonization of diffuse ambient radiation by a relativistic jet: The source of gamma rays from blazars?*, *Astrophys. J.* **421** (1994) 153.

[6] M. Blazejowski, M. Sikora, R. Moderski, and G. Madejski, *Comptonization of infrared radiation from hot dust by relativistic jets in quasars*, *Astrophys. J.* **545** (2000) 107, [astro-ph/0008154].

[7] F. Tavecchio, G. Ghisellini, G. Bonnoli, and L. Foschini, *Extreme TeV blazars and the intergalactic magnetic field*, *Mon. Not. Roy. Astron. Soc.* **414** (2011) 3566, [arXiv:1009.1048].

[8] M. Boettcher, A. Reimer, K. Sweeney, and A. Prakash, *Leptonic and Hadronic Modeling of Fermi-Detected Blazars*, *Astrophys. J.* **768** (2013) 54, [arXiv:1304.0605].

[9] A. Abdo et al., *The Spectral Energy Distribution of Fermi bright blazars*, *Astrophys. J.* **716** (2010) 30–70, [arXiv:0912.2040].

[10] G. Sentürk, M. Errando, M. Böttcher, and R. Mukherjee, *Gamma-Ray Observational Properties of TeV-Detected Blazars*, *Astrophys. J.* **764** (2013) 119, [arXiv:1301.3697].

[11] M. Punch et al., *Detection of TeV photons from the active galaxy Markarian 421*, *Nature* **358** (1992) 477–478.

[12] **MAGIC, VERITAS** Collaboration, M. Ahnen et al., *Multiband variability studies and novel broadband SED modeling of Mrk 501 in 2009*, *Astron. Astrophys.* **603** (2017) A31, [arXiv:1612.09472].

[13] E. Aliu et al., *A three-year multi-wavelength study of the very-high-energy γ-ray blazar 1ES 0229+200*, *Astrophys. J.* **782** (2014), no. 1 13, [arXiv:1312.6592].

[14] H. Krawczynski et al., *Multiwavelength observations of strong flares from the TeV - blazar 1ES 1959+650*, *Astrophys. J.* **601** (2004) 151–164, [astro-ph/0310158].

[15] M. Blazejowski et al., *A Multi-wavelength view of the TeV blazar Markarian 421: Correlated variability, flaring, and spectral evolution*, *Astrophys. J.* **630** (2005) 130–141, [astro-ph/0505325].

[16] W. Essey, O. Kalashev, A. Kusenko, and J. F. Beacom, *Role of line-of-sight cosmic ray interactions in forming the spectra of distant blazars in TeV gamma rays and high-energy neutrinos*, *Astrophys. J.* **731** (2011) 51, [arXiv:1011.6340].

[17] M. Cerruti, A. Zech, C. Boisson, and S. Inoue, *A hadronic origin for ultra-high-frequency-peaked BL Lac objects*, *Mon. Not. Roy. Astron. Soc.* **448** (2015), no. 1 910–927, [arXiv:1411.5968].

[18] S. Sahu, L. S. Miranda, and S. Rajpoot, *Multi-TeV flaring from blazars: Markarian 421 as a case study*, *Eur. Phys. J. C* **76** (2016), no. 3 127, [arXiv:1501.00973].

[19] A. Dominguez et al., *Extragalactic Background Light Inferred from AEGIS Galaxy SED-type Fractions*, *Mon. Not. Roy. Astron. Soc.* **410** (2011) 2556, [arXiv:1007.1459].

[20] S. Sahu, A. R. de León, and L. S. Miranda, *Photohadronic scenario in interpreting the February–March 2014 flare of 1ES 1011+496*, *Eur. Phys. J. C* **77** (2017), no. 11 741, [arXiv:1610.01709].

[21] S. Sahu, *Multi-TeV flaring in nearby High Energy Blazars: A photohadronic scenario*, *Rev. Mex. Fis.* **65** (2019), no. 4 307–320, [arXiv:1907.01174].

[22] G. Cao and J. Wang, *The Hadronic Origin of the Hard Gamma-Ray Spectrum from Blazar 1ES 1101-232*, *Astrophys. J.* **783** (2014) 108, [arXiv:1401.3970].

[23] G. Ghisellini, F. Tavecchio, and M. Chiaberge, *Structured jets in TeV BL Lac objects and radiogalaxies: Implications on the observed properties*, *Astron. Astrophys.* **432** (2005) 401–410, [astro-ph/0406093].

[24] **LAT, MAGIC, VERITAS** Collaboration, A. Abdo et al., *Insights Into the High-Energy Gamma-ray Emission of Markarian 501 from Extensive Multifrequency Observations in the Fermi Era*, *Astrophys. J.* **727** (2011) 129, [arXiv:1011.5260].

[25] F. W. Stecker, O. C. de Jager, and M. H. Salamon, *TeV gamma rays from 3C 279 - A possible probe of origin and intergalactic infrared radiation fields*, *Astrophys. J. Lett.* **390** (1992) L49.

[26] A. Franceschini, G. Rodighiero, and M. Vaccari, *The extragalactic optical-infrared background radiations, their time evolution and the cosmic photon-photon opacity*, *Astron. Astrophys.* **487** (2008) 837, [arXiv:0805.1841].

[27] C. D. Dermer and R. Schlickeiser, *Model for the high-energy emission from blazars*, *Astrophys. J.* **416** (1993) 458.

[28] S. Sahu, C. E. López Fortín, and S. Nagataki, *Multi-TeV flaring from high energy blazars: An evidence of the photohadronic process*, *Astrophys. J. Lett.* **884** (2019), no. 1 L17, [arXiv:1909.10634].

[29] J. F. Schachter et al., *Ten new BL Lacertae objects discovered by an efficient X-ray/radio/optical technique*, *Astrophys. J.* **412** (1993), no. 541.

[30] **H.E.S.S.** Collaboration, F. Aharonian et al., *Discovery of VHE gamma-rays from the distant BL Lac 1ES 0347-121*, *Astron. Astrophys.* **473** (2007) L25–L28, [arXiv:0708.3021].

Review of results on forward physics and diffraction by CMS

Cristian Baldenegro
(on behalf of the CMS Collaboration)

E-Mail: c.baldenegro@cern.ch

University of Kansas

Presented at the Workshop of QCD and Forward Physics at the EIC, the LHC, and Cosmic Ray Physics in Guanajuato, Mexico, November 18-21 2019

Abstract

Results by the CMS Collaboration on forward physics, diffraction, and physics in the small-x limit of quantum chromodynamics (QCD), are presented. In particular, results on azimuthal angle decorrelations between two jets in events where two outermost jets are separated by a large rapidity interval are discussed. In addition, results based on the production of two jets separated by a large rapidity gap (interval void of radiation) are presented. These dijet production processes are expected to be sensitive to Balitsky-Fadin-Kuraev-Lipatov (BFKL) evolution effects. We highlight results on inclusive forward jet production and on exclusive vector meson production in proton-lead collisions, which access gluon densities in the small-x and Q^2 where saturation effects may play a role. A summary of results on underlying event activity studies based on inclusive Z boson production, charged particle spectra in minimum bias events, and energy density in forward pseudorapidities is presented. These studies provide valuable inputs for Monte Carlo event generator tuning, and test predictions based on perturbative and non-perturbative QCD techniques.

1 Introduction

Present particle physics searches rely on collisions of protons at very high energies. We are mostly interested in the interactions of quarks and gluons of the protons. Thus, a fundamental ingredient in our understanding of particle physics in modern colliders relies in our description of the strong interaction, based on quantum chromodynamics (QCD), the quantum theory of strong interactions. At very short distances (much smaller than the size of the proton), we can rely on perturbation theory techniques, where production rates are presented in a power series expansion in the strong coupling constant, $\alpha_s \ll 1$. However, at large distances (larger than the proton size), this is no longer possible, and a phenomenological approach has to be adopted instead. For these reasons, a tremendous amount of work has gone in further understanding the regimes of short and long distance physics in QCD.

Of particular interest is the so-called small-x limit of QCD, where x represents the parton momentum fraction relative to the proton. Indeed, the large density of gluons at small-x can be understood in terms of the myriad of parton splittings occurring at small-x within the proton. The parton density evolution in the small-x limit is described by the Balitsky-Fadin-Kuraev-Lipatov (BFKL) evolution equation. The latter predicts a power-law growth of parton densities at low x. Smoking-gun experimental evidence for BFKL dynamics has yet to be found. On the other hand, the parton cascade described by BFKL evolution leads to a violatfion of unitarity at very small values of x. Non-linear evolution of parton distribution functions (PDFs), which incorporate gluon-gluon recombination mechanism, may play a role in this regime. Said mechanism is believed to slow down the rapid growth of the proton structure function at very small values of the parton momentum fraction x. So far, experimental evidence in support of parton saturation effects has not yet been found.

In addition, we want to refine our understanding of the underlying dynamics in low-momentum exchange processes in hadronic collisions. The description of these phenomena rely on phenomenological models whose parameters are "tuned" to data. Dedicated measurements sensitive to soft physics effects provide valuable inputs for Monte Carlo (MC) event generators. The latter are widely used for precision studies of standard model processes, searches for new physics, and in cosmic-ray physics.

In this report, we present a selected number of results by the CMS Collaboration [1] related to forward physics, small-x, and diffraction. These were presented at the QCD and Forward Physics meeting held in Guanajuato, Mexico from November 18 through November 21st 2019.

2 Mueller-Navelet jets at 7 TeV

BFKL dynamics can be probed in the production of two jets separated by a large interval in rapidity. This configuration is known as Mueller-Navelet jets. The parton cascade described in the BFKL approach would induce angular decorrelations between the final-state jets. These decorrelations are expected to be stronger than those expected from the parton cascade described by Dokshitzer-Gribov-Lipatov-Altarelli-Parisi (DGLAP) evolution, where parton emissions are strongly ordered in transverse momentum.

The CMS experiment reported a study on Mueller-Navelet jets based 7 TeV pp data [2]. The number of overlapping pp collisions within a single bunch crossing ("pileup" events) was low for the data used in this analysis. The selection criteria considers two jets with $p_T > 35$ GeV reconstructed with the anti-k_t algorithm [3] with distance parameter $R = 0.5$ within the full acceptance of CMS, $|y| < 4.7$. The key observable here is the distribution of the azimuthal angle separation between the jets, $\Delta\phi \equiv |\phi_{\text{jet1}} - \phi_{\text{jet2}}|$, normalized to unity, in bins of $\Delta y \equiv |y_{\text{jet1}} - y_{\text{jet2}}|$. Based on these distributions, one can extract the average cosines of $(\pi - \Delta\phi)$, $2(\pi - \Delta\phi)$, $3(\pi - \Delta\phi)$, and ratios of these average cosines.

Predictions based on various MC event generators based on DGLAP evolution, on BFKL evolution with resummation of logarithms of energy at leading-logarithm (LL), and analytical prediction based on BFKL evolution at next-to-leading-logarithm (NLL) accuracy are presented for these observables. BFKL at NLL calculations describe data at large Δy within uncertainties. HEJ+ARIADNE [4], based on LL BFKL amplitudes, underestimates data at large Δy. PYTHIA8 [5], HERWIG++ [6], SHERPA [7], based on leading order (LO) DGLAP calculation, are able to describe data over wide range in Δy within uncertainties. POWHEG next-to-leading order (NLO) predictions supplemented with PYTHIA6 [8] or PYTHIA8 for parton shower and hadronization effects underestimates or overestimates data at large Δy, respectively. With the present observables and experimental uncertainties, it was found that both BFKL or DGLAP based approaches are able

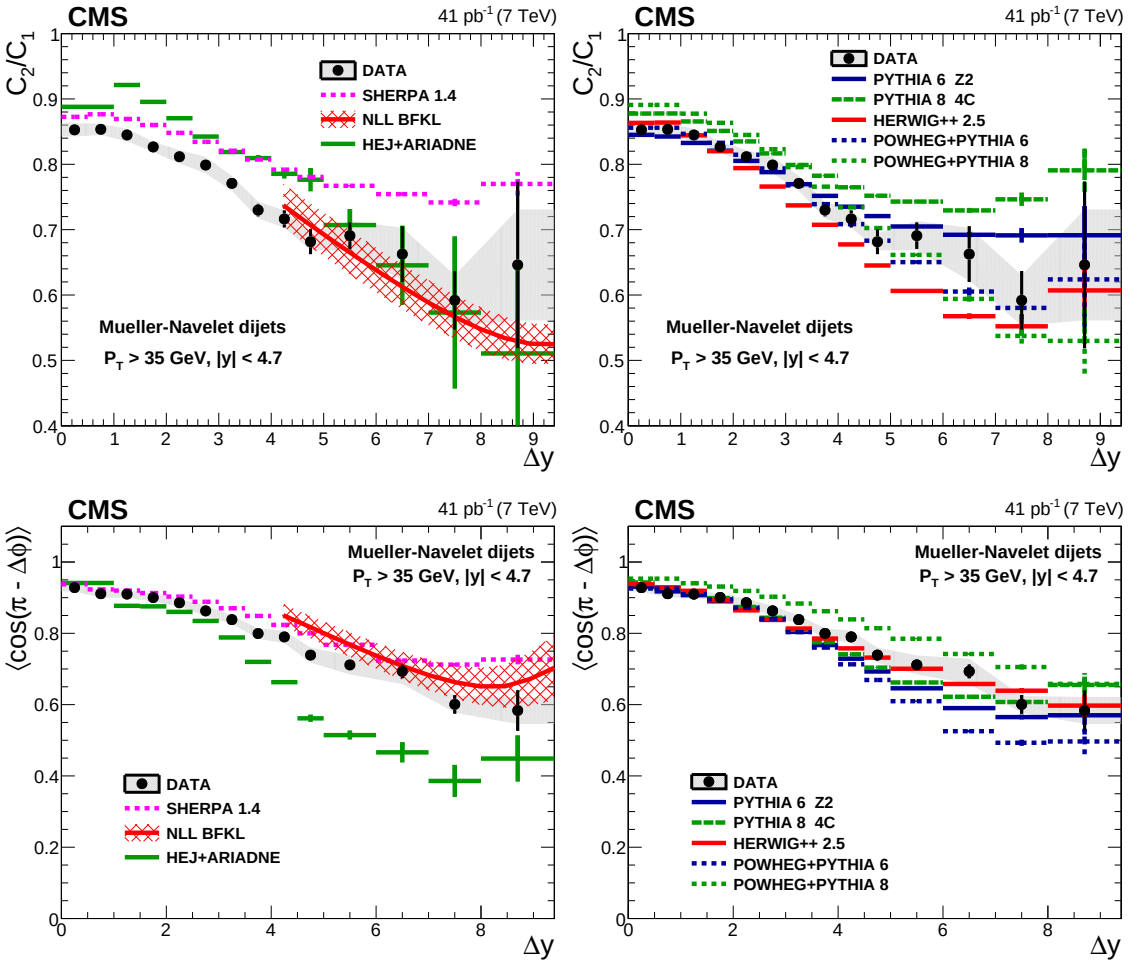

Figure 1: (Top) Ratio of the coefficients C_2 and C_1 as a function of the rapidity difference between the outermost jets, Δy. The coefficients C_n are the average cosine of $n(\pi - \Delta\phi)$. CMS results are represented by the data points. (Bottom) Average cosine of the azimuthal angle separation between the outermost jets as a function of the rapidity difference Δy between the jets. Predictions based on BFKL-NLL calculations are represented by the red band. Predictions based on DGLAP and BFKL-LL MC generators are represented by the other curves, as described in text. Figures are extracted from Ref. [2].

to describe the data. Extensions of this study that account for the interjet activity may be able to isolate BFKL dynamics better, in addition to these observables based on the $\Delta\phi$ distributions.

3 Jet-gap-jet at 7 TeV

Another process that is potentially highly sensitive to BFKL dynamics is the production of two jets separated by a large rapidity gap, where the rapidity gap is an interval void of particle activity. This is known as jet-gap-jet or Mueller-Tang jets. Here, DGLAP dynamics are heavily suppressed due to the rapidity gap requirement by way of a Sudakov form factor. In jet-gap-jet events, contributions from color-singlet exchange are largely favored. In presence of a hard energy scale (given

by the p_T of the jets), the perturbative pomeron exchange is the preferred mechanism in strong interactions to generate the rapidity gap. The perturbative pomeron exchange consists of two-gluon ladder exchange in the BFKL framework.

CMS has presented results on jet-gap-jet events in low pileup 7 TeV pp collisions [9]. In said study, anti-k_t particle-flow jets of distance parameter of $R = 0.5$ are considered. The leading two jets are required to have $p_T^{\text{jet}} > 40$ GeV and $1.5 < \eta_{\text{jet}}| < 4.7$ each, with opposite signed pseudorapidities $\eta_{\text{jet1}} \times \eta_{\text{jet2}} < 0$. The rapidity gap is defined by means of the charged particle multiplicity in $|\eta| < 1$, where each charged particle has $p_T > 200$ MeV. Data-based methods are used to estimate the contribution of color exchange dijet events with downwards fluctuations in the particle multiplicity, such that they yield a rapidity gap. The latter are subtracted from the data in order to extract the color-singlet exchange contribution.

The ratio of events identified as originating from color-singlet exchange divided by the total number of dijet events is measured as a function of the subleading jet p_T^{jet2} and the pseudorapidity difference between the jets $\Delta\eta_{\text{jj}}$, as shown in Fig. 2. Predictions based on BFKL NLL calculations supplemented with survival probability effects based on multiple partonic interactions (MPI) or the soft color interaction model (SCI) by Ingelman-Ekstedt-Enberg (IEE) [10] are shown in Fig. 2. The predictions based on BFKL NLL calculations are not able to simultaneously describe the results in p_T^{jet2} and $\Delta\eta_{\text{jj}}$. A larger dataset at a higher $\sqrt{s}$ may provide additional insight into the nature of the mechanism behind rapidity gap generation in these events. Since these results were presented in this meeting, preliminary results by the CMS and TOTEM Collaborations on jet-gap-jet production at 13 TeV have been publicly presented, as shown in Ref. [11]. The corresponding paper is in preparation.

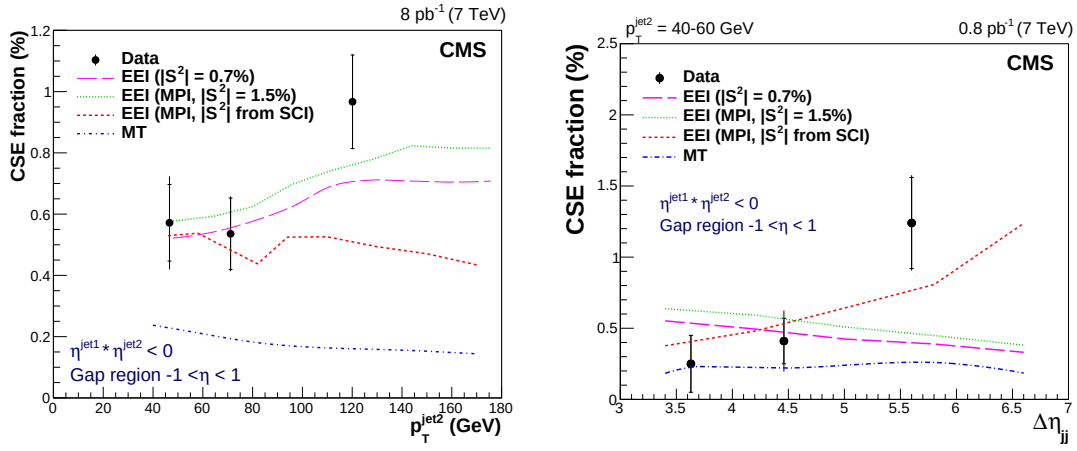

Figure 2: Fraction of color-singlet exchange dijet events, f_{CSE}, as a function of the subleading jet transverse momentum, p_T^{jet2} (Left) and pseudorapidity difference between the jets, $\Delta\eta_{jj}$ (Right). Predictions based on BFKL calculations based on the IEE model. Figures are extracted from Ref. [9].

4 Very forward jet production cross section in pPb collisions

The CMS experiment is equipped with the CASTOR electromagnetic and hadronic calorimeter [1], which extends the measurable jets pseudorapidity acceptance up to $-6.6 < \eta < -5.2$ with approx. $p_T \geq 4$ GeV. A study of jets in CASTOR in p+Pb collisions possesses unique sensitivity to non-

linear evolution effects due to the very forward acceptance for jet reconstruction ($x \sim 10^{-6}$) and the enhancement of the parton densities in the ion (scales with the number of nucleons as $A^{1/6}$).

The measurement of forward inclusive jet cross section is done for the p+Pb (proton towards CASTOR) and the Pb+p (Pb-ion towards CASTOR) configurations. The p+Pb configuration is ideal to probe small-x physics [12]. The sample was collected in pPb collisions at a center-of-mass energy per nucleon pair of $\sqrt{s_{\mathrm{NN}}} = 5.02$ TeV in the laboratory frame (proton beam energy of 4 TeV and 1.6 TeV per nucleon for the Pb beam) using a minimum bias trigger. To suppress the contribution from diffractive and photon-induced processes, a requirement of minimum one calorimeter tower with energy above 4 GeV in $3 < |\eta| < 5$ on both sides is applied. The main result of the study is the differential cross section as a function of the jet energy deposited in CASTOR. The cross sections are unfolded to particle level jets, and are shown in Fig. 3. The leading systematic uncertainty comes from the CASTOR jet energy scale, followed by uncertainties associated to the model dependence from the unfolding procedure and the alignment and calibration corrections. HIJING [13], EPOS [14] and QGSJetII [15] event generators are compared to data; they each have a different treatment for non-linear evolution effects of the parton PDFs, as described in Ref. [12]. HIJING predictions are in agreement with data in the p+Pb configuration, while EPOS and QGSJetsII progressively underestimate the cross section with increasing energy. In the Pb+p configuration, HIJING and EPOS give a reasonable description of the shape of the distribution found in data. To further enhance the model discrimination power in the analysis, the ratio of the p+Pb and Pb+p spectra is measured as a function of the jet energy. The ratio approximately cancels the jet energy scale uncertainties, leaving the model dependence from the unfolding procedure as the leading systematic uncertainty. This observable has the caveat that the ratio is performed on proton-lead collision configurations boosted with respect to each other; therefore, the same values of the parton momentum fraction x is not probed in both configurations simultaneously. HIJING describes the shape well, but the normalization disagrees by a factor of 2. EPOS and QGSJetII are off in shape and show a large discrepancy at increasingly large energies. Other predictions that treat the low-x gluon densities differently than the aforementioned models are described in Ref. [12].

5 Exclusive vector meson production in ultraperipheral pPb collisions

At the CERN LHC, one can use ultraperipheral proton-lead collisions to study exclusive vector meson production. Indeed, the electromagnetic field generated by the relativistic lead-ion can be treated as a source of quasi-real photons. The photon luminosity receives an enhancement proportional to the square of the number of protons in the nucleus, Z^2. The quasi-real photons emitted by the lead nucleus can then probe the proton, and if the interaction is hard enough, it can probe the parton densities of the proton. Due to the asymmetry of the type of beams, one can unambiguously identify the direction of the photon emission. This renders a situation similar to that of electron-proton collisions at HERA.

Diffractive photoproduction of quarkonia offers a clean probe of gluon densities of the proton at small values of $x = 10^{-4}$–10^{-2} and small values of $Q^2 \approx m_V^2$. In these interactions, the quasi-real photon emitted by the lead nucleus fluctuates into a vector meson, which probes the gluon PDFs of the proton via two-gluon exchange (pomeron exchange). At LO in perturbative QCD (pQCD), the production rate is proportional to the square of the gluon PDF. The latter suggests that exclusive production of vector mesons is highly sensitive to physics effects that may take place at low-x, such as parton saturation effects.

The CMS experiment has presented results on exclusive Υ(nS) ($n = 1, 2, 3$) bottomonium meson production in proton-lead collisions at $\sqrt{s_{NN}} = 5.02$ TeV [16]. The rest mass of the Υ meson is large enough (of the order of 10 GeV) to have stable pQCD calculations, but is small enough such

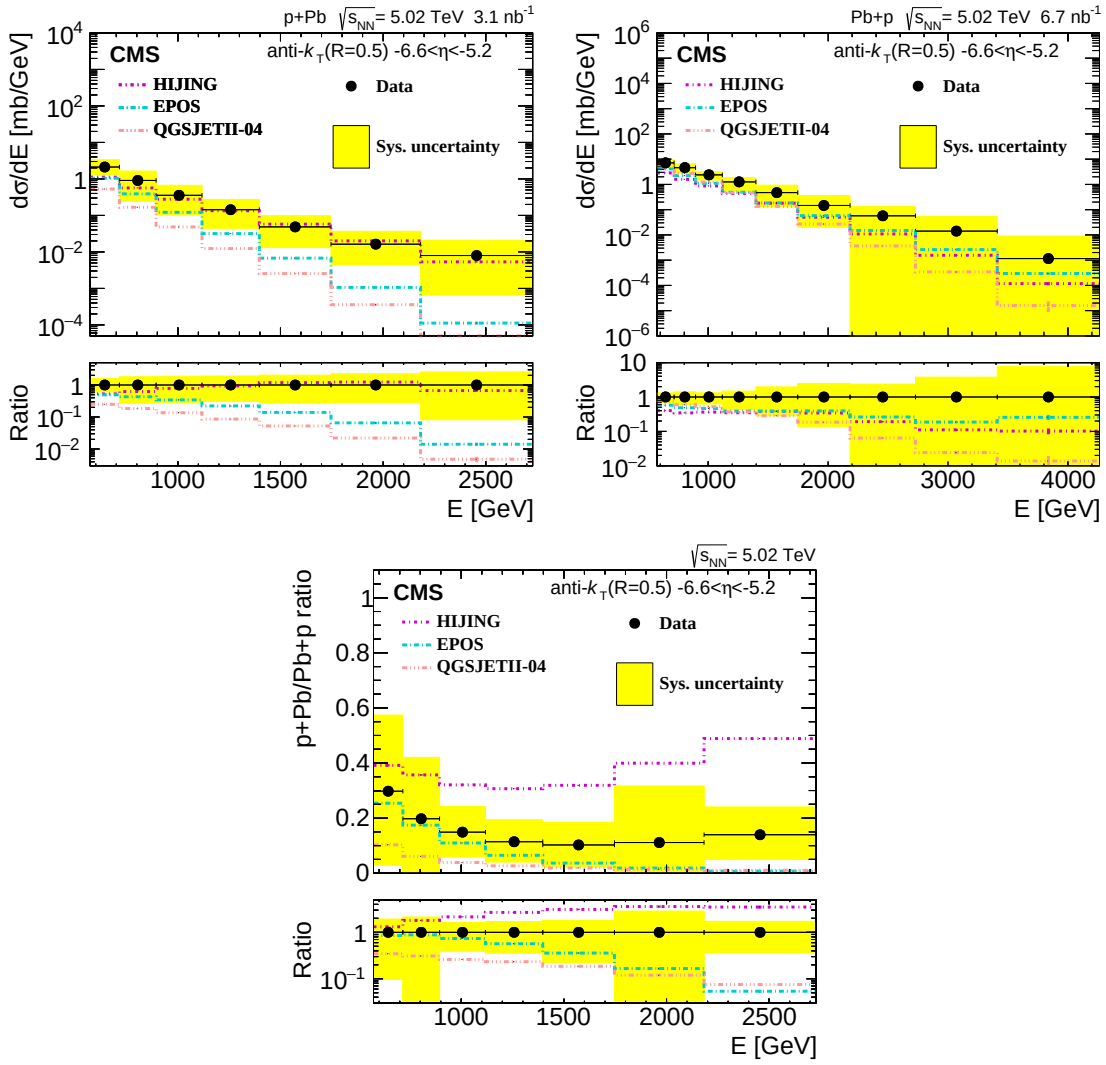

Figure 3: Differential cross section as a function of the jet energy in CASTOR for the p+Pb configuration (left), the Pb+p configuration (right), and the ratio of the differential cross section in p+Pb to Pb+p as a function of the jet energy(bottom). Predictions based on HIJING, EPOS-LHC, and QGSJETII are shown on top of the data. Figures are extracted from Ref. [12].

that saturation effects may still play an important role in the small-x regime of gluon densities. In the study, Υ meson decays in muon pairs in the rapidity range $|y| < 2$ are considered.

Upon subtraction of photoproduction of lepton pairs, and non-diffractive Υ production, one can reconstruct the p_T of the extracted exclusive Υ candidates. The latter is a good approximation to the four-momentum transfer square at the proton vertex, and can be seen in Fig. 4. The resulting distribution is fit with an exponential function $\exp(-bp_T^2)$. The slope is found to be $b = 6.0 \pm 2.1$ (stat) ± 0.3 (syst) GeV^{-2}, in agreement with the value measured by ZEUS at lower photon-proton masses. The slope of the distribution gives information on the gluon PDFs in impact parameter space. The photon-proton center-of-mass energy $W_{\gamma p}$ can be deduced from the rapidity of the Υ in the laboratory frame via $W_{\gamma p}^2 = E_p m_\Upsilon \exp(\pm y)$, where $E_p = 4$ TeV. The photoproduction cross section $\sigma(\gamma p \to \Upsilon p)$ is extracted from $\frac{d\sigma}{dy}(\mathrm{pPb} \to \mathrm{p}\Upsilon(1S)\mathrm{Pb})$ in bins of $\langle y \rangle$, based on the photon

spectrum embedded in STARLIGHT [17]. The CMS pPb results cover a region unexplored by H1, ZEUS, and LHCb. Predictions that account for different Υ wave function parametrizations or small-x gluon PDF models are shown in Fig. 4.

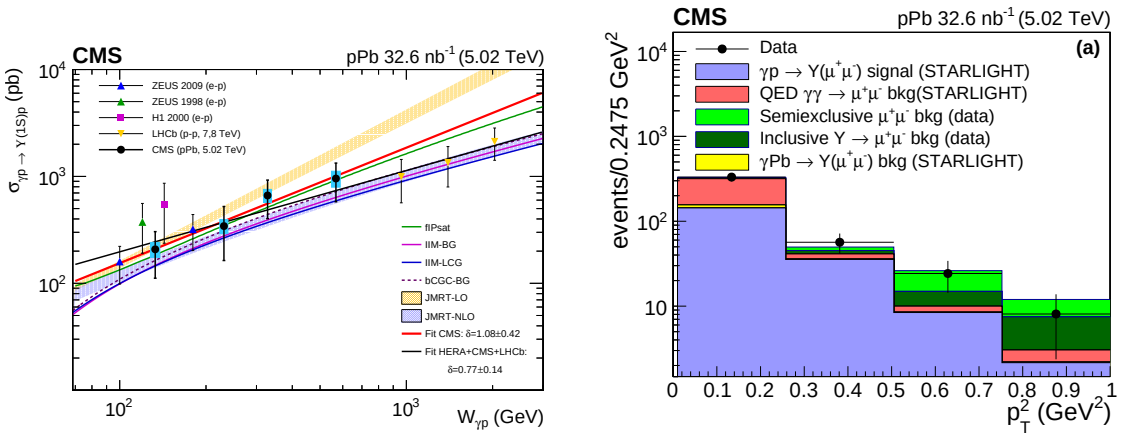

Figure 4: (Left) Photoproduction cross section as a function of the photon-proton center-of-mass energy, $W_{\gamma p}$. Previous measurements by the H1, ZEUS and LHCb Collaboration are shown as well. (Right) Number of events as a function of the transverse momentum of exclusive Υ meson event candidates, together with background and signal contributions. Figures are extracted from Ref. [16].

CMS has also presented results in exclusive $\rho(770)^0$ photoproduction from protons in pPb collisions at $\sqrt{s}_{NN} = 5.02$ TeV [18]. The smaller mass of the ρ meson corresponds to a larger effective color-dipole size to probe the proton. This renders better sensitivity of possible parton saturation effects. The analysis strategy is very similar to that of exclusive Υ meson production described above. In the analysis, decays of the $\rho(770)^0 \to \pi^+\pi^-$ are considered. The p_T of the leading and subleading pions is of at least 0.4 and 0.2 GeV, respectively, within $|\eta| < 2$. Here, the dominant backgrounds correspond to resonant and non-resonant $\pi^+\pi^-$ (simulated with the STARLIGHT event generator [17]) production, photoproduction of $\rho^0(770)$ with proton dissociation (based on normalization at large $p_T^{\pi^+\pi^-}$), and $\rho(1700)$ production.

Upon subtraction of background, just as with the aforementioned exclusive Υ production, one can estimate the four-momentum transfer at the proton vertex $-t \approx p^2_{T,\pi^+\pi^-}$, as shown in Fig. 5. Additional studies related to the b slope parameter extracted from the $d\sigma/d|t|$ in bins of $W_{\gamma p}$ are discussed in Ref. [18]. Following a similar technique as with exclusive Υ production, one can extract the photoproduction cross section as a function of the photon-proton center-of-mass energy $W_{\gamma p}$. The main results of the latter are shown in Fig. 5. The CMS results in both of these observables are consistent with similar studies done by the H1 and ZEUS experiments.

6 Charged particle production in minimum bias events

Particle production without any selection bias arising from the requirement of the presence of a hard scattering process is known as "minimum bias" (MB). The bulk of these events occur at low momentum exchanges between the interacting partons inside the hadrons, where diffractive scattering or MPI play a significant role. Theoretical descriptions of these components of particle production are based on phenomenological models, whose parameters need to be "tuned" to reproduce experimental data. Given the large cross section of MB events in high energy pp collisions,

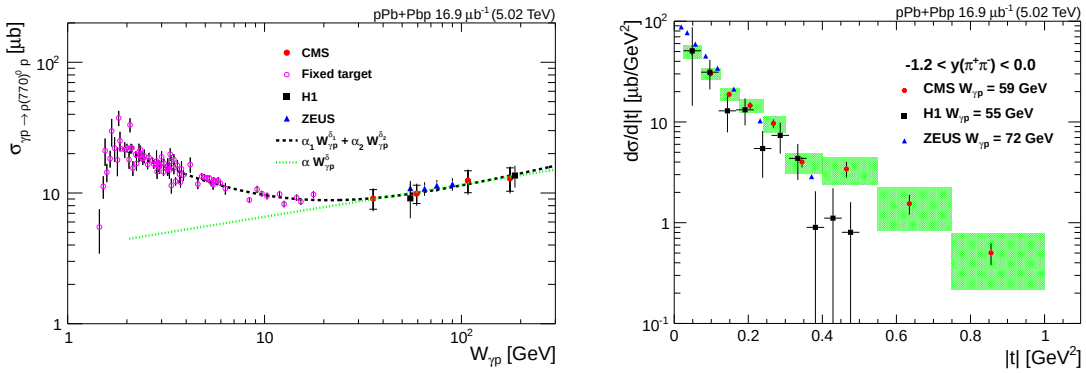

Figure 5: (Left) Photoproduction cross section as a function of the photon-proton center-of-mass energy, $W_{\gamma p}$. (Right) Number of events as a function of the transverse momentum of exclusive ρ meson event candidates. Previous results by the H1 and ZEUS Collaborations are shown as well in both figures. Figures are extracted from Ref. [18].

it is of primary importance to have a good understanding of these processes, as they characterize properties of typical pileup interactions in each bunch crossing at the interaction point of CMS and other LHC experiments. One can characterize MB events by means of charged particle distributions. Charged particle distributions are measured for charged particles with $p_T > 0.5$ GeV and $|\eta| < 2.4$ for events collected with a trigger selection MB events. The measured distributions are presented for different event data samples classifed by the calorimeter activity in the forward region. In this study, one considers the presence of at least one calorimeter tower with energy above 5 GeV in $3 < |\eta| < 5$, and in some cases with a veto condition for towers with energy below 5 GeV. The different event classes are as non-single diffractive enriched sample (NSD-enhanced) when there is calorimeter activity in both sides, as single diffractive enriched (SD-enhanced) when there is calorimeter activity on one side and a veto on the opposite side, and as inelastic when there is calorimeter activity on at least one side of CMS. The distribution labelled as SD-One-Side enhanced sample corresponds to the symmetrized distribution constructed from the SD-minus and SD-plus enhanced samples.

The normalized particle distribution is measured as a function of the charged particle pseudorapidity for the four different selections, as shown in Fig. 6. The results are unfolded to particle level. PYTHIA8-CUETM1, PYTHIA8-MBR 4C [19], and EPOS-LHC results are compared to the data. PYTHIA8 MBR 4C describes reasonably well the data for the SD-enhanced samples,but overestimates the yield in central pseudorapidities for the non-diffractive samples. PYTHIA8-CUETM1 and EPOS-LHC give a fair description for the non-diffractive samples, but they are off w.r.t. data for the SD-enhanced selection. Additional observables based on the leading p_T charged particle, and the per-event charged particle density, are shown in Ref. [20].

7 Underlying event activity in Drell-Yan events at 13 TeV

The underlying event (UE) activity is any activity stemming from beam-beam remnants and MPI. The UE produces particles carrying low transverse momentum, and are hard to disentangle from the initial-state radiation (ISR) and final-state radiation (FSR) present in the hard scattering process. The UE activity is usually quantified in terms of the charged particle multiplicity, as well as the scalar sum of the charged particles' transverse momenta, in different angular regions defined with respect to a clean hard scattering process probe.

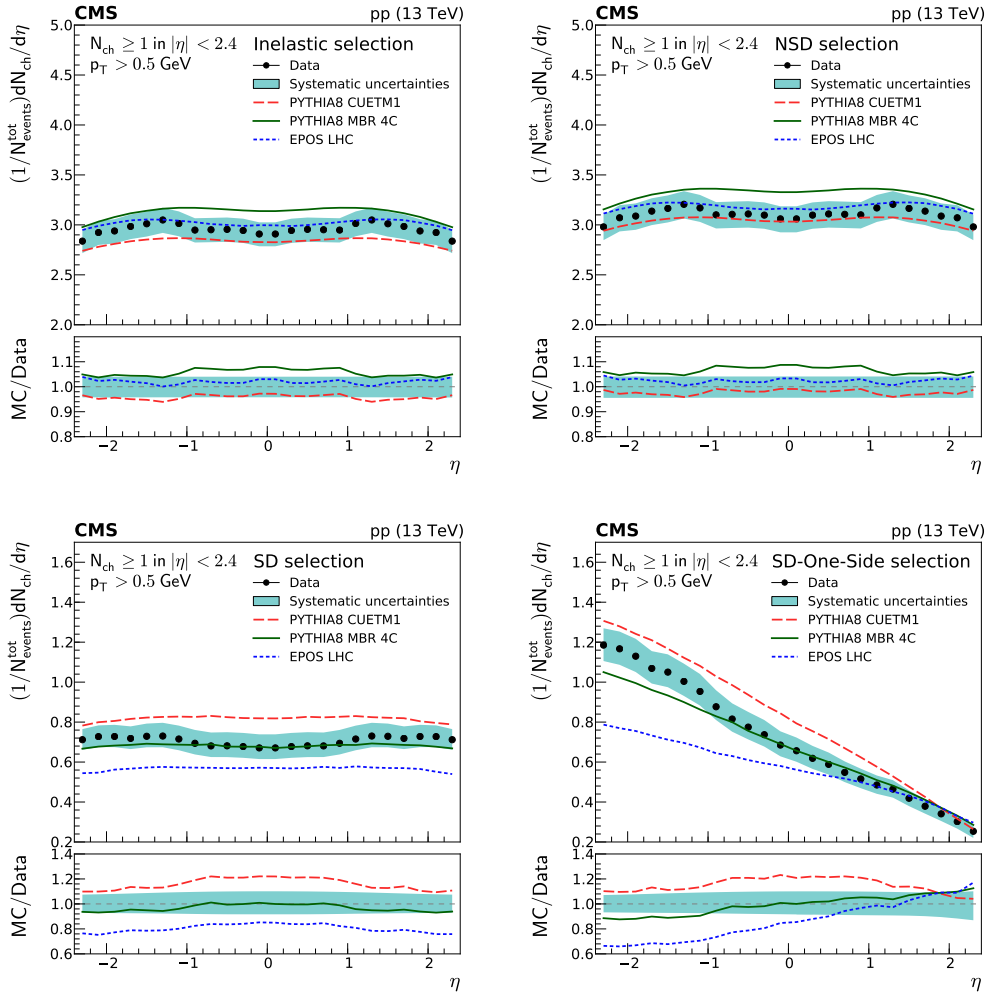

Figure 6: Charged particle pseudorapidity densities averaged over both positive and negative η ranges. Top to bottom, left to right: inelastic, NSD-, SD-, and SD-One-Side enhanced eventsamples. The measurements are compared to the predictions of the PYTHIA8 CUETM1 (long dashes), PYTHIA8 MBR4C (continuous line), and EPOS-LHC (short dashes) event generator. The error band represents the total systematic uncertainty. Figures are extracted from Ref. [20].

The CMS Collaboration presented a study of the UE activity based on 13 TeV pp collision data where the Z boson ($pp \rightarrow Z + X$) is the hard scattering probe [21]. In this study, the Z boson decays into a $\mu^+\mu^-$ pair. This process is theoretically well understood, and has the additional advantage that FSR effets are not present. Muons are required to have $p_T^{\mu} > 20$ GeV, $|\eta^{\mu}| < 2.4$, and $81 < m_{\mu\mu} < 101$ GeV.

The charged particle activity relative to the Z boson direction is studied in three angular regions labelled as "towards", "transverse", and "away" regions, which are respectively defined by $|\Delta\phi| < 60°$, $60 < |\Delta\phi| < 120°$, and $|\Delta\phi| > 120°$, where $\Delta\phi$ is the azimuthal angle separation between the charged particle and the dimuon direction. Charged particles are requiredto satisfy $p_T > 0.5$ GeV and $|\eta| < 2$ for the measured distributions. The average particle density as a function of the dimuon transverse momentum is shown in Fig. 7. Combinations of MAD-

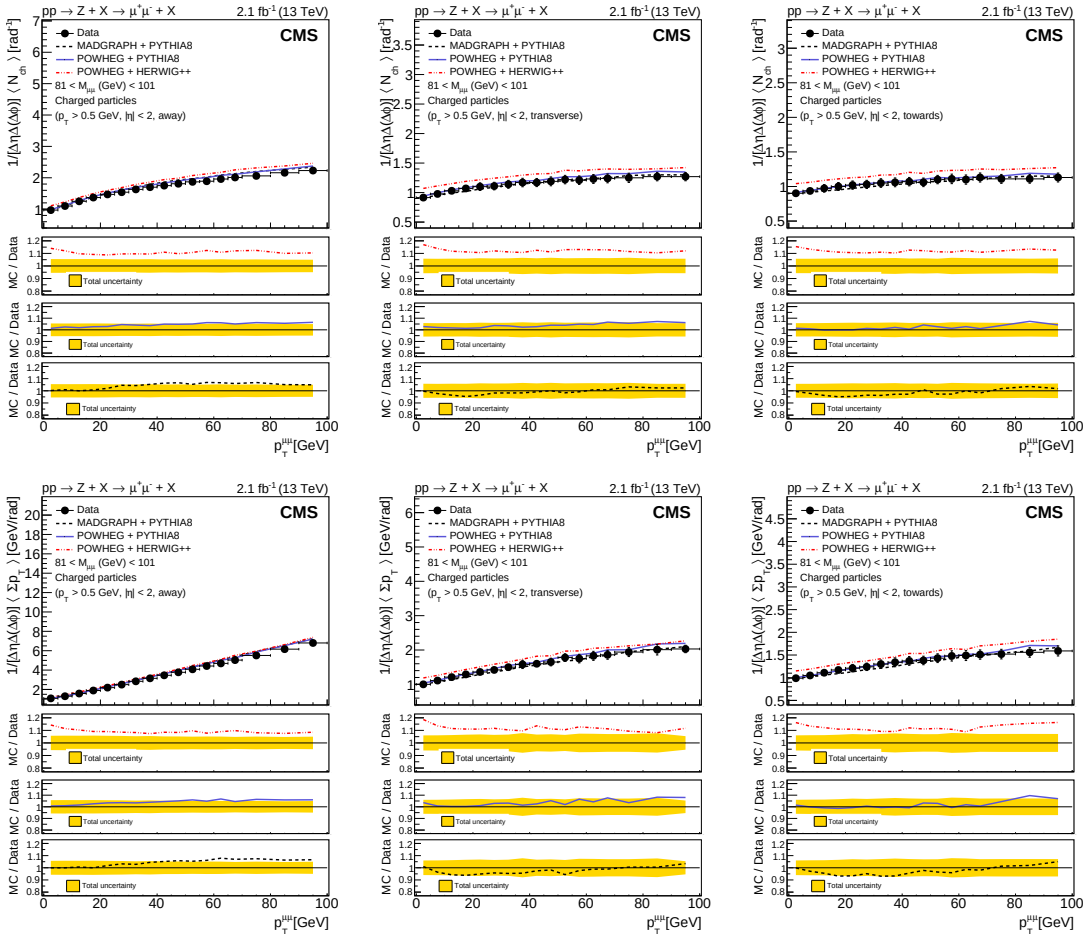

Figure 7: Particle density (top) and Σp_T density (bottom) as a function of the dimuon transverse momenta in the away (left), transverse (center) and towards (right) regions. Figures are extracted from Ref. [21].

GRAPH and POWHEG (which include ISR effects for inclusive Z boson production) interfaced with PYTHIA8 and HERWIG++ for parton shower, hadronization effects, and UE activity, are compared to data. These combinations give reasonable agreement in shape w.r.t. the data, with the POWHEG+HERWIG++ off in normalization by 10–20%.

8 Energy density as a function of pseudorapidity at 13 TeV

A measurement of the energy density in MB events in proton-proton collisions $\sqrt{s} = 13$ TeV within $-6.6 < \eta < -5.2$ and $3.15 < |\eta| < 5.20$ has been presented in Ref. [22]. Similar to the study of charged particle spectra in MB events, one is interested in characterizing soft particle production over a wide interval in pseudorapidity. In this study, the main focus is in forward pseudorapidities. The CASTOR calorimeter of CMS is used for negative pseudorapidities. The main observable in this study is the average energy density per collision, $dE/d|\eta|$. The energy density is extracted in three main event categories defined by the forward particle activity: inclusive inelastic (INEL) selection, non-single-diffractive-enhanced (NSD-enhanced), and single-diffractive-enhanced (SD-enhanced). Similar to the study described in Sec. 6, these event categories are defined based on

calorimeter energy deposits above noise level on at least one side (INEL), on both sides (NSD-enhanced), or in exactly one side (SD-enhanced). Comparisons are made to predictions based on PYTHIA8 + Monash2013, EPOS-LHC, and QGSJETII.

The resulting $dE/d|\eta|$ per category are shown in Fig. 8. The INEL and NSD-enhanced categories are extremely sensitive to MPI, while the SD-enhanced category is essentially unaffected. The Pythia8 Monash2013, EPOS-LHC, QGSJETII predictions overshoot the data for $|\eta| \approx 4.5$–5. The EPOS-LHC and QGSJETII models exhibit the largest differences when compared to the SD-enhanced results. A comparison with other PYTHIA8 tunes are described in Ref. [22].

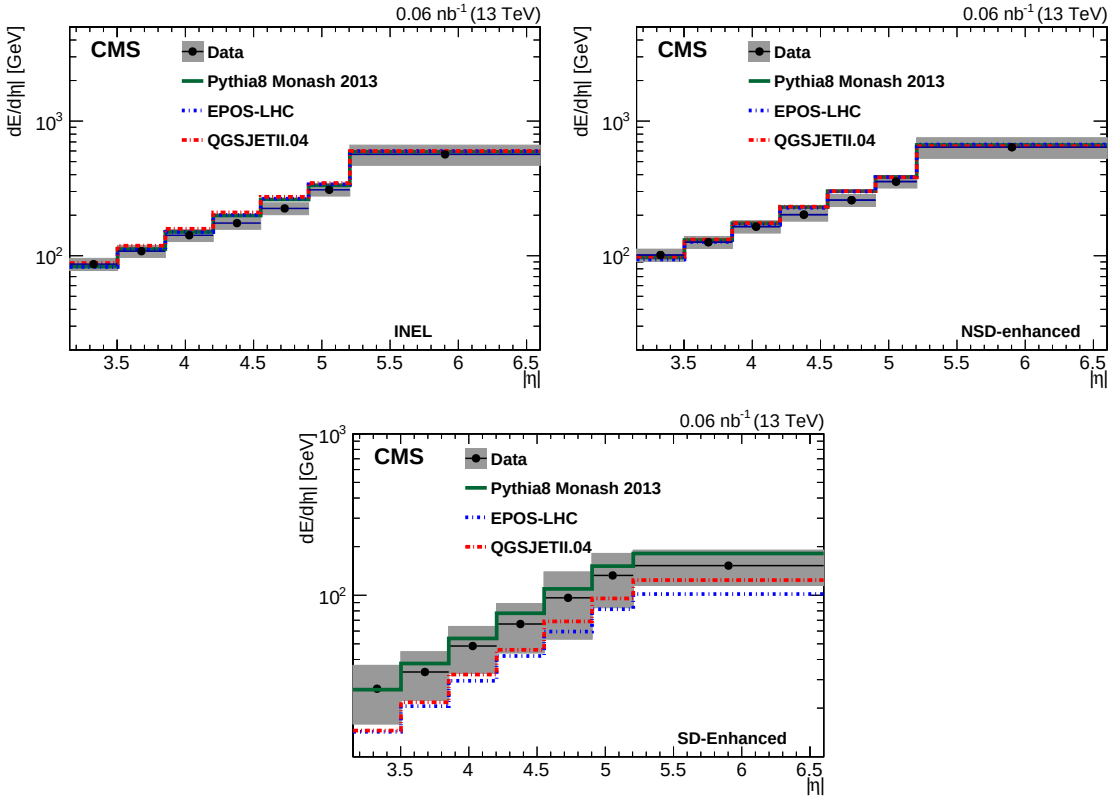

Figure 8: Energy density at the stable-particle level for the INEL (Left), NSD-enhanced (Right), and SD-enhanced (Bottom) categories are compared to predictions from PYTHIA8 MONASH, EPOS-LHC, and QGSJETII.04. The gray band shows the total systematic uncertainty. Figures are extracted from Ref. [22].

At high energies the hypothesis of limiting fragmentation assumes a longitudinal scaling behaviour in terms of shifted pseudorapidity $\eta' = \eta - y_{\text{beam}}$, where y_{beam} is the beam rapidity. Thus, soft-particle production in the projectile fragmentation region ($\eta' \approx 0$) is predicted to be independent of the center-of-mass energy. In this measurement, this is studied by measuring the transverse energy density $dE_T/d\eta$ with $E_T = E\cosh(\eta)$, and comparing it to measurements performed in pp collisions at different $\sqrt{s}$, as shown in Fig. 9. Predictions based on EPOS-LHC and QGSJETII models nicely describe the combined data in forward pseudorapidities, close to the projectile fragmentation region. Thus, the limiting fragmentation hypothesis is consistent with data. This is very important for the modelling of ultra-high energy interactions that typically occur in cosmic ray collisions.

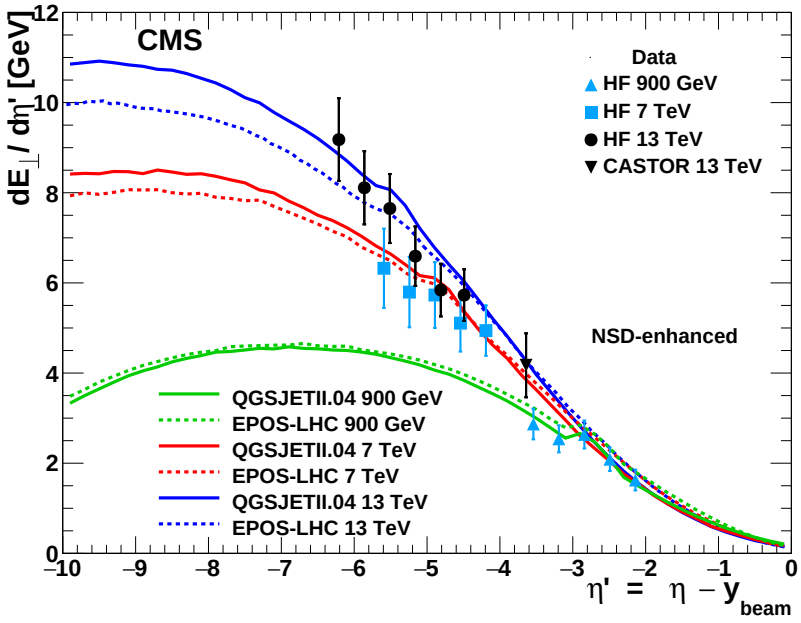

Figure 9: A comparison of the measurements of transverse energy density $\frac{dE_T}{\eta'}$ at 13 TeV, as a function of shifted pseudorapidity, $\eta' = \eta - y_{\text{beam}}$, to predictions for an NSD-enhanced selected sample at several different centre-of-mass energies. The error bars indicate the total systematic uncertainties. Figure is extracted from Ref. [22].

9 Summary

Recent studies by the CMS experiment continue to shed light on regions of phase space highly relevant for the study of strong interactions at high energies. In these Proceedings, we have presented results by the CMS Collaboration related to the small-x limit of QCD, where gluon densities are expected to grow rapidly due to multiple parton splitting within the proton or lead-nucleus, particle production in minimum bias events, and aspects related to multiparton interactions and beam-beam remnants.

Predictions based on BFKL calculations are consistent with results on azimuthal angle decorrelations in dijet events, where the two jets are separated by a large rapidity interval. However, predictions based on DGLAP evolution alone are also compatible with data for a wide range of rapidity. An extension of this study at higher energies and possibly with additional observables may help better disentangle BFKL dynamics from DGLAP dynamics. For events with two jets separated by a rapidity gap, we have the advantage that DGLAP dynamics is heavily suppressed, allowing for a description of jet-gap-jet events based on BFKL pomeron exchange. The challenge here is to simultaneously describe the short distance physics effects with the long distance physics effects (survival probability). A publication is in preparation regarding an extension of this study at $\sqrt{s} = 13$ TeV, which may help to better discriminate the existing models for jet-gap-jet event production.

Forward jet production in proton-nucleus collisions are very promising, and need to be further interpreted for stronger assessments on potential parton saturation effects observed in data. The results in exclusive quarkonia production in proton-lead collisions demonstrate the feasibility of continuing the program first started by the HERA experiments. An extension of these studies at larger energies and larger samples in proton-lead collision data collected in 2016 would help

constrain better the gluon density in the small-x region.

Measurement of MB events and UE activity are sensitive to the various mechanisms for particle production in proton-proton collisions with increasing precision at various center-of-mass energies at the CERN LHC. The latter provide very important inputs and constraints for MC generator tuning necessary for collider searches and cosmic-ray physics studies.

Acknowledgements

I would like to thank the U.S. Department of Energy for their generous support (grant number DE-SC0019389.). I would also like to thank Universidad de Guanajuato for hosting and organizing this event.

References

[1] **CMS** Collaboration, *The CMS experiment at the CERN LHC*, *Journal of Instrumentation* **3** (aug, 2008) S08004–S08004.

[2] **CMS** Collaboration, V. Khachatryan et al., *Azimuthal decorrelation of jets widely separated in rapidity in pp collisions at $\sqrt{s} = 7$ TeV*, *JHEP* **08** (2016) 139, [arXiv:1601.06713].

[3] M. Cacciari, G. P. Salam, and G. Soyez, *The anti-ktjet clustering algorithm*, *Journal of High Energy Physics* **2008** (apr, 2008) 063–063.

[4] L. Lonnblad, *Ariadne version 4–a program for simulation of qdc cascades implementing the colour dipole model*, *Computer Physics Communications* **71** (1992), no. 1 15 – 31.

[5] T. Sjostrand, S. Mrenna, and P. Z. Skands, *A Brief Introduction to PYTHIA 8.1*, *Comput. Phys. Commun.* **178** (2008) 852–867, [arXiv:0710.3820].

[6] M. Bahr et al., *Herwig++ Physics and Manual*, *Eur. Phys. J. C* **58** (2008) 639–707, [arXiv:0803.0883].

[7] T. Gleisberg, S. Hoeche, F. Krauss, M. Schonherr, S. Schumann, F. Siegert, and J. Winter, *Event generation with SHERPA 1.1*, *JHEP* **02** (2009) 007, [arXiv:0811.4622].

[8] T. Sjostrand, S. Mrenna, and P. Z. Skands, *PYTHIA 6.4 Physics and Manual*, *JHEP* **05** (2006) 026, [hep-ph/0603175].

[9] **CMS** Collaboration, A. M. Sirunyan et al., *Study of dijet events with a large rapidity gap between the two leading jets in pp collisions at $\sqrt{s} = 7$ TeV*, *Eur. Phys. J. C* **78** (2018), no. 3 242, [arXiv:1710.02586]. [Erratum: Eur.Phys.J.C 80, 441 (2020)].

[10] A. Ekstedt, R. Enberg, and G. Ingelman, *Hard color singlet BFKL exchange and gaps between jets at the LHC*, 3, 2017. arXiv:1703.10919.

[11] **CMS Collaboration, TOTEM Collaboration** Collaboration, *Study of hard color singlet exchange in dijet events with proton-proton collisions at $\sqrt{s} = 13$ TeV*, Tech. Rep. CMS-PAS-SMP-19-006, CERN, Geneva, 2020.

[12] **CMS** Collaboration, A. M. Sirunyan et al., *Measurement of inclusive very forward jet cross sections in proton-lead collisions at $\sqrt{s_{\mathrm{NN}}}$ = 5.02 TeV*, *JHEP* **05** (2019) 043, [arXiv:1812.01691].

[13] M. Gyulassy and X.-N. Wang, *HIJING 1.0: A Monte Carlo program for parton and particle production in high-energy hadronic and nuclear collisions*, *Comput. Phys. Commun.* **83** (1994) 307, [nucl-th/9502021].

[14] T. Pierog, I. Karpenko, J. Katzy, E. Yatsenko, and K. Werner, *EPOS LHC: Test of collective hadronization with data measured at the CERN Large Hadron Collider*, *Phys. Rev. C* **92** (2015), no. 3 034906, [arXiv:1306.0121].

[15] S. Ostapchenko, *Monte Carlo treatment of hadronic interactions in enhanced Pomeron scheme: I. QGSJET-II model*, *Phys. Rev. D* **83** (2011) 014018, [arXiv:1010.1869].

[16] **CMS** Collaboration, A. M. Sirunyan et al., *Measurement of exclusive Υ photoproduction from protons in pPb collisions at $\sqrt{s_{\mathrm{NN}}} = 5.02$ TeV*, *Eur. Phys. J. C* **79** (2019), no. 3 277, [arXiv:1809.11080].

[17] S. R. Klein, J. Nystrand, J. Seger, Y. Gorbunov, and J. Butterworth, *STARlight: A Monte Carlo simulation program for ultra-peripheral collisions of relativistic ions*, *Comput. Phys. Commun.* **212** (2017) 258–268, [arXiv:1607.03838].

[18] **CMS** Collaboration, A. M. Sirunyan et al., *Measurement of exclusive $\rho(770)^0$ photoproduction in ultraperipheral pPb collisions at $\sqrt{s_{\mathrm{NN}}} = 5.02$ TeV*, *Eur. Phys. J. C* **79** (2019), no. 8 702, [arXiv:1902.01339].

[19] R. Ciesielski and K. Goulianos, *MBR Monte Carlo Simulation in PYTHIA8*, *PoS* **ICHEP2012** (2013) 301, [arXiv:1205.1446].

[20] **CMS** Collaboration, A. M. Sirunyan et al., *Measurement of charged particle spectra in minimum-bias events from proton–proton collisions at $\sqrt{s} = 13$ TeV*, *Eur. Phys. J. C* **78** (2018), no. 9 697, [arXiv:1806.11245].

[21] **CMS** Collaboration, A. Sirunyan et al., *Measurement of the underlying event activity in inclusive Z boson production in proton-proton collisions at $\sqrt{s} = 13$ TeV*, *JHEP* **07** (2018) 032, [arXiv:1711.04299].

[22] **CMS** Collaboration, A. M. Sirunyan et al., *Measurement of the energy density as a function of pseudorapidity in proton-proton collisions at $\sqrt{s} = 13$ TeV*, *Eur. Phys. J. C* **79** (2019), no. 5 391, [arXiv:1812.04095].

Spin and Forward Physics with the STAR detector: Measurements and Future Plans

David Kapukchyan (for the STAR Collaboration)

E-Mail: dkapu001@ucr.edu

University of California Riverside

Presented at the Workshop of QCD and Forward Physics at the EIC, the LHC, and Cosmic Ray Physics in Guanajuato, Mexico, November 18-21 2019

Abstract

The spin program at the STAR experiment at the Relativistic Heavy Ion Collider (RHIC) has explored many interesting topics and has helped our understanding of nuclear and nucleon structures. In particular, non-vanishing transverse single-spin asymmetry measurements at RHIC and other experiments have shown that there is a rich substructure of the nucleon that needs further exploration in both theory and experiment. The STAR forward upgrade will utilize RHIC's unique capability of colliding polarized proton and heavy ion beams to carry out measurements of Drell-Yan, jets, hadrons in jets, and dijets, among others with improved precision. The new forward system will be in operation for the pp, pA and AA runs starting in Fall 2021 and utilize the latest developments in detector technologies so that they are ready for the Electron-Ion Collider (EIC). The forward upgrade will cover $2.5 < \eta < 4.0$, by installing two new forward tracking systems and a new calorimeter system. The tracking systems will consist of silicon disks and small-strip thin gap chambers. The calorimeter system will consist of a preshower hodoscope, an electromagnetic calorimeter and a hadronic calorimeter. These proceedings will show some of the recent results from STAR's spin program as well as the design and capabilities of the forward upgrade and how it will complement measurements from a future EIC.

1 Introduction

One of the main open questions in nuclear physics today is what is the origin of the proton spin. This question arose from Deep Inelastic Scattering (DIS) experiments that showed that the spin of the quarks is not sufficient to account for the total spin of the proton [1]. The results shown here will highlight some of the work that has been done by the Solenoidal Tracker at RHIC (STAR) to constrain the contribution of the quarks and gluons to the total spin of the proton. Also, I will discuss how the STAR forward upgrade can be used to even further constrain these quantities. Another important question is how we can describe the multi-dimensional landscape of nucleons and nuclei. Transverse momentum dependent PDFs (TMD) are a key aspect of this question. TMDs address how a parton's transverse momentum inside the proton can be related to physics

observables. STAR has measured many TMDs and these proceedings will present the results from only one such TMD, transversity via the Collins fragmentation function, and how the forward upgrade aims to improve upon that result.

2 The Relativistic Heavy Ion Collider

The relativistic heavy ion collider (RHIC) at Brookhaven National Laboratory (BNL) is the only polarized pp collider in the world. In addition, as its name suggests, it can also collide various heavy ion species at a range of energies in both collider and fixed target mode. In the last two decades RHIC has collided various mixtures of p, d, ^{3}He, Al, Cu, Zr, Ru, Au, and U at various energies. Proton-proton collisions have taken place at center-of-mass energies ($\sqrt{s}$) of 62, 200, 500, and 510 GeV. Center-of-mass energies per nucleon-nucleon pair ($\sqrt{s_{NN}}$) in pA and AA collisions have reached up to 200 GeV, while fixed target experiments at STAR have reached as low as $\sqrt{s_{NN}} = 3$ GeV.

The RHIC facility consists of the Brookhaven Linear Accelerator (LINAC), a booster, an Alternating Gradient Synchroton (AGS), two main storage rings, and an Electron Beam Ion Source (EBIS). Polarized pp beams start by inserting transversely polarized protons (~95% polarization) into the LINAC followed by the booster that then feeds into the AGS. The AGS is used to further increase the beam energy and then routes the beam into one of the two main storage rings, where the beams may be further accelerated; the two opposite going beams are named blue and yellow. The polarization is maintained both during acceleration and at collision energy using Siberian Snakes located on the AGS and the main storage rings. To reduce systematic uncertainties, the polarization pattern is chosen from a set of well-defined fill patterns that alternate the polarization direction for consecutive bunches or pairs thereof. In addition, spin rotators are located around the interaction region to allow for either transversely or longitudinally polarized pp or pA collisions. Polarimeters within the ring allow continuous measurements of the beam polarization during a RHIC fill, which typically lasts 8 hours. Unpolarized heavy ion beams start in the EBIS that generates the intial ions that go into the LINAC and then follow the same process [2].

The latest transversely polarized pp run was RHIC Run 17 at $\sqrt{s} = 510$ GeV. It has the highest delivered luminosity per week for all pp runs to date. RHIC has been able to provide highly polarized beams, achieving an average polarization of about 50-60%. Also, of interest, is Run 15 that had a mix of longitudinal and transverse spin pp collisions at $\sqrt{s} = 200$ GeV.

3 STAR Detector

The STAR detector is shown in Fig. 1 [3]. STAR has a Time Projection Chamber (TPC) at mid-rapidity $|\eta| < 1.0$ that covers a full 2π in azimuth [4]. It is used for charged particle reconstruction and identification. Just outside the TPC is the Barrel Electromagnetic Calorimeter (BEMC). The BEMC has the same coverage as the TPC and is used for measuring the energies of electrons and photons. The other two detectors at mid-rapidity are the Time Of Flight (TOF), used to improve particle identification from the TPC, and the Muon Telescope Detector (MTD), which is used to detect muons. In addition, there exist global detectors that have multiple functionalities. These are the Beam-Beam Counter (BBC) located at $3.3 < |\eta| < 5.2$ and the Vertex Position Detector (VPD) located at $4.24 < |\eta| < 5.1$. Lastly, the detectors in forward pseudorapidity (blue beam direction) with full 2π azimuth coverage are the Endcap Electromagnetic Calorimeter (EEMC) $1 < \eta < 2$, and the Forward Electromagnetic Calorimeter (FEMC) $2.5 < \eta < 4.0$.

There were some upgrades completed in 2019 that are not visible in Fig. 1. The inner TPC was upgraded which improved $\frac{dE}{dx}$ resolution and increased coverage to $|\eta| < 1.5$. An Endcap

TOF extends coverage to $1.05 < \eta < 1.7$. Lastly, installed in 2018, the Event Plane Detector (EPD) covers $2.1 < |\eta| < 5.1$. It is used to provide event triggers and improve event plane resolution.

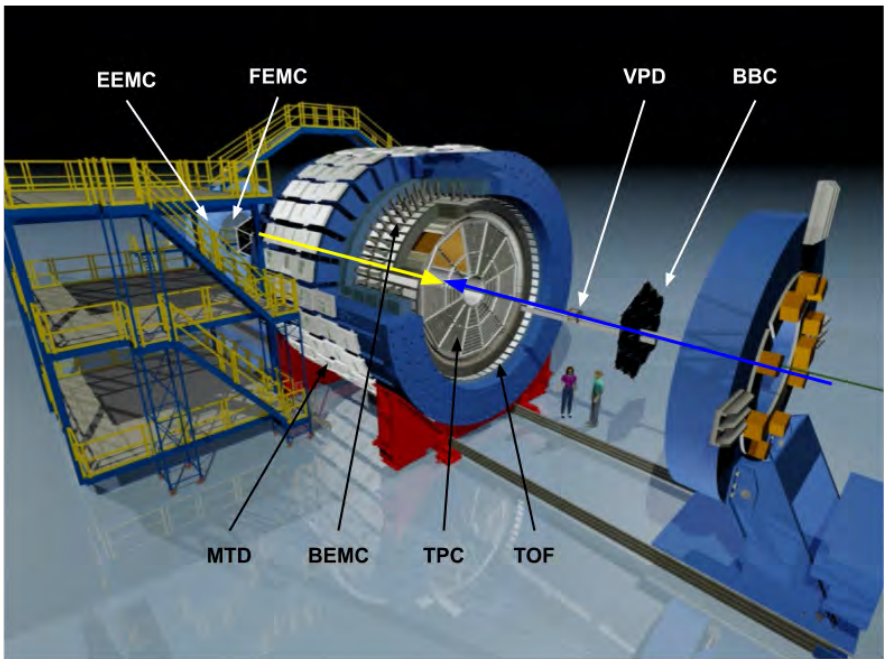

Figure 1: STAR detector and its various detector subsystems. Information on each subsystem can be found in the text.

4 Helicity Structure of Proton

The longitudinal spin of the proton can be decomposed into the various angular momenta of the quarks and gluons that make it up. One such decomposition, the Jaffe-Manohar spin sum rule, decomposes the spin of the proton according to equation (4.1)

$$\frac{1}{2} = \frac{1}{2}\Delta\Sigma + \Delta G + L_z \tag{4.1}$$

where $\Delta\Sigma$ is the quark polarization, ΔG is the gluon polarization and L_z is the orbital angular momentum of the quark-gluon system. The quark polarization can be further broken down into the valence quark and sea quark polarization. The quark polarization has been measured using DIS experiments and accounts for only about 30% of the total proton spin in a limited x range [1]. The EIC will provide better constraints on the valence quark polarization. The sea quark polarization can be probed using the parity violating $W^{\pm}$ production at RHIC. The diagram in Fig. 2 shows how W's are produced. This production is maximally parity violating so the quarks must have opposite helicities. An up quark from one

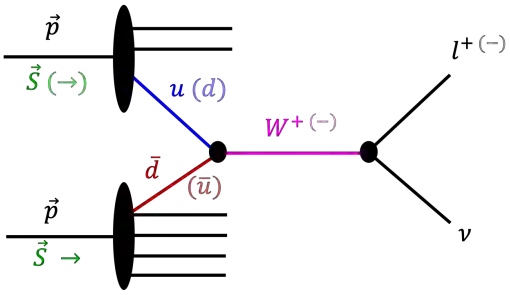

Figure 2: Feynman diagram showing parity violating W production. It requires the $u(d)$ quark must interact with a $\bar{d}(\bar{u})$ quark.

proton must interact with an anti-down quark from the other proton to produce a W or vice versa. This measurement is complementary to Semi-Inclusive DIS (SIDIS) as there is no fragmentation to tag the flavor. STAR measures the single-spin asymmetry A_L (equation (4.2)) of W's via its leptonic decay in longitudinal pp collisions,

$$A_L^{W^+} = \frac{\sigma^+ - \sigma^-}{\sigma^+ + \sigma^-} \sim \frac{\Delta\bar{d}(x_1)u(x_2) - \Delta u(x_1)\bar{d}(x_2)}{\bar{d}(x_1)u(x_2) + u(x_1)\bar{d}(x_2)} \tag{4.2}$$

where the "+" denotes positive helicity and "-" denotes negative helicity. The A_L measurement for $W^\pm$ from STAR in the region $|\eta| < 1.2$ is shown in Fig. 3. The lepton pseudorapidity is used to dial into the sea quark polarization. These data show a positive $\Delta\bar{u}$ in $0.05 < x < 0.25$. Furthermore, the NNPDF reweighting of the new data, shown in Fig. 4 in the blue band, shows a clear sea quark polarization asymmetry $\Delta\bar{u} > \Delta\bar{d}$ [5].

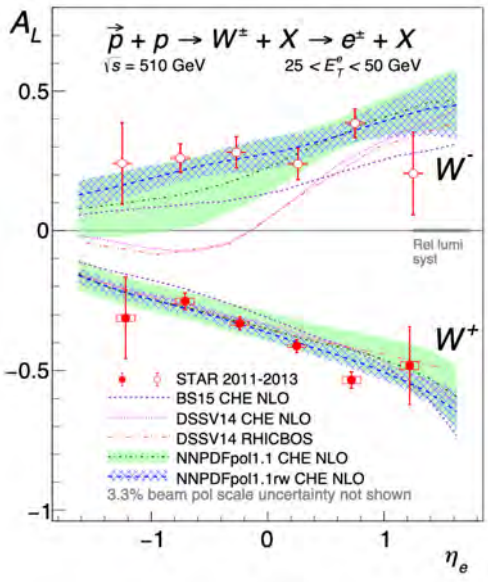

Figure 3: Measured A_L for $W^\pm$ vs. lepton psuedorapidity (η_e) together with theory expectations (curves and bands). Data shown are combined from 2011, 2012 and 2013 [5].

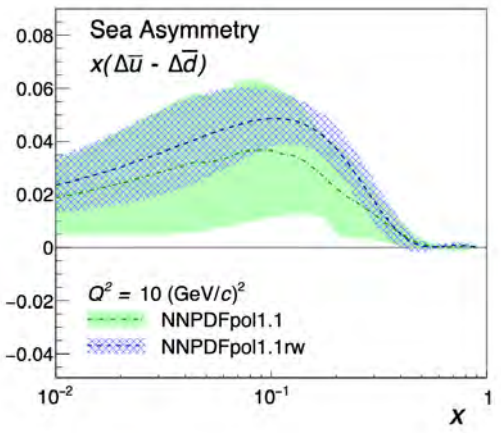

Figure 4: Difference in light sea-quark polarizations as a function of x at $Q^2 = 10$ GeV^2. The green band shows the NNPDFpol1.1 results before the 2013 STAR data shown in Fig. 3. The blue hatched band is a reweighting of the PDF after the 2013 STAR data was included. A clear sea quark polarization asymmetry of $\Delta\bar{u} > \Delta\bar{d}$ is seen [5].

The gluon polarization can be measured using jet, dijet and π^0 production at RHIC. Figure 5 shows the relative fractions of different processes that contribute to inclusive jet production as a function of $x_T = 2p_T/\sqrt{s}$. It shows that at low x_T gluon-gluon subprocesses dominate over the quark-quark subprocesses [6]. The longitudinal double-spin asymmetry (A_{LL}) for inclusive jets, defined in equation (4.3), in this regime is sensitive to the gluon polarization.

$$A_{LL} = \frac{\sigma^{++} - \sigma^{+-}}{\sigma^{++} + \sigma^{+-}} = \frac{1}{P_1 P_2} \frac{N^{++} - RN^{+-}}{N^{++} + RN^{+-}} \tag{4.3}$$

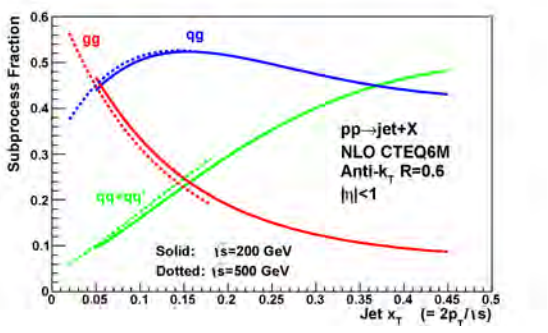

Figure 5: Subprocesses that dominate inclusive jet production as a function of x_T. At low x_T gluon-gluon scattering dominates [6].

In equation (4.3) σ is the inclusive jet cross section, P_1 and P_2 are the polarization of beam 1 and 2 respectively, R is the relative luminosity and N is the number of events with "++" denoting same helicity and "+-" denoting opposite helicity. Measurements of A_{LL} of inclusive jets at STAR mid-rapidity ($|\eta| < 1.0$) are shown in Fig. 6 for both $\sqrt{s} = 200$ GeV and 510 GeV energies. At both energies there is a clear asymmetry at low x_T. These results will provide important new constraints on the magnitude of the gluon polarization [6].

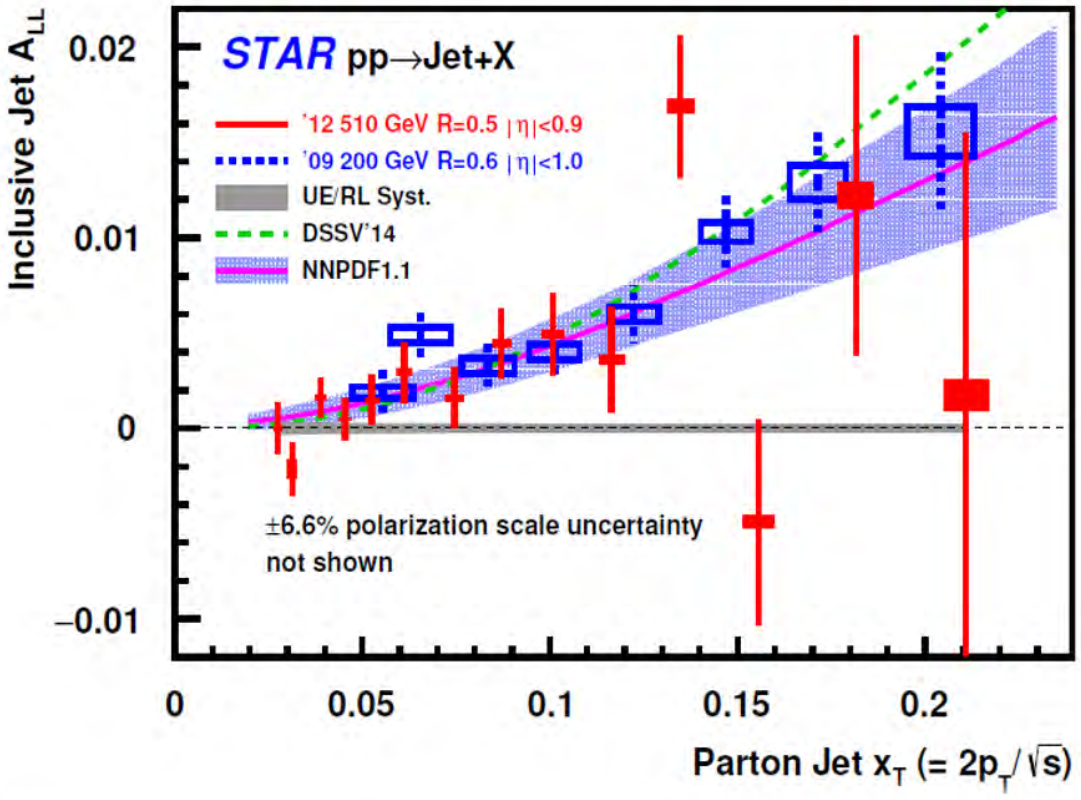

Figure 6: A_{LL} of inclusive jets as a function of x_T, where $x \approx x_T e^{\pm\eta}$. Data are for both 200 GeV and 510 GeV pp collisions. A clear asymmetry exists in the low x_T region [6].

Inclusive di-jet A_{LL} was also measured at STAR at various pseudorapidity bins or topologies. Figure 7 shows the measured A_{LL} in each topology where the designation central corresponds to the pseudorapidity bin $|\eta| < 0.3$ and forward/backward corresponds to $0.3 < |\eta| < 0.9$. It also shows the various x regions probed by the different bins, where

$$x_1 = \frac{1}{\sqrt{s}}(p_{T,3}e^{\eta_3} + p_{T,4}e^{\eta_4}) \tag{4.4a}$$

$$x_2 = \frac{1}{\sqrt{s}}(p_{T,3}e^{-\eta_3} + p_{T,4}e^{-\eta_4}) \tag{4.4b}$$

The x values as shown in the left panel of Fig. 7 become more equal as you go from forward-forward to central-central and forward-backward. These A_{LL} measurements, when combined with global analyses, will help to constrain the shape of $\Delta g(x)$ [6].

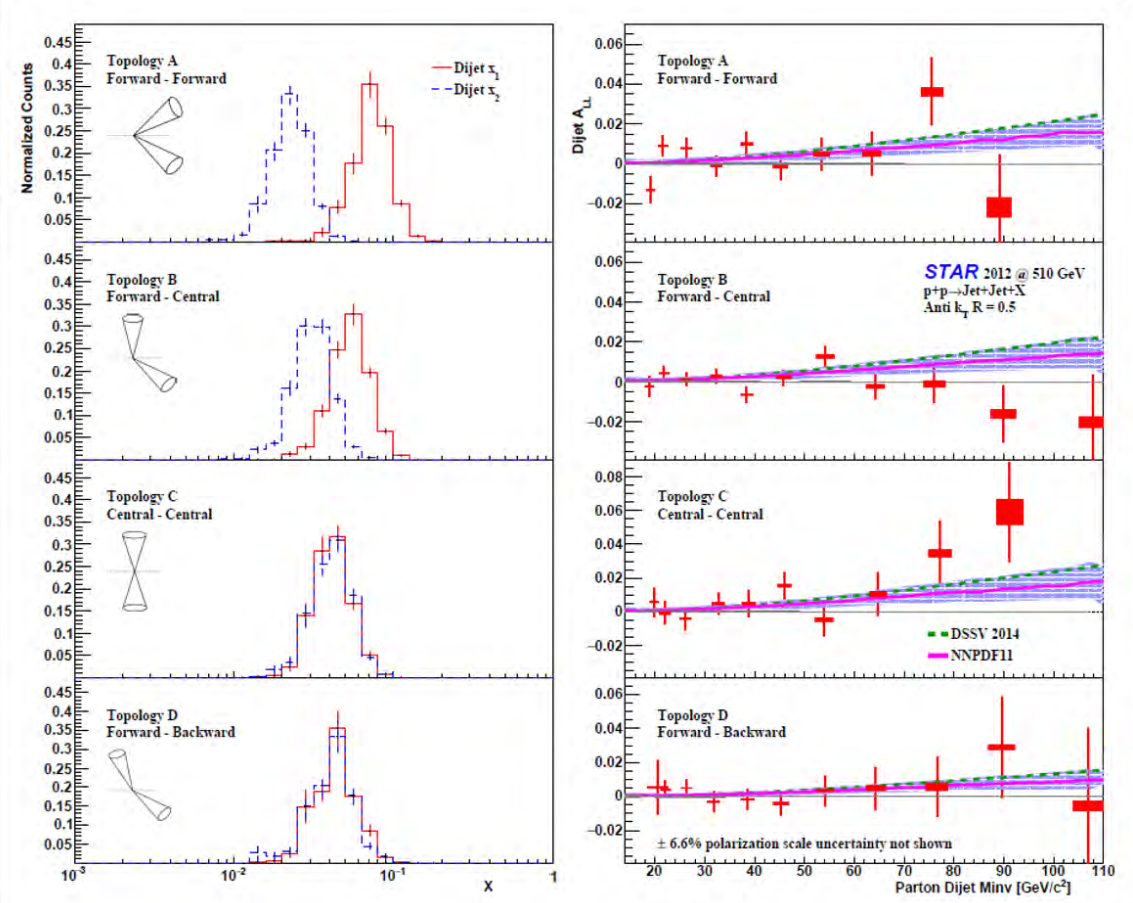

Figure 7: A_{LL} of inclusive dijets as a function of parton dijet invariant mass ($Minv$) at various η topologies. Central corresponds to the pseudorapidity bin $|\eta| < 0.3$ and forward/backward corresponds to $0.3 < |\eta| < 0.9$. Left panel shows the x of the two partons in the various psuedorapidity bins. As you go from forward-forward to central-central and forward-backward the x of the two partons becomes equal. These measurements will help to constrain the shape of $\Delta g(x)$ [6].

5 Transverse Structure of Proton

Transverse momentum dependent PDFs (TMD) are used to go beyond the one-dimensional picture of the nucleon by adding more degrees of freedom. This allows a three-dimensional picture of the proton momentum to be constructed. STAR has made measurements that are sensitive to several of the TMDs, one of which is transversity. The transversity TMD relates the transverse quark spin to the transverse nucleon spin $\delta q(x)$. Transversity is chiral odd and therefore needs an additional chiral-odd function (Collins fragmentation function $H_1^{\perp}$) to be accessible in a physics observable. The Collins asymmetry is the azimuthal distribution of hadrons inside a jet and is defined in equation (5.1)

$$A_{UT}^{sin(\phi_s - \phi_h)} = \frac{d\sigma^{\uparrow} - d\sigma^{\downarrow}}{d\sigma^{\uparrow} + d\sigma^{\downarrow}} \tag{5.1}$$

Here ϕ_s is the angle of the proton spin with respect to the proton-jet momentum plane and ϕ_h is the angle of the jet-pion momentum plane to the proton-jet momentum plane as depicted in Fig. 8; $d\sigma^{\uparrow(\downarrow)}$ is the cross section when spin is up (down) with respect to the proton momentum. The Collins asymmetry for $p^{\uparrow} + p \rightarrow jet + \pi^{\pm} + X$ at $\sqrt{s} = 500$ GeV at $0 < \eta < 1$ is shown in Fig. 9, where z is the fractional hadron momentum to the jet momentum i.e. $z = \frac{\text{hadron momentum}}{\text{jet momentum}}$. The asymmetry is with respect to the azimuthal distribution of pions inside jets. Figure 9 shows the asymmetry growing as z increases which is the first sign that TMDs survive at high Q^2 [7].

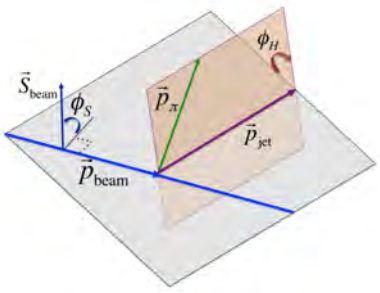

Figure 8: The angles used in the Collins asymmetry definition in equation (5.1) [7].

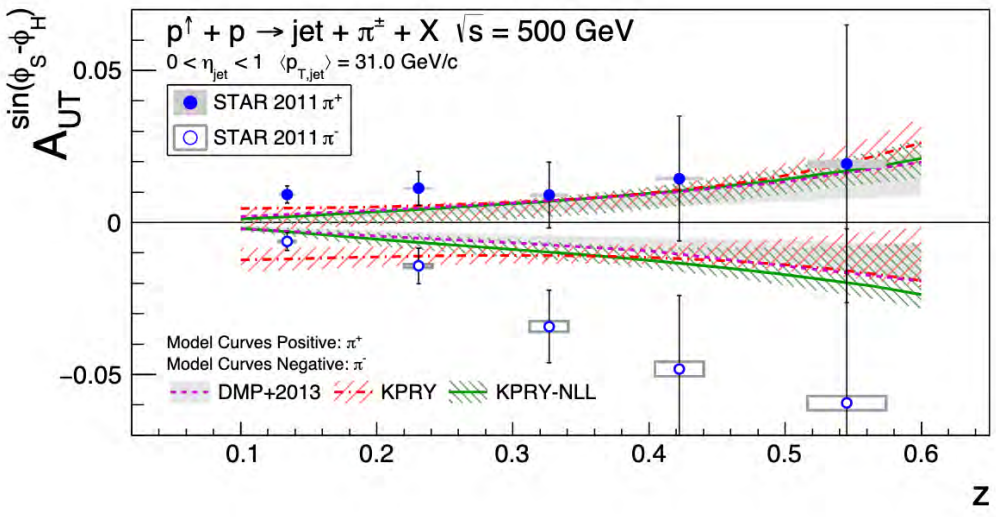

Figure 9: Measured Collins asymmetry A_{UT} as a function of z. This shows the first sign that TMDs survive at high Q^2 [7].

6 STAR Forward Upgrade Capabilities

To improve and expand on the measurements already discussed, STAR is in the process of upgrading several detector subsystems. RHIC data as of 2009 show $\int_{0.05}^{1} \Delta g dx \sim 0.2 \pm^{0.06}_{0.07}$ at $Q^2 = 10$ GeV^2 which is also depicted as the light blue band in Fig. 10. The dark blue band in Fig. 10 shows a projection with RHIC data up to and including the 2015 run. In order to constrain $\Delta g(x)$ at lower x either one has to go to higher $\sqrt{s}$, which is not feasible at RHIC, or larger pseudorapidity. The STAR forward upgrade will do the latter and extend STAR's forward capabilities in the region $2.5 < \eta < 4.0$ to go to lower x. Figure 11 shows the projected x_1 and x_2 for inclusive dijets with the proposed upgrade. In addition, the Collins asymmetry measurement shown in Fig. 9 can also be improved. Figure 12 shows the projected Collins asymmetry precision as well as the asymmetries

Detector	pp and pA	AA
EM calorimeter	$\sim 10\%/\sqrt{E}$	$\sim 20\%/\sqrt{E}$
Hadron calorimeter	$\sim 60\%/\sqrt{E}$	
Tracking system	Charge separation; photon suppression	$0.2 < p_T < 2$ GeV/c with 20-30% $* 1/p_T$

Table 1: Table of hardware requirements for STAR forward upgrade to achieve physics goals

obtained from transversity extractions for one jet p_T and psuedorapidity bin [8]. The black triangle points represent the uncertainties while the red curve indicates the asymmetries for π^+ and the blue curve indicates π^-. In fact, this projection shows only one of several x and Q^2 bins that the STAR forward upgrade will be able to access. Figure 13 shows both the current data on TMDs, which come from DIS experiments, and the projected x and Q^2 accessible with the STAR forward upgrade at RHIC as black filled squares. At $\sqrt{s} = 500$ GeV the new kinematic coverage of STAR will range from 0.05 to 0.5 in x and 10 to 100 GeV^2 in Q^2. In order to accomplish these tasks, the forward upgrade requires a tracking system to deliver good electron-hadron separation, as well as electromagnetic and hadronic calorimeters to provide hadron, π^0, and photon identification. Table 1 shows the individual requirements broken down by species and hardware performance [8].

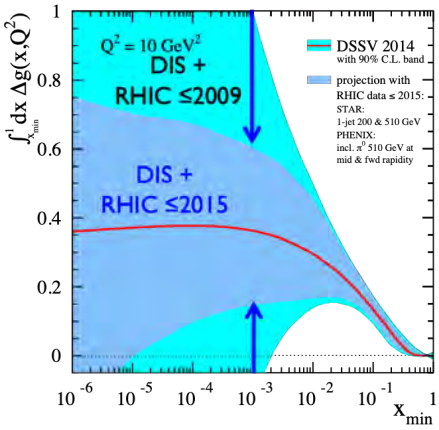

Figure 10: ΔG from DIS and RHIC data in light blue until 2009. Projected ΔG from RHIC data up to and including 2015 in darker blue.

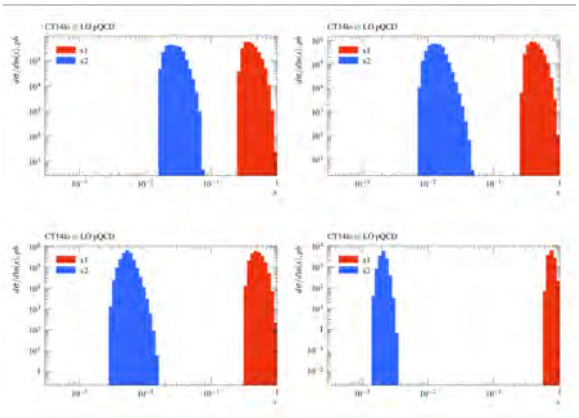

Figure 11: The projected dijet x_1 and x_2 range to be accessed by the STAR forward upgrade, where x_1 and x_2 are defined in equation (4.4).

7 STAR Forward Upgrade Design

The design of the STAR forward upgrade side view can be seen in Fig. 14. It spans $2.5 < \eta < 4.0$ with nearly 2π coverage. The trackers consist of three layers of silicon disks and 4 layers of small-strip Thin Gap Chamber (sTGC). The calorimeters consist of a preshower, an electromagnetic calorimeter (ECal), and a hadronic calorimeter (HCal).

The silicon disks will be located between 140 to 170 cm from the STAR interaction region (IR). Each disk contains 12 modules. They consist of an inner and outer portion that are connected via mechanical structures. A cooling system will also be installed. The sTGC modules consist of 4

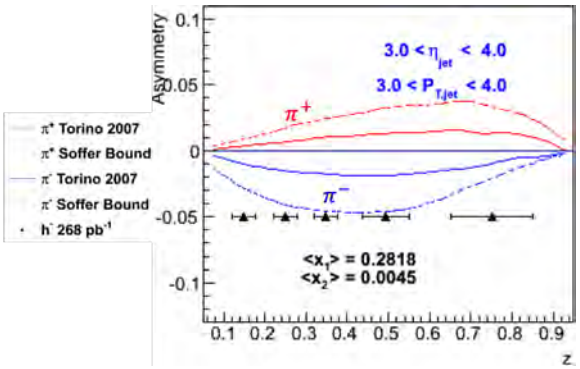

Figure 12: Projected Collins asymmetry uncertainties with pion asymmetries based on transversity extractions as a function of fractional energy z. The projected asymmetry uncertainties are the black triangles with the asymmetries of π^+ in red and π^- in blue. Solid and dashed designate the two different extractions. Only one jet p_T and pseudorapidity bin is shown.

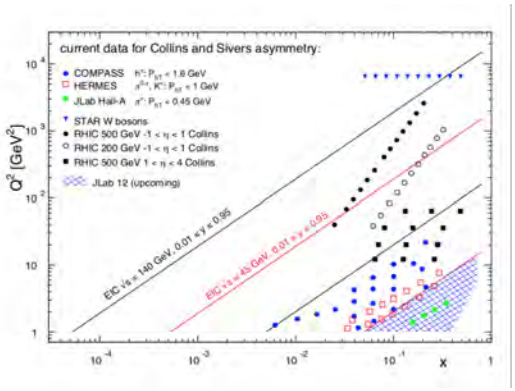

Figure 13: Current TMD data from SIDIS with the STAR forward upgrade projected region of coverage in black squares. One set of the black squares ($x = 0.05$ and $Q^2 = 10\,\mathrm{GeV}^2$) represents the kinematic region for which the Collins asymmetry was projected as shown in Fig. 12.

layers and will be located between 270 to 370 cm. Each layer is double sided to provide x, y and diagonal (45° with respect to x, y) coordinates. It has a position resolution of about 100 μm. It has almost 2π coverage as there needs to be room for the beam pipe support. The sTGC uses the same technology as the ATLAS design [9].

The ECal is a Pb/Sc sandwich that was repurposed from PHENIX. It has been modified to use SiPM readout. It is split into two halves that are located on North side of STAR (right of blue going beam) and South side of STAR (left of blue going beam) with no coverage above and below the beam pipe. It is positioned 7 m from the STAR IR and at a slight angle so that the front face of the ECal is oriented towards the IR to mitigate incident angle effects at this distance. It is $18X_0$ lengths long. The preshower will be a scintillator hodoscope. The hadronic calorimeter will be used for the first time at STAR and needs to be built from scratch. It is a steel (Fe) scintillator (Sc) sandwich with 20 mm Fe/3 mm Sc. It will also utilize SiPM readout and will be located directly behind the EM calorimeter and can be seen in Fig. 14. It is $\sim 4.5\lambda$ long and the lateral size of each HCal tower is 10x10 cm^2, i.e. one HCal tower covers an area roughly equal to a 2x2 set of towers in ECal [8].

8 Conclusions

STAR has made key measurements that have helped in our understanding of the proton structure. Results from longitudinally polarized pp collisions have shown a clear sea quark polarization asymmetry. Also, they have provided constraints for the magnitude of the gluon polarization and the shape of $\Delta g(x)$ using inclusive jets, and dijets at mid-rapidity. Measurements of the Collins asymmetry have shown the first sign that TMDs survive at high Q^2. The STAR forward upgrade plans to both improve on these measurements as well as explore a region of x and Q^2 that has yet to be probed with any facility. The STAR forward upgrade will accomplish this by installing a new tracking system and a new calorimeter system. This upgrade will utilize the newest available technology and build on RHIC and STAR's unique capabilities to carry out measurements in polarized pp collisions.

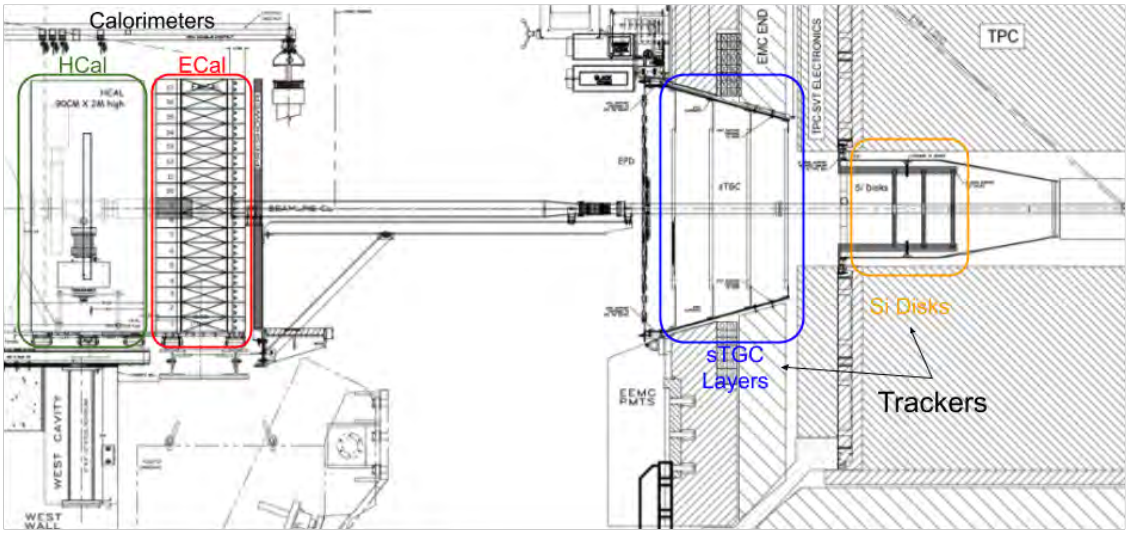

Figure 14: Side view of proposed STAR forward upgrade showing the various components to be installed and some of their details.

References

[1] E.-C. Aschenauer, C. Aidala, A. Bazilevsky, M. Diehl, R. Fatemi, C. Gagliardi, Z. Kang, Y. V. Kovchegov, J. Jalilian-Marian, J. Lajoie, D. V. Perepelitsa, R. Seidl, R. Sassot, E. Sichter-mann, M. Stratmann, S. Trentalange, W. Vogelsang, A. Vossen, and P. Zurita, *The RHIC Cold QCD Plan for 2017 to 2023: A Portal to the EIC*, arXiv:1602.03922.

[2] H. Hahn, E. Forsyth, H. Foelsche, M. Harrison, J. Kewisch, G. Parzen, S. Peggs, E. Raka, A. Ruggiero, A. Stevens, S. Tepikian, P. Thieberger, D. Trbojevic, J. Wei, E. Willen, S. Ozaki, and S. Y. Lee, *The RHIC design overview*, *Nuclear Instruments and Methods in Physics Research Section A: Accelerators, Spectrometers, Detectors and Associated Equipment* **499** (2003), no. 2 245–263.

[3] K. H. Ackermann et al., *STAR detector overview*, *Nuclear Instruments and Methods in Physics Research Section A: Accelerators, Spectrometers, Detectors and Associated Equipment* **499** (2003), no. 2 624–632.

[4] M. Anderson et al., *The STAR time projection chamber: a unique tool for studying high multiplicity events at RHIC*, *Nuclear Instruments and Methods in Physics Research Section A: Accelerators, Spectrometers, Detectors and Associated Equipment* **499** (mar, 2003) 659–678.

[5] **STAR** Collaboration, J. Adam et al., *Measurement of the longitudinal spin asymmetries for weak boson production in proton-proton collisions at* $\sqrt{s} = 510$ *GeV*, *Physical Review D* **99** (mar, 2019) 051102, [arXiv:1812.04817].

[6] **STAR** Collaboration, J. Adam et al., *Longitudinal double-spin asymmetry for inclusive jet and dijet production in pp collisions at* $\sqrt{s} = 510$ *GeV*, *Phys. Rev. D* **100** (sep, 2019) 52005, [arXiv:1906.02740].

[7] **STAR** Collaboration, L. Adamczyk et al., *Azimuthal transverse single-spin asymmetries of inclusive jets and charged pions within jets from polarized-proton collisions at* $\sqrt{s} = 500$ *GeV*, *Phys. Rev. D* **97** (aug, 2017) 32004, [arXiv:1708.07080].

[8] **STAR** Collaboration, *The STAR Forward Calorimeter System and Forward Tracking System beyond BES-II*. https://drupal.star.bnl.gov/STAR/starnotes/public/sn0648.

[9] A. Abusleme et al., *Performance of a full-size small-strip thin gap chamber prototype for the ATLAS new small wheel muon upgrade*, *Nuclear Instruments and Methods in Physics Research, Section A: Accelerators, Spectrometers, Detectors and Associated Equipment* **817** (may, 2016) 85–92, [arXiv:1509.06329].

Diffractive jet production in eletron-ion collisions

Guilherme Müller Peccini

E-Mail: guilherme.peccini@ufrgs.br

High Energy Physics Phenomenology Group (GFPAE) - Federal University of Rio Grande do Sul (UFRGS), Brazil

Presented at the Workshop of QCD and Forward Physics at the EIC, the LHC, and Cosmic Ray Physics in Guanajuato, Mexico, November 18-21 2019

Abstract

We investigate the diffractive gluon jet production in eletron-ion collisions at the energies of the EIC and the LHeC. In addition, the assumption that the diffractive mass is much bigger than the photon virtuality is taken, applying a model inspired in the GBW parametrization to describe the dipole amplitude. We show that the diffrative cross section is strongly sensitive to the saturation scale. Furthermore, we verify that it is possible to infer this scale from the experiment.

1 Introduction

The Electron - Ion Colliders will open the possibility of probing the hadronic structure in the regime of large partonic densities and high strong field strengths, which are expected to alter the linear evolution equations. The EICs allow the measurement of inclusive and exclusive observables which are afected by the enhancement of non-linear effects in terms of the nuclear mass number. [1, 2].

The EICs can perform a detailed investigation of the hadronic structure in the non-linear regime of QCD, determining the presence of gluon saturation effects, the magnitude of the associated non-linear corrections and what is the correct theoretical framework for their description. Such things can be accomplished by the enhancement of the non-linear effects with the nuclear mass number through the nuclear saturation scale, $Q^2_{s,A}$. In particular, within the parton saturation framework, the nuclear saturation scale, Q_s, is enhanced with respect to the nucleon one by a factor A^{Δ}, with $\Delta \simeq 2/9$ or less. For instance, for lead targets this increases the nuclear saturation momentum, $Q_{s,A}$, by a factor 3 in contrast to the proton one where $Q_{s,p}(x = 10^{-5}) \approx 1$ GeV.

A remarkable prediction of saturation formalism is the constant ratio of the diffractive versus inclusive cross sections observed at HERA in terms of the photon-proton centre-of-mass energy, $W_{\gamma^* p}$. Furthermore, it was verified that Diffractive Deep Inelastic Scattering (DDIS) is a semi-hard process [3], that is, the diffractive cross section is highly sensitive to the infrared cutoff given by $R_s = 1/Q_s(x)$. Thereby, DDIS clearly probes the transition region between the dilute and saturated regimes.

Deep Inelatic Scattering on large nuclei is one of the best ways to investigate gluon dynamics. This is due to the fact that strong gluon fields resulted from the large number of nucleons in a heavy nuclei lead to gluon saturation, which is the non-linear regime characterized by the saturation momentum scale, Q_s. In the case of large nuclei, Q_s may be very large, which allows us to perform perturbative calculations in the complex non-linear QCD dynamics of these strong gluon fields. An Electron Ion Collider would be an ideal facility to probe the wave functions of high energy nuclei as the high electron energy would make possible to probe deeper the particles structure. The experiments DESY-HERA, BNL-RHIC and CERN-LHC have already shown evidence of the saturation regime. However, the EICs would have a strong potencial to perform a profound investigation of these processes started at those accelerators. The European Muon Colaboration discovery at CERN that showed a specific pattern of nuclear modification of the DIS cross section as a function of Bjorken x reveals strong evidence that the momentum distributions of the quarks in a fast-moving nucleus are highly modificated by the binding and the nuclear environment. The EICs will be able to investigate the influence of the binding on the momentum distribution of sea quarks and gluons. Furthermore, for the first time it will determine the spatial distribution of quarks and gluons in a nulceus through diffractive and exclusive processes. Such an achievements are possible due to the wider kinematic regime in Q and x, as well as the high luminosity. [1]

There are many attempts to describe the diffractive contribution to the total cross section in DIS within perturbative QCD. One of them is based on the color dipole picture, which is a very successful approach to describe processes at high energies. In the next sections, we apply the dipole picture to describe diffractive inelastic scattering on nuclei, namely gold (Au) and lead (Pb). The process considered is $e + A \to e' + A + jet + X$, where the transverse momentum of the gluon from the $|q\bar{q}g\rangle$ component of the virtual photon is measured as a final-state jet. This paper is organized as follows: in the next section, we determine the expression for the diffractive differential cross section in terms of the transverse momentum scale of the gluon jet and the diffractive mass. Moreover, we discuss the ansatz proposed for the nuclear saturation scale. Afterwards, we show the results applying this formalism taking into account the EIC [4] and LHeC [5] center-of-mass energies, as well as considering different diffractive masses. Finally, we conclude the paper summarizing the main ideas that can be extracted from our results.

This proceeding is a preliminary study of Ref. [6], in which the High Energy mode of the LHeC (HE-LHeC) [7, 8] and the Future Circular Collider (FCC-eh) [9] are also considered. For a careful discussion and a better understanding on the calculations procedure, we quote the reference above.

2 Diffractive cross section calculation

The dipole approach is a convenient way to calculate observables at high energies, such as the total and diffrative cross sections once the dipole picture makes possible the factorization of the entire process, which in turn is divided in a QED (the photon fluctuating into a quark-antiquark pair) and a QCD (the interaction between the dipole and the hadron) sub-processes . Such a mechanism is only possible due to the fact that the time of fluctuation of the photon is much bigger than the time of interaction between the dipole and the target at high energies.

In this formalism, the photon fluctuates into a quark-antiquark pair of transverse size $r \sim 1/Q$, where Q^2 is the photon virtuality. The wave function corresponding to the photon fluctuating into this pair is taken from light cone perturbative theory, and is given by

$$|\Psi_T(z, \vec{r}, Q^2)|^2 = \frac{6\alpha_{em}}{4\pi^2} \sum_f e_f^2 [z^2 + (1-z)^2] \epsilon^2 K_1^2(\epsilon r) + m_f^2 K_0(\epsilon r), \tag{2.1}$$

$$|\Psi_L(z,\vec{r},Q^2)|^2 = \frac{6\alpha_{em}}{\pi^2}\sum_f e_f^2[Q^2z^2(1-z)^2K_0^2(\epsilon r)], \tag{2.2}$$

where $\Psi_T(z,\vec{r},Q^2)$ stands for the transverse part of the photon wave function, whereas $\Psi_L(z,\vec{r},Q^2)$ is its longitudinal contribution. The variable $\vec{r}$ is the relative transverse separation between the quark and the antiquark and $z(1-z)$ is the longitudinal momentum fraction of the quark (antiquark) whose flavor is f. Also in this picture, the total and diffractive cross sections can be calculated as follows:

$$\sigma_{L,T}^{tot}(x,Q^2) = \sum_f \int dz d^2\vec{r} |\Psi_{L,T}^f(z,\vec{r},Q^2)|^2 \, 2\int d^2\vec{b} N(x,\vec{r},\vec{b}), \tag{2.3}$$

$$\sigma_{L,T}^{diff}(x,Q^2) = \sum_f \int dz d^2\vec{r} |\Psi_{L,T}^f(z,\vec{r},Q^2)|^2 \int d^2\vec{b} |N(x,\vec{r},\vec{b})|^2. \tag{2.4}$$

In the above expressions, the variable ϵ is defined as $\epsilon = \sqrt{z(1-z)Q^2+m_f^2}$, where m_f is the quark mass of flavor f. For simplicity, we will only consider light quarks (u, d, s) with masses $m_u = m_d = m_s = 1.4\ GeV$. The quantities K_0 and K_1 are the Modified Bessel Functions of the Second Kind of order zero and one, respectively.

In this work our goal is to investigate the diffractive gluon jet production in diffractive dissociation of photons in DIS, analyzing the nuclear effects when considering nuclei as targets. The corresponding kinematical variables are the same as in the case of diffractive DIS [10]:

$$x = \frac{Q^2}{Q^2+W^2}, \tag{2.5}$$

$$x_{I\!P} = \frac{Q^2+M_x^2}{Q^2+W^2}, \tag{2.6}$$

$$\beta = \frac{Q^2}{Q^2+M_X^2}, \tag{2.7}$$

where x is the x-Bjorken and $x_{I\!P}$ is the longitudinal momentum fraction carried by the Pomeron. These variables are related as $x = \beta x_{I\!P}$.

Initially, the diffractive cross section is written in terms of Fock states of the incident virtual photon, $|\gamma^*\rangle = |q\bar{q}\rangle + |q\bar{q}g\rangle \ldots$, where the $q\bar{q}$ dipole is characterized by the wavefunctions in Eqs. (2.1) and (2.2). The second Fock state includes the emission of a soft gluon (small longitudinal momentum fraction, z_g) off a $q\bar{q}$ dipole. The transverse momentum of the gluon may be identified with the momentum of the jet closest to the rapidity gap. We are interested in this last component, which dominates in the kinematic regime where the diffractive mass, M_X, is bigger than the photon virtuality ($M_X^2 \gg Q^2$). The terms from jets started by quarks in such a kinematic domain are suppressed. According to the Pomeron language, this corresponds to a momentum fraction of the parton with respect to the diffractive exchange having $\beta \ll 1$. The diffractive mass is simply calculated as follows [11]:

$$M_X^2 = \frac{k_q^2}{z_q} + \frac{k_{\bar{q}}^2}{z_{\bar{q}}} + \frac{k_g^2}{z_g}. \tag{2.8}$$

This condition is satisfied by several configurations. However, the dominant contribution to the cross section is established by

$$\frac{k_g^2}{z_g} \gg \frac{k_q^2}{z_q}, \frac{k_{\bar{q}}^2}{z_{\bar{q}}}, Q^2, \tag{2.9}$$

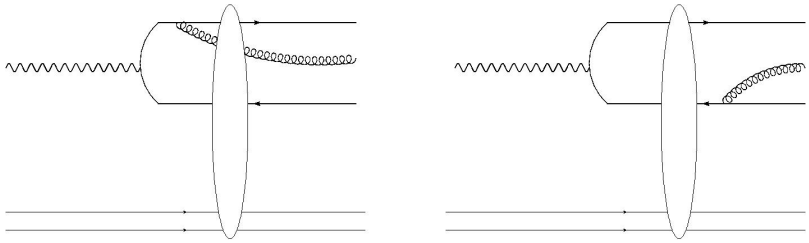

Figure 1: The $|q\bar{q}g\rangle$ component. Left diagram: the gluon emission takes place before the interaction with the nucleus. Right diagram: the gluon emission occurs after the interaction with the nucleus.

where k_q, $k_{\bar{q}}$ and k_g are the transverse momenta of the quark, antiquark and gluon, respectively, and z_q, $z_{\bar{q}}$ and z_g are their longitudinal momentum fractions.

The diffractive cross section for the production of a gluon with transverse momentum $k_\perp$ and rapidity y when considering a collision of a $q\bar{q}$ of transverse size r with the target has been derived in Ref. [11]. The most relevant diagrams include the cases where the interaction with the target occurs before and after the gluon emission, as seen in Fig. (1). The corresponding differential cross section in leading $\ln(1/\beta)$ accuracy is given by [11]:

$$\frac{d\sigma_{\rm diff}^{q\bar{q}g}}{d^2k_\perp dM_X} = \frac{2M_X}{Q^2+M_X^2}\int d^2\vec{r}d^2\vec{b}\,\rho(r,Q^2)\frac{d\sigma_g(\vec{r},\vec{b})}{d^2k_\perp dy}, \tag{2.10}$$

$$\frac{d\sigma_g(\vec{r},\vec{b})}{d^2k_\perp dy} = \frac{\alpha_s N_c^2}{4\pi^2 C_F}\,A(k_\perp,x_{0,1};\Delta\eta)A^*(k_\perp,x_{0,1};\Delta\eta),$$

where $\rho(r,Q^2)=\int dz(|\psi_T^\gamma(r,z;Q^2)|^2+|\psi_L^\gamma(r,z;Q^2)|^2)$ and $x_{0,1}=b\pm(r/2)$ (x_0 and x_1 are the transverse positions of the quark and the antiquark, respectively). The rapidity gap can be written as $\Delta\eta=\log(1/x)=Y-y$ with $Y=\log(1/x)$ being the total rapidity. The function $A(k_\perp,x_0,x_1;\Delta\eta)$ is written as a function of the elastic S-matrix taking into account the collision between one dipole and the target evolved at the rapidity $\Delta\eta$, $S(x_0,x_1;\Delta\eta)$, as well as the elastic S-matrix for the collision of two dipoles and the target, $S^{(2)}(X_0,x_g,x_1;\Delta\eta)$, where x_g is the gluon transverse coordinate [11]. To understand the use of $S^{(2)}$, we recall the BK evolution equation [12, 13], where the gluon emitted by the dipole is treated as a quark-antiquark pair at large N_c limit. Regardless the specific form of S-matrices, the quantity $k_\perp^2 d\sigma/d^2k_\perp dM_X$ rises as $k_\perp^2$ for small gluon transverse momenta and falls as $1/k_\perp^2$ for large ones. A maximum takes place for a typical transverse momentum where parton saturation becomes relevant, i.e., $(k_\perp)_{max}\propto Q_s$ where $Q_s(x)$ is the saturation scale.

In Ref. [11] a simplified model for the S-matrices has been used. Inspired in the GBW parametrization [3] and neglecting correlations between the two dipoles in $S^{(2)}$, they read as

$$\begin{aligned} S(x_0,x_1;\Delta\eta) &= e^{-\frac{(Q_s r)^2}{4}}\Theta(R-|b|)+\Theta(|b|-R),\\ S^{(2)}(x_0,x_1,x_g;\Delta\eta) &= e^{-\frac{Q_s^2[(x_0-x_g)^2+((x_g-x_1)^2]}{4}}\Theta(R-|b|)\\ &\quad+\Theta(|b|-R), \end{aligned} \tag{2.11}$$

where R is the target radius and the saturation scale depends on the x variable. The Heaviside functions appearing in S-matrices will give an overall normalization factor after b-integration in Eq. (2.10) in the form $\bar{\sigma}_0=\pi R^2$. The parameter $\sigma_0=2\pi R^2=2\bar{\sigma}_0=27.32$ mb for proton target has been fitted from HERA data on proton structure functions at small-x [3].

Taking into account the GBW-like parametrization, Eqs. (2.11), the integration over impact parameter in Eq. (2.10) can be done. That model contains the main features also presented in more

sophisticated models for the dipole amplitude. This will give a semi-analytical expression for the differential cross section:

$$k^2 M_X \frac{d\sigma^{\gamma}_{diff}}{d^2 k dM_X} = \frac{\alpha_s N_c^2 \sigma_0}{4\pi^2 C_F} \frac{M_X^2}{M_X^2 + Q^2} \int \frac{r dr d\theta}{(k/(rQ_s^2) - rQ_s^2/(4k))^2 + cos^2(\theta)} \, \rho(r, Q^2) \, e^{-r^2 Q_s^2/2}$$

$$\times \left[\left(cos\left(\frac{1}{2} krcos(\theta)\right) - e^{-k^2/(2Q_s^2) + Q_s^2 r^2/8} \right)^2 + \frac{Q_s^4 r^4}{4k^2} sin^2\left(\frac{1}{2} krcos(\theta)\right) + \frac{rQ_s^2}{k} cos(\theta) \, sin\left(\frac{1}{2} krcos(\theta)\right) \right.$$

$$\left. \times \left(cos\left(\frac{1}{2} krcos(\theta)\right) - e^{-k^2/(2Q_s^2) + Q_s^2 r^2/8} \right) \right]. \tag{2.12}$$

To avoid the uncertainties concerning the running coupling α_s and the parameter σ_0 (which comes from the GBW parametrization), we define the following variable:

$$\sigma(k, Q^2, Q_s) = \frac{1}{\alpha_s \sigma_0} \left(\frac{M_X^2 + Q^2}{M_X^2} \right) M_X \frac{d\sigma^{\gamma}_{diff}}{d^2 k dM_X}. \tag{2.13}$$

Regarding the saturation scale, Q_s, in Eq. (2.12), we take its form as defined in GBW model:

$$Q_s(x_P) = (x_0/x_{I\!P})^{\lambda/2} \, GeV \tag{2.14}$$

Above, the parameters λ and x_0 were taken by fitting HERA data and their values are $\lambda = 0.248$ and $x_0 = 4.2 \times 10^{-5}$ [14], respectively. The variable $x_{I\!P}$ is defined in Eq. (2.6).

As we aim to investigate collisions of dipoles on nuclei, we shall consider the nuclear saturation scale, $Q_{s,A}$. Hence, we take the ansatz proposed in Ref. [15], where the nucleus growth depends on the quotient of the transverse parton densities to the power $1/\delta$:

$$Q_{s,A}^2 = Q_{s,p}^2 \left(\frac{A\pi R_p^2}{\pi R_A^2} \right)^{1/\delta}, \tag{2.15}$$

where $Q_{s,p}$ is the saturation scale of a single proton, R_p is the proton radius and R_A is the nucleus radius. For the later, we take the usual parametrization $R_A = (1.12A^{1/3} - 0.86A^{-1/3})$. The quantities δ and πR_p^2 are fitted by χ^2 minimization and their values are 0.79 ± 0.02 and $\pi R_p^2 = 1.55 \pm 0.02 \; fm^2$, respectively. At this point, it is important to mention that in this work we are considering the Glauber multiple scattering approach. At high energies, it is completely justified as the particle passes through the nucleus in a very short time, which make possible to neglect the change of the positions of nucleons [2]. In the next section we carry out the numerical calculations of Eq. (2.12) taking into consideration two different nuclei, namely Gold (Au) and Lead (Pb). The former will be utilized at the EIC, whereas the later at the LHeC. In addition, we discuss the main points concerning the results.

3 Numerical results

We start our analysis presenting the plot of the quantity $\sigma(k, Q^2, Q_{s,A})$ as a function of jet transverse momentum, $k_\perp$, at the center-of-mass energies of the EIC and the LHeC referred in Table I. The results are shown in Fig. (2) and take into account two distinct values for the diffractive mass, M_X. The more prominent feature is the plateau for $k_\perp \lesssim 1$ GeV for the EIC and $k_\perp \lesssim 3$ GeV for the LHeC. This feature is also observed in ep case [11] and explained by the fact that the differential cross section $k_\perp^2 d\sigma/d^2 k_\perp dM_X$ rises as $k_\perp^2$ for small transverse momentum as referred already. This happens regardless the particular model for the S-matrices. In opposite, at relative large $k_\perp$, the cross section falls as $1/k_\perp^2$ and the transition region is driven by the nuclear saturation scale. The

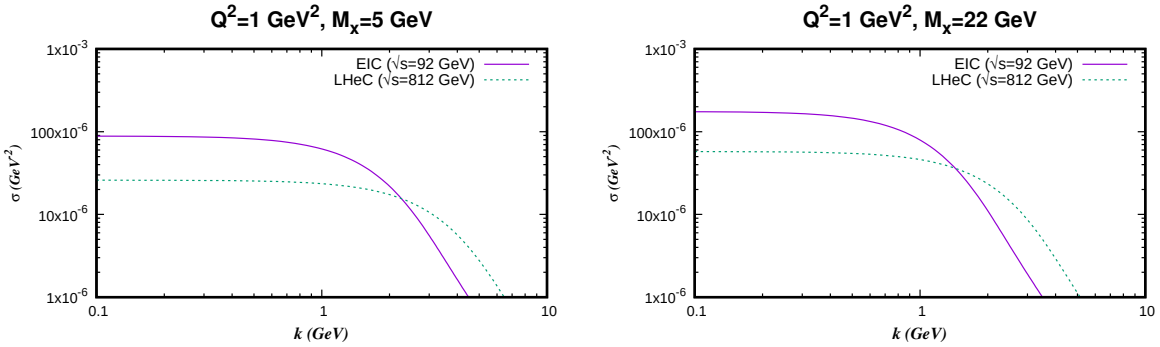

Figure 2: $\sigma(k, Q^2, Q_s)$ versus k for two different diffractive masses.

Table 1: The design center-of-mass energy (in unities of GeV) for electron-nucleus collisions in the machines EIC and LHeC.

Collider	E_e	E_A	$\sqrt{s}$
EIC	21	100	92
LHeC	60	2760	812

difference between the curves of the EIC and the LHeC is due to the fact that the values of $x_{I\!P}$ are distinct in each case. As a result, the saturation effects set in at different points, which can be understood by means of the distinct values of $Q_{s,A}$.

In Fig. (3), $k_\perp^2 d\sigma/d^2k_\perp dM_X$ as a function of $k_\perp$ is plotted. The curves for both colliders are displayed. The bumps can be clearly seen in each case and their positions are translated by means of the $x_{I\!P}$-dependence of saturation scale. The interface between the non-linear regime of QCD and the linear one is given by the position of the peak.

At last, we considered $k_\perp^2 d\sigma/d^2k_\perp dM_X$ in terms of the scaling ratio k/Q_s. As verified in Fig. (4) , this ratio is $k/Q_{s,A} \approx 1.5$ for the EIC and the LHeC regardless the value of Q^2. Using such a fact the absolute value of $Q_{s,A}$ could be determined by considering a wide interval of Q^2 in the limit $\beta \ll 1$.

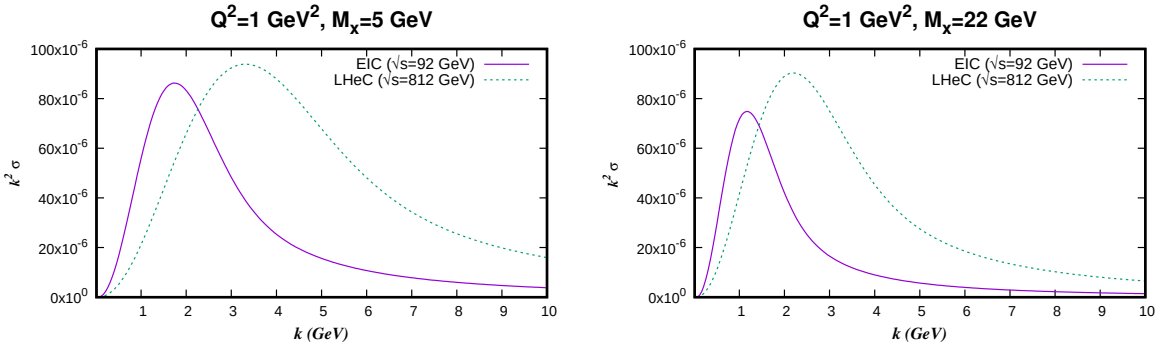

Figure 3: $k^2\ \sigma(k, Q^2, Q_s)$ versus k for two different diffractive masses.

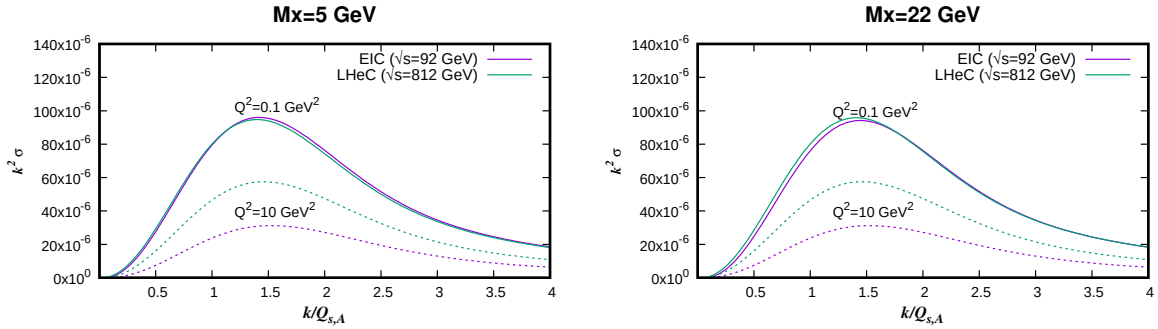

Figure 4: $k^2\ \sigma(k, Q^2, Q_s)$ as a function of k/Q_s for two different diffractive masses.

4 Summary and Conclusions

In this work, we have investigated the diffractive jet production in the small-β region, which is translated by high diffractive mass, $M_X \gg Q^2$. In the color dipole formalism the main contribution comes from the $q\bar{q}g$ Fock state and the jet is associated with the soft gluon emitted by the quark-antiquark pair. We look into the possibility of the future EIC and LHeC colliders for the measurement of gluon jet diffractive cross section and the consequent extraction of the nuclear saturation scale. A simplified model for the S-matrices has been used and this might be an origin of possible theoretical sources of uncertainty. An example of such sources is the dipole-nucleus amplitude, for which more realistic expressions could be applied (Glauber model, Glauber-Gribov model or numerical solutions of BK equation). Besides, a different ansatz for the nuclear saturation scale can be used. Furthermore, we demonstrated that the nuclear saturation scale, $Q_{s,A}$, could be extracted from data in terms of $x_{I\!P}$ by measuring the bump in the differential cross section $\kappa^2 d\sigma/d^2k_\perp dM_X$ as a function of jet transverse momentum. Correlated procedures for extracting saturation scale from data are already known in literature. For example, in Ref. [16] the proton saturation scale, $Q_{s,p}$, is obtained from the multiplicities of charged hadrons in pp collisions considering local parton-hadron duality and the geometric scaling property (similar investigations were done for pA [17] and AA collisions [18]). We present the probable region where the peaks occur, $\kappa \approx a \times Q_{s,A}(x)$ (a is a constant of order of unity), and it was shown that the quantity $\kappa^2\sigma^{\rm scaled}$ presents universal behavior as a function of the scaling variable $\tau = \kappa/Q_s$.

Acknowledgements

This work was financed by the Brazilian funding agencies CNPq and CAPES.

References

[1] A. Accardi et al., *Electron Ion Collider: The Next QCD Frontier*, *Eur. Phys. J.* **A52** (2016), no. 9 268, [arXiv:1212.1701].

[2] V. P. Goncalves, M. V. T. Machado, F. S. Navarra, and D. Spiering, *Coulomb corrections to inclusive cross sections at the future Electron - Ion Collider*, *Phys. Rev.* **C97** (2018), no. 1 015204, [arXiv:1708.09279].

[3] K. J. Golec-Biernat and M. Wusthoff, *Saturation in diffractive deep inelastic scattering*, *Phys. Rev.* **D60** (1999) 114023, [hep-ph/9903358].

[4] B. S. Page, X. Chu, and E. C. Aschenauer, *Experimental Aspects of Jet Physics at a Future EIC*, *Phys. Rev.* **D101** (2020), no. 7 072003, [arXiv:1911.00657].

[5] **LHeC Study Group** Collaboration, J. L. Abelleira Fernandez et al., *On the Relation of the LHeC and the LHC*, arXiv:1211.5102.

[6] G. Peccini, L. Moriggi, and M. Machado, *Investigating the diffractive gluon jet production in lepton-ion collisions*, arXiv:2003.13882.

[7] **LHeC, PERLE** Collaboration, O. Brüning and M. Klein, *Exploring the energy frontier with deep inelastic scattering at the LHC*, *J. Phys. G* **46** (2019), no. 12 123001.

[8] F. Bordry, M. Benedikt, O. Brüning, J. Jowett, L. Rossi, D. Schulte, S. Stapnes, and F. Zimmermann, *Machine Parameters and Projected Luminosity Performance of Proposed Future Colliders at CERN*, arXiv:1810.13022.

[9] **FCC** Collaboration, A. Abada et al., *FCC Physics Opportunities: Future Circular Collider Conceptual Design Report Volume 1*, *Eur. Phys. J. C* **79** (2019), no. 6 474.

[10] C. Marquet, *A Unified description of diffractive deep inelastic scattering with saturation*, *Phys. Rev.* **D76** (2007) 094017, [arXiv:0706.2682].

[11] K. J. Golec-Biernat and C. Marquet, *Testing saturation with diffractive jet production in deep inelastic scattering*, *Phys. Rev.* **D71** (2005) 114005, [hep-ph/0504214].

[12] I. Balitsky, *Operator expansion for high-energy scattering*, *Nucl. Phys. B* **463** (1996) 99–160, [hep-ph/9509348].

[13] Y. V. Kovchegov, *Small x F(2) structure function of a nucleus including multiple pomeron exchanges*, *Phys. Rev.* **D60** (1999) 034008, [hep-ph/9901281].

[14] K. Golec-Biernat and S. Sapeta, *Saturation model of DIS : an update*, *JHEP* **03** (2018) 102, [arXiv:1711.11360].

[15] N. Armesto, C. A. Salgado, and U. A. Wiedemann, *Relating high-energy lepton-hadron, proton-nucleus and nucleus-nucleus collisions through geometric scaling*, *Phys. Rev. Lett.* **94** (2005) 022002, [hep-ph/0407018].

[16] T. Osada and T. Kumaoka, *Saturation momentum scale extracted from semi-inclusive transverse spectra in high-energy pp collisions*, *Phys. Rev.* **C100** (2019), no. 3 034906, [arXiv:1904.10823].

[17] L. McLerran and M. Praszalowicz, *Fluctuations and the rapidity dependence of charged particles spectra in fixed centrality bins in pA collisions*, *Annals Phys.* **372** (2016) 215–225, [arXiv:1507.05976].

[18] C. Andres, A. Moscoso, and C. Pajares, *Universal geometrical scaling for hadronic interactions*, *Nucl. Phys.* **A901** (2013) 14–21, [arXiv:1212.3102].

Recent results from the TOTEM collaboration at the LHC

Christophe Royon

E-Mail: christophe.royon@ku.edu

Department of Physics and Astronomy, The University of Kansas, Lawrence KS 66047, USA

Presented at the Workshop of QCD and Forward Physics at the EIC, the LHC, and Cosmic Ray Physics in Guanajuato, Mexico, November 18-21 2019

We describe the most recent results from the TOTEM collaboration at the LHC, namely the elastic cross section measurements at a center-of-mass on 2.76, 7, 8 and 13 TeV. No structure or resonance is observed at high t at high center-of-mass energies. A pure exponential form of $d\sigma/dt$ is excluded both at 8 and 13 TeV. Accessing the very low t region allows measuring the ρ parameter at 13 TeV.

1 Method to measure elastic events at the LHC

The TOTEM collaboration measured the elastic $pp \rightarrow pp$ cross sections by detecting both intact protons in the final state and vetoing on activities in the main CMS detector. It installed sets of vertical roman pot detectors at about 147 and 220-240 meters from the interaction point that have good acceptance in detecting intact protons in elastic interactions. The elastic event trigger requires the presence of one intact proton on each side of the interaction point on UP-DOWN or DOWN-UP configurations. In addition to the roman pots detectors, the TOTEM collaboration installed two inelastic telescopes called T_1 and T_2 covering respectively the region $3.1 < |\eta| < 4.7$ and $5.3 < |\eta| < 6.5$ for charged particle p_T above 100 and 40 MeV, respectively. Requesting no activity in $T1$ and $T2$ allows suppressing 92% of inelastic background.

Before the TOTEM measurements, it is worth noticing that the predictions of elastic cross sections were showing large differences by orders of magnitude especially at large t. Some models even predicted the existence of diffractive structures at medium t at LHC energies. Elastic events allow probing soft diffraction and Pomeron exchange at low t, diffractive structures at medium t and parton scattering and perturbative QCD effects at larger t.

In Fig. 1, we display the different domains of measurement for the $d\sigma/dt$ elastic cross section. At very low t, the cross section is proportional to $1/t^2$ (Coulomb region) and at higher t, we reach the nuclear region where the cross section is proportional to e^{bt}. Between these two regions, we need to take into account the interferences between the nuclear and Coulomb cross sections (called C-N interference in the figure or CNI) where we can measure the ρ parameter, the ratio of the imaginary part to the real part of the elastic cross section. At higher t, we reach the resonance or

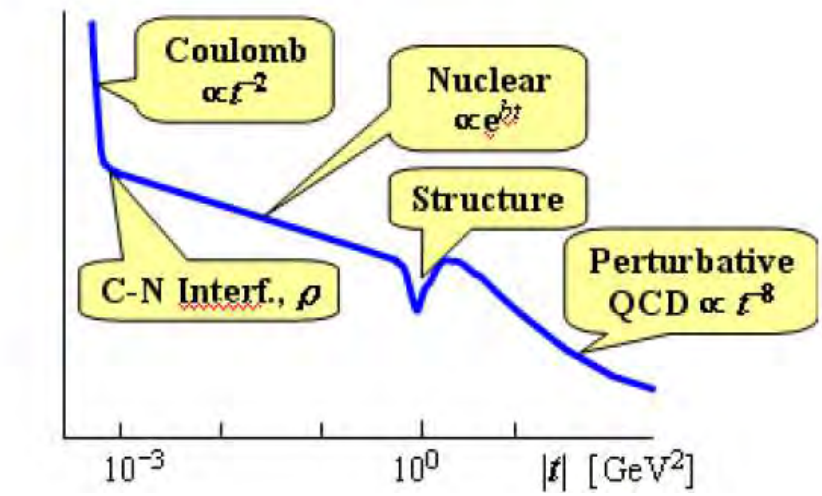

Figure 1: Schematic of elastic cross section measurement.

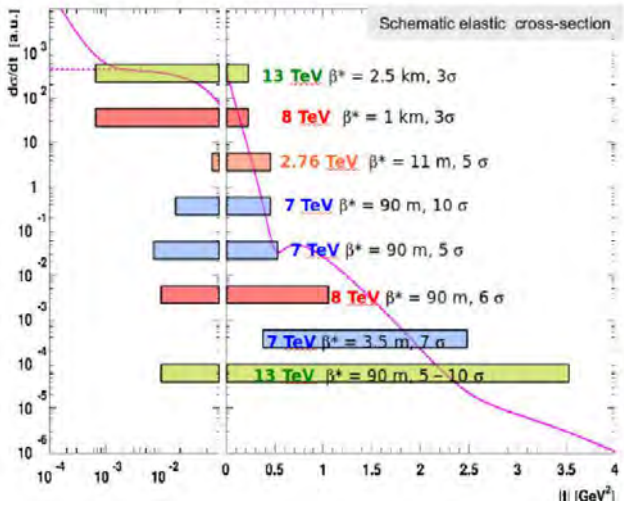

Figure 2: Different kinematical domains and β^* values where the elastic cross section $d\sigma/dt$ was measured by the TOTEM experiment.

"structure" region and at even higher t, the perturbative QCD region where the cross section varies as $1/t^8$. It means that one needs to access a very wide range in t if one wants to measure precisely the elastic cross section.

For this sake, many different beam lattices were used at the LHC as shown in Fig. 2. Accessing very low t values means going to very low angles of scattered protons. High values of β^* such as 2.5 km at 13 TeV or 1 km at 8 TeV allow reaching low values of t, and the CNI region. The accumulated luminosity is small at high β^* and higher values of β^* are used to cover the higher t region in order to collect more luminosity since the cross falls exponentially as a function of t.

Technically, in oder to measure the elastic cross section as a function of t, one needs to count the number of elastic protons as a function of t in the TOTEM roman pot detectors with a precision better than 2 or 3%. Measuring the cross section at very low t in the CNI region requires going

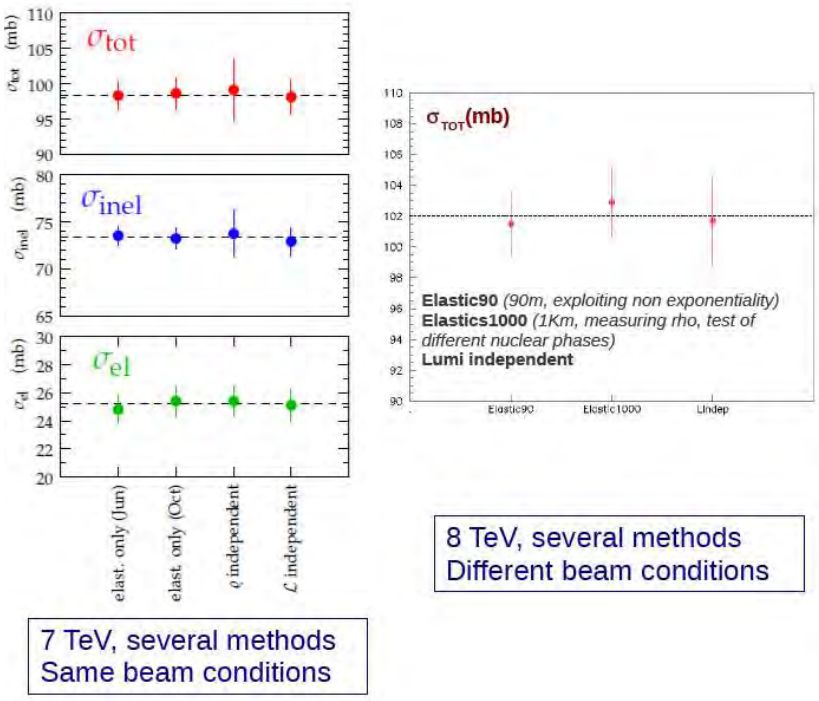

Figure 3: Measurements of the elastic, inelastic and total cross sections at a center-of-mass energy of 7 and 8 TeV using the different methods described in the text.

down to proton scattering angles of 3.5μrad, or t ~6.5 10^{-4} GeV^2. This requires the special high β^* beam optics as we mentioned already, detectors at $\sim$ 1.5 mm from LHC beam axis, spatial resolution well below 100 μm and no significant inactive edge ($< 100\mu$m).

2 TOTEM measurements

2.1 Total cross section and ρ measurements

The number of elastic events N_{el} is measured by tagging the protons in the roman pot detectors while vetoing on the T_1 and T_2 telescopes, while the number of inelastic events N_{intel} is counted using the activity in T_1 and T_2. The method to extract the total cross sections uses the optical theorem

$$L\sigma_{tot}^2 = \frac{16\pi}{1+\rho^2}(dN_{el}/dt)_{t=0} \tag{2.1}$$

$$L\sigma_{tot} = N_{el} + N_{inel} \tag{2.2}$$

where L is the integrated luminosity, ρ the ratio of the real to the imaginary part of the total cross section, and σ_{tot} the total cross section. It leads to three different methods to extract σ_{tot}

- The luminosity independent measurement

$$\sigma_{tot} = \frac{16\pi}{(1+\rho^2)}\frac{(dN_{el}/dt)_{t=0}}{(N_{el}+N_{inel})} \tag{2.3}$$

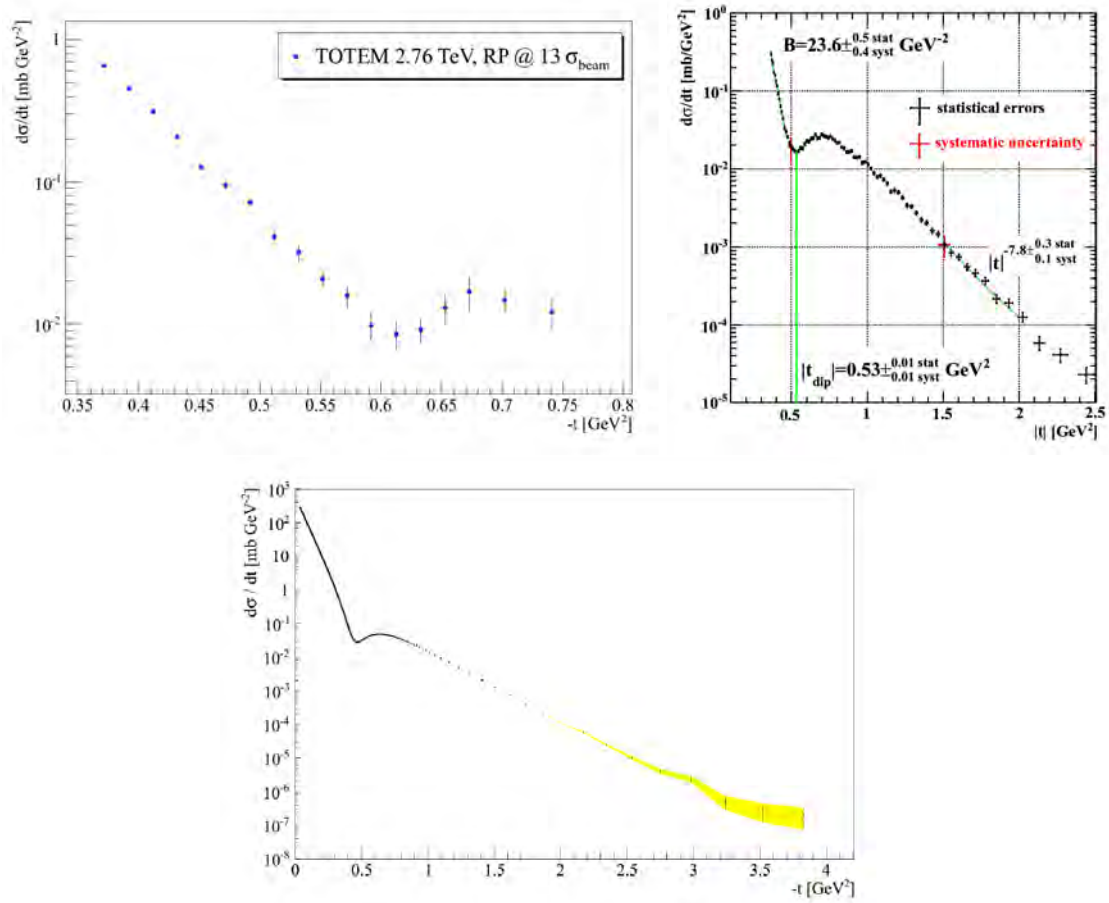

Figure 4: Elastic $d\sigma/dt$ cross sections measured by the TOTEM collaboration at center-of-mass energies of 2.76, 7 and 13 TeV.

- The luminosity dependent measurement (elastic only)

$$\sigma_{tot}^2 = \frac{16\pi}{(1+\rho^2)} \frac{1}{L} (dN_{el}/dt)_{t=0} \tag{2.4}$$

- The ρ independent measurement

$$\sigma_{tot} = \sigma_{el} + \sigma_{inel} \tag{2.5}$$

At very low t, in the CNI region, $d\sigma/dt$ can be rewritten as

$$\frac{d\sigma}{dt} \sim |A^C + A^N(1 - \alpha G(t))|^2 \tag{2.6}$$

where A^C and A^N are the Coulomb and Nuclear amplitudes, and $G(t)$ the interference term. The differential cross section is sensitive to the phase of the nuclear amplitude, and in the CNI region, both the modulus and the phase of the nuclear amplitude can be used to determine

$$\rho = \frac{Re(A^N(0))}{Im(A^N(0))} \tag{2.7}$$

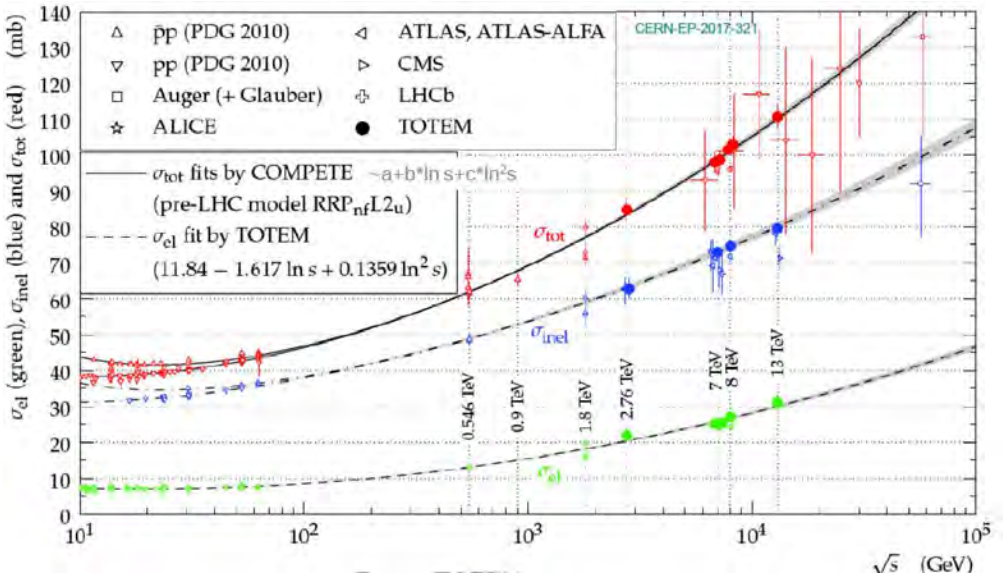

Figure 5: Elastic, inelastic and total cross sections measured at the LHC by the ALICE, ATLAS, CMS, LHCb and TOTEM collaborations compared to previous measurements and to fits performed by the TOTEM and COMPETE collaborations

where the modulus is constrained by the measurement in the hadronic region and the phase by the t dependence.

The three independent methods to measure the elastic, inelastic and total cross sections are in good agreement, and as an example, the results are shown in Fig. 3 for a center-of-mass energy of 7 and 8 TeV. In addition, the elastic, inelastic and total cross section measurements performed by all LHC experiments are shown in Fig. 5. The total cross section at high energies is compatible within uncertainties with previous results from cosmic ray experiments. The increase of σ_{el}/σ_{tot} with energy is confirmed at LHC energies up to 13 TeV. A recent measurement of the total cross section from LHCb at 13 TeV is also compatible with TOTEM results [2]. It is worth noticing that there is a discrepancy of about 1.9σ at 8 TeV between ATLAS and TOTEM results, and new measurements by ATLAS at 13 TeV will be of great interest in order to check if this discrepancy persits at higher center-of-mass energies. As we will see in the following, ρ was also measured using the β^* =2500 m data.

2.2 Measurements of $d\sigma/dt$ and implications

The t-dependent measurements of the elastic cross section for center-of-mass energies of 2.76, 7 and 13 TeV are shown in Fig. 4. We note the presence of a dip and a maximum towards $|t| \sim 0.5-0.6$ GeV^2 at all center-of-mass energies [1]. The dip position in t also decreases with increasing $\sqrt{S}$. The other noticeable result is that there is no structure at high t at high center-of-mass energies as shown in Fig 4 contrary to what some parameterizations assumed before the LHC era.

The B-slope of the elastic $d\sigma/dt$ cross section is shown in Fig. 6. It is found to be larger at 13 TeV than at lower center-of-mass energies and a linear behavior (lns) is compatible up to $\sqrt{s} < 3$ TeV, but it becomes non-linear at higher energy. An attempt to fit the elastic cross section $d\sigma/dt$ using a usual simple exponential fit at low t was performed

$$d\sigma/dt = A\exp(-B(t)|t|) \tag{2.8}$$

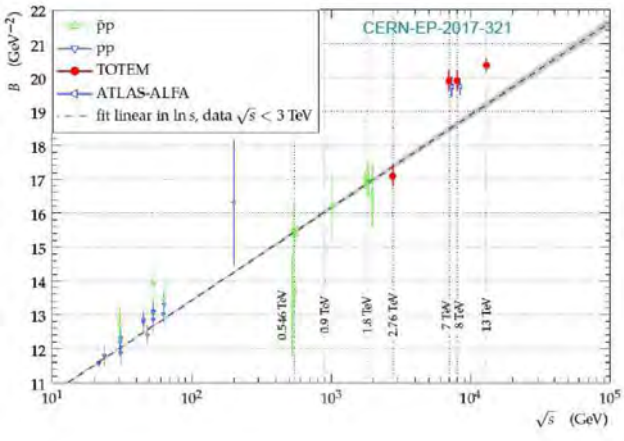

Figure 6: B-slope of the elastic cross section as a function of center-of-mass energy.

and different polynomial fits of $B(t)$ were used

- 1st order polynomial fit ($N_b = 1$): $B = b_1$, seen as a reference
- 2nd order polynomial fit ($N_b = 2$): $B = b_1 + b_2 t$
- 3rd order polynomial fit ($N_b = 3$): $B = b_1 + b_2 t + b_3 t^2$

A pure simple exponential form ($B = b_1$) is excluded at 7.2σ with 8 TeV data as shown in Fig. 7, where we display the relative difference with the ($N_b = 1$) fit. The uncorrelated uncertainties are in red and the full systematic in yellow. Similar results were found using 13 TeV data.

The very precise measurement of the total cross section at 13 TeV down to very low $|t|$ allows to measure with high accuracy the ρ parameter, $\rho = 0.09 \pm 0.01$ [4]. The values of the total cross section σ_{tot} and the ρ parameter as a function of $\sqrt{s}$ are shown in Fig. 8. They are compared to a linear, or a quartic fit to σ_{tot} as a function of $\sqrt{s}$ as well as to a combined linear and quartic fit. σ_{tot} data clearly favor the combined fit whereas the ρ measurement at 13 TeV favors the linear fit. The difference between these two observables can be interpreted as an additional colorless exchange not introduced in these simple fits, namely the Odderon or 3-gluon exchanges. In order to have better evidence for the existence of the Odderon, it is useful to compare directly pp and $p\bar{p}$ cross sections. pp and $p\bar{p}$ data from the TOTEM and D0 [5] are shown in Fig. 9. Even if data were not taken at the same $\sqrt{s}$, it is worth noticing that the pp data at 2.76 TeV show a dip and maximum whereas $p\bar{p}$ data do not show such a structure. The idea is to identify characteristic features of pp data and compare them with $p\bar{p}$ results, for instance the dip and bump that are not visible in $p\bar{p}$ interactions. While some quantitative studies are still being performed by the D0 and TOTEM collaborations, it is clear that a natural explanation for the difference between both colliders is due to Odderon exchanges.

3 Conclusion

In this article, we reviewed the most recent results from the TOTEM collaboration. Accessing low values of t allowed the TOTEM collaboration to measure the elastic $d\sigma/dt$ cross section at 2.76, 7, 8, and 13 TeV with unprecedented precision. The B-slope of the elastic cross section is found to be larger at 13 TeV. The dip position in $d\sigma/dt$ decreases with $\sqrt{S}$ and no structure or resonance is

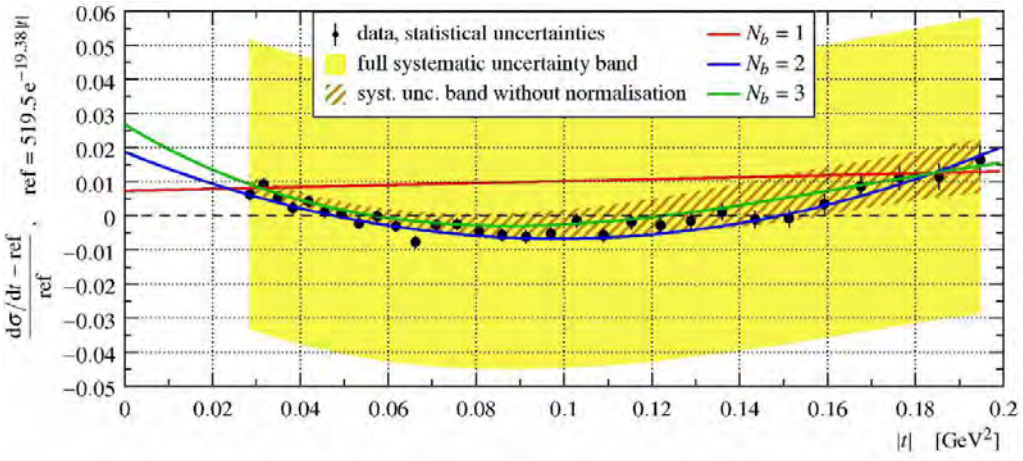

Figure 7: Non-exponential behavior of TOTEM elastic data at a center-of-mass energy of 8 TeV

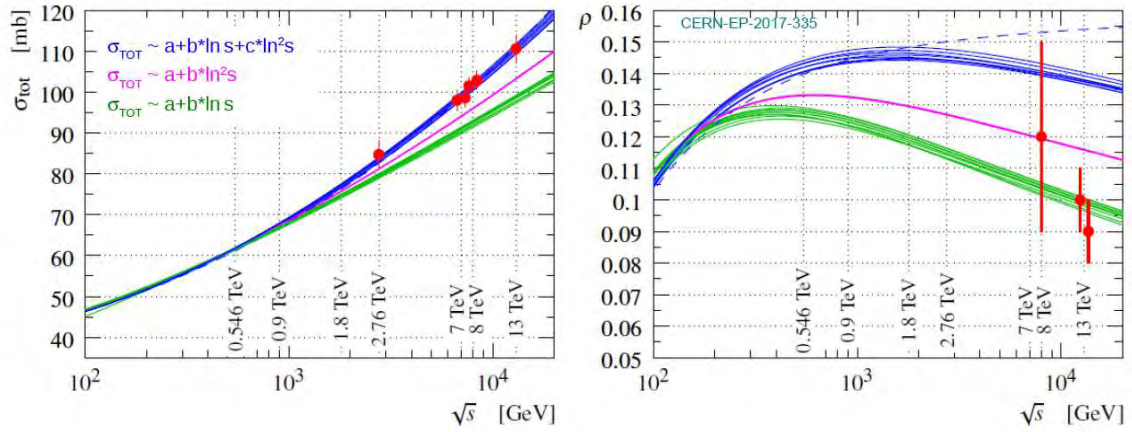

Figure 8: Measurements of the total cross sections and the ρ parameter as a function of $\sqrt{s}$ compared to fits using linear, quartic and a combination of linear and quartic terms.

observed at high t at high center-of-mass energies. The high precision on data allowed to show that a pure exponential form of $d\sigma/dt$ is excluded both at 8 and 13 TeV. Going to very low t allowed to measure ρ at 13 TeV and ρ and $d\sigma/dt$ cannot be easily described within the same model. This can be interpreted as the possible existence of the Odderon. The observation of a potential difference between pp and $p\bar{p}$ elastic cross sections would lead to a clean observation of the Odderon.

Acknowledgements

The author thanks the support from the Department of Energy, contract DE-SC0019389.

References

[1] TOTEM Coll., Eur. Phys. J. C**80** (2020) no.2, 91; TOTEM Coll., Eur. Phys. J. C**79** (2019) no.10, 861; TOTEM Coll. Eur. Phys.J. C**79** (2019) no.2, 103; TOTEM Coll., Eur. Phys. J. C**76** (2016) no.12, 661; TOTEM Coll.,

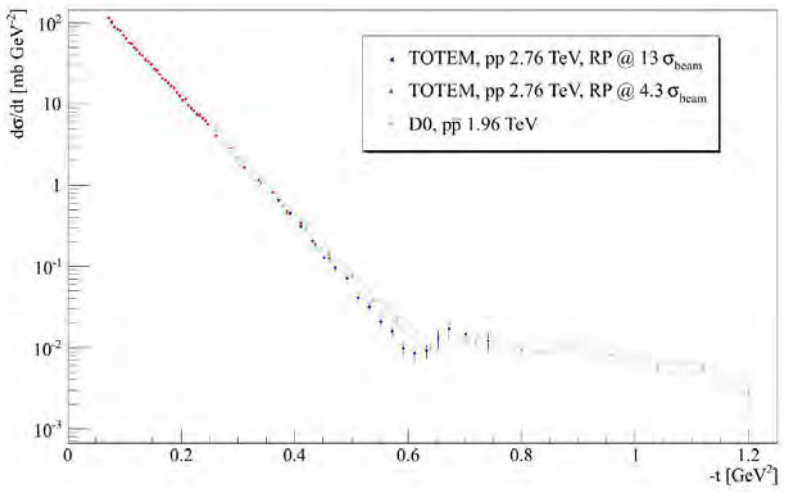

Figure 9: Comparison between the pp TOTEM cross section measurement at 2.76 Tev and the $p\bar{p}$ measurement from D0 at 1.96 TeV.

EPL **101** (2013) no.2, 21004; TOTEM Coll., EPL **101** (2013) no.2, 21002; TOTEM Coll., EPL **101** (2013) no.2, 21003; TOTEM Coll., Phys. Rev. Lett. **111** (2013) no.1, 012001; TOTEM Coll., EPL **96** (2011) no.2, 21002; TOTEM Coll., EPL **95** (2011) no.4, 41001.

[2] LHCb Coll., JHEP **1806** (2018) 1000.

[3] TOTEM Coll., Nucl. Phys. B**899** (2015) 527;

[4] TOTEM Coll., Eur. Phys. J. C**79** (2019) no.9, 785.

[5] D0 Coll., Phys. Rev. D **86** (2012) 012009.

PPS results and prospects from CMS/TOTEM collaborations

Christophe Royon

E-Mail: christophe.royon@ku.edu

Department of Physics and Astronomy, The University of Kansas, Lawrence KS 66047, USA

Presented at the Workshop of QCD and Forward Physics at the EIC, the LHC, and Cosmic Ray Physics in Guanajuato, Mexico, November 18-21 2019

Abstract

We describe the most recent results from the Proton Precision Spectrometer from the CMS and TOTEM collaborations, namely the first observation of exclusive di-lepton production at high mass at the LHC, and the prospects concerning the sensitivity to quartic anomalous couplings..

1 Exclusive diffraction and photon-exchange

We will first define what we call “Exclusive" diffraction. The first left diagram of Fig. 1 corresponds to Double Pomeron Exchange in inclusive diffraction. In this event, both protons are intact in the final state and two Pomerons are exchanged. Gluons are extracted from each Pomeron in order to produce jets (or diphotons, Ws...). Some energy is “lost" in Pomeron remnants. The three other diagrams in Fig. 1 are exclusive in the sense that the full energy is used to produce the diffractive object. In other word, there is no energy loss in Pomeron remnants. The second diagram corresponds to exclusive diffraction [1], the third one to photon exchanges and the last one to photon Pomeron exchanges that produce vector mesons. Exclusive events are specially interesting since it is possible to reconstruct the properties of the exclusively produced object from the tagged proton. By comparing the information from the central CMS detector and the protons, it is possible to reduce the backgorund to a negligible level [2].

2 The Precision Proton Spectrometer

The CMS-TOTEM Precision Proton Spectrometer [3] (PPS) was installed recently in order to detect and measure intact protons in the final state that lead to a possible better identification of exclusive events. The LHC magnets bend the scattered protons outside the beam envelope. The roman pots detectors are located at about 210-220 m from the center part of the CMS detector and cover a region in diffractive mass between typically 350 and 2000 GeV in standard luminosity runs at the LHC, depending on the exact beam lattice. A schematic view of the PPS roman pot detectors is

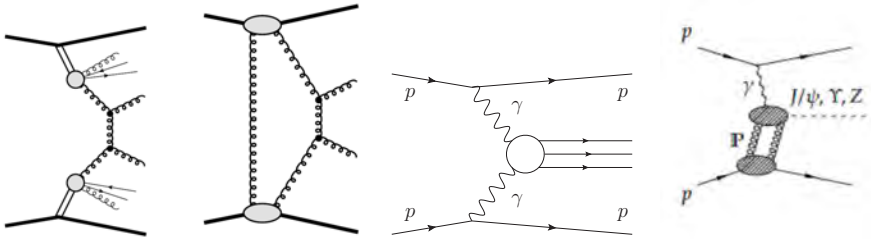

Figure 1: Diagrams of inclusive and exclusive diffractive processes.

shown in Fig. 2. Two kinds of detectors are hosted in PPS. The Silicon pixel and strip detectors allow to measure precisely the position of the intact proton and their distance from the beam axis, allowing to measure ξ, the proton fractional momentum loss, and t, the transferred energy squared at the proton vertex. In addition, timing detectors made of ultra-fast Silicon or diamond detectors allow measuring the proton time-of-flight.

The PPS detector started taking data in 2016 and could accumulate about 15 fb^{-1} in 2016, and about 115 fb^{-1} between 2016 and 2018. While the full data set is still being analyzed, we will describe the first observation of exclusive di-leptons using 9.4 fb^{-1}. Roman pots are being inserted routinely during normal data taking at the LHC.

One of the most difficult aspects of dealing with roman pot detectors is to align them with high precision with respect to the beams. The procedure is described in Fig. 3. The first step is the absolute alignment. The elastic $pp \to pp$ events in a special alignment run are used where both horizontal and vertical roman pots get very close to the beam. This allows to obtain an absolute alignment of all vertical detectors with respect to the beam. The alignment of roman pots with respect to each other is then performed using inclusive events. This leads to the black points in Fig. 3. The second step is to perform a relative alignment. The inclusive sample of protons triggered by CMS in standard runs is used and the distribution of proton track positions is matched to that of alignment as illustrated in Fig. 3 in blue and red points.

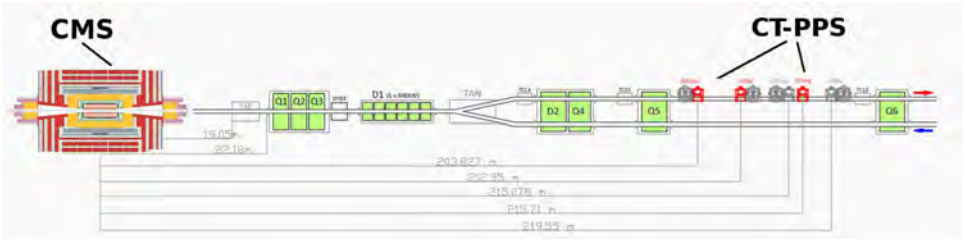

Figure 2: Schematic view of the PPS detector by the CMS and TOTEM collaborations. The detectors are only depicted on one side of CMS for simplicity. Both sides of CMS are equipped with similar roman pot detectors.

3 Exclusive dilepton processes

The CMS and TOTEM collaborations measured in 2016 the exclusive di-lepton production with 9.4 fb^{-1}. The corresponding diagrams are shown in Fig. 4. The LHC is turned into a $\gamma\gamma$ collider and the flux of quasi-real photons is computed using the Equivalent Photon Approximation (EPA). Using the PPS detector, CMS and TOTEM measured exclusive di-lepton production by tagging one intact proton in the final state. This is the first time the semi-exclusive di-lepton processes are

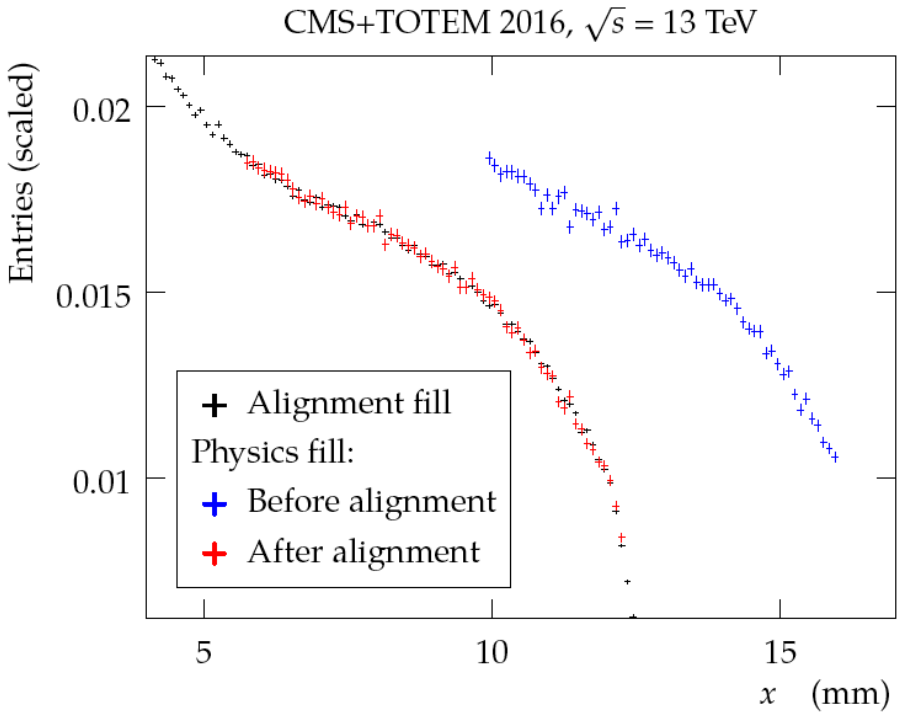

Figure 3: Alignment procedure of the PPS detectors.

measured with proton tag at high mass. In Fig. 4, the two left diagrams correspond to the signal whereas the rightmost diagram is part of the background. The reason that only one proton is requested to be tagged is that less than one event is expected for double tagged events with about 10 fb^{-1} of data due to the mass acceptance above about 350 GeV for the forward proton detectors.

A pair of opposite sign muons or electrons with $p_T > 50$ GeV and $M_{ll} > 110$ GeV above the Z boson peak is requested. In order to suppress background, there is a veto on additional tracks around the di-lepton vertex (within 0.5 mm) and leptons are required to be back-to-back, $|1 - \Delta\Phi/\pi| < 0.006$ for electrons (0.009 for muons) as shown in Fig. 5. The main background is due to Drell-Yan di-lepton production with the intact proton originating from pile up events. This background is estimated using Drell-Yan Z events in data and extrapolating from the Z peak region to our exclusive di-lepton signal region. 40 events (17 $\mu\mu$ and 23 ee) are found with protons in the PPS acceptance and 20 (12 $\mu\mu$ and 8 ee) show a less than 2σ matching between the values of ξ computed using the TOTEM roman pots and using the di-lepton measured in CMS as shown in Fig. 6 [4]. This leads to a significance larger than 5σ to observe 20 events for a background of 3.85 $(1.49 \pm 0.07(stat) \pm 0.53(syst)$ for $\mu\mu$ and $2.36 \pm 0.09(stat) \pm 0.47(syst)$ for $ee)$. As expected, no event was double tagged with an intact proton on each side.

4 Anomalous coupling studies

Using PPS, it is also possible to search for $\gamma\gamma\gamma\gamma$ anomalous couplings in a very clean way. Within the acceptance of the PPS detectors during standard high luminosity runs at the LHC (basically for a di-photon mass above 350 GeV), it is possible to show that the exclusive production of di-photons is completely dominated by photon exchange processes and gluon exchanges can be neglected [6]. The QCD and QED diagrams leading to exclusive di-photon production are shown in Fig. 7. The

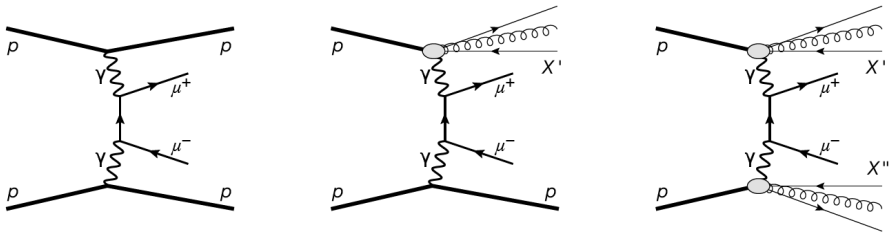

Figure 4: Diagrams leading to di-muon production via photon exchanges.

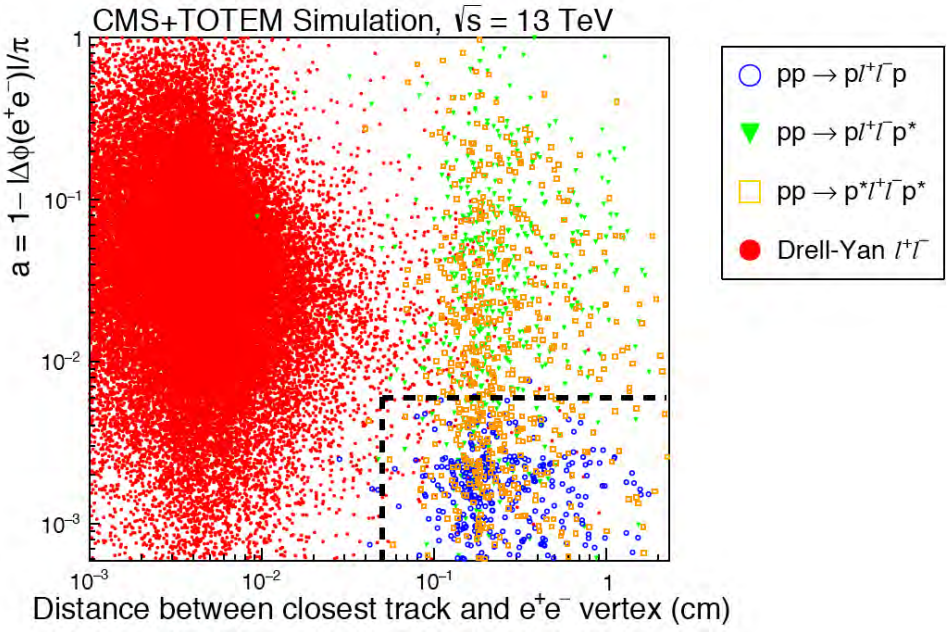

Figure 5: Correlation between the acoplanarity and the distance between the closest track and the e^+e^- vertex. The exclusive signal is in blue, while the single and double dissociative events are respectively in green and orange. The Drell-Yan background is in red.

di-photon exclusive cross sections are given in Fig. 8 for different contributions: QCD contribution in full purple line, QED contributions from quark and lepton loops in dashed green line, W loop contribution in dotted red line, and the total QED contribution in black dashed dotted line. We note that the QCD contribution can be neglected above a di-photon mass of 200 GeV. It means that measuring two photons in CMS and two protons in TOTEM corresponding to the same interactions is a photon-induced process.

Four-photon couplings can be modified by loops of new particles or produced resonances that decay into two photons. In case of loops $\zeta_1 = \alpha_{em}^2 Q^4 m^{-4} N c_{1,s}$ where the coupling depends only on the fourth power of the charge and mass of the charged particle, and on spin, $c_{1,s}$. This leads to ζ_1 of the order of 10^{-14}-10^{-13}. In case of resonances, $\zeta_1 = (f_s m)^{-2} d_{1,s}$ where f_s is the $\gamma\gamma X$ coupling of the new particle to the photon, and $d_{1,s}$ depends on the spin of the particle. For instance, 2 TeV dilatons lead to $\zeta_1 \sim 10^{-13}$.

The number of events for 300 fb^{-1} as a function of di-photon mass is displayed in Fig. 9 for signal and background. The exclusive di-photon and double Pomeron exchange (DPE) backgrounds are found to be negligible at high mass. The only backgrounds that contribute at high mass are the

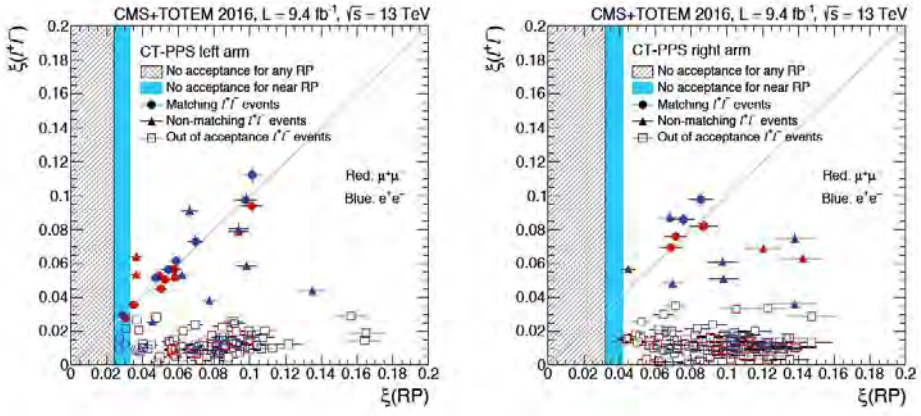

Figure 6: Correlation between the ξ values computed using the TOTEM roman pots and the di-lepton measured in CMS. The 20 semi-exclusive events are indicated in red. The left (right) plot displays the left (right) arm of TOTEM.

non-diffractive di-photon production + pile up and di-lepton production + pile up where leptons are misidentified as photons. Pile up events can be as large as 50 at the LHC at high luminosity and a typical pile up event contaminating our sample will be made of one di-photon non-diffractive event and two intact protons originating from soft diffractive events.

Since the signal only shows two photons and two intact protons in the final state, we measure all final state particles. That allows us to obtain a negligible background for 300 fb^{-1} at the LHC. The basic idea is to compare the proton missing mass and the di-photon mass as shown in Fig. 10, left [6]. The signal peaks around 1.0 and the gaussian width is due to the detector resolution whereas the pile-up background leads to a much flatter distribution since the two protons are not related with the two photons. The same requirement can be performed using the difference in rapidity between the di-photon and di-proton systems, as shown in Fig. 10, right. This leads to a background of less than 0.1 event for 300 fb^{-1} [6]. The gain on sensitivity compared to other methods at the LHC without detecting intact protons is more than two orders of magnitude on the $\gamma\gamma\gamma\gamma$ anomalous coupling, reaching values down to a few 10^{-15}. It is worth noticing that, without exclusivity cuts described in Fig. 10, the background would be much larger for 300 fb^{-1}, namely about 80.3 events. We also extrapolated our results to high luminosity LHC for a luminosity of about 3000 fb^{-1}, and the sensitivity can be even improved by a factor 10 as shown in Fig. 11 in a conservative way.

Looking for exclusive di-photon events with tagged protons can be directly applied to the search for axion-like particles (ALPs) at high mass [9]. The ALP would be produced by $\gamma\gamma$ interactions and would decay into two photons. The sensitivity in the coupling versus ALP mass is shown in Fig. 12 and we see the gain of about two orders of magnitude in coupling at high mass using this method with 300 fb^{-1} at the LHC. We also note that this is complementary to looking for exclusive di-photons in pPb, $PbPb$, and $ArAr$ collisions at lower masses of ALPs. This is due to the fact that the cross section is enhanced by a factor Z^4 in heavy ion collisions but the sensitivity at high mass is reduced to a large suppression at small impact parameter due to the size of the heavy ion [10].

The gain of two orders of magnitude on photon anomalous couplings is also true for $\gamma\gamma WW$ and $\gamma\gamma ZZ$ whereas the gain reaches three orders of magnitude for $\gamma\gamma\gamma Z$ [5, 8]. The search for anomalous couplings with tagged protons is now being pursued by the PPS collaboration.

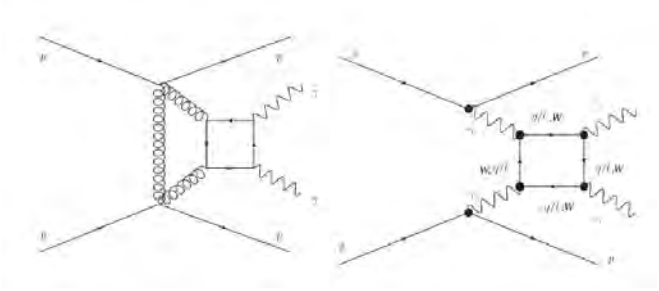

Figure 7: Exclusive di-photon production. Left: QCD process, Right: QED process.

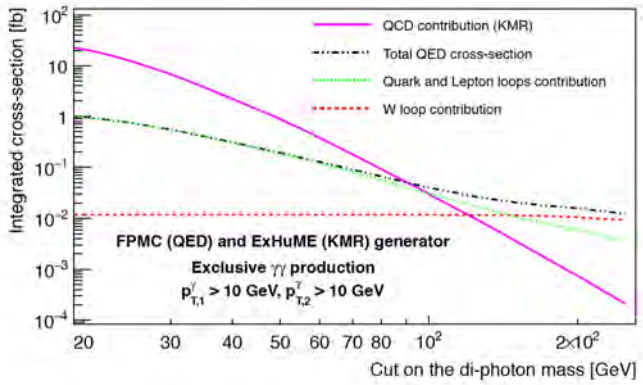

Figure 8: Exclusive di-photon cross section above a given diphoton mass (in abscissa) for different processes.

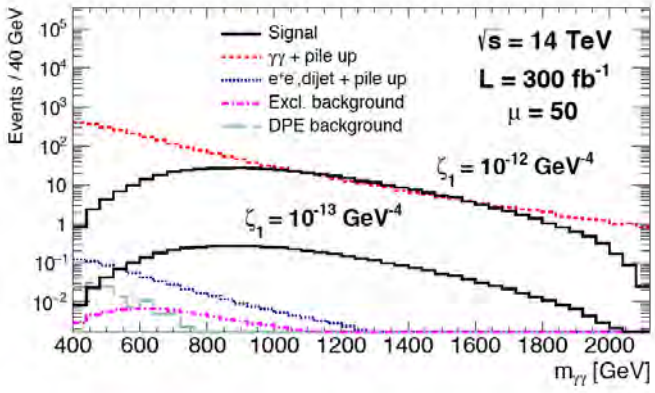

Figure 9: Number of events as a function of the di-photon mass for signal ($\zeta_1 = 10^{-12}$ and 10^{-13} GeV^{-4}) and background.

5 Conclusion

In this report, we first described the first observation of high-mass exclusive dilepton production, leading to a significance larger than 5σ for observing 20 events for a background of 3.85 $(1.49 \pm 0.07(stat) \pm 0.53(syst)$ for dimuons and $2.36 \pm 0.09(stat) \pm 0.47(syst)$ for dielectrons. In a second part, we described the prospects for PPS, leading to the highest possible sensitivities to

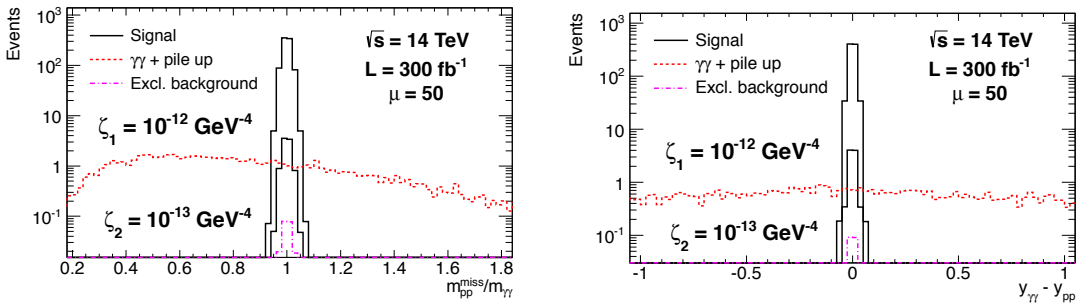

Figure 10: Left: Ratio between the proton missing mass and di-photon mass for exclusive di-photon signal events and background. Right: Difference between the di-photon and di-proton rapidity for exclusive di-photon signal and background.

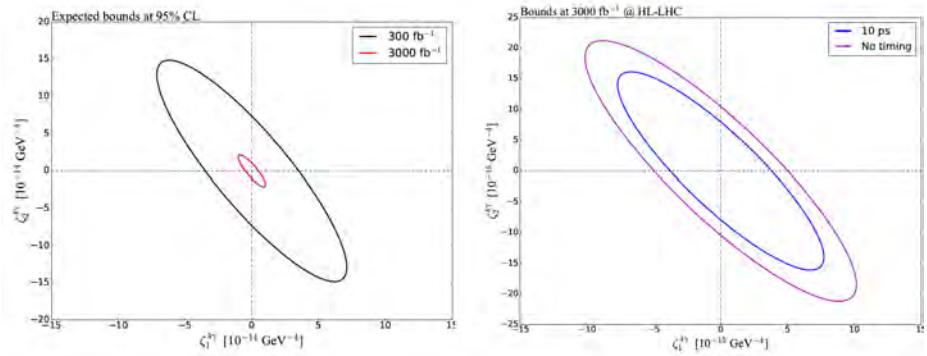

Figure 11: Sensitivity contours on photon quartic anomalous couplings at the LHC with 300 and 3000 fb^{-1}.

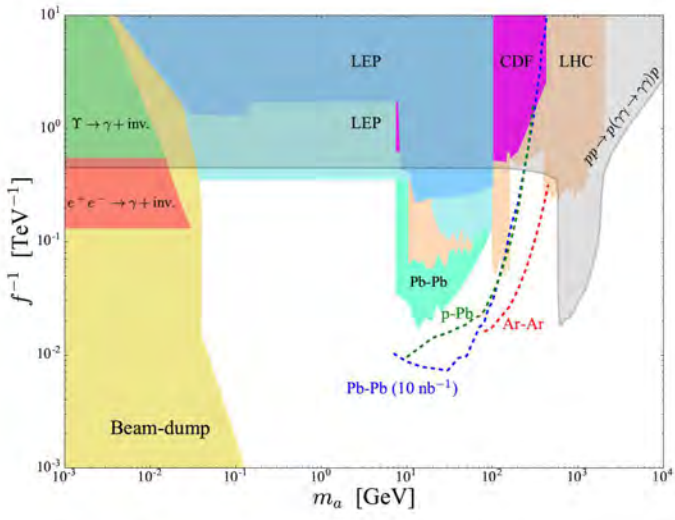

Figure 12: Exclusion plot on axion like particles in the coupling versus mass plane and sensitivity at the LHC in pp collisions with 300 fb^{-1} (grey band) and in $PbPb$ (blue dashed line), pPb (green dashed line), $ArAr$ (red dashed lines) collisions.

$\gamma\gamma\gamma\gamma$, $\gamma\gamma WW$, $\gamma\gamma ZZ$, $\gamma\gamma\gamma Z$ anomalous couplings that can appear due to new resonances, extra-dimensions. axion-like particles, or composite Higgs... First results on these anomalous couplings are expected to come out soon.

Acknowledgements

The author thanks the support from the Department of Energy, contract DE-SC0019389.

References

[1] V. Khoze, A. Martin, M. Ryskin, Eur. Phys. J. C**23** (2002) 311.

[2] S. Fichet, G. von Gersdorff, B. Lenzi, C. Royon, M. Saimpert, JHEP **1502** (2015) 165;

[3] CT-PPS project, see https://cds.cern.ch/record/1753795; CMS and TOTEM coll., CERN-LHCC-2014-021.

[4] CMS and TOTEM Coll., JHEP **1807** (2018) 153.

[5] E. Chapon, O. Kepka, C. Royon, Phys. Rev. D**81** (2010) 074003; O. Kepka, C. Royon, Phys. Rev. D**78** (2008) 073005.

[6] S. Fichet, G. von Gersdorff, O. Kepka, B. Lenzi, C. Royon, M. Saimpert, Phys. Rev. D**89** (2014) 114004. S. Fichet, G. von Gersdorff, C. Royon, Phys. Rev. Lett. **116** (2016) no 23, 231801; S. Fichet, G. von Gersdorff, C. Royon, Phys. Rev. D**93** (2016) no 7, 075031;

[7] M. Boonekamp et al., preprint ArXiv:1102.2631.

[8] C. Baldenegro, S. Fichet, G. von Gersdorff, C. Royon, JHEP **1706** (2017) 142; O. Kepka, C. Royon, Phys. Rev. D**78** (2008) 073005.

[9] C. Baldenegro, S. Fichet, G. von Gersdorff, C. Royon, JHEP **1806** (2018) 131.

[10] C. Baldenegro, S. Hassani, C. Royon, L. Schoeffel, Phys. Lett. B**795** (2019) 339.

Recent status and prospects of LHCf and RHICf

Takashi Sako for the LHCf and RHICf Collaborations

E-Mail: sako@icrr.u-tokyo.ac.jp

Institute for Cosmic Ray Research, University of Tokyo

Presented at the Workshop of QCD and Forward Physics at the EIC, the LHC, and Cosmic Ray Physics in Guanajuato, Mexico, November 18-21 2019

Abstract

The Large Hadron Collider forward (LHCf) and the Relativistic Heavy Ion Collider forward (RHICf) experiments are dedicated to measure neutral particles produced around zero degree of the hadron interactions. In this paper, recent results of LHCf on photons, neutrons and π^0's mainly obtained from 13 TeV p-p collisions are summarized. Differential cross sections are compared with predictions of various event generators. Some new analyses such as the joint analyses with ATLAS, total energy and cross section as a function of pseudorapidity are also presented. A new result of RHICf for the first detection of a finite single-spin asymmetry of π^0 production at very forward pseudorapidity region, $\eta > 6$, in the polarized p-p collisions is also presented. Plan of the LHCf in LHC Run 3 is also introduced.

1 Introduction

Origin of cosmic rays is a long standing mystery in astrophysics [1]. Because of their power law energy spectrum, high-energy cosmic rays, typically above 10^{14} eV, have very low flux and they are observed through atmospheric air shower phenomenon that significantly enlarges the effective detection area. To estimate the fundamental properties of primary cosmic rays such as energy and particle type, it is required to compare the observed data of shower particles with Monte Carlo simulation. Therefore simulation needs a reliable hadronic interaction model, but the difficulty of modeling the forward particle production makes uncertainty large.

Thanks to the early LHC results, many generators are updated to so-called post-LHC models and discrepancy between predictions become smaller [2]. However, there are still apparent discrepancies between model predictions and data-model comparison. A recent hot topic in the air shower analyses is so-called muon excess (in experiment than simulation) problem [3]. The primary mass estimated using the surface detectors data and fluorescence telescope data are systematically different. Also the estimated average primary mass exceeds the mass of Iron in some cases, which is not naturally accepted according to the element abundance in the universe. These problems are solved if the simulation underestimates the number of muons.

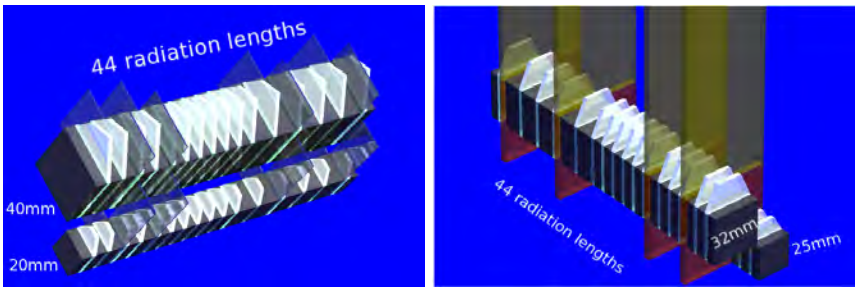

Figure 1: Schematic view of the LHCf Arm1 (left) and Arm2 (right) detectors.

Dedicated measurements at the current high-energy colliders allow access to the forward particle production in the laboratory energy of 10^{14} eV to 10^{17} eV, at RHIC and LHC, respectively. The LHCf and RHICf experiments were designed to measure very forward neutral particles to improve the knowledge of air shower development and hence the origin of cosmic rays. By using the polarized beam collisions at RHIC, measurements of spin asymmetry is another key science in RHICf.

2 LHCf and RHICf experiments

The Large Hadron Collider forward (LHCf) experiment was designed to measure the particles produced around zero degrees in the hadron collisions at LHC [4] [5]. Two independent detectors called Arm1 (IP8 side) and Arm2 (IP2 side) shown in Fig.1 were installed at 140 m from the interaction point 1 (IP1) where the ATLAS experiment is located. The detectors are located in the Target Neutral Absorbers (TANs) downstream of the beam separation dipole magnet and only neutral particles, predominantly photons and neutrons, are observed. Each detector is composed of two independent sampling calorimeter towers with position sensitive layers. By determining the invariant mass of two photons simultaneously observed, π^0's and η's immediately decayed into photon pairs near the interaction point are identified and their momenta are also reconstructed.

The Relativistic Heavy Ion Collider forward (RHICf) experiment was designed to install the LHCf Arm1 detector at the interaction point of the STAR experiment at RHIC [6] [7]. Because the installation slot at RHIC is 18 m from the interaction point, the coverage of transverse momentum p_T is equivalent to that in LHC although the collisions energy is 510 GeV. Thanks to this advantage particle production can be compared in a same x_F-p_T phase space, where x_F is Feynman x. Another unique point of RHIC is to collide polarized beams. It is known that in the collisions of transversely-polarized protons cross section of the forward particle production exhibits right-left asymmetry with respect to the polarization direction. Asymmetry of very forward neutron production is well measured [8] and even used to measure the polarization of the beams. While the π^0 or photon asymmetry is measured up to the pseudorapidity η $\sim$4 [9] [10] [11], no finite asymmetry is detected at more forward region [12]. RHICf is expected to measure the neutron asymmetry in wider phase space than the previous measurements and the π^0 asymmetry with a higher sensitivity to detect finite asymmetry for the first time in this pseudorapidity.

LHCf started its data taking at LHC in 2009 and until 2016 data were collected at various operation conditions at LHC. RHICf took data in 2017. Table 1 summarizes the operation of LHCf and RHICf.

Table 1: Summary of the data taking period and condition for LHCf and RHICf.

Year	Experiment	$\sqrt{s_{NN}}$	particles
2009	LHCf	900 GeV	p-p
2010	LHCf	7 TeV, 900 GeV	p-p
2013	LHCf (Arm2 only)	2.76 TeV	p-p
2013	LHCf (Arm2 only)	5.02 TeV	p-Pb
2015	LHCf	13 TeV	p-p
2016	LHCf (Arm2 only)	8.16 TeV	p-Pb
2017	RHICf (Arm1 only)	510 GeV	p-p (polarized)

3 Recent results of LHCf

3.1 Photons in 13 TeV collisions

Differential cross sections, $d\sigma/dE$, of photon production at pseudorapidity η >10.94 and 8.81< η <8.99 are reported [13]. Most of these photons are supposed to be produced as decay products of π^0. The results are compared with various generator predictions and it is found that the generators tuned with the early LHC results such as EPOS-LHC [14] and QGSJET II-04 [15] popular in the CR researches show reasonable agreements with the experimental results.

On the other hand, PYTHIA 8.212 [16] shows a significant excess in the very high energy photon production at η >10.94. The origin of this excess was studied and it was found that the diffractive processes are dominant source of high-energy photons in PYTHIA [17]. To experimentally elucidate the contribution of diffractive process as proposed in [17], a joint analysis of ATLAS and LHCf was performed [18]. Because the diffractive process produces less particles in the central region, using the number of particles detected in the ATLAS tracker, photons observed in the LHCf detector are classified into diffractive-like and non-diffractive-like categories. Although the diffractive-like events in the η >10.94 region are found to have a flatter spectrum than the inclusive events, the excess in the PYTHIA prediction is still obvious. On the other hand, PYHIA gives the best prediction of diffractive-like events in the 8.81< η <8.99 region. Angular dependence of modeling the diffractive process can be improved using these measurements.

3.2 Neutrons in 13 TeV collisions

Neutrons, or stable hadrons, are important to determine the core structure of air showers. Differential cross sections of forward neutron production at η >10.76, 8.99< η <9.22 and 8.81< η < 8.99 are reported [19]. The spectral shapes are very different between the most forward region η >10.76 and the others. The result of η >10.76 is shown in Fig.2 (left). A characteristic peak at 5 TeV is observed and none of the compared generators can explain this structure. Similar spectra reported by the PHENIX experiment at RHIC $\sqrt{s}$=200 GeV p-p collisions together with the lower energy data reported from the ISR experiment at $\sqrt{s}$=30-60 GeV shown in Fig.2 (right) exhibit a same peak position at x_F ~0.8 [8]. Already in the report of the ISR result [20] one pion exchange process is proposed to explain this peak. It is interesting if a same fundamental process dominates the particle production in a wide range of collision energy corresponding to a factor 13 TeV/30 GeV = 430.

Recently LHCf published the neutron cross sections with extended pseudorapidity regions [21]. New analyses are also performed to extract the total neutron energy and cross section as a function of pseudorapidity as shown in Fig.3, and an average inelasticity defined by neutrons. It is clear that the energy flow peaks at around η=9.5.

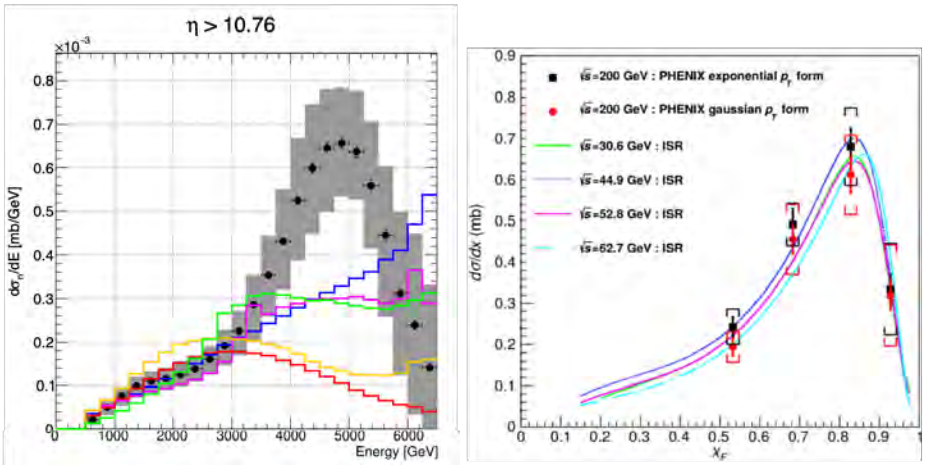

Figure 2: Energy (x_F) spectra of neutrons around zero degrees. (Left) Result of LHCf at $\sqrt{s}$=13 TeV p-p collisions for p_T<0.28x_F GeV/c [19]. (Right) Results of PHENIX and ISR at $\sqrt{s}$=30-200 GeV p-p collisions for p_T<0.11x_F GeV/c [8].

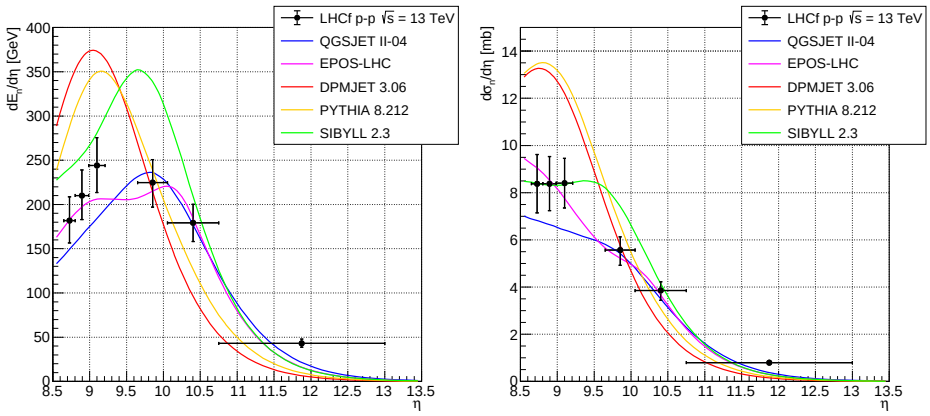

Figure 3: Total energy (left) and cross section (right) of forward neutrons as a function pseudorapidity η measured by LHCf at $\sqrt{s}$=13 TeV p-p collisions [21].

3.3 π^0's in 13 TeV collisions

π^0 is the main source of photons discussed in Sec.3.1 and the source of electro-magnetic component in air showers that determines the number of particles and hence represents the energy of primary particle. From the analyses of 2.76 TeV and 7 TeV p-p collision data, LHCf so far reported the production cross sections of π^0 and found a x_F scaling in this energy range as shown in Fig.4 [22] [23].

Analysis on 13 TeV data is on going and a preliminary result of p_T spectra at various x_F ranges is shown in Fig.5 [24]. Type 1 (black) and Type 2 (red and blue) indicate the events with two photons in two towers and two photons in a single tower, respectively. The latter having small opening angles are sensitive to the high energy (x_F) π^0's. By using the event with different categories, the coverage in phase space is enlarged. Smooth connection between different colors assures the validity of the analysis. More detail of this analysis is found in [24]. Extension of the scaling study

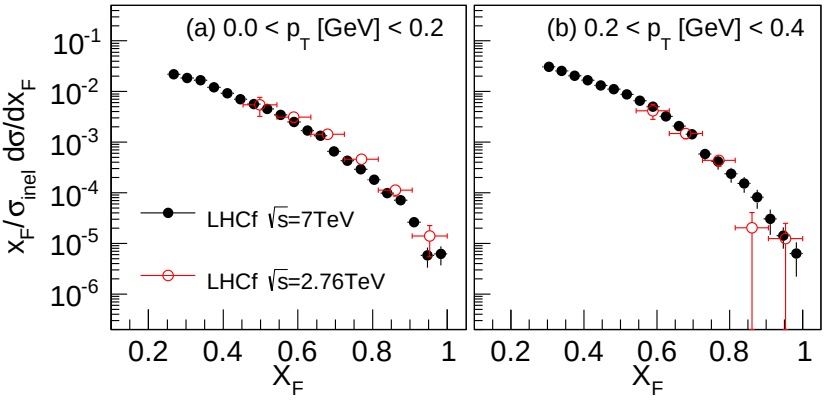

Figure 4: π^0 production cross sections as a function of x_F for two p_T ranges [23]. Results of 7 TeV and 2.76 TeV p-p collisions are plotted in black and red markers, respectively.

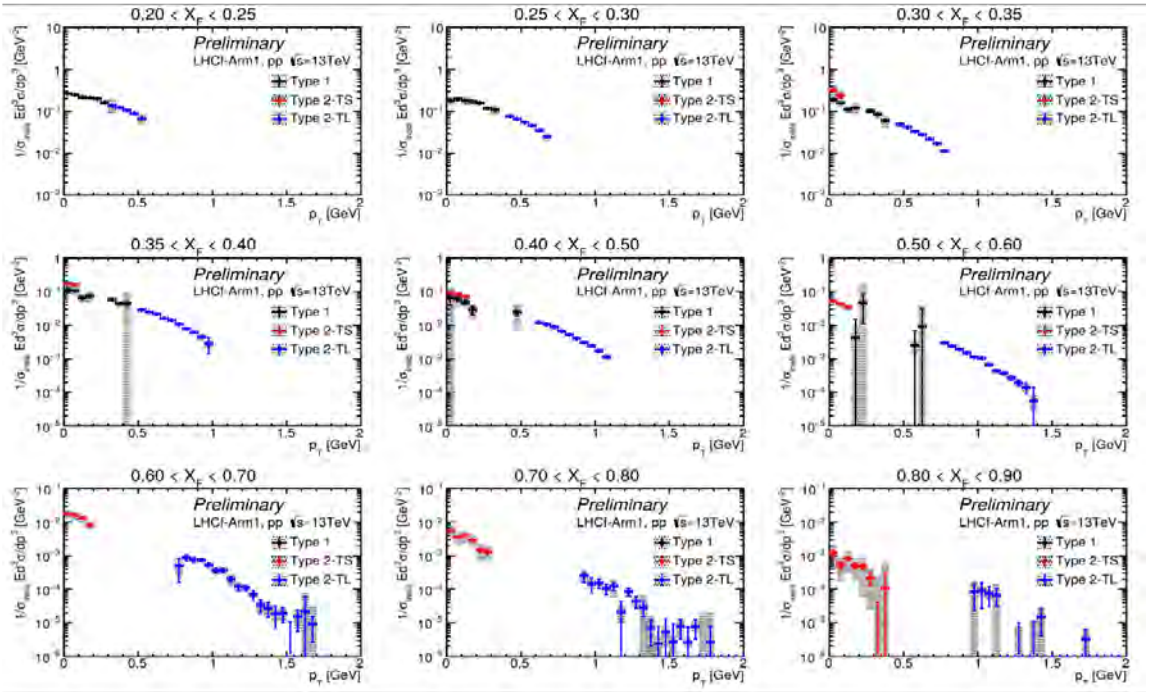

Figure 5: Preliminary p_T spectra of forward π^0 production at $\sqrt{s}$=13 TeV measured by LHCf [24]. Different panels show the results at different x_F ranges. Colors of markers indicate the different categories of event. See text and [24] for more detail.

shown in Fig.4 from $\sqrt{s}$=510 GeV to 13 TeV using the RHICf and latest LHCf results are foreseen as the next step.

4 Recent results of RHICf

RHICf analyzed the transverse single-spin asymmetry, A_N, of π^0 production as shown in Fig.6 [25]. Previous experiments reported finite A_N at moderately forward pseudorapidity, η ~3, and the

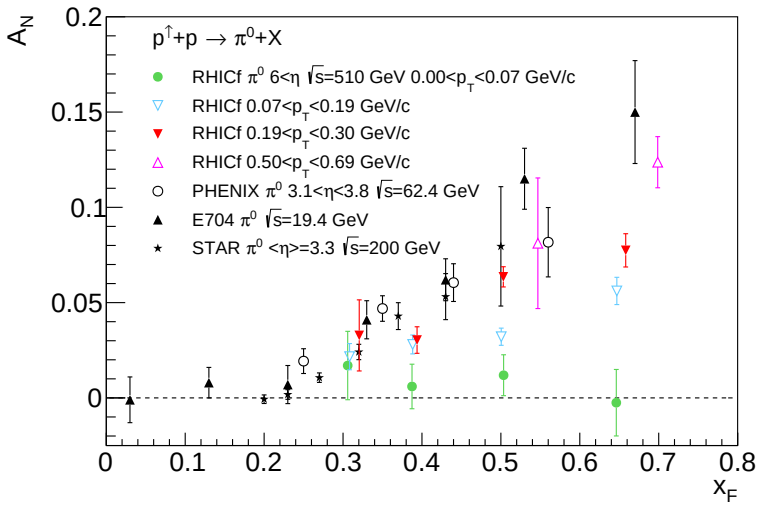

Figure 6: Transverse single-spin asymmetry, A_N, of π^0 production measured by RHICf (colors) compared with previous experiments (black) [25].

RHICf result at high p_T (η ~6.5) shows a good agreement with them. RHICf first time succeeded to measure finite A_N in more forward region. Around zero degree region A_N is consistent with zero (green points) as expected and it gradually increases with p_T. Though large asymmetry known near the central region has been explained by hard processes, recent measurements suggested contributions from soft processes such as diffractive processes are important in the forward region [11] [10]. The result of RHICf supports this idea. Because the particle production in the RHICf phase space has a larger contribution from diffractive processes, this observation will shed light on the nature of asymmetry. More detail analyses by classifying the events in diffractive and non-diffractive processes are planned using the information from the STAR detector. Data of TPC, TOF, BBC, ZDC and Roman Pots are stored when RHICf triggered high-energy event in its detector. Event matching of this common trigger is already confirmed.

5 Plan in LHC Run 3

LHCf is planning to take data in Run 3 starting in 2021. Detail ideas and technical discussions are found in the Technical Report [26]. Here summarizes two main ideas in this operation.

- Data taking with $\sqrt{s}$=14 TeV p-p collisions.
- Data taking with $\sqrt{s_{NN}}$=9.9 TeV p-O collisions, where O designates Oxygen beam.

The latter is an ideal collision for cosmic-ray physics to realize the collisions between cosmic-ray nucleon and atmosphere. By taking into account the early LHC data, so-called post-LHC generators show reasonable agreements in particle productions in p-p collisions. On the other hand, still sizable differences exist between the predictions of p-O collisions [2]. Study of the nuclear effects in the condition close to the atmosphere gives a new and direct impact on the CR physics. Note that LHCf already published the results of forward π^0 production in p-Pb collisions, where the generators reasonably described the LHCf results [27] [23]. However in this data half of the observed π^0's are produced through the Ultra Peripheral Collisions between the proton

and virtual photons around the Pb nuclei. To test the hadronic interaction, a subtraction of UPC contribution by calculation is required and it is the dominant source of uncertainty in the final result. In case of light ion collisions like Oxygen, contribution from UPC is largely suppressed and uncertainty to study the hadronic interaction is also reduced. General physics motivations of heavy and light ion collisions in Run 3 and Run 4 are summarized in [28].

Though the energy of p-p collisions does not change significantly from Run 2 to Run 3, new programs are planned. Because of steep energy spectra especially in photons and π^0's, the LHCf results have large statistical errors in high-energy range. A new and simple trigger logic that preferentially selects high-energy electromagnetic showers was successfully implemented in the operation of RHICf. By applying the same trigger logic in the LHCf Run 3 operation with a slightly higher luminosity than Run 2, LHCf can accumulate more high-energy events. To accommodate to the limited data taking speed, low energy trigger events will be prescaled. At the same time, an upgrade for speed up of the data taking system is also in progress. High-energy and high-speed data taking allows analysis of η and K meson productions. Detection of η was already confirmed with the LHCf Run 1 and Run 2 data, but because the detector is sensitive only above 2 TeV, the event statistics was limited.

Finally new possibilities are open for the common data taking and analyses with ATLAS. As described in Sec.3.1, common data taking was already successfully performed and initial analyses are ongoing. However because of the short preparation time only central detectors were included in the past operation. By including the other forward detectors such as ZDCs (behind the LHCf detectors) and roman pots, more interesting possibilities in forward physics analyses will be available. More details of the ideas are shown in [26].

6 Summary

LHCf was motivated to improve the knowledge of forward particle productions, which is directly connected to the developments of cosmic-ray induced air showers and hence the high-energy astrophysics. LHCf so far succeeded data taking at various run conditions at LHC. Results are first presented in the form of differential cross sections such as $d\sigma/dE$, $d\sigma/dp_T$ as well as invariant cross sections $Ed^3\sigma/dp^3$ for photons, neutrons and π^0's. Results are compared with the predictions of generators popular in the air shower studies and also PYTHIA. Generally EPOS-LHC model shows a good agreement with the LHCf results, but depending on the particle type and phase space to be compared different models are preferred.

Not only deriving the cross sections, LHCf also continues further studies such as

- Test of x_F scaling comparing the data at different $\sqrt{s}$
- Event-by-event classification into diffractive and non-diffrative origins collaborating with ATLAS
- Analysis of total energy and cross section as a function of η
- Analysis of elasticity carried by forward neutrons

LHCf is also preparing data taking during LHC Run 3 starting from 2021. Using a special trigger logic and updated system, more events will be collected especially in high-energy range. This allows, even under a short operation period, analyses of high-energy photons and π^0, η and K mesons with sufficient statistics. Thanks to the successful operation and first analysis with ALTAS in Run 2, more subdetectors will join the common data taking. Participation of ZDC and roman pots are of prime interest. Highlight in Run3 is possible operation of Oxygen beam. Either p-O and

O-O collisions realize the collisions really happening in the atmosphere hit by cosmic-ray particles. Still unknown nuclear effects at high-energy collisions will be understood in these operation.

One of the LHCf detectors, Arm1, was transported beyond the Atlantic ocean and used as the RHICf detector at RHIC. Not only to enlarge the $\sqrt{s}$ coverage, the spin physics is one of the main targets. The data taking at $\sqrt{s}$=510 GeV with transversely polarized proton beams was successfully done in 2017. The first impressive result is recently published. RHICf first time detected the finite single-spin asymmetry of very forward π^0 production and also its onset by reducing the p_T coverage down to zero. A good agreement between the previous experiments at η ~3 and RHICf result at η ~6.5 indicates an importance of soft processes such as diffractive dissociation in a wide pseudorapidity range. Further analyses with the STAR experiment are on going.

Acknowledgements

We thank the CERN staff and ATLAS Collaboration for their essential contributions to the successful operation of LHCf. We are grateful to S. Ostapchenko for useful comments about QGSJET II-04 generator and to the developers of CRMC interface tool for its implementation. We thank the staff of the Collider-Accelerator Department at Brookhaven National Laboratory, the STAR Collaboration and the PHENIX Collaboration for supporting the experiment. We are also grateful to Dr. Daniel Pitonyak for the calculation of the π^0 asymmetry. This program is partly supported by the U.S.-Japan Science and Technology Cooperation Program in High Energy Physics, by JSPS KAKENHI (No. JP26247037, JP23340076 and JP18H01227), by Istituto Nazionale di Fisica Nucleare (INFN), by the joint research program of the Institute for Cosmic Ray Research (ICRR), University of Tokyo, by the National Research Foundation of Korea (No. 2016R1A2B2008505 and 2018R1A5A1025563), and by "UNICT 2020-22 Linea 2" program, University of Catania. This work took advantage of computer resource supplied by ICRR (University of Tokyo), RIKEN, CERN and CNAF (INFN).

References

[1] R. A. Batista et al., *Open Questions in Cosmic-Ray Research at Ultrahigh Energies*, *Frontiers in Astronomy and Space Sciences* **6** (2019) 23.

[2] **LHC forward physics working group** Collaboration, K. Akiba et al., *LHC forward physics*, *J. Phys. G: Nucl. Part. Phys.* **43** (2016) 110201.

[3] L. Cazon et al., *Working Group Report on the Combined Analysis of Muon Density Measurements from Eight Air Shower Experiments*, *PoS (ICRC2019)* (2019) 214.

[4] **LHCf** Collaboration, M. Haguenauer et al., *Technical Design Report of the LHCf experiment : Measurement of Photons and Neutral Pions in the Very Forward Region of LHC*, .

[5] **LHCf** Collaboration, . Adriani et al., *The LHCf detector at the CERN Large Hadron Collider*, *JINST* **3** (2008) S08006.

[6] **RHICf** Collaboration, Y. Itow et al., *Letter of intent; Precise measurements of very forward particle production at RHIC*, arXiv:1401.1004.

[7] **RHICf** Collaboration, Y. Itow et al., *Proposal; Precise measurements of very forward particle production at RHIC*, arXiv:1409.4860.

[8] **PHENIX** Collaboration, A. Adare et al., *Inclusive cross section and single transverse spin asummetry for very forward neutron production in polarized $p+p$ collisions at $\sqrt{s}$=200 GeV*, *Phys. Rev. D* **88** (2013) 032006.

[9] **PHENIX** Collaboration, A. Adare et al., *Measurement of transverse-single-spin asymmetries for midrapidity and forward-rapidity production of hadrons in polarized p+p collisions at $\sqrt{s}$=200 and 62.4 GeV*, *Phys. Rev. D* **90** (2014) 012006.

[10] **STAR** Collaboration, M. M. Mondal et al., *Measurement of the Transverse Single-Spin Asymmetry for π^0 and Jet-like Events at Forward Rapidity at STAR in p+p Collisions at $\sqrt{s}$=500 GeV*, *PoS (DIS2014)* (2014) 216.

[11] **A_NDY** Collaboration, L. C. Bland et al., *Cross sections and transverse single-spin asymmetry in forward jet production from proton collisions at $\sqrt{s}$=500 GeV*, *Phys. Lett. B* **750** (2015) 660–665.

[12] Y. Fukao et al., *Single transverse-spin asymmetry in very forward and backward particle production for polarized proton collisions at $\sqrt{s}$=200 GeV*, *Phys. Lett. B* **650** (2007) 325–330.

[13] **LHCf** Collaboration, O. Adriani et al., *Measurement of forward photon production cross-section in proton-proton collisions at $\sqrt{s}$=13 TeV with the LHCf detector*, *Phys. Lett. B* **780** (2018) 233–239, [arXiv:1703.07678].

[14] T. Pierog et al., *EPOS LHC: Test of collective hadronization with data measured at the CERN Large Hadron Collider*, *Phys. Rev. C* **92** (2015) 034906.

[15] S. Ostapchenko, *Monte Carlo treatment of hadronic interactions in enhanced Pomeron scheme: QGSJET-II model*, *Phys. Rev. D* **83** (2011) 014018.

[16] T. Sjöstrand et al., *An introduction to PYTHIA 8.2*, *Com. Phys. Comm.* **191** (2015) 159–177.

[17] Q. D. Zhou et al., *Monte Carlo study of particle production in diffractive proton-proton collisions at $\sqrt{s}$=13 TeV with the very forward detector combined with central information*, *Eur. Phys. J. C.* **77** (2017) 212.

[18] **ATLAS and LHCf** Collaboration, *Measurement of contributions of diffractive processes to forward photon spectra in pp collisions at $\sqrt{s}$=13 TeV*, .

[19] **LHCf** Collaboration, O. Adriani et al., *Measurement of inclusive forward neutron production cross section in proton-proton collisions at $\sqrt{s}$=13 TeV with the LHCf Arm2 detector*, *JHEP* **11** (2018) 073, [arXiv:1808.09877].

[20] W. Flauger and F. Mönnig, *Measurement of inclusive zero-angle neutron spectra at the CERN ISR*, *Nucl. Phys. B* **109** (1976) 347–356.

[21] **LHCf** Collaboration, O. Adriani et al., *Measurement of energy flow, cross section and average inelasticity of forward neutrons produced in $\sqrt{s}$=13 TeV proton-proton collisions with the LHCf Arm2 detector*, *JHEP* **in press** (2020) [arXiv:2003.02192].

[22] **LHCf** Collaboration, O. Adriani et al., *Measurement of forward neutral pion transverse momentum spectra for $\sqrt{s}$=7 TeV proton-proton collisions at the LHC*, *Phys. Rev. D* **86** (2012) 092001, [arXiv:1205.4578].

[23] **LHCf** Collaboration, O. Adriani et al., *Measurements of longitudinal and transverse momentum distributions for neutral pions in the forward-rapidity region with the LHCf detector*, *Phys. Rev. D* **94** (2016) 032007, [arXiv:1507.08764].

[24] **LHCf** Collaboration, H. Menjo et al., *The results and future prospects of the LHCf expereiment*, *PoS (ICRC2019)* (2019) 349.

[25] **RHICf** Collaboration, M. H. Kim et al., *Transverse single-spin asymmetry for very forward neutral pion production in polarized p+p collisions at $\sqrt{s}$=510 GeV*, *Phys. Rev. Lett.* **124** (2020) 252501, [arXiv:2003.04283].

[26] **LHCf** Collaboration, O. Adriani et al., *Technical Proposal for the LHC Run3 : Addressing Cosmic Ray physics with forward measurements in proton-proton and proton-light nuclei collisions at LHC*, .

[27] **LHCf** Collaboration, O. Adriani et al., *Transverse-momentum distribution and nuclear modification factor for neutral pions in the forward-rapidity region in proton-lead collisions at $\sqrt{s_{NN}}$=5.02ṪeV*, *Phys. Rev. C* **89** (2014) 065209.

[28] **Working Group 5 on the Physics of the HL-LHC, and Perspectives at the HE-LHC** Collaboration, Z. Citron et al., *Future physics opportunities for high-density QCD at the LHC with heavy-ion and proton beams*, arXiv:1812.06772.

Novel Phenomena in QCD: Heavy Flavor and Higgs Production at High x_F from Intrinsic Heavy Quarks

Stanley J. Brodsky

E-Mail: sjbth@slac.stanford.edu

SLAC National Accelerator Laboratory, Stanford University

Presented at the Workshop on QCD and Forward Physics at the EIC, the LHC, and Cosmic Ray Physics in Guanajuato, Mexico, November 18-21, 2019

Abstract

Calculations from lattice gauge theory have recently verified the contribution of intrinsic heavy quarks to the nonperturbative structure of the proton in QCD. The lattice results show that the intrinsic charm contribution to the proton's heavy quark distribution is maximal at large $x \sim 0.4$, and that the $c(x) vs. \bar{c}(x)$ distributions differ strongly. I discuss the implications of the LGTH results for LHC and EIC collider phenomenology, including Higgs and heavy hadron production at high x_F, as well as the proposed AFTER fixed target facility at CERN.

1 Introduction

Quantum Chromodynamics (QCD), the underlying theory of strong interactions, with quarks and gluons as the fundamental degrees of freedom, predicts that the heavy quarks in the nucleon-sea to have both perturbative "extrinsic" and nonperturbative "intrinsic" origins. The extrinsic sea arises from gluon splitting which is triggered by a probe in the reaction. It can be calculated order-by-order in perturbation theory. In contrast, the intrinsic sea is encoded in the nonperturbative wave functions of the nucleon eigenstate. The existence of nonperturbative intrinsic charm (IC) was originally proposed in the BHPS model [1] and developed further in subsequent papers [2–4]. The intrinsic contribution to the heavy quark distributions of hadrons at high x corresponds to Fock states such as $|uudQ\bar{Q}>$ where the heavy quark pair is multiply connected to two or more valence quarks of the proton. It is maximal at minimal off-shellness; i.e., when the constituents all have the same rapidity y_I, and thus $x_i \propto \sqrt{(m_i^2 + \vec{k}_{\perp i}^2)}$. Here $x = \frac{k^+}{P^+} = \frac{k^0+k^3}{P^0+P^3}$ is the frame-independent light-front momentum fraction carried by the heavy quark in a hadron with momentum P^μ. In the case of deep inelastic lepton-proton scattering, the LF momentum fraction variable x in the proton structure functions can be identified with the Bjorken variable $x = \frac{Q^2}{2p\cdot q}$. These heavy quark contributions to the nucleon's PDF thus peak at large x_{bj} and thus have important implication for LHC and EIC collider phenomenology, including Higgs and heavy hadron production at high

x_F [5]. It also opens up new opportunities to study heavy quark phenomena in fixed target experiments such as the proposed AFTER [6] fixed target facility at CERN. The existence of intrinsic heavy quarks also illuminates fundamental aspects of nonperturbative QCD.

In light-front (LF) Hamiltonian theory, the intrinsic heavy quarks of the proton are associated with non-valence Fock states. such as $|uudQ\bar{Q}>$ in the hadronic eigenstate of the LF Hamiltonian; this implies that the heavy quarks are multi-connected to the valence quarks. The probability for the heavy-quark Fock states scales as $1/m_Q^2$ in non-Abelian QCD. Since the LF wavefunction is maximal at minimum off-shell invariant mass; i.e., at equal rapidity, the intrinsic heavy quarks carry large momentum fraction x_Q. A key characteristic is different momentum and spin distributions for the intrinsic Q and $\bar{Q}$ in the nucleon; for example the charm-anticharm asymmetry, since the comoving quarks are sensitive to the global quantum numbers of the nucleon [6]. Furthermore, since all of the intrinsic quarks in the $|uudQ\bar{Q}>$ Fock state have similar rapidities they can re-interact, leading to significant Q vs $\bar{Q}$ asymmetries. The concept of intrinsic heavy quarks was also proposed in the context of meson-baryon fluctuation models [7, 8] where intrinsic charm was identified with two-body state $\bar{D}^0(u\bar{c})\Lambda_c^+(udc)$ in the proton. This identification predicts large asymmetries in the charm versus charm momentum and spin distributions, Since these heavy quark distributions depend on the correlations determined by the valence quark distributions, they are referred to as *intrinsic* contributions to the hadron's fundamental structure. A specific analysis of the intrinsic charm content of the deuteron is given in ref. [9]. In contrast, the contribution to the heavy quark PDFS arising from gluon splitting are symmetric in Q vs $\bar{Q}$. The contributions generated by DGLAP evolution at low x can be considered as *extrinsic* contributions since they only depend on the gluon distribution. The gluon splitting contribution to the heavy-quark degrees of freedom is perturbatively calculable using DGLAP evolution. To first approximation, the perturbative extrinsic heavy quark distribution falls as $(1-x)$ times the gluon distribution and is limited to low x_{bj}.

In an important recent development [10], the difference of the charm and anticharm quark distributions in the proton $\Delta c(x) = c(x) - \bar{c}(x)$ has been computed from first principles in QCD using lattice gauge theory. A key theoretical tool is the computation of the charm and anticharm quark contribution to the $G_E(Q^2)$ form factor of the proton which would vanish if $c(x) = \bar{c}(x)$. The results are remarkable. The predicted $c(x) - \bar{c}(x)$ distribution is large and nonzero at large at $x \sim 0.4$, consistent with the expectations of intrinsic charm. The $c(x)$ vs. $\bar{c}(x)$ asymmetry can be understood physically by identifying the $|ududc\bar{c}>$ Fock state with the $|\Lambda_{udc}D_{u\bar{c}}>$ off shell excitation of the proton. See Fig. 1. A related application of lattice gauge theory to the nonperturbative strange-quark sea from lattice QCD is given in ref. [11].

Thus QCD predicts two separate and distinct contributions to the heavy quark distributions $q(x, Q^2)$ of the nucleons at low and high x. Here $x = \frac{k^+}{P^+} = \frac{k^0+k^3}{P^0+P^3}$ is the frame-independent light-front momentum fraction carried by the heavy quark in a hadron with momentum P^μ. In the case of deep inelastic lepton-proton scattering, the LF momentum fraction variable x in the proton structure functions can be identified with the Bjorken variable $x = \frac{Q^2}{2p\cdot q}$. At small x, heavy-quark pairs are dominantly produced via gluon-splitting subprocess $g \to Q\bar{Q}$. The presence of the heavy quarks in nucleon from this standard contribution is a result of the QCD evolution of the light quark and gluon PDFs. Unlike the conventional $\log m_Q^2$ dependence of the low x extrinsic gluon-splitting contributions, the probabilities for the intrinsic heavy quark Fock states at high x scale as $\frac{1}{m_Q^2}$ in non-Abelian QCD. Thus the relative probability of intrinsic bottom to charm is of order $\frac{m_c^2}{m_b^2} \sim \frac{1}{10}$. In contrast, the probability for a higher Fock state containing heavy leptons in a QED atom scales as $\frac{1}{m_\ell^4}$, corresponding to the twist-8 Euler-Heisenberg light-by-light self-energy insertion. Detailed derivations based on the OPE have been given in Ref. [2, 4].

There have been many phenomenological calculations involving the existence of a non-zero

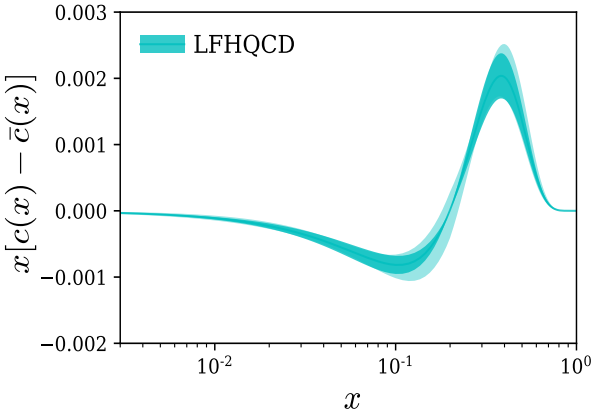

Figure 1: The distribution function $x[c(x) - \bar{c}(x)]$ obtained from the LFHQCD formalism using the lattice QCD input of charm electromagnetic form factors $G^c_{E,M}(Q^2)$. The outer cyan band indicates an estimate of systematic uncertainty in the $x[c(x) - \bar{c}(x)]$ distribution obtained from a variation of the hadron scale κ_c by 5%. From ref. [10]

.

IC component to explain anomalies in the experimental data and to predict its novel signatures of IC in upcoming experiments [6]. The new LGTH results will make these predictions precise.

2 Higgs production at High x_F and the Intrinsic Heavy-Quark Distributions of the Proton

The conventional pQCD mechanisms for Higgs production at the LHC, such as gluon fusion $gg \to H$, lead to Higgs boson production in the central rapidity region. However, the Higgs can also be produced at very high x_F by the process $[Q\bar{Q}] + g \to H$ [12], where both heavy quarks from the proton's five quark Fock state $|uudQ\bar{Q}>$ couple directly to the Higgs. See. fig. 2. Since the Higgs couples to each quark proportional to its mass, one has roughly equal contributions from intrinsic $s\bar{s}, c\bar{c}, b\bar{b}$ and even $t\bar{t}$ Fock states. The intrinsic heavy-quark distribution of the proton at high x leads to Higgs production with as much as 80% of the beam momentum. One can also use the x_F distribution of the produced Higgs boson to discriminate Higgs production from strange, charm, and bottom quarks. The same intrinsic mechanism produces the J/ψ at high x_F as observed in fixed-target experiments such as NA3.

The decay of the high-x_F Higgs to muons could be observed using very forward detectors at the LHC. The predicted cross section $d\sigma/dx_F(pp \to HX)$ for Higgs production at high $x_F \sim 0.8$ computed by Kopeliovitch, Schmidt, Goldhaber, and myself [12] is of order of 50 fb. We have also computed with Soffer [13] the corresponding double-diffractive rate $pp \to HppX$. Testing these predictions would open up a new domain of Higgs physics at the LHC.

3 The Hadronic Phenomenology of Intrinsic Heavy Quarks

The existence of intrinsic heavy quarks in the proton leads leads to a broad array of heavy hadron production processes in the high x_F forward domain at the EIC and LHC colliders When a proton collides with other protons at the LHC or in a fixed target, the heavy quark Fock states in the proton, such as $|uudc\bar{c}>$ are materialized and can produce open or hidden charm states at high

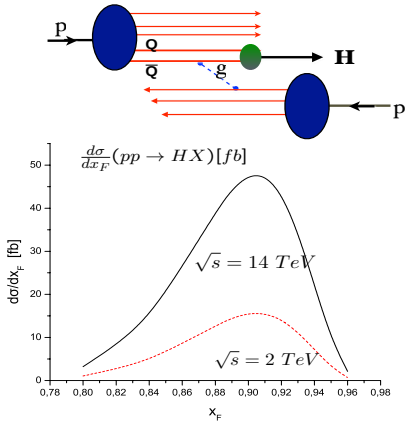

Figure 2: Intrinsic Heavy Quark Mechanism and cross section for Higgs Production at LHC and Tevatron energies. From ref. [12]

momentum fraction x_F. For example, the comoving udcquarks in a Fock state such as $|uudc\bar{c}>$ can coalesce to produce a $\Lambda_c(udc)$ baryon with a high Feynman momentum fraction $x_F = x_c + x_u + x_d$ or produce a J/ψ with $x_F = c\bar{c}$. Such high x_F heavy hadron events have been observed and measured with substantial cross sections at the ISR proton-proton collider and at fixed target experiments such as NA3 at CERN and SELEX at FermiLab. Intrinsic charm components in the proton can explain [1] the large cross-section for the forward open charm production in pp collision at ISR energies [17, 26–28]. The $\Lambda_b(udb)$ baryon was first observed at the ISR in forward $pp \to \Lambda_b X$ reactions at high x_F as expected from intrinsic bottom.

The first direct experimental indication for the intrinsic heavy quarks in a nucleon was observed in the EMC deep inelastic muon experiment at CERN. The measurement of the charm structure function at high x_{Bj} by the EMC experiment at CERN using deep inelastic muon-nucleus scattering showed a significant contribution to the proton structure function at large x_{bj} [14]. In fact, the charm structure function $c(x, Q)$ measured by the EMC collaboration was approximately 30 times higher than expected from gluon splitting and at $x_{Bj} = 0.42$ and $Q^2 = 75\ GeV^2$.

The effect of whether the IC parton distribution is either included or excluded in the determinations of charm parton distribution functions (PDFs) can induce changes in other parton distributions through the momentum sum rule, which can indirectly affect the analyses of various physical processes that depend on the input of various PDFs. On the experimental side, an estimate of intrinsic charm (c) and anticharm ($\bar{c}$) distributions can provide important information to the understanding of charm quark production in deep inelastic $lp \to l'cX$ scattering in the EMC experiment [14]. The enhancement of charm distribution in the measurement the charm quark structure function F_2^c compared to the expectation from the gluon splitting mechanism in the EMC experimental data has been interpreted as evidence for nonzero IC in several calculations [2, 3, 15, 16]. A precise determination of charm and anticharm PDFs by considering both the perturbative and nonperturbative contributions is important in understanding charmonia and open charm productions, such as the J/ψ production at large momentum from pA collisions at CERN [30], from πA collisions at FNAL [31], from pp collisions at LHC [32], and charmed hadron or jet production from pp collisions at ISR, FNAL, and LHC [32, 35–37].

The cross sections for forward heavy quark or quarkonium production include contributions from diffractive reactions such as $\gamma^* p \to Q + X + p$, where the proton target remains intact. The final-state interactions of the outgoing state can lead to additional strong nuclear effects not asso-

ciated with shadowing of the nuclear structure functions [34] The interference of different amplitudes leads to shadowing and flavor-specific antishadowing of the DIS cross section on nuclei. An important consequence is the inapplicability of the OPE and the violation of the momentum sum rule for nuclear structure functions. See ref. [33].

An investigation of prompt photon and $c(b)$-jet production in $p\bar{p}$ collisions at $\sqrt{s} = 1.96$ TeV was carried out at the Tevatron [19–22]. The observed cross section for $\bar{p}p \to \gamma cX$ is significantly larger than predictions without the IC contribution at photon transverse momenta above 110 GeV – by a factor of 3. The ratio of the cross section using the NLO calculations of the p_T -spectrum is consistent with the BHPS model and CTEQ66c with intrinsic charm probability in the proton about 3.5 %. [23] In the case of the prompt photon production accompanied by the b-jet in $p\bar{p}$ annihilation, the Tevatron data do not show any signal of the intrinsic b contribution, as expected from the small intrinsic beauty probability in a proton.

LHC measurements associated with cross section of inclusive production of Higgs, Z, W bosons via gluon-gluon fusion, and productions of charm jet and Z^0 [38–41], J/ψ and D^0 mesons at LHCb experiment [32] can also be sensitive to the intrinsic charm distribution. The J/ψ photo- or electro-productions near the charm threshold is sensitive to intrinsic charm; experiments have been proposed at JLab [44] as well as for the future EIC to measure the production cross section near the threshold. The existence of IC in the proton will provide additional production channels and thus enhance the cross section for both open and hidden charm, especially near threshold [47, 52]. If the c and $\bar{c}$ quarks have different distributions in the proton, the enhancements on D and $\bar{D}$ productions will appear at slightly different kinematics. IC has also been proposed to have an impact on estimating the astrophysical neutrino flux observed at the IceCube experiment [45].

A recent calculation of the intrinsic charm contribution to the production of double charm baryons at both colliders and fixed target experiments is given in ref. [48]. The resolution of the SELEX-LHCb double-charm baryon conflict between SELEX and LHCb due to intrinsic heavy-quark hadroproduction is given in ref. [49].

A review of collider tests of heavy quark distributions is given in ref. [23] The constraints on the intrinsic charm content of the proton that can be obtained from ATLAS data is given in ref. [24]. A global analysis of intrinsic charm signals in the nucleon is given in ref. [51].

The elimination of renormalization scale and scheme ambiguities in pQCD predictions for hard QCD processes will greatly improve predictions for intrinsic heavy quark cross sections, especially for EIC tests. Recent applications of the BLM/PMC method to jet production and Heavy Quark Pair Production in e^+e^- Annihilation are given in refs. [42, 43]. The presence of intrinsic heavy quarks in the Fock states of light hadrons can also lead to new signals such as novel effects in B decay [25] and the resolution of issues, such as the $\rho - \pi$ puzzle [50].

4 Future Experiments

The measurement of $D^0 \to K^{\pm}\pi^{\mp}$ and $\Lambda_c \to pK^-\pi^+$ at $x_F > 0.7$ at the LHC at $\sqrt{s}$ = 14 TeV would be possible in the forward multiparticle spectrometer (FMS) being proposed as a new sub-detector for CMS [53]. The FMS measurements will also be sensitive to the large asymmetries $c(x, Q)$ vs. $\bar{c}(x, Q)$ predicted for intrinsic charm.

A primary objective of the proposed fixed-target experiment AFTER@LHC will be to study heavy hadron production at high x_F in pA collisions at far forward rapidities [6]. These measurements will also have direct impact for astrophysics since intrinsic charm is important for charm production in cosmic ray experiments that measure charm production from high energy experiments interacting in the earth's atmosphere. It is also important for estimating the high energy flux of neutrinos observed in the IceCube experiment. In fact, one finds [45] that the prompt neutrino flux arising from charm hadroproduction by protons interacting in the earth's atmosphere which

is due to intrinsic charm is comparable to the extrinsic contribution if one normalizes the intrinsic charm differential cross sections to the ISR and the LEBC-MPS collaboration data.

The intrinsic heavy quark Fock states in the nuclear target itself will also be excited in a high energy LHC proton-nucleus collision. The resulting heavy quarks will be produced at small rapidities relative to to the target rapidity; i.e., *nearly at rest in the laboratory*. For example, the coalescence of the produced heavy quarks with comoving light quarks will lead to the production of a heavy hadron such as a $\Lambda_b(udb)$ at *small rapidity* $y_{\Lambda_b} \simeq \ln x_b$, relative to the rapidity of the nucleon in the target.

In addition, heavy-quark hadrons such as double-charm baryons, and exotic multiquark hadrons such as $|[u\bar{u}][Q\bar{Q}]$, tetraquarks, pentaquarks, and even octoquarks containing heavy quarks will be produced nearly at rest in the nuclear target rest frame in the pA collision in a fixed target experiment where they can be easily observed. One can also study the hadro-production of exotic hadrons such a heavy hexa-diquarks [46] (the color singlet bound state of six diquarks) containing a heavy quark. The IC signal can also be studied in hard processes such as the production of prompt photons or Z^0- or W bosons accompanied by heavy quark jets. Typical underlying subprocesses are $gc \to \gamma c$ or $gc \to Z^0 c$

5 Conclusions

The existence of the nonperturbative intrinsic heavy quarks in the hadronic eigenstates of hadrons and nuclei highlights the importance of experiments for studying the high x_F and threshold domains of heavy particle production both at colliders and fixed target facilities. Measurements of the strong asymmetry of the intrinsic quark and antiquark distributions predicted by LGTH is particularly important. As I have reviewed here, the presence of intrinsic heavy quark degrees of freedom in hadrons also illuminates many new and subtle aspects of QCD phenomena.

Acknowledgements

I am grateful to my many collaborators who have contributed to the development of intrinsic heavy quark theory and phenomenology. This work was supported by the Department of Energy under contract DE-AC02-76SF00515. SLAC-PUB-17520

References

[1] S. J. Brodsky, P. Hoyer, C. Peterson, and N. Sakai, "The intrinsic charm of the proton," Phys. Lett. **93B**, 451 (1980).

[2] S. J. Brodsky, J. C. Collins, S. D. Ellis, J. F. Gunion, and A. H. Mueller, "Intrinsic Chevrolets at the SSC," in *Proceedings of the 1984 Summer Study on the SSC, Snowmass, CO*, edited by R. Donaldson and J. G. Morfin (AIP, New York, 1985).

[3] B. W. Harris, J. Smith and R. Vogt, "Reanalysis of the EMC charm production data with extrinsic and intrinsic charm at NLO," Nucl. Phys. B **461**, 181 (1996).

[4] M. Franz, M. V. Polyakov, and K. Goeke, "Heavy quark mass expansion and intrinsic charm in light hadrons," Phys. Rev. D **62**, 074024 (2000).

[5] C. Royon, "Forward physics using proton tagging at the LHC," AIP Conf. Proc. **1654**, no.1, 040004 (2015) doi:10.1063/1.4915969

[6] S. J. Brodsky, A. Kusina, F. Lyonnet, I. Schienbein, H. Spiesberger and R. Vogt, "A review of the intrinsic heavy quark content of the nucleon," Adv. High Energy Phys. **2015**, 231547 (2015).

[7] F. S. Navarra, M. Nielsen, C. A. A. Nunes and M. Teixeira, "On the intrinsic charm component of the nucleon," Phys. Rev. D **54**, 842 (1996).

[8] J. Pumplin, "Light-cone models for intrinsic charm and bottom," Phys. Rev. D **73**, 114015 (2006).

[9] S. J. Brodsky, K. Y. J. Chiu, J. P. Lansberg and N. Yamanaka, "The gluon and charm content of the deuteron," Phys. Lett. B **783**, 287-293 (2018) doi:10.1016/j.physletb.2018.06.070 [arXiv:1805.03173 [hep-ph]].

[10] R. S. Sufian, T. Liu, A. Alexandru, S. J. Brodsky, G. F. de Téramond, H. G. Dosch, T. Draper, K. F. Liu and Y. B. Yang, "Constraints on charm-anticharm asymmetry in the nucleon from lattice QCD," [arXiv:2003.01078 [hep-lat]].

[11] R. S. Sufian, T. Liu, G. F. de Téramond, H. G. Dosch, S. J. Brodsky, A. Deur, M. T. Islam and B. Q. Ma, "Nonperturbative strange-quark sea from lattice QCD, light-front holography, and meson-baryon fluctuation models," Phys. Rev. D **98**, 114004 (2018).

[12] S. J. Brodsky, A. S. Goldhaber, B. Z. Kopeliovich and I. Schmidt, "Higgs hadroproduction at large Feynman x," Nucl. Phys. B **807**, 334 (2009).

[13] S. J. Brodsky, B. Kopeliovich, I. Schmidt and J. Soffer, "Diffractive Higgs production from intrinsic heavy flavors in the proton," Phys. Rev. D **73**, 113005 (2006) doi:10.1103/PhysRevD.73.113005 [arXiv:hep-ph/0603238 [hep-ph]].

[14] J. J. Aubert *et al.* [European Muon Collaboration], "Production of charmed particles in 250-GeV μ^+ - iron interactions," Nucl. Phys. B **213**, 31 (1983).

[15] E. Hoffmann and R. Moore, "Subleading contributions to the intrinsic charm of the nucleon," Z. Phys. C **20**, 71 (1983).

[16] S. J. Brodsky, P. Hoyer, A. H. Mueller and W. K. Tang, "New QCD production mechanisms for hard processes at large x," Nucl. Phys. B **369**, 519 (1992).

[17] D. Drijard *et al.* [CERN-College de France-Heidelberg-Karlsruhe], "Observation of Charmed d Meson Production in p p Collisions," Phys. Lett. B **81**, 250-254 (1979) doi:10.1016/0370-2693(79)90535-5

[18] R. Vogt, S. J. Brodsky and P. Hoyer, "Systematics of charm production in hadronic collisions," Nucl. Phys. B **383**, 643-684 (1992) doi:10.1016/0550-3213(92)90091-O

[19] V. Abazov *et al.* [D0], "Measurement of gamma + b + X and gamma + c + X production cross sections in p anti-p collisions at s**(1/2) = 1.96-TeV," Phys. Rev. Lett. **102**, 192002 (2009) doi:10.1103/PhysRevLett.102.192002 [arXiv:0901.0739 [hep-ex]].

[20] V. M. Abazov *et al.* [D0], "Measurement of the differential photon + c-jet cross section and the ratio of differential photon+ c and photon+ b cross sections in proton-antiproton collisions at $\sqrt{s} = 1.96$ TeV," Phys. Lett. B **719**, 354-361 (2013) doi:10.1016/j.physletb.2013.01.033 [arXiv:1210.5033 [hep-ex]].

[21] T. Aaltonen *et al.* [CDF], "A Study of the associated production of photons and b-quark jets in p p-bar collisions at s**(1/2) = 1.96-TeV," Phys. Rev. D **81**, 052006 (2010) doi:10.1103/PhysRevD.81.052006 [arXiv:0912.3453 [hep-ex]].

[22] V. Abazov *et al.* [D0], "Measurement of the photon+b-jet production differential cross section in $p\bar{p}$ collisions at $\sqrt{s} = 1.96$ TeV," Phys. Lett. B **714**, 32-39 (2012) doi:10.1016/j.physletb.2012.06.056 [arXiv:1203.5865 [hep-ex]].

[23] S. Brodsky, V. Bednyakov, G. Lykasov, J. Smiesko and S. Tokar, "The Physics of Heavy Quark Distributions in Hadrons: Collider Tests," Prog. Part. Nucl. Phys. **93**, 108-142 (2017) doi:10.1016/j.ppnp.2016.12.001 [arXiv:1612.01351 [hep-ph]].

[24] V. Bednyakov, S. Brodsky, A. Lipatov, G. Lykasov, M. Malyshev, J. Smiesko and S. Tokar, "Constraints on the intrinsic charm content of the proton from recent ATLAS data," Eur. Phys. J. C **79**, no.2, 92 (2019) doi:10.1140/epjc/s10052-019-6605-y [arXiv:1712.09096 [hep-ph]].

[25] S. Brodsky and S. Gardner, "Evading the CKM hierarchy: Intrinsic charm in B decays," Phys. Rev. D **65**, 054016 (2002) doi:10.1103/PhysRevD.65.054016 [arXiv:hep-ph/0108121 [hep-ph]].

[26] K. Giboni, D. DiBitonto, M. Barone, M. Block, A. Bohm, R. Campanini, F. Ceradini, J. Eickmeyer, D. Hanna, J. Irion, A. Kernan, H. Ludwig, F. Muller, B. Naroska, F. Navach, M. Nussbaum, J. O'Connor, C. Rubbia, D. Schinzel, H. Seebrunner, A. Staude, R. Tirler, G. J. VanDalen, R. Voss and R. Wojslaw, "Diffractive Production of the Charmed Baryon Lambda(c)+ at the CERN ISR," Phys. Lett. B **85**, 437-442 (1979) doi:10.1016/0370-2693(79)91291-7

[27] W. S. Lockman, T. Meyer, J. Rander, P. Schlein, R. Webb, S. Erhan and J. Zsembery, "Evidence for Lambda(c)+ in Inclusive p p —> (Lambda0 pi+ pi+ pi-) x and p p —> (K- pi+ p) x at s**(1/2) = 53-GeV and 62-GeV," Phys. Lett. B **85**, 443-446 (1979) doi:10.1016/0370-2693(79)91292-9

[28] D. Drijard *et al.* [ACCDHW], "Charmed Baryon Production at the CERN Intersecting Storage Rings," Phys. Lett. B **85**, 452-457 (1979) doi:10.1016/0370-2693(79)91294-2

[29] R. Vogt and S. J. Brodsky, "Intrinsic charm production of doubly charmed baryons: Collider vs. fixed-target," Sci. China Phys. Mech. Astron. **63**, no.2, 221066 (2020) doi:10.1007/s11433-019-1496-7

[30] J. Badier *et al.* [NA3 Collaboration], "Experimental J/Ψ hadronic production from 150 to 280 GeV/c," Z. Phys. C **20**, 101 (1983).

[31] M. J. Leitch *et al.* [NuSea Collaboration], "Measurement of J/Ψ and Ψ' suppression in $p-A$ collisions," Phys. Rev. Lett. **84**, 3256 (2000).

[32] R. Aaij *et al.* [LHCb Collaboration], "First measurement of charm production in its fixed-target configuration at the LHC," Phys. Rev. Lett. **122**, 132002 (2019).

[33] S. J. Brodsky, I. Schmidt and S. Liuti, "Is the Momentum Sum Rule Valid for Nuclear Structure Functions ?," [arXiv:1908.06317 [hep-ph]].

[34] R. Vogt, S. J. Brodsky and P. Hoyer, "Systematics of charm production in hadronic collisions," Nucl. Phys. B **383**, 643-684 (1992) doi:10.1016/0550-3213(92)90091-O

[35] P. Chauvat *et al.* [R608 Collaboration], "Production of Λ_c with large x_F at the ISR," Phys. Lett. B **199**, 304 (1987).

[36] E. M. Aitala *et al.* [E791 Collaboration], "Asymmetries in the production of Λ_c^+ and Λ_c^- baryons in 500 GeV/c π^- nucleon interactions," Phys. Lett. B **495**, 42 (2000).

[37] E. M. Aitala *et al.* [Fermilab E791 Collaboration], "Differential cross sections, charge production asymmetry, and spin-density matrix elements for $D^{*\pm}(2010)$ produced in 500-GeV/c π^--nucleon interactions," Phys. Lett. B **539**, 218 (2002).

[38] G. Aad *et al.* [ATLAS Collaboration], "Measurement of $W^\pm$ and Z-boson production cross sections in pp collisions at $\sqrt{s} = 13$ TeV with the ATLAS detector," Phys. Lett. B **759**, 601 (2016).

[39] G. Aad *et al.* [ATLAS Collaboration], "Measurement of the Z/γ^* boson transverse momentum distribution in pp collisions at $\sqrt{s}$ = 7 TeV with the ATLAS detector," JHEP **1409**, 145 (2014).

[40] G. Aad *et al.* [ATLAS Collaboration], "Measurement of the transverse momentum and ϕ_η^* distributions of Drell-Yan lepton pairs in proton-proton collisions at $\sqrt{s} = 8$ TeV with the ATLAS detector," Eur. Phys. J. C **76**, 291 (2016).

[41] V. Khachatryan *et al.* [CMS Collaboration], "Measurement of the Z boson differential cross section in transverse momentum and rapidity in proton-proton collisions at 8 TeV," Phys. Lett. B **749**, 187 (2015).

[42] S. Q. Wang, S. J. Brodsky, X. G. Wu, L. Di Giustino and J. M. Shen, "Renormalization Scale Setting for Heavy Quark Pair Production in e^+e^- Annihilation near the Threshold Region," [arXiv:2002.10993 [hep-ph]].

[43] S. Q. Wang, S. J. Brodsky, X. G. Wu, J. M. Shen and L. Di Giustino, "Novel method for the precise determination of the QCD running coupling from event shape distributions in electron-positron

annihilation," Phys. Rev. D **100**, no.9, 094010 (2019) doi:10.1103/PhysRevD.100.094010 [arXiv:1908.00060 [hep-ph]].

[44] Jefferson Lab experiment E12-12-006, "Near Threshold Electroproduction of J/ψ at 11 GeV," spokespersons: K. Hafidi, Z.-E. Meziani, X. Qian, N. Sparveris, Z. W. Zhao.

[45] R. Laha and S. J. Brodsky, "IceCube can constrain the intrinsic charm of the proton," Phys. Rev. D **96**, 123002 (2017).

[46] J. R. West, S. J. Brodsky, G. F. de Teramond, A. S. Goldhaber and I. Schmidt, [arXiv:2004.14659 [hep-ph]].

[47] S. J. Brodsky, "Hadron Physics at the Charm and Bottom Thresholds and Other Novel QCD Physics Topics at the NICA Accelerator Facility," SLAC-PUB-15050.

[48] R. Vogt and S. J. Brodsky, Sci. China Phys. Mech. Astron. **63**, no.2, 221066 (2020) doi:10.1007/s11433-019-1496-7

[49] S. Brodsky, S. Groote and S. Koshkarev, "Resolving the SELEX-LHCb double-charm baryon conflict: the impact of intrinsic heavy-quark hadroproduction and supersymmetric light-front holographic QCD," Eur. Phys. J. C **78**, no.6, 483 (2018) doi:10.1140/epjc/s10052-018-5955-1 [arXiv:1709.09903 [hep-ph]].

[50] S. J. Brodsky and M. Karliner, "Intrinsic charm of vector mesons: A Possible solution of the 'rho pi puzzle'," Phys. Rev. Lett. **78**, 4682-4685 (1997) doi:10.1103/PhysRevLett.78.4682 [arXiv:hep-ph/9704379 [hep-ph]].

[51] S. J. Brodsky and S. Gardner, "Comment on New Limits on Intrinsic Charm in the Nucleon from Global Analysis of Parton Distributions," Phys. Rev. Lett. **116**, no.1, 019101 (2016) doi:10.1103/PhysRevLett.116.019101 [arXiv:1504.00969 [hep-ph]].

[52] S. Brodsky, E. Chudakov, P. Hoyer and J. Laget, "Photoproduction of charm near threshold," Phys. Lett. B **498**, 23-28 (2001) doi:10.1016/S0370-2693(00)01373-3 [arXiv:hep-ph/0010343 [hep-ph]].

[53] M. G. Albrow, Talk at this conference.

Opportunities for Indirect Searches of Flavor Violation Higgs in Future DIS

M. Gómez-Bock[1], W. Gonzalez[2], M. Hentschinski[1], A. Rosado[2]

melina.gomez@udlap.com, wendyg@ifuap.buap.mx,
martin.hentschinski@udlap.com, rosado@ifuap.buap.mx

[1]Departamento de Actuaria, Física y Matemáticas, Universidad de las Américas Puebla,
Ex-Hacienda Santa Catarina Martir S/N, San Andrés Cholula, C.P. 72820, Puebla, Mexico
[2] Instituto de Física, Benemérita Universidad Autónoma de Puebla,
Apartado Postal J-48, Puebla, C.P. 72570, Puebla, Mexico

Presented at the Workshop of QCD and Forward Physics at the EIC, the LHC, and Cosmic Ray Physics in Guanajuato, Mexico, November 18-21 2019

Abstract

Processes of Flavor Changing Neutral Currents are present at tree level in Beyond Standard Models which makes them an important source of new physics signals. To examine the scenarios that could exhibit such events, we have performed a search in the parameter space to determine the possible production of a single top quark in ep Deep Inelastic Scattering, in the context of a flavor violation extended model, the THDM type III, for energies given by current and future colliders. We show the order of magnitude for the model parameter $|\tilde{\chi}^f_{ij}|$ that would allow for the observation of flavor violation through the scalar sector.

1 Introduction

Within the Standard Model (SM) quarks acquire their mass through spontaneous symmetry breaking [1]. This mechanism can however not explain the mass spectrum or hierarchy. In particular, the coefficients directly related to the mass values, the Yukawa couplings, are only determined experimentally, for example in CMS [2]. The Higgs mechanism can be performed with more than one Higgs doublet [3]. The way to establish the precise model is by direct search of new scalars, but also through indirect searches such as rare processes. In order to arrive at a better understanding of possible new physics scenarios, we therefore need to consider new models beyond SM, where the requirement of non zero flavor mixing couplings are part of the model.

Adding another Higgs doublet to the Standard Model is the simplest extension possible. It leads to the the Two Higgs Doublets Models (THDM) in which masses of the quarks origin from two considered doublets and not only from one as in the SM. For type III models the two doublets are furthermore coupled to the two types of quarks (up and down) [4]. These features of the model

would explain in a more natural way the mass hierarchy of the SM fermions.

Flavor Changing Neutral Currents (FCNC) are a promising process to search for physics beyond the Standard Model. This kind of processes are also present through radiative corrections in the SM, but at tree level in extended models. Their measurement would therefore yield an intermediate new physics signal. The experimental results for single top production as searched for within the CMS experiment [2], already reveals a first excess of events, although still within the statistical error and it remains to be seen whether this excess can be further established or not.

Flavor violating processes have been widely studied in literature, in particular for the so called exotic decays via neutral Higgs boson, for instance, with a top quark involved using an effective Lagrangian [5], through higher dimension operators in the context of THDM [6], and in the specific scenario of THDM-III [7, 8]. In order to know with certainty if we are in extended model domains, an excellent candidate to study such processes is given by events which come with a top quark: the top quark mass mass is the largest of the known elementary particles and its behavior sets experimental boundaries. Additionally, we have selected t-channel production since is the biggest cross section measured at the LHC. [9]

In the following we present cross sections of the top quark production processes in Deep Inelastic Scattering (DIS) in the context of the THDM-III for the current and future colliders energies.

2 Cross Section

To describe the cross-section of electron + proton $\to$ 2 fermions via neutral Higgs boson exchange, we make use of factorization of strong interaction matrix elements in the collinear limit, where the hard scales $M \gg \Lambda_{\rm QCD}$ is given by the mass of the produced top quark $M = m_t = 173.0$ GeV. We therefore find for cross-section the following factorized expression,

$$\sigma(ep \to l'q') = \sum_i \int_0^1 dx f_i(x, M^2)\, \hat{\sigma}^{eq}, \tag{2.1}$$

where $\hat{\sigma}^{eq}$ denotes the partonic electron-quark (eq) cross sections with i the quark flavor index and $f_i(x', M^2)$ the Parton Distribution Function of quark with flavor i. For the actual implementation we make use of of the pdf set MMHT2014 NLO 120 set [10]. The partonic cross-section $\hat{\sigma}^{eq}$ is given

$$\hat{\sigma}^{eq} = \frac{1}{16\pi(xs)^2} \int_{t^-}^{t^+} |\mathcal{M}(t)|^2 dt, \tag{2.2}$$

where $|\mathcal{M}(t)|^2$ is the squared matrix element of the process $ep \to l'q'$ and x denote the proton momentum fraction. It is important to keep in mind that we are looking for a single top production via neutral Higgs boson exchange (but with flavor exchange) at tree level. The reaction of interest process is therefore $ep \to \mu\, t$; for the relevant Feynman Diagram see Fig. 1

The quarks couplings with the neutral Higgs bosons [11] can be obtained from the the follow-

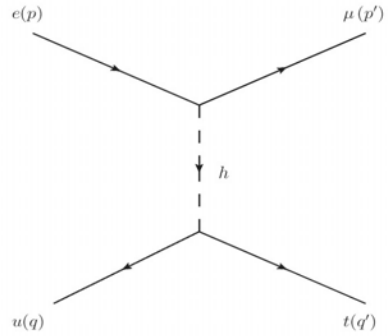

Figure 1: Process $eu \to \mu t$

ing Lagrangian:

$$\begin{aligned}
\mathcal{L}_Y^q =& \frac{g}{2}\left(\frac{m_{d_i}}{M_W}\right)\bar{d}_i\left[\frac{\cos\alpha}{\cos\beta}\delta_{ij}+\frac{\sqrt{2}\sin(\alpha-\beta)}{g\cos\beta}\left(\frac{m_W}{m_{d_i}}\right)(\tilde{Y}_2^d)_{ij}\right]d_jH^0 \\
&+\frac{g}{2}\left(\frac{m_{d_i}}{M_W}\right)\bar{d}_i\left[-\frac{\sin\alpha}{\cos\beta}\delta_{ij}+\frac{\sqrt{2}\cos(\alpha-\beta)}{g\cos\beta}\left(\frac{m_W}{m_{d_i}}\right)(\tilde{Y}_2^d)_{ij}\right]d_jh^0 \\
&+i\frac{g}{2}\left(\frac{m_{d_i}}{M_W}\right)\bar{u}_i\left[-\tan\beta\delta_{ij}+\frac{\sqrt{2}}{g\cos\beta}\left(\frac{m_W}{m_{d_i}}\right)(\tilde{Y}_2^d)_{ij}\right]\gamma^5d_jA^0 \\
&+\frac{g}{2}\left(\frac{m_{u_i}}{M_W}\right)\bar{u}_i\left[\frac{\sin\alpha}{\sin\beta}\delta_{ij}+\frac{\sqrt{2}\sin(\alpha-\beta)}{g\sin\beta}\left(\frac{m_W}{m_{u_i}}\right)(\tilde{Y}_1^u)_{ij}\right]u_jH^0 \\
&+\frac{g}{2}\left(\frac{m_{u_i}}{M_W}\right)\bar{u}_i\left[\frac{\cos\alpha}{\sin\beta}\delta_{ij}+\frac{\sqrt{2}\cos(\alpha-\beta)}{g\sin\beta}\left(\frac{m_W}{m_{u_i}}\right)(\tilde{Y}_1^u)_{ij}\right]u_jh^0 \\
&+i\frac{g}{2}\left(\frac{m_{u_i}}{M_W}\right)\bar{u}_i\left[-\cot\beta\delta_{ij}+\frac{\sqrt{2}}{g\sin\beta}\left(\frac{m_W}{m_{u_i}}\right)(\tilde{Y}_2^d)_{ij}\right]\gamma^5u_jA^0
\end{aligned} \tag{2.3}$$

The leptonic part is obtained by replacing $d_i \to l_i$. By using the Cheng-Sher ansatz to reproduce the mass hierarchy, the Yukawa couplings from the previous Lagrangian can be described in terms of dimensionless experimental parameters $\tilde{\chi}_{i,j}$.,

$$\begin{aligned}
\left(\tilde{Y}_2^{d,l}\right)_{i,j} &= \frac{\sqrt{m_i^{d,l}m_j^{d,l}}}{v}\tilde{\chi}_{i,j}^{d,l} \\
\left(\tilde{Y}_1^{u,l}\right)_{i,j} &= \frac{\sqrt{m_i^{u}m_j^{u}}}{v}\tilde{\chi}_{i,j}^{u}.
\end{aligned} \tag{2.4}$$

Similar to Eq. (2.4), a large number of proposals to a achieve specific fermion mass matrices are possible, see for instance reference [12]. The four zero texture matrix fits however quite well with the quark mixing data. It is worth to point out that, as a consequence of regarding $\tilde{\chi}_{i,j}^f$ as experimental parameters, we will be able to define a range where it would be feasible to measure this FCNC processes. According to Eqs. (2.3) and (2.4), the vertex factor at the leptonic line reads:

$$\frac{g}{2}\bar{l}_i\left[-\left(\frac{m_{l_i}}{m_W}\right)\frac{\sin\alpha}{\cos\beta}\delta_{ij}+\frac{\cos(\alpha+\beta)}{\sqrt{2}\cos\beta}\left(\frac{\sqrt{m_{l_i}m_{l_j}}}{m_W}\tilde{\chi}_{ij}^l\right)l_j\right]h^0, \tag{2.5}$$

while one has for up type quarks:

$$\frac{g}{2}\bar{u}_i\left[\left(\frac{m_{u_i}}{m_W}\right)\frac{\cos\alpha}{\sin\beta}\delta_{ij}-\frac{\cos(\alpha-\beta)}{\sqrt{2}\sin\beta}\left(\frac{\sqrt{m_{u_i}m_{u_j}}}{m_W}\tilde{\chi}_{ij}^u\right)u_j\right]h^0. \tag{2.6}$$

To obtain the corresponding terms for down quarks, we perform the substitution $l \rightarrow d$ in Eq. (2.5). Hence for the case shown in the Fig. 1 we obtain:

$$|\mathscr{M}|^2 = \frac{1}{\left[(p-p')^2 - m_H^2\right]^2} \sum_{s,s'} \mathscr{M}_{leptonic}\, \mathscr{M}^{quark}, \tag{2.7}$$

with

$$\mathscr{M}_{leptonic} = \bar{\mu}(p') \left[\frac{\cos(\alpha-\beta)}{\sqrt{2}\cos\beta} \frac{\sqrt{m_e m_\mu}}{m_W} \tilde{\chi}^l_{ij} \right] e(p)\bar{e}(p) \left[\frac{\cos(\alpha-\beta)}{\sqrt{2}\cos\beta} \frac{\sqrt{m_e m_\mu}}{m_W} \left(\tilde{\chi}^l_{ij}\right)^* \right] \mu(p'), \tag{2.8}$$

$$\mathscr{M}^{quark} = \bar{t}'(q') \left[\frac{\cos(\alpha-\beta)}{\sqrt{2}\sin\beta} \frac{\sqrt{m_u m_t}}{m_W} \tilde{\chi}^u_{ij} \right] u(q)\bar{u}(q) \left[\frac{\cos(\alpha-\beta)}{\sqrt{2}\sin\beta} \frac{\sqrt{m_u m_t}}{m_W} \left(\tilde{\chi}^u_{ij}\right)^* \right] t(q'), \tag{2.9}$$

and

$$|\mathscr{M}|^2 = CW|\tilde{\chi}^l_{12}|^2|\tilde{\chi}^u_{13}|^2 \frac{\left[t-(m_\mu-m_e)^2\right]\left[t-(m_q-m_t)^2\right]}{(t-m_H^2)^2}, \tag{2.10}$$

where

$$C = \frac{\cos^4(\alpha-\beta)}{\cos^2\beta\sin^2\beta} \quad \text{and} \quad W = \frac{m_e m_\mu m_u m_t}{m_W^4}.$$

Combining Eqs. (2.1) and (2.2) we find

$$\sigma^{ep}(ep \rightarrow \mu\, t) = CW|\tilde{\chi}^l_{12}|^2|\tilde{\chi}^u_{13}|^2 \sum_i \int_0^1 dx' \frac{f_i(x',\tilde{Q}^2)}{x' s} \cdot \int_{-t}^{+t} dt \frac{\left[t-(m_\mu-m_e)^2\right]\left[t-(m_q-m_t)^2\right]}{(t-m_H^2)^2}. \tag{2.11}$$

For the following analysis we further define

$$k = CW|\tilde{\chi}^l_{12}|^2|\tilde{\chi}^u_{13}|^2, \tag{2.12}$$

which collects the model dependent coupling constants. In the next section, we will discuss the consequences of the k value on the total cross section given by Eq. (2.11), particularly the effects on the $|\tilde{\chi}^{u,d,l}_{i,j}|^2$ parameters.

3 Results

Once we have obtained Eq. (2.11) we are in a position to make an important assignment: for the case where $k \neq 1$, the parameters $|\tilde{\chi}^{u,d,l}_{i,j}|$ are of the order of magnitude of about $\sim 10^1$ as proposed in [11]. Using this approximations, the cross section gets reduced in a notable way due to the value of W which has an order of magnitude of about 10^{-13}, making the observation of a flavor violating process highly unlikely. On the other hand if we had an scenario with $k = 1$ then the cross section σ^{ep} would be experimentally observable. In such case the order of magnitude of the parameters must be of order $|\tilde{\chi}^{u,d,l}_{ij}|^2 \sim 10^3$.

Our results are shown in Fig. 2 and Fig. 3. Fig. 2 shows electron and up quark (eu) at the initial state and Fig. 3 electron and charm quark (ec); note that convolutions with the corresponding parton distribution functions have been taken. Each figure display two cases, $k = 1$ where $|\tilde{\chi}^{u,d,lf}_{i,j}|^2 \sim 10^3$ and $k \neq 1$ where $|\tilde{\chi}^f_{12}|^2 \sim 10^1$. The center of mass energies used for calculation are: HERA $\sqrt{s} = 0.310$ TeV, LHeC $\sqrt{s} = 1.3$ TeV, LHeC-he $\sqrt{s} = 1.9$ TeV, and FCC-he $\sqrt{s} = 3.5$ TeV (see also [13])

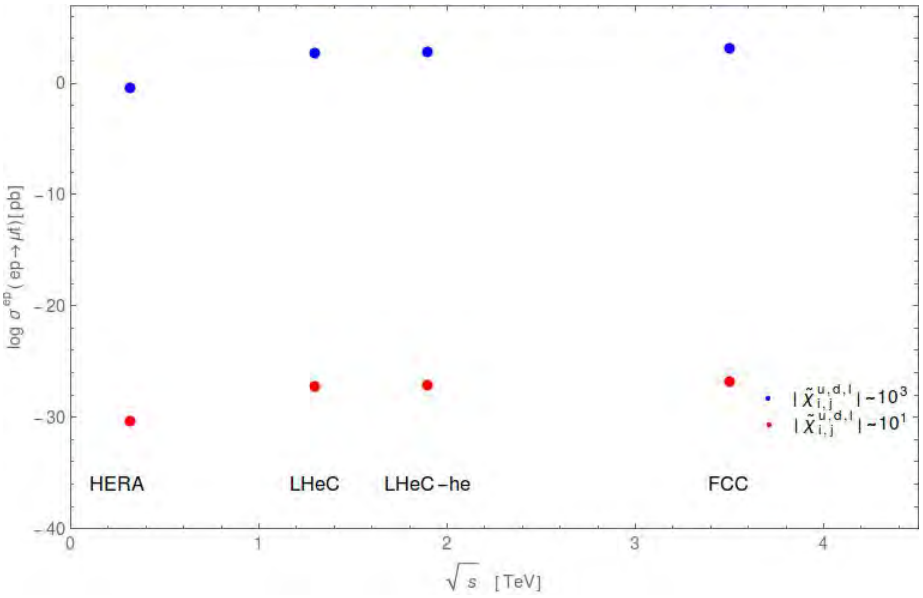

Figure 2: eu as initial state

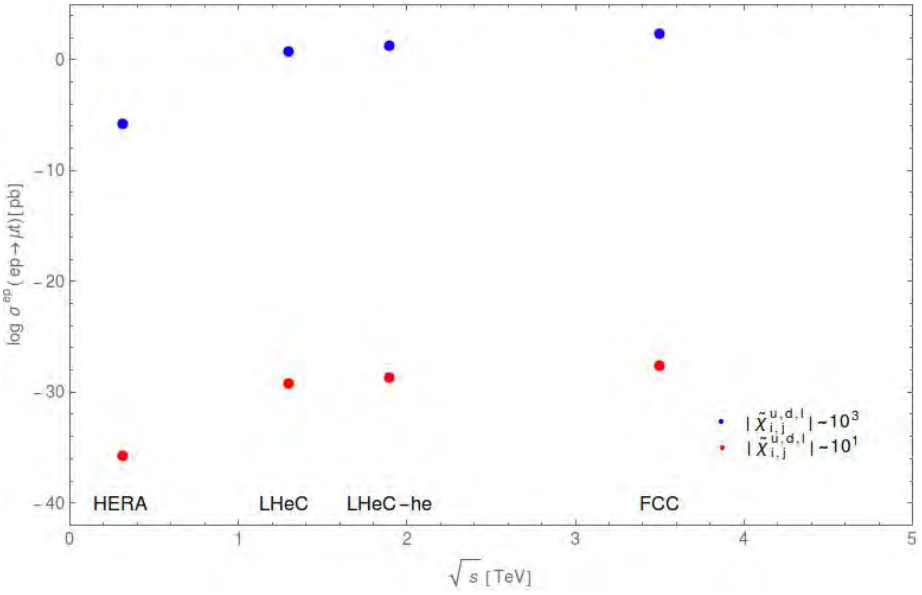

Figure 3: ec as initial state

4 Conclusions

In this contribution we discussed the possiblity to observe effects of a flavor violating Higgs boson in Deep Inelastic Scattering processes at current and future colliders. While cross-sections are small and their observation would be challenging, it can be seen that in the case of $k = 1$ experimental detection might be possible, especially as the highest center of mass energies.

In general, Flavour Changing Neutral Currents interactions where Higgs Boson and top quark are involved, are an excellent source to seek beyond Standard Model signals. In addition, according to [14] those kind of processes have not been reviewed so far, so we continue investigating

what will be observed in different scenarios. In fact it is the goal of our work to know which conditions would lead us to a $k = 1$ scenario. For $|\tilde{\chi}^f_{12}|^2 \sim 10^1$ the cross section is on the other hand too small and an experimental observation appears hardly possible. It seems therefore not possible to exclude this kind of scenarios through Deep Inelastic Scattering processes.

Acknowledgements

We want to thank Cristian Baldenegro for his useful discussion on experimental results. W. Gonzalez gratefully acknowledges the scholarship from CONACyT which allowed development of the present work and also thankful to Dr. A. Rosado for for financial support at the project. Support by Consejo Nacional de Ciencia y Tecnología grant number A1 S-43940 (CONACYT-SEP Ciencias Básicas) as well as funds assigned by the Decanato de Investigación y Posgrado UDLAP are gratefully acknowledged.

References

[1] J. D. Wells, *Lectures on Higgs Boson Physics in the Standard Model and Beyond*, in *38th British Universities Summer School in Theoretical Elementary Particle Physics*, 9, 2009. arXiv:0909.4541.

[2] **CMS** Collaboration, A. M. Sirunyan et al., *Search for associated production of a Higgs boson and a single top quark in proton-proton collisions at $\sqrt{s} =$ TeV*, *Phys. Rev. D* **99** (2019), no. 9 092005, [arXiv:1811.09696].

[3] M. P. Bento, H. E. Haber, J. Romão, and J. P. Silva, *Multi-Higgs doublet models: physical parametrization, sum rules and unitarity bounds*, *JHEP* **11** (2017) 095, [arXiv:1708.09408].

[4] J. Diaz-Cruz, R. Noriega-Papaqui, and A. Rosado, *Mass matrix ansatz and lepton flavor violation in the THDM-III*, *Phys. Rev. D* **69** (2004) 095002, [hep-ph/0401194].

[5] R. Goldouzian, *Search for top quark flavor changing neutral currents in same-sign top quark production*, *Phys. Rev. D* **91** (2015), no. 1 014022, [arXiv:1408.0493].

[6] M. Buschmann, J. Kopp, J. Liu, and X.-P. Wang, *New Signatures of Flavor Violating Higgs Couplings*, *JHEP* **06** (2016) 149, [arXiv:1601.02616].

[7] S. Das, J. Hernández-Sánchez, S. Moretti, A. Rosado, and R. Xoxocotzi, *Flavor violating signatures of lighter and heavier Higgs bosons within the Two Higgs Doublet Model Type-III at the LHeC*, *Phys. Rev. D* **94** (2016), no. 5 055003, [arXiv:1503.01464].

[8] A. Arhrib, R. Benbrik, C.-H. Chen, M. Gomez-Bock, and S. Semlali, *125 GeV Higgs decays into $\gamma\gamma, \gamma$ Z and rare top quark decay in generic 2HDM*, *Nucl. Part. Phys. Proc.* **273-275** (2016) 2430–2432.

[9] **CERN-LHC-CMS, CERN-LHC-ATLAS** Collaboration, A. Giammanco, *Single top quark production at the LHC*, *Rev.Phys.* **v1** (2016) 1–12, [arXiv:1511.06748].

[10] L. Harland-Lang, A. Martin, P. Motylinski, and R. Thorne, *Parton distributions in the LHC era: MMHT 2014 PDFs*, *Eur. Phys. J. C* **75** (2015), no. 5 204, [arXiv:1412.3989].

[11] M. Gomez-Bock and R. Noriega-Papaqui, *Flavor violating decays of the Higgs bosons in the THDM-III*, *J. Phys. G* **32** (2006) 761–776, [hep-ph/0509353].

[12] C. A. Jimenez-Cruz, R. Martinez, and J. A. Rodriguez Lopez, *Light higgs boson production in two higgs doublets models type III*, *Braz. J. Phys.* **v38** (2008) 455–458, [arXiv:0810.4313].

[13] O. Bruning, F. Zimmermann, M. Klein, J. Jowett, D. Pellegrini, and D. Schulte, *Future circular collider study fcc-he baseline parameters*, tech. rep., FCC-DRAFT-ACC-2017-004, 2017.

[14] J. G. Santi Bejar and J. Sola, *Higgs Boson Flavor-Changing Neutral Decays into Top Quark in a General Two-Higgs-Doublet Model*, *Nucl.Phys.* **v3** (2003) 270–288, [hep-ph/0307144v3].

Study of the potential transverse momentum and potential angular momentum within the scalar diquark model

David Arturo Amor-Quiroz[1]
Matthias Burkardt[2]
William Focillon[1]
Cédric Lorcé[1]

E-Mail: arturo.amor-quiroz@polytechnique.edu
burkardt@nmsu.edu
william.focillon@polytechnique.edu
cedric.lorce@polytechnique.edu

[1]CPHT, CNRS, Ecole Polytechnique, Institut Polytechnique de Paris, Route de Saclay, 91128 Palaiseau, France.
[2]Department of Physics, New Mexico State, University, Las Cruces, New Mexico 88003, USA.

Presented at the Workshop of QCD and Forward Physics at the EIC, the LHC, and Cosmic Ray Physics in Guanajuato, Mexico, November 18-21 2019

Abstract

We make use of a simple scalar diquark model to study the potential transverse momentum and potential angular momentum, defined as the difference between the Jaffe-Manohar and Ji notions of transverse momentum and orbital angular momentum, respectively. A non-vanishing potential angular momentum has been previously found in lattice calculations and is believed to appear due to the effects of initial/final state interactions between the spectator system and the struck quark in high energy scattering processes. Such re-scattering phenomena are similar in nature to those who are responsible for generating the Sivers shift. This motivates us to search for an estimate of the potential angular momentum in terms of the expectation value of the transverse momentum of the struck quark.

1 Introduction

One of the goals to be addressed by future experiments at the Electron Ion Collider (EIC) at the Brookhaven National Laboratory is to understand the origin of the spin of the proton [1, 2]. From a theoretical point of view, achieving such an ambitious objective requires a proper decomposition of the nucleon total angular momentum (AM) into the orbital motion and intrinsic spin of

its constituents. While many decompositions with different properties and physical interpretations are possible, the most common decompositions of AM are the Jaffe-Manohar (JM) [3] and Ji [4] decompositions. They induce different notions of orbital angular momentum (OAM) that depend on how the interacting contributions are attributed to either quarks or gluons. Providing a broader insight on other kinds of decompositions is beyond the scope of the present document. Nevertheless, for a clear explanation of the differences and the physical interpretation of some standard decompositions, the reader is referred to the reviews by Leader and Lorcé [5, 6] and Wakamatsu [7].

The fundamental difference between Ji and JM decompositions of AM is that the former is related to the usual gauge covariant derivative D_μ, while the latter is associated with the *pure* gauge covariant derivative D^μ_{pure} defined as $D^\mu_{\text{pure}} = \partial^\mu - igA^\mu_{\text{pure}}$. The notation refers to the *Chen et al.* [8] splitting of the (generally non-abelian) fields provided by [9, 10]

$$\begin{aligned} A^\mu &= A^\mu_{\text{pure}} + A^\mu_{\text{phys}} \\ F^{\mu\nu}_{\text{pure}} &= \partial^\mu A^\nu_{\text{pure}} - \partial^\nu A^\mu_{\text{pure}} - ig[A^\mu_{\text{pure}}, A^\nu_{\text{pure}}] = 0 \,, \end{aligned} \tag{1.1}$$

where gauge transformations act differently on the pure and physical fields. The *physical* part of the field A^μ_{phys} can be fixed by a condition similar to a gauge-fixing. We choose the light-front (LF) condition $A^+_{\text{phys}} = 0$ since it appears to be convenient for simplifying some calculations, as the pure gauge derivative D^μ_{pure} coincides with the common partial derivative provided by ∂^μ in the corresponding LF gauge. We also use advanced boundary conditions and omit any label indicating such a choice.

Let us start with the potential AM, defined as the difference between the Ji and Jaffe-Manohar (JM) notions of OAM $L^z_{\text{pot}} \equiv L^z_{\text{JM}} - L^z_{\text{Ji}}$ where [9, 11]

$$L^z_{\text{Ji}} \equiv \lim_{\Delta\to 0} \frac{\langle p',S'| \int \mathrm{d}^4 r\, \delta(r^+)\, \overline{\psi}(r)\gamma^+ [\boldsymbol{r}_\perp \times i\boldsymbol{D}_\perp]_z \psi(r)|p,S\rangle}{\langle P,S|P,S\rangle} \,, \tag{1.2}$$

is the Ji definition for the quark OAM inside a nucleon with initial (final) four-momentum $p^{(\prime)}$ and covariant spin $S^{(\prime)}$, while $P = \frac{p+p'}{2}$ is the average 4-momentum. On the other hand, the JM notion of quark OAM in the LF gauge is provided by

$$L^z_{\text{JM}} \equiv \lim_{\Delta\to 0} \frac{\langle p',S'| \int \mathrm{d}^4 r\, \delta(r^+)\, \overline{\psi}(r)\gamma^+ [\boldsymbol{r}_\perp \times i\boldsymbol{D}_{\text{pure},\perp}]_z \psi(r)|p,S\rangle}{\langle P,S|P,S\rangle} \,, \tag{1.3}$$

The computation of the matrix elements should first be considered with $p' \neq p$, and the forward limit $\Delta = p' - p \to 0$ has to be taken at the end. We also consider initial and final nucleon states with the same rest-frame polarization $s = s' = (\boldsymbol{s}_\perp, s_z)$ so that the covariant spin vector[1] is given by

$$S^\mu = \left[s_z P^+, -s_z P^- + \frac{\boldsymbol{P}_\perp}{P^+} \cdot (M\boldsymbol{s}_\perp + \boldsymbol{P}_\perp s_z), M\boldsymbol{s}_\perp + \boldsymbol{P}_\perp s_z\right] \tag{1.4}$$

satisfying $P \cdot S = 0$ and $S^2 = -M^2$.

By means of Eqs. (1.2) and (1.3) it is easy to verify that the difference between the Ji and JM notions of the longitudinal component of the quark OAM in the LF gauge is proportional to the gauge fields. The potential AM is consequently provided by [11]

$$\begin{aligned} L^z_{\text{pot}} &= \lim_{\Delta\to 0} \frac{\langle p',S'| \int \mathrm{d}^4 r\, \delta(r^+)\, (-g)\overline{\psi}(r)\gamma^+ [\boldsymbol{r}_\perp \times \boldsymbol{A}_{\text{phys},\perp}(r)]_z \psi(r)|p,S\rangle}{\langle P,S|P,S\rangle} \\ &= \frac{-g\,\epsilon^{ij}_\perp}{2P^+} \left[-i\nabla^i_{\Delta_\perp} \langle p', S'|\overline{\psi}(0)\gamma^+ A^j_{\text{phys},\perp}(0)\psi(0)|p,S\rangle\right]_{\Delta=0} . \end{aligned} \tag{1.5}$$

[1] In light-front coordinates any 4-vector is given by $x^\mu = [x^+, x^-, \boldsymbol{x}_\perp]$ with $x^\pm = \frac{1}{\sqrt{2}}(x^0 \pm x^3)$.

The potential AM is interpreted as the accumulated change in OAM experienced by the struck quark due to the color Lorentz forces as it leaves the target in high-energy scattering processes [12].

Similarly, the potential transverse momentum (TM) is defined as the difference between JM and Ji notions of the transverse momentum of a parton inside the nucleon [11]

$$\langle k^i_\perp \rangle_{\text{pot}} \equiv \langle k^i_\perp \rangle_{\text{JM}} - \langle k^i_\perp \rangle_{\text{Ji}} = \tfrac{-g}{2P^+} \, \langle P,S|\overline{\psi}(0)\gamma^+ A^i_{\text{phys},\perp}(0)\psi(0)|P,S\rangle \, . \tag{1.6}$$

The potential TM can be related to the Sivers shift (as justified with more detail in Section 2), which is the non-vanishing average transverse momentum of individual partons orthogonal to the nucleon transverse spin resulting from the Sivers mechanism.

Using perturbation theory, explicit calculations found that L_{pot} vanishes at tree level [13]. The aim of the present document is to check within a model calculation wether the difference between Ji and JM decompositions of OAM appears at two-loop level and to compare its magnitude with that of $\boldsymbol{k}_{\text{pot}}$ [12].

A non-vanishing potential AM is supported by recent lattice calculations which demonstrate that it can be clearly resolved and furthermore, that the JM OAM appears to be "significantly enhanced" when compared with Ji OAM [14, 15]. Additionally, the renormalization scale dependence of L_{pot} was recently studied in lattice QCD by Hatta and Yao [16] with results that seem to be compatible with those previously found in [13]. For a recent discussion of the potential AM in the Landau problem, see [17].

Both the potential TM and the potential AM are gauge invariant quantities that can in principle be experimentally observed. The reason for comparing their magnitudes is motivated by Burkardt's proposal of defining a lensing effect due to soft gluon rescattering in deep-inelastic and other high-energy scatterings. Originally, such effect was described by factorizing the Sivers function $f_{1T}^\perp$ into a distortion effect in position space (described by the distortion GPD E) times a lensing function $\mathcal{I}(\boldsymbol{b}_\perp)$ that accounts for the effect of attractive initial/final state interactions (ISI/FSI) in the impact parameter space denoted by $\boldsymbol{b}_\perp$. Such interactions are responsible for providing both TM to the outgoing quark, as well as exerting a torque on it as it leaves the target [18, 19].

Even if the notion of a lensing function is intuitive and is supported by some model calculations [19–22], we emphasize that the possibility of factorizing $\mathcal{I}(\boldsymbol{b}_\perp)$ is model dependent [23]. We argue, nevertheless, that a non-vanishing Sivers function is both a direct probe of orbital motion of the partons inside the nucleus and a necessary condition for a non-vanishing potential AM, as both mechanisms have the same physical foundations in ISI/FSI.

In the present document, we compute both the potential TM and potential AM in the framework of a simple scalar diquark model (SDM) of the nucleon at $\mathcal{O}(\lambda^2 e_q e_s)$ in perturbation theory. The model is based on the assumption that the nucleon splits into a quark and a scalar diquark structure, which are regarded as elementary fields of the theory [24]. The lagrangian for the SDM is

$$\begin{aligned}\mathcal{L}_{\text{SDM}} = &-\frac{1}{4} F^{\mu\nu}F_{\mu\nu} + \bar{\Psi}_N \left(i\partial\!\!\!/ - M\right)\Psi_N + \bar{\psi}\left(i\partial\!\!\!/ - m_q\right)\psi + \partial_\mu\phi\partial^\mu\phi^* - m_s^2\phi^*\phi \\ &+ \lambda\left(\bar{\psi}\Psi_N\phi^* + \bar{\Psi}_N\psi\phi\right) - e_q\bar{\psi}A\!\!\!/\psi - ie_s\left(\phi^*\overleftrightarrow{\partial^\mu}\phi\right)A_\mu + e_s^2 A_\mu A^\mu\phi^*\phi \, .\end{aligned} \tag{1.7}$$

In this expression, ψ represents the quark field with mass m_q; ϕ denotes the charged scalar diquark field with mass m_s; Ψ_N is the neutral nucleon field with mass M; and A are abelian gauge fields that could represent either photons or gluons, as any non-abelian effects would appear at three-loop order. The stability condition for the target nucleon is $M < m_q + m_s$. Furthermore, the photon-quark and photon-diquark couplings are given by e_q and e_s respectively, while λ is the coupling constant of the point-like scalar quark-nucleon-diquark vertex.

The target field considered in the present model has no charge, emulating either a neutron in QED or the fact that in QCD a hadron is color neutral. Such condition simplifies the calculations as no gauge fields can couple to the target. Moreover, it implies that the photon-quark and photon-diquark coupling constants are equal but with opposite sign, for instance, $e_q = -e_s$ for QED. For the corresponding QCD generalization of the results in the following sections, it suffices to do the replacement $e_q^2 \to 4\pi C_F \alpha_s$ [24].

The SDM has the feature of maintaining explicit Lorentz covariance and provides analytic results that have broadly been explored in the literature. Because of this, the SDM presents a good framework for providing an estimate of the magnitude of potential AM with respect to the magnitude of potential TM. The effect of introducing a vector diquark on said observables is beyond the interest of the present document.

The manuscript is organized as follows. In Sec. 2 we define and compute the potential TM of an unpolarized parton in a transversely polarized nucleon. Thereafter we report the potential AM in Section 3 for a parton in a longitudinally polarized nucleon and provide an estimate of its magnitude with respect to the potential TM. Finally, we summarize our results in Sec. 4.

2 The transverse momentum of unpolarized quarks inside a transversely polarized nucleon

A non-zero average transverse momentum of a parton inside a nucleon (and eventually a non-vanishing potential TM) implies the existence of a privileged direction that breaks the cylindrical symmetry induced by the axis of propagation of the nucleon. Such phenomenon can only arise due to the presence of spin correlations in the plane transverse to said propagation.

The mathematical object of interest in the transverse plane is the transverse momentum dependent correlation function, which is defined as

$$\Phi^{[\gamma^+]}(P, x, \boldsymbol{k}_\perp, S) = \frac{1}{2}\int \frac{\mathrm{d}z^- \mathrm{d}^2 z_\perp}{(2\pi)^3} e^{ik\cdot z} \langle P, S|\bar{\psi}(-\tfrac{z}{2})\gamma^+ \mathcal{W}(-\tfrac{z}{2}, \tfrac{z}{2})\psi(\tfrac{z}{2})|P, S\rangle\Big|_{z^+=0}, \tag{2.1}$$

where $\boldsymbol{k}_\perp$ is the quark transverse momentum inside a transversely polarized target with average 4-momentum P and spin vector S. The parameter x is the fraction of the total nucleon momentum carried by such quark along the LF direction. Furthermore, the LF gauge with advanced boundary conditions simplifies the Wilson line $\mathcal{W}(-\frac{z}{2}, \frac{z}{2}) \mapsto 1$ that would otherwise appear explicitly in expression (2.1) to ensure gauge invariance.

The correlation function $\Phi^{[\gamma^+]}$ can be parametrized in terms of transverse-momentum distributions (TMDs). They can be interpreted in terms of three-dimensional densities in momentum space. For the leading-twist vector operator we have for $\boldsymbol{P}_\perp = \boldsymbol{0}_\perp$

$$\Phi^{[\gamma^+]}(P, x, \boldsymbol{k}_\perp, S) \;=\; f_1(x, \boldsymbol{k}_\perp^2) - \frac{\epsilon_\perp^{ij} k_\perp^i S_\perp^j}{M} f_{1T}^\perp(x, \boldsymbol{k}_\perp^2). \tag{2.2}$$

We will focus only on the Sivers TMD $f_{1T}^\perp$ which corresponds to a correlation of the type $\boldsymbol{S}\cdot(\boldsymbol{P}\times\boldsymbol{k})$ [25]. The Sivers function describes the left-right distortion in the distribution of partons known as the Sivers effect. This effect was proposed by D. Sivers in 1990 as a way to explain large left-right asymmetries observed in pion-nucleus collisions [26]. This effect was thought to vanish due to time-reversal symmetry, but nowadays we know that processes that are odd under naive time reversal (T-odd) transformations allow the existence of mechanisms such as Sivers' [27]. The Sivers asymmetry has indeed been experimentally observed in both SIDIS [28–30] and Drell-Yan [31] processes.

In the following subsections we will discuss and try to clarify the relation between the Sivers function, the different notions of transverse momentum and the potential TM.

2.1 JM notion of transverse momentum

The Sivers mechanism gives rise to a non-zero average parton transverse momentum (TM) of the type a inside the nucleon by means of the following identity [32]

$$\langle k_\perp^{(a)i}\rangle_{\rm JM} = -\int \mathrm{d}x \int \mathrm{d}^2 k_\perp \, k_\perp^i \, \frac{\epsilon_\perp^{jk} k_\perp^j S_\perp^k}{M} f_{1T}^{\perp a}(x, \boldsymbol{k}_\perp^2) \, . \tag{2.3}$$

Due to the T-odd nature of the Sivers function, this notion of transverse momentum exactly coincides with the JM notion, as the latter refers to a non-local notion of the covariant derivative and can in principle contain a mixed symmetry under naive time reversal. The possible T-even contribution corresponding to the unpolarized TMD f_1 vanishes due to time reversal symmetry.

Moreover, total TM is conserved as long as the contributions from the partons sum up to zero in what is known as Burkardt sum rule, irrespective of the decomposition used [33]. In the case of the SDM it takes the form $\sum_{a=q,s}\langle \boldsymbol{k}_\perp^{(a)}\rangle = \boldsymbol{0}_\perp$ where q and s denote the quark and the scalar diquark, respectively. Using the expression for the quark Sivers function within the SDM provided in [34]

$$\begin{aligned} f_{1T}^{\perp q}(x, \boldsymbol{k}_\perp^2) &= \frac{\lambda^2 e_q e_s (1-x)}{4(2\pi)^4} \frac{M(m_q + xM)}{(\boldsymbol{k}_\perp^2 + \Lambda_q^2(x))} \ln\left(\frac{\boldsymbol{k}_\perp^2 + \Lambda_q^2(x)}{\Lambda_q^2(x)}\right) \\ \Lambda_q^2(x) &= x m_s^2 + (1-x) m_q^2 - x(1-x) M^2 \end{aligned} \tag{2.4}$$

and by virtue of Eq. (2.3), Goeke *et al.* found that the Burkardt sum rule is fulfilled for the JM notion of transverse momentum [35].

From the integration of Eq. (2.3) using the quark Sivers function in (2.4) and dimensional regularization, we obtained that the leading divergent piece of the JM notion of TM is provided by

$$\langle k_\perp^{(q)i}\rangle_{\rm JM} = -\frac{1}{6}\left(\frac{\lambda}{4\pi\epsilon}\right)^2 \frac{\epsilon_\perp^{ij} s_\perp^j}{(4\pi)^2} (3m_q + M)\pi e_s e_q + \mathcal{O}\left(\frac{1}{\epsilon}\right) \, . \tag{2.5}$$

In this equation, $s_\perp$ denotes the transverse polarization of the target. The factor $4\pi\epsilon$ comes from the dimensional regularization for the integral over TM, meaning that only the leading divergence is retained. The calculation requires some care as the expression in Eq. (2.4) results from a previous integral

$$\int \frac{\mathrm{d}^2 l_\perp}{(2\pi)^2} \frac{l_\perp^j}{\boldsymbol{l}_\perp^2 [(\boldsymbol{k}_\perp^2 + \boldsymbol{l}_\perp^2) + \Lambda_q^2(x)]} = -\frac{k_\perp^j}{4\pi \boldsymbol{k}_\perp^2} \ln\left(\frac{\boldsymbol{k}_\perp^2 + \Lambda_q^2(x)}{\Lambda_q^2(x)}\right) \tag{2.6}$$

which is finite in $D = 2$, that also leads to contributions of $\mathcal{O}(\epsilon^{-2})$ when making the replacement $D = 2 \to 2 - 2\epsilon$ in the integrals over the momenta $\boldsymbol{k}_\perp^2$ and $\boldsymbol{l}_\perp^2$ at the same time.

2.2 Potential transverse momentum

It is due to the local description of the full covariant derivative that Ji notion of partons TM is even under naive time-reversal transformations (T-even) and therefore it has to vanish to all orders in perturbation theory. This means that the potential TM is equal to the JM notion of TM, i.e., $\langle \boldsymbol{k}_\perp\rangle_{\rm pot} = \langle \boldsymbol{k}_\perp\rangle_{\rm JM}$, where the latter can be obtained from Eq. (2.3). The potential TM is therefore a pure naive T-odd function.

We corroborated by means of an explicit calculation that the naive T-even contributions to the potential TM do vanish up to $\mathcal{O}(\lambda^2 e_q e_s)$. The non-vanishing difference between the Ji and JM

notions of TM appears only when one photon is attached to the spectator system, as a naive T-odd contribution comes from the gauge-link at the LF infinity. This supports the interpretation of such a difference as originating from ISI/FSI between the spectator system and the struck quark.

The expression we found for $\langle \boldsymbol{k}_\perp \rangle_{\rm pot}$ coincide exactly with the result displayed in Eq. (2.5) in agreement with the previous statement that $\langle \boldsymbol{k}_\perp \rangle_{\rm pot} = \langle \boldsymbol{k}_\perp \rangle_{\rm JM}$. Furthermore, the Burkardt sum rule for the JM notion of TM is confirmed for the two-loop calculation by using the equivalent expression

$$\sum_{a=q,s} \langle \boldsymbol{k}_\perp^{(a)} \rangle_{\rm pot} = \boldsymbol{0}_\perp . \tag{2.7}$$

For the sake of completeness, we shall mention that Burkardt sum rule is trivially fulfilled for the Ji decomposition as $\langle \boldsymbol{k}_\perp^{(q)} \rangle_{\rm Ji} = \langle \boldsymbol{k}_\perp^{(s)} \rangle_{\rm Ji} = \boldsymbol{0}_\perp$. This is supported by the physical intuition given that Ji decomposition excludes the effects of ISI/FSI that can provide a spin asymmetry.

3 Quark potential AM in a longitudinally polarized nucleon

Using the LF gauge it has also been computed that the Ji and JM notions of OAM coincide ($L^z_{\rm Ji} = L^z_{\rm JM}$) in the absence of gauge fields within the SDM [36]. Such result was later confirmed for the same model in the impact parameter space [37]. Furthermore, a vanishing difference between both decompositions ($L^z_{\rm pot} = 0$) was proven directly for QED [13].

As a consequence, the potential AM vanishes at one-loop order and any difference between Ji and JM decompositions can only be observed at higher order. At tree level we are able to provide analytical expressions for the OAM distributions of the partons as

$$\begin{aligned} L^{q,z}_{\rm Ji}(x) &= \frac{\lambda^2}{4\pi}(1-x)^2 \int \frac{{\rm d}^2 k_\perp}{(2\pi)^2} \frac{\boldsymbol{k}_\perp^2}{(\boldsymbol{k}_\perp^2 + \Lambda_q^2(x))^2} \\ L^{s,z}_{\rm Ji}(x) &= \frac{x}{1-x} L^{q,z}_{\rm Ji}(x) \, , \end{aligned} \tag{3.1}$$

where $\Lambda_q^2(x)$ was defined in Eq. (2.4) and $x \equiv x_q$ is the fraction of the nucleon 4-momentum carried by the quark in the LF direction. By momentum conservation, we can write for the diquark $x_s \equiv 1 - x$.

Furthermore, at the same order in perturbation theory we can make use of the expression for the longitudinal helicity parton distribution function $g^q_{1L}(x)$ in [32], which accounts for the contribution to the total AM coming from the quark spin projection along the propagation axis

$$g^q_{1L}(x) = \frac{\lambda^2}{4\pi}(1-x) \int \frac{{\rm d}^2 k_\perp}{(2\pi)^2} \frac{(m_q + xM)^2 - \boldsymbol{k}_\perp^2}{(\boldsymbol{k}_\perp^2 + \Lambda_q^2)^2} \, . \tag{3.2}$$

From the expressions in Eq. (3.1) and (3.2) it is possible to check that Ji sum rule [4] is also fulfilled at this order within the SDM

$$J = \int {\rm d}x \left[L^{q,z}_{\rm Ji}(x) + L^{s,z}_{\rm Ji}(x) + \frac{1}{2} g^q_{1L}(x) \right] = \frac{1}{2} \, . \tag{3.3}$$

A first two-loop calculation of the potential AM as defined in Eq. (1.5) will soon be reported in another publication.

4 Summary and Outlook

The potential transverse momentum was computed within the scalar diquark model as an alternative way of obtaining the difference between Ji and JM average transverse momenta, which turns out to be non-zero in perturbation theory at $\mathcal{O}(\lambda^2 e_q e_s)$.

In order to generate the Sivers effect the impact parameter distribution of unpolarized quarks in a transversely polarized target has to be distorted (non-zero E) and the fragmenting struck quark has to experience either initial or final state interactions. A non-vanishing Sivers function therefore suggests a difference between Ji and JM decompositions to appear at best at two-loop order to include initial or final state interactions between the struck quark and the spectator system.

For the moment, only one-loop calculations were carried out in the literature for Ji and JM decompositions for OAM, where they coincide as expected from the lack of initial or final state interactions. At this order it was also explicitly verified that Ji sum rule is satisfied. Further results on the two-loops calculation of the potential AM will be published in a future work.

Acknowledgements

The author D. A. Amor-Quiroz acknowledges financial support from Consejo Nacional de Ciencia y Tecnología (CONACyT) postdoctoral fellowship number 711226 (CVU 449539) and from Ecole Polytechnique. C. Lorcé by the Agence Nationale de la Recherche under the Projects No. ANR-18-ERC1-0002 and No. ANR-16-CE31-0019. M. Burkardt was supported by the DOE under grant number DE-FG03-95ER40965 and is grateful for the hospitality of Ecole Polytechnique.

References

[1] A. Accardi *et al.*, Eur. Phys. J. A **52** (2016) no.9, 268.

[2] C. A. Aidala *et al.*, arXiv:2002.12333 [hep-ph]

[3] R. L. Jaffe and A. Manohar, Nucl. Phys. B **337**, (1990) 509.

[4] X. Ji, Phys. Rev. Lett. **78**, (1997) 610.

[5] E. Leader and C. Lorcé, Phys. Rep. **541(3)**, (2014) 163.

[6] E. Leader and C. Lorcé, Phys. Rep. **802**, (2019) 23.

[7] M. Wakamatsu, Int. J. Mod. Phys. A **29**, (2014) 1430012.

[8] X.S. Chen *et al.*, Phys. Rev. Lett. **100**, (2008) 232002.

[9] Y. Hatta, Phys. Lett. B **708**, (2011) 186.

[10] C. Lorcé, Phys. Lett. B **719**, (2013) 185.

[11] M. Wakamatsu, Phys. Rev. D **81** (2010), 114010.

[12] M. Burkardt, Phys. Rev. D **88**, (2013) 014014.

[13] X. Ji *et al.*, Phys. Rev. D **93**, (2016) 054013.

[14] M. Engelhardt, Phys. Rev. D **95**, (2017) 094505.

[15] M. Engelhardt et al., PoS SPIN2018, (2019) 047.

[16] Y. Hatta, X. Yao, Phys. Lett. B **798**, (2019) 134941.

[17] M. Wakamatsu, Y. Kitadono and P.-M. Zhang, Annals Phys. **392** (2018), 287.

[18] M. Burkardt, Phys. Rev. D **66**, (2002) 114005.

[19] M. Burkardt, Nucl. Phys. A **735**, (2004) 185.

[20] M. Burkardt and D. S. Hwang, Phys. Rev. D **69**, (2004) 074032.

[21] A. Bacchetta and M. Radici, Phys. Rev. Lett. **107**, (2011) 212001.

[22] L. Gamberg and M. Schlegel, Phys. Lett. B **685**, (2010) 95.

[23] B. Pasquini, S. Rodini and A. Bacchetta, Phys. Rev. D **100**, (2019) 054039.

[24] S. J. Brodsky, D.S. Hwang and I. Schmidt, Phys. Lett. B **530**, (2002) 99.

[25] D. Sivers, Phys. Rev. D **41**, (1990) 83.

[26] J. Antille *et al.*, Phys. Lett. B **94**, (1980) 523.

[27] J.C. Collins, Phys. Lett. B **536** (2002) 43.

[28] A. Airapetian *et al.* (HERMES Collaboration), Phys. Rev. Lett. **94**, (2005) 012002.

[29] V.Y. Alexakhin *et al.*, (COMPASS Collaboration), Phys. Rev. Lett. **94** (2005) 202002.

[30] M. Alekseev *et al.* (COMPASS Collaboration), Phys. Lett. B **692**, (2010) 240–246.

[31] M. Aghasyan *et al.* (COMPASS Collaboration) Phys. Rev. Lett. **119**, (2017) 112002.

[32] S. Meissner, A. Metz, and K. Goeke, Phys. Rev. D **76**, (2007) 034002.

[33] M. Burkardt, Phys. Rev. D **69**, (2004) 091501.

[34] X. Ji and F. Yuan, Phys. Lett. B **543**, (2002) 66.

[35] K. Goeke *et al.*, Phys. Lett. B **637**, (2006) 241.

[36] M. Burkardt and Hikmat BC, Phys. Rev. D **79**, (2009) 071501(R).

[37] C. Lorcé, L. Mantovani and B. Pasquini, Phys. Lett. B **776**, (2018) 38.

Search for the gluon saturation in the deep small-x region with the LHCb Experiment.

Cesar L. da Silva

E-Mail: cesar_luiz@lanl.gov

Los Alamos National Lab

Presented at the Workshop of QCD and Forward Physics at the EIC, the LHC, and Cosmic Ray Physics in Guanajuato, Mexico, November 18-21 2019

Abstract

High-energy collisions and the excellent instrumentation in the forward direction makes LHCb one of the best candidates to confirm and explore the expected gluon saturation regime. This manuscript describe the ongoing efforts in LHCb to explore the small-x region in the search of the gluon saturation scale Q_S^2.

1 Introduction

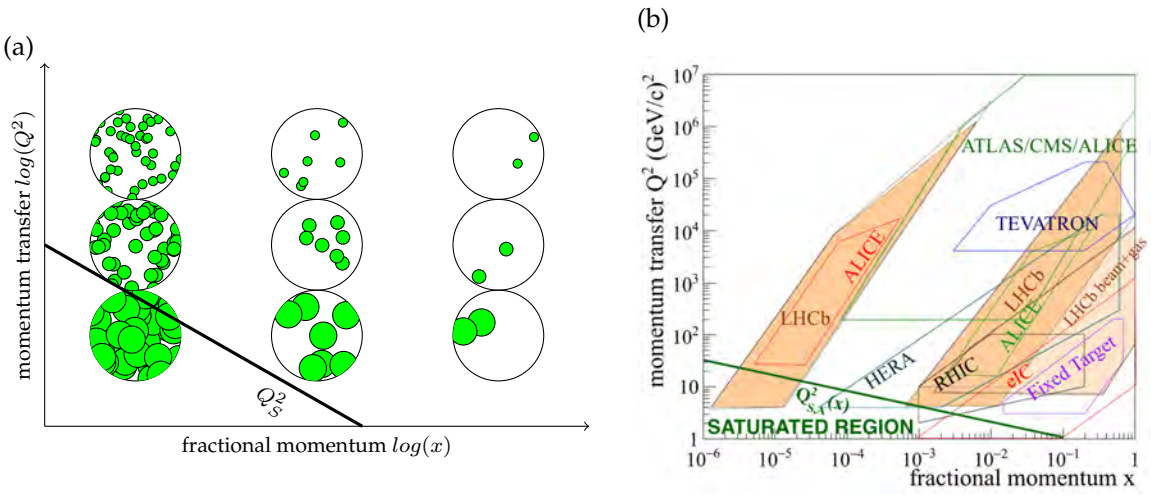

Figure 1: (a) Gluon (green circles) distribution evolution in a nucleus. (b) Kinematic coverage of past, current and future experimental facilities and the expected gluon saturation scale as estimated in [1, 2].

One of the most impacting results from DESY was the observation of a rapid growing of gluon densities towards the small-x region [3]. The measurement immediately implied that the unitarity

must be violated at some point at small-x if gluon densities grow on the scales which was observed in these $e-p$ collisions. The increasing gluon densities towards small-x are attributed to bremsstrahlung of large-x gluons. Gluon with virtuality smaller than $Q_S(x)$ will start to overlap their wave functions with neighbors (Fig. 1-a). In this saturated scenario gluons may start to fuse forming large-x gluons. Phenomenological work in [1] used HERA data to parameterize the saturation scale according to $Q_S(x) = (x_0/x)^{\lambda}$. Later work in [2] stipulated that in nucleus collisions the gluon density is enhanced by the Lorentz contraction of the nucleus at the probe rest frame. That is, the saturation scale in the nucleus is amplified by a factor $A^{1/3}$ relative to the saturation in protons. This theory turns pA collisions an interesting environment for the gluon saturation search, not requiring a too small virtuality of the probe to observe it.

The observation of gluon saturation would be a benchmark in QCD studies and astrophysics. At some point after the Big Bang there was a gluon saturated regime which may defined the fate of the universe. Saturated gluon regime and gluon fluxes, such as glasmas, may dominate the initial stages of high-energy nuclear collisions. Future high-energy colliders, such as FCC, may have particle production mostly from the gluon saturated regime. The Color-Glass Condensate (CGC) is the effective theory to calculate non-perturbative QCD using the saturation scale as a reference. The model presume that in the saturated regime the wall of condensate gluons in the nucleon looks static in the short time scale of the crossing species [4].

The unambiguous experimental evidence of the gluon saturation regime is still lacking. The approache to observe gluon saturation in hadronic colliders is to measure particle yields at forward directions in pA and pp collisions. If gluon saturation is amplified in pA collisions, we should see a large suppression of particle yields in these collisions relative to the same scaled yields in pp. Large π^0 [5] and dijet-like [6] yield suppression were observed in forward measurements at RHIC. However, other nuclear effects can also produce yield suppressions, such as parton shadowing and initial-state parton energy loss. A review of initial-state effects in nucleus can be found in [7]. Similar measurements at LHC usually lacks the forward coverage to reach the small-x region or the probes which can be measured carry a large virtuality Q^2 which is out of the range of the expected saturation scale in nucleus.

2 The LHCb Experimental Apparatus.

The LHCb experiment [8] is a single arm general purpose detector covering the pseudorapidity range 1.6$<\eta<$4.9 with e, μ, π, K, p, γ identification in a momentum range 1$< p(GeV/c) <$100. The detector has jet reconstruction capabilities and interaction point detection resolution $<$ 80 μm. During the LHC Run1 and Run2 the experiment operate with data acquisition rate of 1 MHz which is going to increase to 40 MHz rate with no hardware trigger and online reconstruction after the current long shutdown. This setup makes LHCb the sole detector fully instrumented at forward rapidity at LHC. Figure 1-b shows the kinematic coverage of several experimental facilities with emphasis on the broad coverage of LHCb and its reach into the expected gluon saturated regime.

Central exclusive processes (CEP) in pp and ultra-peripheral in PbPb events are detected with a high-rapidity detector (HeRSHeL) covering 5$<|\eta|<$9 [9]. LHCb has two modes of operation for nuclear physics: i) the collider mode which is what all LHC detectors operate, and ii) the fixed target mode, or SMOG, where the beam species collide with a low pressure noble gas inside the vertex detector (VELO). The center of mass energies reached in SMOG mode are $\sqrt{s_{NN}}$ =110 GeV in p+gas and $\sqrt{s_{NN}}$=69 GeV in Pb+gas. The rapidity at the center of the mass in p+gas is -3$< y^* <$0.5 and in Pb+gas is -2.5$< y^* <$1, depending on the gas. Details on the current and future SMOG program can be found in [10].

3 Recent results from the LHCb nuclear physics program.

Thanks to its excellent particle identification, momentum resolution and vertex determination, the LHCb is pioneering in the study of exotic particles in high multiplicity environments. A 20-year long debate on the nature of the X(3872) particle may be close to the end with the observation of its significant suppression in high multiplicity pp collisions at $\sqrt{s}$ =8 TeV [11]. The rate which the X(3872) suppress may be crucial in determining if it is a compact tetraquark or a molecular two-mesons structure. The X(3872) peak was also observed in pPb and Pbp collisions at $\sqrt{s_{NN}}$= 8.16 TeV.

Heavy flavor production in pPb collisions is one of the well known probes for initial-state nuclear effects and nuclear Parton Density Function (nPDF) constraints. LHCb has measured D-hadrons [12], B-hadrons [13] and non-prompt J/ψ [14] in forward (pPb collisions) and backward (Pbp collisions) rapidities spanning its coverage between -4.5< $|y^*|$ <4. The LHCb data is typically more precise than the current nPDFs and it has been used to additionally constrain the EPPS16 nPDF [15].

LHCb has accumulated several results with quarkonia in CEP events covering different scales of γ-pomeron fusion with J/ψ and ψ(2S) [16, 17] and bottomonia [18]; di-pomeron exchange with χ_c [19]; and double pomeron exchange with double charmonia [20]. Photon interaction with nucleus is explored with coherent J/ψ production in ultra-peripheral PbPb collisions [21]. The most recent PbPb data taken in 2018 provided 20 times more statistics for the coherent J/ψ measurement which will allow the discrimination of several models describing the small-x gluon distribution inside the nucleus.

4 Upcoming results with direct photons.

One of the few gaps of opportunities to access the expected gluon sautared region is direct photon production from inverse Compton process ($q + g \rightarrow \gamma + q$). This process has no significant NLO contribution and the kinematic variables Q^2 and x can be easily calculated from

$$x_{Pb} \approx \frac{p_{T,\gamma}}{\sqrt{s_{NN}}} e^{-y_\gamma} + \frac{p_{T,\gamma}}{\sqrt{s_{NN}}} e^{-y_h} \qquad\qquad Q^2 \approx 2p^2_{T,\gamma}, \tag{4.1}$$

assuming the transverse momentum of the photon $p_{T,\gamma}$ and the final-state quark are balanced. The rapidity of the photon y_γ and the leading hadron in the fragmented quark y_h complete the input needed in the calculation. Initial-state effect computations including dynamical shadowing and quark energy loss indicate that these effects are small in forward measurements at LHC [22]. The CGC indicates a strong suppression of direct photon [23] compared to other nuclear effects.

In LHCb photons can be measured mostly in the electromagnetic calorimeter (ECAL) but with limited momentum resolution and background from neutral pion mergers. Photons converted in di-electron pairs inside the detector material, despite its small detection efficiency, are cleaner and profits from the good tracking momentum resolution. Isolated photon+hadron angular correlations provides large statistics, nearly full access to the Compton process kinematics and the possibility to implement a subtraction technique to statistically remove the large dijet background contribution. Figure 2 shows the kinematic reach of the isolated γ+hadron pairs and the angular distribution in three distinct kinematic regions. The excess in the away-side peak indicates the inverse Compton signal.

5 Conclusions.

Despite the large theoretical work regarding gluon saturation, experimental evidences are still blurred by limited experimental coverage at small-x, small Q^2 and competing initial-state effects in

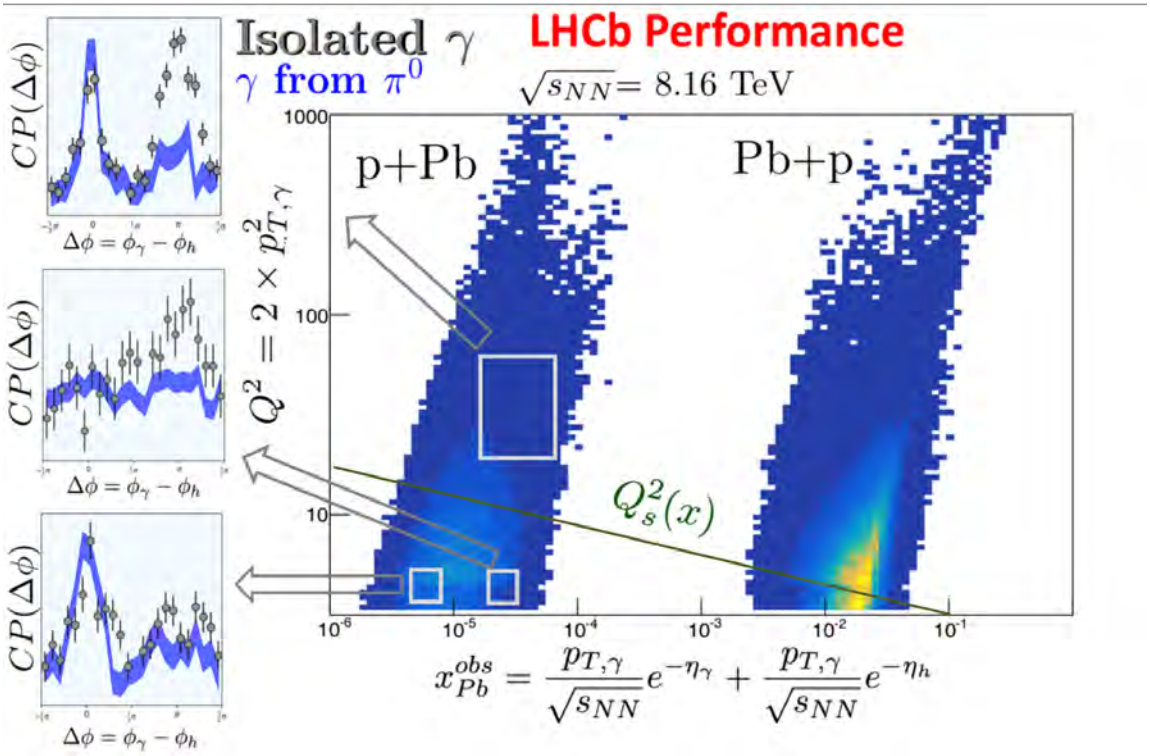

Figure 2: Correlated isolated γ+hadron angular distribution in three kinematic regions measured in pPb and Pbp collisions at $\sqrt{s_{NN}}$=8.16 TeV by LHCb. The blue band in the angular distributions corresponds to scaled dijet contributions measured from $\pi^0\gamma$+hadron pairs.

nucleus. LHCb has to date a unique coverage and instrumentation in the potential gluon saturated region. The experiment is already able to impose stringent constraints to nuclear PDFs with heavy flavor probes, CEP and γ+A processes. Further exploration in the small-x, small Q^2 region has been explored with a well control inverse Compton process obtained in isolated γ+hadron or γ+jet correlations.

Acknowledgements

This work is supported by the Office of Science of the US Department of Energy, Nuclear Physics department.

References

[1] K. J. Golec-Biernat and M. Wusthoff, *Saturation effects in deep inelastic scattering at low Q**2 and its implications on diffraction*, *Phys. Rev.* **D59** (1998) 014017, [hep-ph/9807513].

[2] H. Kowalski, T. Lappi, and R. Venugopalan, *Nuclear enhancement of universal dynamics of high parton densities*, *Phys. Rev. Lett.* **100** (2008) 022303, [arXiv:0705.3047].

[3] **ZEUS, H1** Collaboration, F. D. Aaron et al., *Combined Measurement and QCD Analysis of the Inclusive e+-p Scattering Cross Sections at HERA*, *JHEP* **01** (2010) 109, [arXiv:0911.0884].

[4] L. D. McLerran, *The Color glass condensate and small x physics: Four lectures*, *Lect. Notes Phys.* **583** (2002) 291–334, [hep-ph/0104285].

[5] **STAR** Collaboration, J. Adams et al., *Forward neutral pion production in p+p and d+Au collisions at s(NN)**(1/2) = 200-GeV*, *Phys. Rev. Lett.* **97** (2006) 152302, [nucl-ex/0602011].

[6] **PHENIX** Collaboration, A. Adare et al., *Suppression of back-to-back hadron pairs at forward rapidity in d+Au Collisions at* $\sqrt{s_{NN}} = 200$ *GeV*, *Phys. Rev. Lett.* **107** (2011) 172301, [arXiv:1105.5112].

[7] J. L. Albacete et al., *Predictions for cold nuclear matter effects in p+pb collisions at snn=8.16 tev*, *Nuclear Physics A* **972** (2018) 18 – 85.

[8] T. L. Collaboration, *The lhcb detector at the lhc*, *Journal of Instrumentation* **3** (2008), no. 08 S08005.

[9] K. Akiba et al., *The HeRSCheL detector: high-rapidity shower counters for LHCb*, *JINST* **13** (2018), no. 04 P04017, [arXiv:1801.04281].

[10] A. Bursche, H. P. Dembinski, P. Di Nezza, M. Ferro-Luzzi, F. Fleuret, G. Graziani, G. Manca, E. A. Maurice, N. Neri, L. L. Pappalardo, P. Robbe, M. Schmelling, M. A. Winn, and V. Zhukov, *Physics opportunities with the [U+FB01]xed-target program of the LHCb experiment using an unpolarized gas target*, Tech. Rep. LHCb-PUB-2018-015. CERN-LHCb-PUB-2018-015, CERN, Geneva, Dec, 2018.

[11] **LHCb Collaboration** Collaboration, *Multiplicity-dependent modification of* $\chi_{c1}(3872)$ *and* $\psi(2S)$ *production in pp collisions at* $\sqrt{s}$*= 8 TeV*, Tech. Rep. LHCb-CONF-2019-005. CERN-LHCb-CONF-2019-005, CERN, Geneva, Nov, 2019.

[12] **LHCb** Collaboration, R. Aaij et al., *Study of prompt* D^0 *meson production in pPb collisions at* $\sqrt{s_{\rm NN}} = 5$ *TeV*, *JHEP* **10** (2017) 090, [arXiv:1707.02750].

[13] **LHCb** Collaboration, R. Aaij et al., *Measurement of* B^+, B^0 *and* Λ_b^0 *production in* pPb *collisions at* $\sqrt{s_{\rm NN}} = 8.16\,$TeV, *Phys. Rev. D* **99** (2019), no. 5 052011, [arXiv:1902.05599].

[14] **LHCb** Collaboration, R. Aaij et al., *Prompt and nonprompt J/*ψ *production and nuclear modification in pPb collisions at* $\sqrt{s_{NN}} = 8.16$ *TeV*, *Phys. Lett. B* **774** (2017) 159–178, [arXiv:1706.07122].

[15] A. Kusina, J.-P. Lansberg, I. Schienbein, and H.-S. Shao, *Gluon Shadowing in Heavy-Flavor Production at the LHC*, *Phys. Rev. Lett.* **121** (2018), no. 5 052004, [arXiv:1712.07024].

[16] **LHCb** Collaboration, R. Aaij et al., *Updated measurements of exclusive* J/ψ *and* $\psi(2S)$ *production cross-sections in pp collisions at* $\sqrt{s} = 7$ *TeV*, *J. Phys. G* **41** (2014) 055002, [arXiv:1401.3288].

[17] **LHCb** Collaboration, R. Aaij et al., *Central exclusive production of* J/ψ *and* $\psi(2S)$ *mesons in pp collisions at* $\sqrt{s} = 13$ *TeV*, *JHEP* **10** (2018) 167, [arXiv:1806.04079].

[18] **LHCb** Collaboration, R. Aaij et al., *Measurement of the exclusive* Υ *production cross-section in pp collisions at* $\sqrt{s} = 7$ *TeV and 8 TeV*, *JHEP* **09** (2015) 084, [arXiv:1505.08139].

[19] **LHCb Collaboration** Collaboration, *Central Exclusive Dimuon Production at* $\sqrt{s} = 7$ *TeV*, . LHCb-ANA-2011-033.

[20] **LHCb** Collaboration, R. Aaij et al., *Observation of charmonium pairs produced exclusively in pp collisions*, *J. Phys. G* **41** (2014), no. 11 115002, [arXiv:1407.5973].

[21] **LHCb Collaboration** Collaboration, *Study of coherent* J/ψ *production in lead-lead collisions at* $\sqrt{s_{\rm NN}} = 5$ TeV *with the LHCb experiment*, Tech. Rep. LHCb-CONF-2018-003. CERN-LHCb-CONF-2018-003, CERN, Geneva, May, 2018.

[22] I. Vitev and B.-W. Zhang, *A Systematic study of direct photon production in heavy ion collisions*, *Phys. Lett.* **B669** (2008) 337–344, [arXiv:0804.3805].

[23] J. Jalilian-Marian and A. H. Rezaeian, *Prompt photon production and photon-hadron correlations at RHIC and the LHC from the Color Glass Condensate*, *Phys. Rev.* **D86** (2012) 034016, [arXiv:1204.1319].

The use of QCD evolution to detect gluon saturation in exclusive photo-production of vector mesons

Martin Hentschinski

E-Mail: martin.hentschinski@udlap.mx

Departamento de Actuaria, Física y Matemáticas, Universidad de las Américas Puebla,
Ex-Hacienda Santa Catarina Martir S/N, San Andrés Cholula 72820 Puebla, Mexico

Presented at the Workshop of QCD and Forward Physics at the EIC, the LHC, and Cosmic Ray Physics in Guanajuato, Mexico, November 18-21 2019

Abstract

We investigate photo-production of vector mesons J/Ψ and Υ measured both at HERA and LHC, using 2 particular fits of inclusive unintegrated gluon distributions. The fits are based on non-linear Balitsky-Kovchegov evolution (Kutak-Sapeta gluon; KS) and next-to-leading order Balitsky-Fadin-Kuraev-Lipatov evolution (Hentschinski-Sabio Vera-Salas gluon; HSS). We find that linear next-to-leading order evolution can only describe production at highest energies, if perturbative corrections are increased to unnaturally large values; rendering this corrections to a perturbative size, the growth with energy is too strong and the description fails. We interpret this observation as a clear signal for the presence of high gluon densities in the proton, characteristic for the onset of gluon saturation.

1 Introduction

The perturbative high energy limit of strong interactions is defined as the the limit where the center-of-mass energy $\sqrt{s}$ of a certain hadronic scattering process is pushed to infinity, while the hard scale M, which justifies the use of perturbative methods for its description, is kept fixed. One is therefore lead to consider $x \to 0$ with $x = M^2/s$ and M =fixed. Power-like growth of both the gluon and the sea-quark distribution in this region of phase space is both experimentally confirmed (in particular by the HERA collaborations) and theoretically well understood: in the low x region, quantum fluctuations in the hadron, which constantly create and annihilate quarks and gluons, are time dilated; long lived gluons therefore radiated more and more low x gluon which then leads to the observed characteristic growth. On the level of perturbative Quantum Chromodynamics (QCD), this becomes at first directly visible at the level of DGLAP splitting kernels, which lead to an enhancement of the low x region in the evolution of quark- and gluon distribution. A systematic power expansion and resummation of logarithmic enhanced terms in the low x limit is finally achieved by the Balitsky-Fadin-Kuraev-Lipatov (BFKL) evolution equation [1, 2]. While the strong coupling is in the presence of a hard scale M small, $\alpha_s = \alpha_s(M^2) \ll 1$, terms

enhanced by a low x logarithm $\alpha_s(M^2)\ln(1/x) \sim 1$ need to be resummed to all orders to leading and next-to-leading accuracy. Fixing the large x transverse momentum distribution through a fit of combined HERA data, the resulting hard or BFKL Pomeron allows for successful description of the observed rise at low x, see *e.g.* [3].

Despite of all of this, we know very well that the resulting theoretical picture must be still incomplete. The observed power-like rise of the gluon distribution at small x cannot continue forever: Unitarity dictates that the observed rise in x must eventually slow down and come to hold. It is generally believed that this happen through the formation of an over occupied system of gluons, which leads to saturation of gluon densities [4] and stops the growth. Finding convincing phenomenological evidence for gluon saturation is one of the open problems of Quantum Chromodynamics and at the core of the physics program of the future Electron Ion Collider [5]. The evolution from the low to large gluon densities is described by a set of nonlinear evolution equations, known as Balitsky-Jalilian-Marian-Iancu-McLerran-Weigert-Leonidov-Kovner evolution; its frequently used mean field version is given by the Balitsky Kovchegov (BK) [6] evolution equation.

2 The setup of our study

The central idea of our study can be easily seen from the generic form of the leading order BK evolution equation, if written in terms of the normalized dipole cross-section $N(x, \boldsymbol{r})$ (with the impact parameter dependence already integrated out); $\boldsymbol{r}$ denotes in this context the transverse separation of two colored objects in the color singlet, such as a quark-antiquark system. The equation reads:

$$\frac{d}{d\ln 1/x} N(x, \boldsymbol{r}) = \int d^2\boldsymbol{r}_1 K(\boldsymbol{r}, \boldsymbol{r}_1) \left[N(x, \boldsymbol{r}_1) + N(x, \boldsymbol{r}_2) - N(x, \boldsymbol{r}) - N(x, \boldsymbol{r}_1) N(x, \boldsymbol{r}_2) \right] \tag{2.1}$$

where $\boldsymbol{r}_2 = \boldsymbol{r} - \boldsymbol{r}_1$. The last term on the right hand side is the non-linearity, which characterizes the presence of high gluon densities $N \sim 1$. It is apparent that this term is responsible for a slow down of evolution speed if $N \sim 1$. If $N \ll 1$ on the other and, the effect of the last term is negligible and the above equation reduces to the BFKL equation. To answer the question whether we reach already at current collider experiments the region where gluon densities reach values such that the non-linear term of the evolution equation yields a sizeable value, we propose therefore to directly compare energy evolution of both LO BK evolution and NLO BFKL evolution. Only if both evolution equations deviate, we are able to claim to have reached the region of non-linear dynamics, characterized by high gluon densities.

3 Results

At the Large Hadron Collider, the region of interest, namely very low x and a hard scale close to the non-perturbative boundary, can be investigated through exclusive photo-production of vector mesons. For this observable, a large amount of data has been collected both for the production of J/Ψ and Υ vector mesons at different colliders, which allows to compare cross-sections over a wide range in center-of-mass energy and therefore x. The hard scale is in both cases given by the heavy quark mass, *i.e.* the charm (J/Ψ) and bottom (Υ) quark mass. The mass of the charm, roughly $m_c = 1.4$ GeV places us particularly close to the boundary between perturbative and non-perturbative physics., where non-linear effects are expected to manifest themselves at first. In the case of the J/Ψ one is therefore able to reach very small x values at a low transverse scale, which allows for the potential observation of saturation effects. Photo-production of the Υ provides through the larger value of the bottom quark mass a cross-check on the description in the

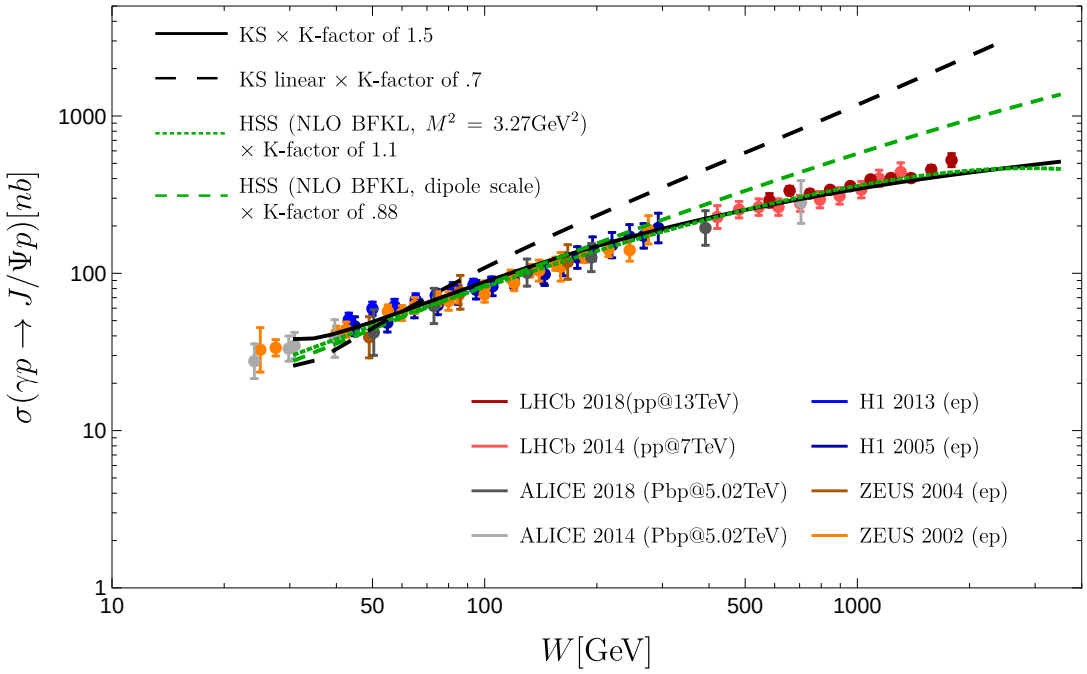

Figure 1: *Energy dependence of the J/Ψ photo-production cross-section as provided by the KS and HSS gluon distribution. The HSS distribution with dipole size scale corresponds to a specific scale setting for the HSS gluon discussed in Sec. 3. We further display photo-production data measured at HERA by ZEUS and H1 collaborations [7] as well as LHC data obtained from ALICE and LHCb [8].*

perturbative domain, where high density effects are suppressed by the hard scale. In the following we present our results, comparing both linear next-to-leading order BFKL evolution, which is based on the the Hentschinski-Salas-Sabio Vera (HSS) [3] unintegrated gluon and a particular solution to BK-evolution, with initial conditions fitted to combined HERA data by Kutak-Sapeta (KS) [9]. As long as the hard scale of the NLO BFKL gluon density is identified with an external scale, related to the heavy quark mass, we find that both linear and non-linear evolution describe data, see Fig. 1 and Fig. 2. Taking however a closer look at the dipole cross-section associated with the HSS-gluon one realizes that it consists of 2 terms:

$$N^{\text{HSS}}(x, \boldsymbol{r}, M) = N^{\text{HSS}}_{\text{dom.}}(x, \boldsymbol{r}, M) - \alpha_s^2(M^2) \ln(1/x) N^{\text{HSS}}_{\text{r.c. correction}}(x, \boldsymbol{r}, M), \tag{3.1}$$

where the second term with label "r.c. correction" contains a certain NLO correction, related to the scale of the running coupling constant, see [10] for details. While this term is small in HERA kinematics (for which the original fit has been performed), it becomes sizeable for LHC kinematics, due to the enhancement by the overall $\ln(1/x)$, altough we are formally dealing with a next-to-leading order correction. In particular, for certain values of $\boldsymbol{r}$, this term – even though formally a perturbative correction – becomes larger than the formally leading term; the perturbative expansion breaks therefore down. Since this correction is negative it is easily identified as the source of the observed slow down of the growth with energy W of the NLO BFKL solution. This instability is easily cured, if one fixes the hard scale to the inverse transverse separation of the quark-anti-quark dipole $|\boldsymbol{r}|$, instead of an external scale. Indeed, both for Υ production and J/Ψ production in the HERA region, changing the scale merely leads to a slight shift of the result, comparable to the order of a typical variation of the renormalization scale, see *e.g.* [11]. On the other hand the stabilized linear NLO BFKL evolution overshoots data for the J/Ψ in the LHC region. At the same

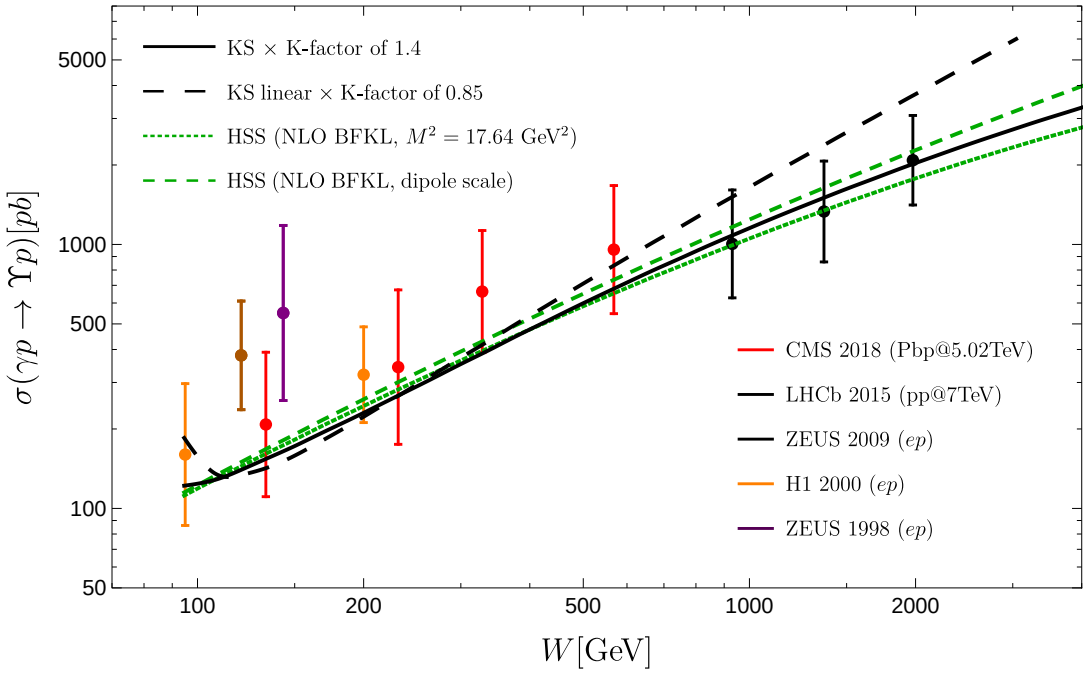

Figure 2: *Energy dependence of the Υ photo-production cross-section as provided by the KS and HSS gluon distribution. The HSS distribution with dipole size scale corresponds to a specific scale setting for the HSS gluon discussed in Sec. 3. We show HERA data measured by H1 and ZEUS [12] and LHC data by LHCb and CMS [13].*

time the energy dependence of the data is very well described by the non-linear KS gluon. To assess the importance of the non-linearities in the solution, we also compare to the KS-gluon with non-linearities turned off (dashed black line): We observe that the linear KS-gluon overshoots data. We therefore conclude that non-linear effects are essential to describe the energy dependence of J/Ψ data in the LHC region. We interpret this as a clear sign for the onset of non-linear evolution effects and therefore gluon in this region of phase space.

4 Conclusions

The observed slow-down of the growth with energy is one of the core predictions of gluon saturation. In our study we find that linear NLO BFKL evolution grows too strong to accommodate data at highest energies, once we ensure stability of the NLO BFKL evolution. It is worth to note in this context that [14] arrives from a different view point at a similar conclusion for the process of photo-production of vector mesons. To further establish the observation made in this contribution it is necessary to search for different observables which probe the low x gluon in a similar kinematic regime and to increase further the theoretical accuracy of the underlying framework. In particular it s urgently needed to establish a NLO BFKL solution which does not suffer from the observed scale ambiguity and which can therefore establish the observed effect with higher theoretical precision.

Acknowledgments

Support by Consejo Nacional de Ciencia y Tecnología grant number A1 S-43940 (CONACYT-SEP Ciencias Básicas) as well as funds assigned by the Decanato de Investigación y Posgrado UDLAP are gratefully acknowledged.

References

[1] L. N. Lipatov, Sov. J. Nucl. Phys. **23** (1976) 338, E. A. Kuraev, L. N. Lipatov, V. S. Fadin, Phys. Lett. B **60** (1975) 50, Sov. Phys. JETP **44** (1976) 443, Sov. Phys. JETP **45** (1977) 199. I. I. Balitsky, L. N. Lipatov, Sov. J. Nucl. Phys. **28** (1978) 822.

[2] V. S. Fadin, L. N. Lipatov, Phys. Lett. B **429** (1998) 127, M. Ciafaloni, G. Camici, Phys. Lett. B **430** (1998) 349.

[3] M. Hentschinski, A. Sabio Vera and C. Salas, Phys. Rev. D **87**, no. 7, 076005 (2013) doi:10.1103/PhysRevD.87.076005 [arXiv:1301.5283 [hep-ph]]; Phys. Rev. Lett. **110** (2013) no.4, 041601 [arXiv:1209.1353 [hep-ph]].

[4] L. V. Gribov, E. M. Levin and M. G. Ryskin, Phys. Rept. **100** (1983) 1. doi:10.1016/0370-1573(83)90022-4

[5] A. Accardi, J. Albacete, M. Anselmino, N. Armesto, E. Aschenauer, A. Bacchetta, D. Boer, W. Brooks, T. Burton, N. Chang, W. Deng, A. Deshpande, M. Diehl, A. Dumitru, R. Dupré, R. Ent, S. Fazio, H. Gao, V. Guzey, H. Hakobyan, Y. Hao, D. Hasch, R. Holt, T. Horn, M. Huang, A. Hutton, C. Hyde, J. Jalilian-Marian, S. Klein, B. Kopeliovich, Y. Kovchegov, K. Kumar, K. Kumerički, M. Lamont, T. Lappi, J. Lee, Y. Lee, E. Levin, F. Lin, V. Litvinenko, T. Ludlam, C. Marquet, Z. Meziani, R. McKeown, A. Metz, R. Milner, V. Morozov, A. Mueller, B. Müller, D. Müller, P. Nadel-Turonski, H. Paukkunen, A. Prokudin, V. Ptitsyn, X. Qian, J. Qiu, M. Ramsey-Musolf, T. Roser, F. Sabatié, R. Sassot, G. Schnell, P. Schweitzer, E. Sichtermann, M. Stratmann, M. Strikman, M. Sullivan, S. Taneja, T. Toll, D. Trbojevic, T. Ullrich, R. Venugopalan, S. Vigdor, W. Vogelsang, C. Weiss, B. Xiao, F. Yuan, Y. Zhang and L. Zheng, Eur. Phys. J. A **52** (2016) no.9, 268 doi:10.1140/epja/i2016-16268-9 [arXiv:1212.1701 [nucl-ex]].

[6] I. Balitsky, Nucl. Phys. B **463** (1996) 99 doi:10.1016/0550-3213(95)00638-9 [hep-ph/9509348]; Y. V. Kovchegov, Phys. Rev. D **60** (1999) 034008 doi:10.1103/PhysRevD.60.034008 [hep-ph/9901281].

[7] S. Chekanov *et al.* [ZEUS Collaboration], Eur. Phys. J. C **24**, 345 (2002) [hep-ex/0201043]; S. Chekanov *et al.* [ZEUS Collaboration], Nucl. Phys. B **695**, 3 (2004) [hep-ex/0404008]; C. Alexa *et al.* [H1 Collaboration], Eur. Phys. J. C **73**, no. 6, 2466 (2013) [arXiv:1304.5162 [hep-ex]]; A. Aktas *et al.* [H1 Collaboration], Eur. Phys. J. C **46**, 585 (2006) [hep-ex/0510016].

[8] B. B. Abelev *et al.* [ALICE Collaboration], Phys. Rev. Lett. **113**, no. 23, 232504 (2014) [arXiv:1406.7819 [nucl-ex]]; S. Acharya *et al.* [ALICE Collaboration], Eur. Phys. J. C **79**, no. 5, 402 (2019) doi:10.1140/epjc/s10052-019-6816-2 [arXiv:1809.03235 [nucl-ex]]; R. Aaij *et al.* [LHCb Collaboration], J. Phys. G **40**, 045001 (2013) [arXiv:1301.7084 [hep-ex]]; J. Phys. G **41**, 055002 (2014) [arXiv:1401.3288 [hep-ex]]; R. Aaij *et al.* [LHCb Collaboration], JHEP **1810**, 167 (2018) doi:10.1007/JHEP10(2018)167 [arXiv:1806.04079 [hep-ex]].

[9] K. Kutak and S. Sapeta, Phys. Rev. D **86** (2012) 094043 doi:10.1103/PhysRevD.86.094043 [arXiv:1205.5035 [hep-ph]].

[10] A. Arroyo Garcia, M. Hentschinski and K. Kutak, Phys. Lett. B **795**, 569 (2019) doi:10.1016/j.physletb.2019.06.061 [arXiv:1904.04394 [hep-ph]].

[11] I. Bautista, A. Fernandez Tellez and M. Hentschinski, Phys. Rev. D **94**, no. 5, 054002 (2016) doi:10.1103/PhysRevD.94.054002 [arXiv:1607.05203 [hep-ph]].

[12] C. Adloff *et al.* [H1 Collaboration], Phys. Lett. B **483**, 23 (2000) [hep-ex/0003020]; J. Breitweg *et al.* [ZEUS Collaboration], Phys. Lett. B **437** (1998) 432 [hep-ex/9807020]; S. Chekanov *et al.* [ZEUS Collaboration], Phys. Lett. B **680**, 4 (2009) [arXiv:0903.4205 [hep-ex]].

[13] R. Aaij *et al.* [LHCb Collaboration], JHEP **1509**, 084 (2015) [arXiv:1505.08139 [hep-ex]]; CMS Collaboration [CMS Collaboration], "Measurement of exclusive Y photoproduction in pPb collisions at $\sqrt{s_{\rm NN}} = 5.02$ TeV," CMS-PAS-FSQ-13-009; A. M. Sirunyan *et al.* [CMS Collaboration], Eur. Phys. J. C **79**, no. 3, 277 (2019) doi:10.1140/epjc/s10052-019-6774-8 [arXiv:1809.11080 [hep-ex]].

[14] D. Schildknecht, Phys. Lett. B **769** (2017) 166 doi:10.1016/j.physletb.2017.03.056 [arXiv:1611.01382 [hep-ph]].

Impact parameter dependence of the collinearly improved Balitsky-Kovchegov evolution equation

Marek Matas

E-Mail: matas.marek1@gmail.com

Dagmar Bendova

Jan Cepila

Jesus Guillermo Contreras

Czech Technical University in Prague, Faculty of Nuclear Sciences and Physical Engineering

Presented at the Workshop of QCD and Forward Physics at the EIC, the LHC, and Cosmic Ray Physics in Guanajuato, Mexico, November 18-21 2019

We have solved the Balistky-Kovchegov evolution equation including the impact-parameter dependence and obtained solutions which are not spoiled by the emergence of non-perturbative effects, dubbed Coulomb tails. This has been achieved due to the fact that using the collinearly-improved kernel to the BK equation suppresses heavily the part of the phase-space of the equation from which the Coulomb tails originate. This, in conjunction with an appropriate initial condition, allows for a correct description of existing data as well as to produce predictions of processes that are feasible for measurement at future facilities such as at the EIC or LHeC.

1 Introduction

The high-energy limit of QCD has been intensively studied in the past years due to the properties of the strong coupling and the applicability of perturbative expansions. This limit is reached from the experimental side by collider experiments and from the theoretical side by evolution equations. The evolution in energy (identified in this approach as rapidity) can be described by the Balitsky-Kuraev-Fadin-Lipatov (BFKL) equation [1, 2] that incorporates gluon branching processes. A non-linear contribution originating from gluon recombination is taken into account in the Balitsky-Kovchegov (BK) evolution equation [3–5]. This equation has been solved in the impact-parameter independent frame with great success in the past [6]. In this proceedings, we report our findings from [7, 8], namely a suppression of the Coulomb tails in the impact-parameter dependent computation in the collinearly improved framework. In this case, the Coulomb tails, that violate the Martin-Froissart bound and make data description impossible [9], are suppressed by the implementation of the recently proposed collinearly improved kernel [10]. The collinear resummation suppresses the contribution of the large daughter dipoles to the evolution, which are also sensitive to the non-perturbative region where Coulomb tails are the strongest. This in turn restores phenomenological predictive power of this equation for future and past experiments as shown in [7, 8].

2 The Balitsky-Kovchegov equation

The BK equation with the impact parameter dependence reads

$$\frac{\partial N(r,b;Y)}{\partial Y} = \int d\vec{r_1} K(r,r_1,r_2)\Big(N(r_1,b_1;Y) + N(r_2,b_2;Y) - N(r,b;Y) - N(r_1,b_1,Y)N(r_2,b_2;Y)\Big), \tag{2.1}$$

where $\vec{r_2} = \vec{r} - \vec{r_1}$ and $|\vec{r_i}| \equiv r_i$. The vectors $\vec{r_i}$ describe the size and orientation of the dipoles. The variables b_i denote the magnitudes of the impact parameters of the daughter dipoles.

The collinearly improved kernel suppresses the part of the phase space of the equation where large daughter dipoles are dominant [10–13] and is written as

$$K(r,r_1,r_2) = \frac{\overline{\alpha}_s}{2\pi}\frac{r^2}{r_1^2 r_2^2}\left[\frac{r^2}{\min(r_1^2,r_2^2)}\right]^{\pm\overline{\alpha}_s A_1} \frac{J_1(2\sqrt{\overline{\alpha}_s\rho^2})}{\sqrt{\overline{\alpha}_s\rho}}. \tag{2.2}$$

The value of A_1 is $11/12$ and the sign in the third factor is chosen positive when $r^2 < \min(r_1^2, r_2^2)$ and negative otherwise. $\rho \equiv \sqrt{L_{r_1 r} L_{r_2 r}}$, J_1 is the Bessel function and $L_{r_i r} \equiv \ln(r_i^2/r^2)$. The smallest dipole prescription was chosen for the running coupling: $\alpha_s = \alpha_s(r_{\min})$, where $r_{\min} = \min(r_1, r_2, r)$ as in [11].

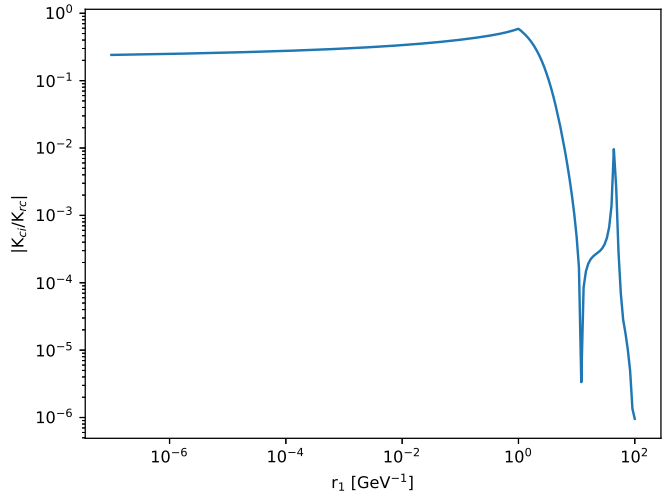

Figure 1: Absolute value of the ratio $K_{\rm ci}/K_{\rm rc}$ at a fixed dipole size $r = 1\,\mathrm{GeV}^{-1}$ and orientation with respect to the daughter dipole $\theta_{rr_1} = \pi/2$ as a function of the daughter dipole size. Figure taken from [7].

The region, where Coulomb tails enter the evolution is the one where large daughter dipoles are emitted due to the fact that those regions allow for a sufficiently small impact-parameter of a daughter dipole even when the mother dipole is far from the target center [7, 9]. As discussed earlier, this region is suppressed in the collinearly improved kernel w.r.t. the running coupling kernel [14] (shown in Fig. 1). We proposed a new prescription for the initial condition used for impact-parameter dependent computations that is motivated by the physical size of the proton target

$$N(r,b,Y=0) = 1 - \exp\left(-\frac{1}{2}\frac{Q_s^2}{4}r^2 T(b_{q_1}, b_{q_2})\right), \tag{2.3}$$

where b_{q_i} are the impact parameters of the individual quark and antiquark of the initial bare dipole and

$$T(b_{q_1}, b_{q_2}) = \left[\exp\left(-\frac{b_{q_1}^2}{2B}\right) + \exp\left(-\frac{b_{q_2}^2}{2B}\right)\right]. \tag{2.4}$$

This initial condition combines the approach of the GBW model [15] for the dipole-size dependence and an exponential fall-off for the proton profile in the impact parameter space [16–20]. More details and the value of the parameters can be found in [7]. The geometry of the target-dipole interaction is taken into account by the fact that we consider the contribution of the two quarks separately to the initial condition [7].

3 Results

Fig. 2 shows the computed dipole scattering amplitude as a function of rapidity, impact parameter and transverse dipole size. Coulomb tails in the large-b regions are strongly suppressed [7] due to the nature of the collinear resummation. We have also used the obtained scattering amplitude to predict various observables that have been measured in the past years to take use of the fact, that these solutions are no longer spoiled by the presence of non-perturbative effects to such extent that it would spoil its predictive abilities (see Figs 3 and 4).

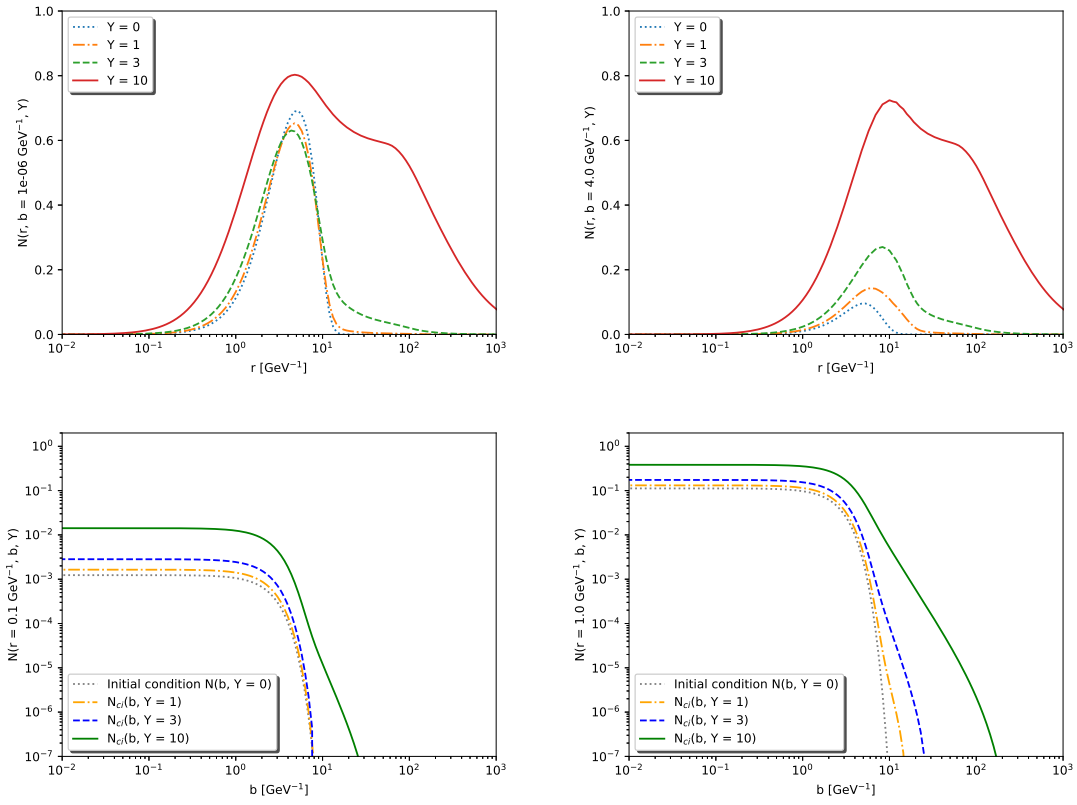

Figure 2: The dipole scattering amplitude as a solution to the BK equation with the collinearly improved kernel as a function of r for $b = 10^{-6}\,\mathrm{GeV}^{-1}$ (upper left) and $b = 4\,\mathrm{GeV}^{-1}$ (upper right), and as a function of b at $r = 0.1\,\mathrm{GeV}^{-1}$ (lower left) and at $r = 1\,\mathrm{GeV}^{-1}$ (lower right). Figure taken from [7].

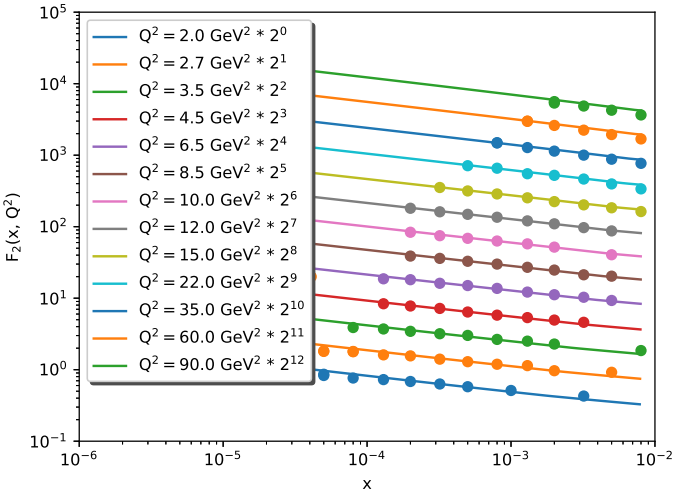

Figure 3: Comparison of the structure function data from HERA [21] (solid circles) to the prediction of the impact-parameter dependent BK equation with the collinearly improved kernel (lines). Figure taken from [7].

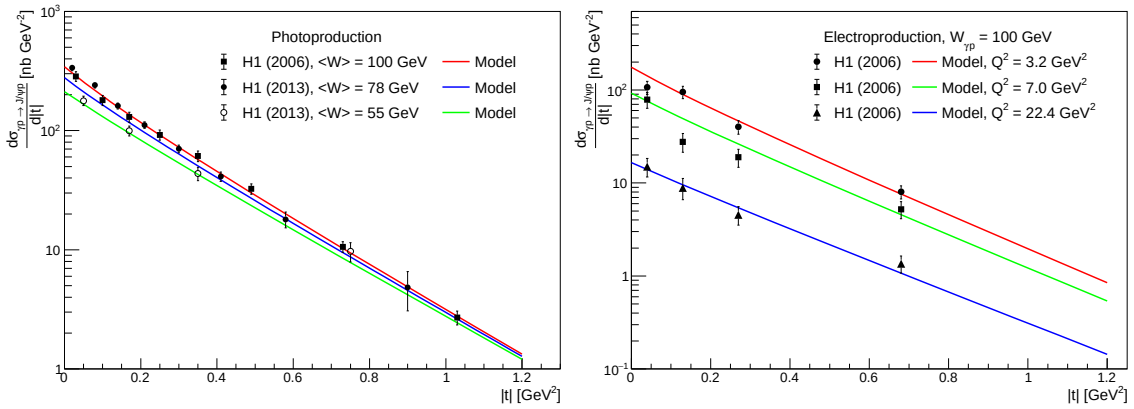

Figure 4: Comparison of the predictions of the model (solid lines) with HERA data from H1 [22, 23] for the $|t|$ dependence of the exclusive photoproduction (left) and electroproduction (right) cross sections of the J/ψ meson. Figure taken from [7].

4 Summary

The collinearly improved kernel along with the impact-parameter dependent BK equation has been used to demonstrate, that the previously established problem of Coulomb tails can be highly suppressed and the new solutions allow for a correct description of data, restoring thus the predictive capabilities of the equation when including the impact-parameter dependence. This is due to the fact, that the time-ordered gluon emissions that are embedded in the collinear resummation [11] suppress the region of large daughter dipoles [7]. This is useful for phenomenological applications in QCD namely for the future planned facilities such as LHeC and the EIC [24, 25].

Acknowledgements

This work has been partially supported from grant LTC17038 of the INTER-EXCELLENCE program at the Ministry of Education, Youth and Sports of the Czech Republic, and the COST Action CA15213 THOR. Computational resources were provided by the CESNET LM2015042 grant and the CERIT Scientific Cloud LM2015085, provided under the program Projects of Large Research, Development, and Innovations Infrastructures.

References

[1] E. A. Kuraev, L. N. Lipatov, and V. S. Fadin, *The Pomeranchuk Singularity in Nonabelian Gauge Theories*, *Sov. Phys. JETP* **45** (1977) 199–204. [Zh. Eksp. Teor. Fiz.72,377(1977)].

[2] I. I. Balitsky and L. N. Lipatov, *The Pomeranchuk Singularity in Quantum Chromodynamics*, *Sov. J. Nucl. Phys.* **28** (1978) 822–829. [Yad. Fiz.28,1597(1978)].

[3] I. Balitsky, *Operator expansion for high-energy scattering*, *Nucl. Phys.* **B463** (1996) 99–160, [hep-ph/9509348].

[4] Y. V. Kovchegov, *Small x F(2) structure function of a nucleus including multiple pomeron exchanges*, *Phys. Rev.* **D60** (1999) 034008, [hep-ph/9901281].

[5] Y. V. Kovchegov, *Unitarization of the BFKL pomeron on a nucleus*, *Phys. Rev.* **D61** (2000) 074018, [hep-ph/9905214].

[6] J. L. Albacete, N. Armesto, J. G. Milhano, P. Quiroga-Arias, and C. A. Salgado, *AAMQS: A non-linear QCD analysis of new HERA data at small-x including heavy quarks*, *Eur. Phys. J.* **C71** (2011) 1705, [arXiv:1012.4408].

[7] D. Bendova, J. Cepila, J. G. Contreras, and M. Matas, *Solution to the Balitsky-Kovchegov equation with the collinearly improved kernel including impact-parameter dependence*, *Phys. Rev.* **D100** (2019), no. 5 054015, [arXiv:1907.12123].

[8] J. Cepila, J. G. Contreras, and M. Matas, *Collinearly improved kernel suppresses Coulomb tails in the impact-parameter dependent Balitsky-Kovchegov evolution*, *Phys. Rev.* **D99** (2019), no. 5 051502, [arXiv:1812.02548].

[9] J. Berger and A. Stasto, *Numerical solution of the nonlinear evolution equation at small x with impact parameter and beyond the LL approximation*, *Phys. Rev.* **D83** (2011) 034015, [arXiv:1010.0671].

[10] E. Iancu, J. D. Madrigal, A. H. Mueller, G. Soyez, and D. N. Triantafyllopoulos, *Resumming double logarithms in the QCD evolution of color dipoles*, *Phys. Lett.* **B744** (2015) 293–302, [arXiv:1502.05642].

[11] E. Iancu, J. D. Madrigal, A. H. Mueller, G. Soyez, and D. N. Triantafyllopoulos, *Collinearly-improved BK evolution meets the HERA data*, *Phys. Lett.* **B750** (2015) 643–652, [arXiv:1507.03651].

[12] L. Motyka and A. M. Stasto, *Exact kinematics in the small x evolution of the color dipole and gluon cascade*, *Phys. Rev.* **D79** (2009) 085016, [arXiv:0901.4949].

[13] A. Sabio Vera, *An 'All-poles' approximation to collinear resummations in the Regge limit of perturbative QCD*, *Nucl. Phys.* **B722** (2005) 65–80, [hep-ph/0505128].

[14] I. Balitsky, *Quark contribution to the small-x evolution of color dipole*, *Phys. Rev.* **D75** (2007) 014001, [hep-ph/0609105].

[15] K. J. Golec-Biernat and M. Wusthoff, *Saturation effects in deep inelastic scattering at low Q**2 and its implications on diffraction*, *Phys. Rev.* **D59** (1998) 014017, [hep-ph/9807513].

[16] H. Kowalski and D. Teaney, *An Impact parameter dipole saturation model*, *Phys. Rev.* **D68** (2003) 114005, [hep-ph/0304189].

[17] G. Watt and H. Kowalski, *Impact parameter dependent colour glass condensate dipole model*, *Phys. Rev.* **D78** (2008) 014016, [arXiv:0712.2670].

[18] C. Marquet, *A Unified description of diffractive deep inelastic scattering with saturation*, *Phys. Rev.* **D76** (2007) 094017, [arXiv:0706.2682].

[19] H. Mantysaari and B. Schenke, *Evidence of strong proton shape fluctuations from incoherent diffraction*, *Phys. Rev. Lett.* **117** (2016), no. 5 052301, [arXiv:1603.04349].

[20] J. Cepila, J. G. Contreras, and J. D. Tapia Takaki, *Energy dependence of dissociative J/ψ photoproduction as a signature of gluon saturation at the LHC*, *Phys. Lett.* **B766** (2017) 186–191, [arXiv:1608.07559].

[21] **ZEUS, H1** Collaboration, F. D. Aaron et al., *Combined Measurement and QCD Analysis of the Inclusive e+- p Scattering Cross Sections at HERA*, *JHEP* **01** (2010) 109, [arXiv:0911.0884].

[22] **H1** Collaboration, A. Aktas et al., *Elastic J/psi production at HERA*, *Eur. Phys. J.* **C46** (2006) 585–603, [hep-ex/0510016].

[23] **H1** Collaboration, C. Alexa et al., *Elastic and Proton-Dissociative Photoproduction of J/psi Mesons at HERA*, *Eur. Phys. J.* **C73** (2013), no. 6 2466, [arXiv:1304.5162].

[24] A. Accardi et al., *Electron Ion Collider: The Next QCD Frontier*, *Eur. Phys. J.* **A52** (2016), no. 9 268, [arXiv:1212.1701].

[25] **LHeC Study Group** Collaboration, J. Abelleira Fernandez et al., *A Large Hadron Electron Collider at CERN: Report on the Physics and Design Concepts for Machine and Detector*, *J.Phys.* **G39** (2012) 075001, [arXiv:1206.2913].

The main purpose of this workshop was to stimulate discussions between experimentalists and theorists in forward hadronic physics, quantum chromodynamics at low-x, diffractive processes, parton saturation effects, and exciting problems in cosmic ray physics. There was special emphasis on physics accessible at the CERN Large Hadron Collider, the Brookhaven National Laboratory Relativistic Heavy Ion Collider, the future U.S. Electron Ion Collider, and cosmic ray physics experiments. The workshop took place in Guanajuato, Mexico in the days of November 18-21, 2019, following the series of meetings held in Nagoya, Japan (2015, 2017), and Stony Brook, New York (2018).